University of Nottingham
UK | CHINA | MALAYSIA
School of Physics and Astronomy

Sir Peter Mansfield Imaging Centre

Thesis submitted in September 2021 for the degree of Doctor of Philosophy

Monitoring head motion in a 7T MRI scanner using an NMR field camera

Supervisor:
Prof. Richard Bowtell

Co-supervisor:
Prof. Penny Gowland

Candidate:
Laura Bortolotti,
Student ID: 14311346

Academic year 2020/2021

Education is not something
you can finish.

Isaac Asimov

Acknowledgements

I would like to take this opportunity to say a massive <u>THANK YOU</u> to all the people that have helped me surviving the PhD.

It wouldn't have been easy to do that without the support of my supervisor and I wish to extend my special thanks to him here: thank you for having dedicated me your time and patience and shared with me your wisdom.

Thank you to everyone that has been somewhat involved in my project, I wouldn't have made it that far without your help. I hope you too have good memories of moments shared together in the lab, even when nothing worked out as expected!

Everyone that has been part of the SPMIC family in these years has contributed to make this experience unforgettable: never underestimate the power of the wish of a "Good morning" in the corridor! I am so grateful that our life-path crossed in these years and I can now call some of you friend. Thanks for having checked on me by coming at my desk on my blue days.

You'll never know who you are going to meet at conferences and I consider myself to have been really lucky so far! Thanks to those who have not disappeared from my life when conferences were over: I am definitively addicted to our video calls now!!

" Time is fleeting, madness takes its toll" – Laura Bortolotti 2021

I will always be grateful to my fiancé, to my family, to my relatives and to my friends for always being there and I would like to say thank you to covid to have brought them closer to me (even if virtually).

Thanks to myself for not giving up in hard times, to have learnt when it is time to say "No" and to take a break, and also that being hard on yourself is not the way to make it through the day!

I am really looking forward to seeing what the future holds and I will always remember to wash my hands before touching the computer from now on!

Contents

List of Figures

List of Tables

Abstract

Magnetic Resonance Imaging (MRI) is a technique for imaging the soft tissues of the human body. Research in medical MRI is moving towards the use of ultra-high field (UHF) MRI scanners since the spatial resolution of MRI increases with the strength of the magnetic field. However, involuntary movements of the subject create artefacts that can corrupt MR images. Since high resolution images are more vulnerable to motion, this effect becomes more relevant at ultra-high field. Motion artefacts can be ameliorated if the movements of the head during the scans are tracked; this is the basis of motion correction (MoCo) techniques.

This thesis explores a novel way to approach the motion tracking step of MoCo techniques in a marker-less way. The core idea is to measure the extra-cranial magnetic field changes produced by changes in head pose, and then to use these measurements to infer information about head motion. The former was measured using a magnetic field camera, a fully MRI compatible tool. In a final implementation of the approach, the field probes were held on the surface of the receiver RF coil of a 7 T scanner using a hand-made probe holder. Measurements were then acquired in the quiet periods of a multi-slice echo planar imaging sequence.

Simultaneous measurements of extra cranial magnetic field changes and head motion parameters were acquired while six collaborative subjects were instructed to perform several different types of head movement inside the scanner. The Moiré Phase Tracking System has been considered as the gold standard for evaluating the six head motion parameters inside the scanner bore.

A spatial filter, based on the use of solid harmonic functions, has been developed in order to reduce the influence of the field changes due to physiological fluctuations. Feature selection on magnetic field data has been computed using Principal Component Analysis. The subgroup of signals were identified by applying Hierarchical Cluster Analysis to signals projected into the principal component space. Furthermore, field changes due to physiological fluctuations have been exploited to generate a simple signal that could be used for respiratory monitoring.

Customised extra-cranial magnetic field simulations were implemented to test the spatial filtering process and the feasibility of using extra-cranial magnetic field changes to track head movements. Head motion parameters were predicted from simulated extra cranial magnetic field changes by using linear and a non-linear regression methods, both previously trained by supervised learning. The linear method chosen was the Partial

Least Squares method. The non-linear method chosen was a single hidden layer, recurrent and dynamic neural network based on Non-linear AutoRegressive eXogenous model (NARX). Results obtained using simulated data were confirmed on experimental data over different subjects, head motion ranges, probe displacements and sessions, using raw and spatially filtered data. A preliminary study on generalising the regression method over twenty subjects has also been conducted on simulated data.

Furthermore, extra-cranial magnetic field changes were used to discriminate between predictable and non-compensable head movements. The former are head movements well predicted by the head motion tracking (either the one developed in this dissertation or not). The latter are head movements that cannot be well compensated by applying MoCo techniques to MRI. Thus, they might lead to the need to repeat the whole MRI acquisition. The solution suggested in this dissertation is to use information given by the magnetic field probes to flag the k-space lines that need to be re-acquired due to motion effects. This could save scanning time and reduce patient discomfort.

A pilot study of an active-magnetic marker based system has been carried out using customised simulations. This system would rely on the use of the NMR field probes to detect a local magnetic field generated by small coils (0.5 cm of diameter) fixed on a pair of plastic glasses. Thanks to the use of an optimisation algorithm, the position of the coil-based system is resolved. In its future development, this system might substitute the use of the optical camera as a stand-alone system or for the purpose of the training of the motion tracking system developed in this dissertation.

Results reported in this thesis represent a step towards the full development of a marker-less technique for head motion tracking that does not require modification of the MR image sequence. In its future development, this technique can be used to improve the outcome of standard MRI procedures.

Introduction

Numerous motion correction techniques (MoCo) have been devised to prevent or correct head motion during an MRI scan [1]. As the level of artefacts tends to increase with the strength of the magnetic field [2], solving head motion problems becomes crucial at Ultra High Field (UHF). Key characteristics of MoCo methods [3] include the phenomenon used to track motion, the degree of image sequence modification that they require, the necessary interaction with the patient and the accuracy and precision of tracking. The main methods that have been developed can be roughly grouped into *field detection*, *navigator* and *optical methods*. A further classification arises from the type of marker used to detect the position of the head.

Field detection can be used for prospective motion correction by detecting the fields produced by the scanner's gradient coils and adjusting the image geometry based on the measured position of the head in the scanner. This approach requires multiple probes to be connected rigidly to the head of the subject in non-colinear positions to evaluate the position and orientation [4, 5].

Navigator methods use fast MRI data acquisitions to measure the position of the head. [6, 7]. For example, the Fat Navigator (FatNav) method is based on rapid imaging and co-registration of the fat layer that covers the skull [7]. The advantages of navigator techniques are that they do not need additional hardware or use of markers bound to the head. It is therefore a comfortable solution for the patient.

The last method is optical tracking [8, 9, 10]. This includes laser systems, bend-sensitive optical fibres and optical camera systems, divided into in-bore and out-bore systems. For the in-bore tracking system, the precision is influenced by the vibrations of the scanner during the image acquisition. The main advantage of optical systems is that their operation is independent from the MR sequence timing. An optical in-bore camera was used in this work to detect the position of the head.

All these methods rely on accurate tracking of the head position inside the scanner. This dissertation concerns the development of a new, marker-less head motion tracking technique for UHF based on the use of NMR field probes fixed inside the scanner bore.

First, the basics of Magnetic Resonance Imaging (MRI) and the physics of the NMR field probes are explored, and a brief overview of the Nuclear Magnetic Resonance (NMR) phenomenon is given (Chapter 1). This starts from the Bloch equations that describe the evolution of the magnetization taking account of the relaxation time constants T_1, T_2. The chapter ends with a comparison between low and high magnetic field MRI scanners and a brief overview of the magnetic field camera system that is used in this thesis. The camera uses 16 NMR probes, each containing a small liquid droplet. These droplets contains fluorine-19 whose NMR signal evolution is used to measure the local magnetic field.

Chapter 2 summarises motion-related problems in MRI and the motion tracking techniques that have been developed to correct motion-related MR image artefacts. This chapter discusses the use of external markers and the need to modify the imaging sequence when applying some MoCo techniques. Also, a brief discussion on how image sequences are affected by motion is given. An overview of how motion confounds clinical MRI at low/medium ($\leq 3\ T$) field is also set out, since 7T scanners are currently not widely used for clinical studies.

This thesis reports results on the development of a new contact-less head motion tracking technique based on the use of a field camera. The idea behind the technique is that the change in head positions changes the magnetic field pattern around the head, so by measuring the change in extra-cranial magnetic field it should be possible to infer the change in head positions.

Chapter 3 describes the experimental set-ups used to perform simultaneous measurements of extra-cranial magnetic field changes (ΔB) related to the changes in head pose (ΔM). The set-up consists on a in-bore magnetic field camera, comprising 16 field probes, and an in-bore optical camera, which tracks an optical marker fixed on a mouthpiece. Two customised probe-holders have been tested, characterised and compared in order to perform the best measurements of the extra-cranial magnetic field with and without simultaneous scanning. One set-up is based on the use of a PVC holder for the NMR probes [11]. This holder allows even sampling of the field in the space around the head, but requires removal of the standard receiver head coil array. The second holds the magnetic field probes in between the standard head transmit and receiver coils [12, 13]. Both the set-ups have been used to perform measurements. The second allowed measurements to be made during quiet periods of a standard EPI sequence. The Appendix B reports acquired data.

In order to study the relationship between magnetic field changes (highly subject-specific), head-probe distances and influences of physiological noise, the experiment has been mimicked in a synthetic environment (Chapter 4). Extra-cranial magnetic fields have been simulated [14] using customised 3D head models (from six subjects), real head motion parameters and respiration signals. In general, magnetic field changes vary by subject and by the proximity of the head to the field probes. Thanks to the use of simulated data, it has been demonstrated that this factors have the strongest influence on the bijective mathematical relationship between the magnetic field and the head motion parameters ($f(\Delta B) \longrightarrow \Delta M$). The Appendix B reports simulated data.

Chapter 5 represents the very core of the development of the contact-less head motion tracking technique. It is shown that head motion can be monitored by using an NMR field camera to measure the extra-cranial field changes (ΔB) produced by changes in head position (ΔM). Experimental data were acquired without simultaneous imaging, using the different set-ups, and simulated data were also used. In order to infer ΔM from ΔB with good accuracy, linear and non-linear regression methods (both based on supervised training)[15] have been tested on predicting ΔM for various head movement regimes, with ant without filtering of physiological noise from ΔB [16, 17]. The methods have been tested on simulated data at first and then the best pipeline for the analysis was validated on real data. Best results were obtained when using the non-linear method to predict small head movements ($\leq 5\ mm\ or\ ^{\circ}$)[15]. The accuracy of the results was mainly limited by the use of the optical camera for the training. The data analysis process is thoroughly explored in the Appendix A, predictions are reported in Appendix C and the code is reported in Appendix D.

Chapter 6 reports pilot studies of modifications to the set-up, that if implemented would improve the accuracy of the prediction. A method to threshold ΔB data when head motion is larger than the predictable range has been retrospectively tested[18] along with idea of using contact-less respiration-like signal measurements to implement respiration gating in an imaging sequence. Simulations of using an active magnetic marker system[19] to infer measurements of ΔM are also presented. The benefits of this approach are that problematic line-of-sight access to markers is not required (cf. optical approaches) and that it could be implemented without modification of the MRI sequence (cf. navigators). The feasibility of bringing the product to the market has also been discussed as outcome on presenting this work at ISMRM Junior Challenge 2021. These pilot studies gave promising results. However, a full implementation was prevented by the lack of access to the laboratory facilities durimg the COVID-19 pandemic.

he tracking method presented in Chapter 5 and the improvements proposed in Chapter 6 have been tested on ΔB data acquired with simultaneous imaging [12, 13] in Chapter 7. The probe-holder that fits in between the head transmitter and receiver coils has been used (Chapter 3). A strategy to acquire ΔB data minimising the influence of noise due to the scanning sequence is presented. As a result, the running of the imaging sequence does not corrupt the data and the prediction of head motion was successful. Large head movements were identified and respiration-like signals were measured retrospectively. The accuracy of the results was comparable with existing techniques. The method developed has the advantages that it can be implemented without requiring image sequence modification, or rigid coupling of a motion marker to the head. As the major downside of the technique is the subject specificity of the data, a pilot study on generalising the predictions using one model over multiple subject has been simulated. In this case, the $f(\Delta B) \longrightarrow \Delta M$, is no longer a bijective function as the same change in head position may correspond different set of magnetic field changes. To attempt to restore the bijective mathematical relationship, further parameters (such as head volume, off-centre position and angulation parameters) have been used as input along with magnetic field changes ($f(\Delta B, V, \dots) \longrightarrow \Delta M$). Predictions of movement from a simulated data sets including data from heads of different sizes, but the same morphology, indicate that incorporating additional information about head size and position in the scanner into the prediction process may improve results. A further test has been conducted on real data over four subjects. Due to the small sample of real data available, predictions were not accurate. Therefore, motion and magnetic field data over 19 subjects have been simulated and successfully predicted using the non-linear method using magnetic field changes, head volumes, off centre and angulation information as input to predict motion parameters. Customised predictions and generalised predictions were both successful and might form the basis of a full implemetation of a MoCo technique in the near future.

Effect of the COVID-19 pandemic on my PhD project

My PhD project started in February 2018, following on from my Master's project [11], and it was funded by the "Vice-Chancellor's Scholarship for Research Excellence". The pandemic outbreak happened at the beginning of the final year of my three years of PhD funding. My plans for the final year were heavily disrupted due to the lack of access to laboratory facilities, and a personal need to reduce the risk to a minimum for my partner who is a vulnerable subject. At that time, there were three main parts ongoing in my project : the development of the motion correction technique (Chapters 3, 6), the development of the motion detection technique (Chapter 3) and the development of the active magnetic marker system (Chapter 6).

The plan to fully develop the motion correction technique at 7T was to test the acquisition of magnetic field data with simultaneous scanning, to exploit already written code used to perform motion correction using data from the optical camera [20] by swapping the measured motion parameters from the optical camera to the magnetic field camera, and to write additional code, to be run by the computer controlling the magnetic field camera, to predict head motion parameters in real time. Then, the system would have been tested by comparing to results obtained with the previous pipeline. There was no commercially available solution to hold the NMR probes in the 7T scanner to perform simultaneous measurements of magnetic field data during scanning using the 32 channel receiver coil, so I was developing one by myself.

The implementation of the real-time motion detection technique was at an early stage. The Matlab code to detect motion in real time was under development, while the code to either send a warning signal to the scanner or to record the moment at which large head motion occurred was not. Old motion correction data were used to develop the code, and the real-time detection was tested by moving a phantom only (December 2019). A further issue to overcome was due to the field camera tool for the real-time control needing internet access to communicate with the scanner. The computer that drives the field camera was in need of an operating system update to be allowed to connect to the University's network after March 2020.

The development of the active magnetic marker system started in Spring 2019. Two, small copper coils were built to be tested by using a magnetometer and the field camera (mounted in a foam rings support I designed to fit inside the transmit head coil) in the 7T scanner. At first, it was necessary to test whether the signal recorded by the field camera was suitable for performing predictions of the coil system's position. The standard dipole equation was used as an objective function and predictions were made by minimising differences from measured fields for the motion parameters. Due to the unsatisfactory results, I designed a foam support designed to: (1) hold the NMR field probes in a hemispherical fashion, (2) hold the coils (mounted in a transparent plastic block) and 2 holographic markers in a rigid fashion on a movable support, and (3) simultaneously measure the position of the holographic markers using the MPT camera. More reliable measurements (November 2019) and better prediction were obtained by minimising the objective function by the rotation matrix that describes the movements of the system, but the way in which the NMR field probes were held was not suitable for MR imaging.

Furthermore, the use of simulations on two out of three parts was running in parallel to drive the further test to be conducted in the laboratory.

At the beginning of my final year (February 2020), I was at the stage of selecting which parts of those projects were worth to be further developed to be included in the Thesis. My supervisor and I decided to give priority to the motion correction part at first. Then, the first lockdown happened (March 2020 - May 2020). During the last laboratory session carried out for the motion correction experiment (February 2020), the main instrument of my research (field camera) broke and it was not possible to ship it to the Swiss company for repair until July 2020 when it was promptly repaired within the month and shipped back to the UK. However, human scanning was not allowed at the Sir Peter Mansfield Imaging Centre (SPMIC) until mid-August 2020. My project was not included in the list of Faculty of Science selected priority projects and it recommenced in October 2020 when I tested the acquisition of magnetic field data with simultaneous scanning, but I was not yet at the stage of performing corrections of MR images. The measurements were carried out by involving the minimum number of people (my supervisor and myself) to reduce the risk of contagion due to (1) the handling of saliva to make the custom bite bar (2) the number of people involved to calibrate the optical camera (usually one scanner operator, one optical camera operator, one subject in the scanner) and to perform measurements (usually one scanner operator, one optical and magnetic field camera operator, one subject in the scanner). During the laboratory session (November 2020), the cable of the optical camera broke. Then, a second lockdown happened (November - December 2020). I requested a six-month extension period for my funding, but unfortunately, the beginning coincided with the third lockdown (January 2021) that was then slowly eased (June 2021) thanks to the effectiveness of the vaccines. My funding ran out in July 2021, when I entered the thesis pending period.

During the extension period then, I have heavily focused on implementing and using simulations to generate useful data for parts one (Chapter 4) and three (Section 6.3.1 of Chapter 6) mentioned above. I also decided to improve the data analysis pipeline (Sections 5.1, 5.1.3 of Chapter 3) on pre-pandemic recorded data in order to apply the best pipeline to newly recorded data (Chapter 5) and to test in post-processing the motion detection (Section 6.1.1 of Chapter 5). The simulations provided important new insights and led to the identification of a possible way to generalise the prediction over multiple subjects (Section 7.2 of Chapter 6).

One of the impacts that lockdown had on researchers is to reduce the possibility to discuss their work and to network at scientific events, two important aspects of research that heavily impacted the career development of early stage researchers. To limit the impact on my career, I did my best to present my work to colleagues (seminar in spring 2020) and at on-line conferences (ISMRM and ESMRMB 2020 and 2021, MoCo workshop 2020). Also, as elected Student Observer of the BIC-ISMRM in 2020, I tested and improved my skills of team leading and networking. Furthermore, I enriched my knowledge by attending free conferences, online classes and seminars on various topics related to my research. In particular, attending the ICMNM (International Conference on Mathematical Neuroscience) and a 10-week Machine learning course helped me improve the data analysis pipeline. I also attended classes held by the Research Academy of the University of Nottingham on paper writing, presentation and communication skills, unconscious bias and EDI. I attended IOP workshops on topics related to my research and how to work safely during the pandemic.

Chapter 1

Nuclear Magnetic Resonance (NMR) phenomena

This chapter explores the basics of NMR (Nuclear Magnetic Resonance) and MRI (Magnetic Resonance Imaging) along with the physics of the NMR field probes. The Bloch equations and relaxation time constants (T_1, T_2) are introduced. Then, an MRI scanner and methods used to obtain MR images from k-space data are reported and ultra high and low field MRI scanner systems are compared. To conclude, the field probe camera system and its operation is described.

1.1 Nuclear Magnetic Resonance (NMR) phenomena

Nuclear magnetic resonance is a quantum mechanical phenomenon that can be explained using classical mechanics for a certain extent [21].

The *nuclear magnetic moment* results from the unpaired spins of the protons and neutrons in the nucleus that we investigate. The overall spin generates a magnetic dipole along the spin axis. Its magnitude is the nuclear magnetic moment. The effect of many nuclei in a sample generates a macroscopic magnetization called $\vec{M}$. It depends on the number of nuclei present in the sample (N), the type of nuclei (the gyromagnetic ratio γ, $[rad/s\ T]$ is unique for each nucleus), Planck's constant ($\hbar = h/2\pi$), Boltzmann constant (k_B) and the temperature of the sample (T, $[K]$). $\vec{M}$ is governed by the *Boltzmann Equilibrium Law*:

$$\vec{M} = N\frac{\gamma^2 s(s+1)\hbar}{3k_B T}\vec{B}_0 \quad [A/m] \tag{1.1}$$

where s is the spin quantum number of the nucleus.

During magnetic resonance (MR), a constant magnetic field (B_0) is used to align the magnetisation $\vec{M}$. An external stimulus (RF pulse) then perturbs $\vec{M}$ for a short period of time. The perturbed $\vec{M}$ then precesses around the constant magnetic field direction (in the laboratory frame). This produces an electromotive force in a nearby coil due to the time variation of the magnetic flux. In general, the frequency of the angular precession is described by the Larmor equation:

$$\omega = \gamma B_0 \quad [rad\ s^{-1}] \tag{1.2}$$

The electromotive force is proportional to the product of ω and the magnetisation. Since both are proportional to the strength of the B_0 field, the sensitivity of the NMR experiment scales as the square of the magnetic field.

1.2 Bloch equations

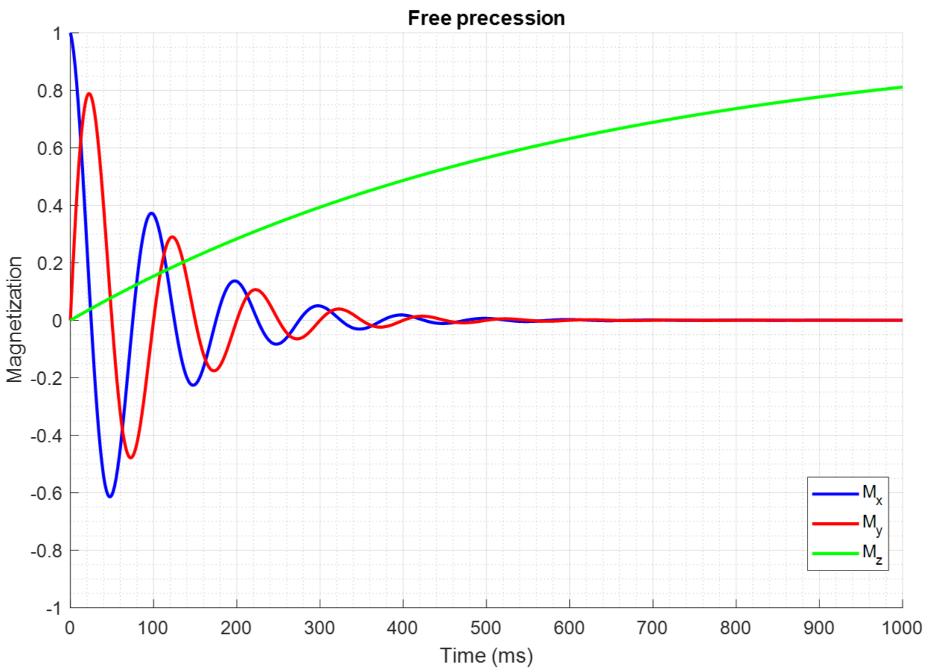

Figure 1.1: Temporal variation of the Cartesian components of the magnetisation, following application of a 90 degree RF pulse ($T1 = 600\ ms,\ T2 = 100\ ms,\ \Delta\omega = 10\ Hz$). The transverse components of the magnetisation undergo free precession. [22]

The Bloch equations are a set of equations describing the properties and origins of the NMR signal. As individual nuclei possesses spin angular momentum ($\vec{I}$), the magnetic

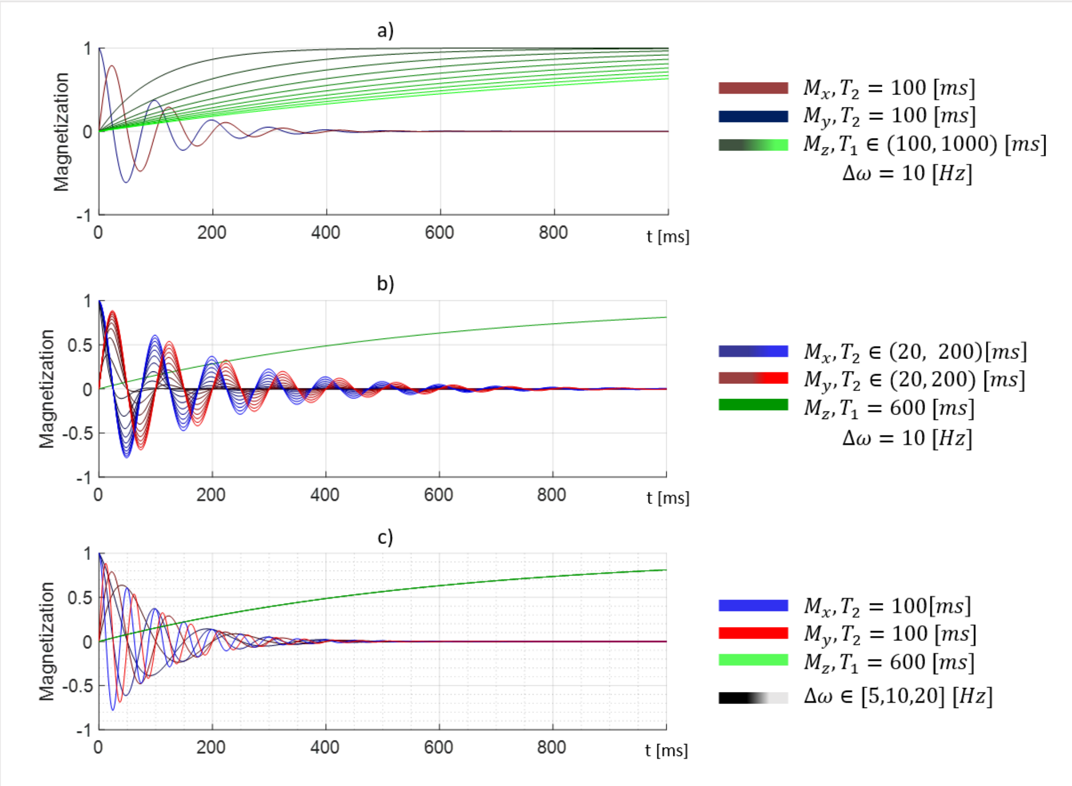

Figure 1.2: *Effect of changing parameters on the temporal evolution of the magnetization vectors [22].* (a) Effect of the changing of T_1 on longitudinal magnetisation M_z. (b) Effect of the changing of T_2 on transverse magnetisation ($M_{X,Y}$). (c) Effect of the changing of the offset of resonance frequency on both longitudinal and transverse magnetisation.

properties of an ensemble of nuclei can be represented by the *net magnetization vector* ($\vec{M}$). $\vec{M}$ is subjected to a torque ($\vec{\tau}$) in magnetic field ($\vec{B}$):

$$\vec{\tau} = \vec{M} \times \mathbf{B}$$

The torque is the temporal derivative of the angular momentum:

$$\frac{d}{dt}\vec{I} = \vec{\tau}$$

The gyro-magnetic ratio (γ) relates the magnetic moment ($\vec{M}$) with the angular momentum ($\vec{I}$):

$$\vec{M} = \gamma\vec{I}$$

So, the Bloch equation without relaxation terms is given by:

$$\frac{d}{dt}\vec{I} = \vec{\tau} \tag{1.3}$$

$$\frac{d}{dt}\frac{\vec{M}}{\gamma} = \vec{M} \times \mathbf{B} \tag{1.4}$$

$$\frac{d}{dt}\vec{M} = \gamma\vec{M} \times \vec{B} \tag{1.5}$$

The three components of the $\vec{M}$ rotating vector are described by:

$$\frac{dM_x(t)}{dt} = \gamma\left(\vec{M}(t) \times \vec{B}\right)_x \tag{1.6}$$

$$\frac{dM_y(t)}{dt} = \gamma\left(\vec{M}(t) \times \vec{B}\right)_y \tag{1.7}$$

$$\frac{dM_z(t)}{dt} = \gamma\left(\vec{M}(t) \times \vec{B}\right)_z \tag{1.8}$$

where calculation of the cross product (using the right-hand rule) leads to:

- the direction of $\vec{\tau}$ is perpendicular to both $\vec{M}$ and $\vec{B}$ and it causes $\vec{M}$ to precess around $\vec{B}$ [1].
- If $\vec{M}$ is along $\vec{B}$, there won't be any change in $\vec{M}$ in time.
- If $\vec{M}$ is transverse to $\vec{B}$, there will be a change in $\vec{M}$ in time.

Individual spins that are part of the ensemble can interact with each other (*spin-spin* interaction) and the environment (*spin-lattice* interaction). The result of these interactions is that $\vec{M}$ relaxes back to the equilibrium state where the magnetisation is aligned $\vec{B}$ and takes a value of $\vec{M}_0$. This *relaxation* process releases energy to the environment.

Introducing the effect of relaxation into the Bloch equation using the *relaxation time constants* T_1, T_2 (assuming that single time constants are sufficient to describe the pro-

[1]The most common analogy to visualize the phenomenon is a gyroscope. The nuclear spin is analagous to the angular momentum. The magnetic moment reflects the moment of inertia. The electromagnetic field replaces the effect of gravity. As soon as the gyroscope is moved away from the parallel direction to gravity, it starts to precess (it rotates on its own axis and precesses around the vertical axis).

cesses) gives:

$$\frac{dM_x(t)}{dt} = \gamma\left(\vec{M}(t) \times \vec{B}\right)_x - \frac{M_x(t)}{T_2} \tag{1.9}$$

$$\frac{dM_y(t)}{dt} = \gamma\left(\vec{M}(t) \times \vec{B}\right)_y - \frac{M_y(t)}{T_2} \tag{1.10}$$

$$\frac{dM_z(t)}{dt} = \gamma\left(\vec{M}(t) \times \vec{B}\right)_z - \frac{M_z(t) - M_0}{T_1} \tag{1.11}$$

$M_x,\ M_y$ are called the *transverse components of magnetisation* whose relaxation is characterised by T_2, while T_1 describes the relaxation of the *longitudinal component of magnetisation* M_z. The vector representation of Equations 1.9−11 is:

$$\gamma\left(\vec{M}(t) \times \vec{B}\right)_{x,y,z} = (\gamma M_y B_0,\ \gamma M_x B_0,\ 0) \tag{1.12}$$

Figure 1.1 shows the evolution of the different magnetization components following a 90 degree RF pulse. The evolution of the magnetization is shown in the rotating frame, with a frequency offset $\Delta\omega$ of 10 Hz. Figure 1.2 shows how this behaviour changes when different parameters are varied.

1.2.1 BPP theory of relaxation

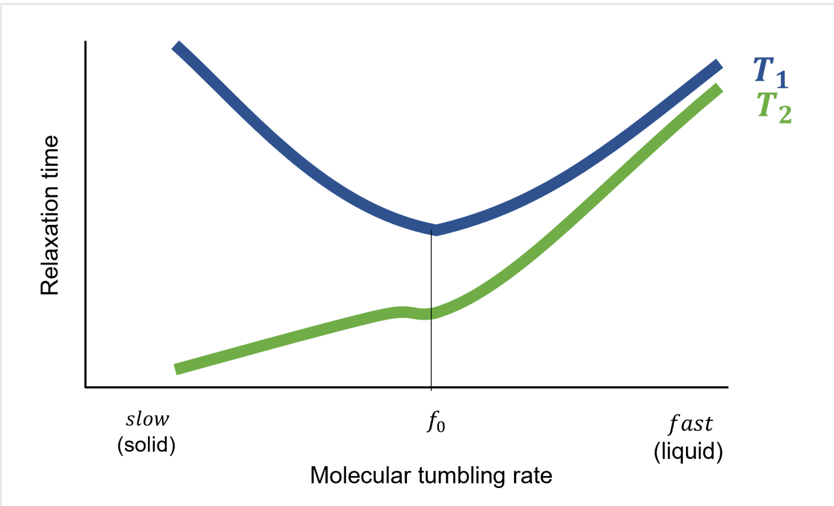

Figure 1.3: *Bloembergen, Purcell and Pound theory of relaxation.* The tumbling rate of molecules (described by the correlation times for rotational motion) vary with the state of aggregation of the matter. T_1 is minimised when the frequency of rotation matches the Larmor frequency (f_0). On the other hand, T_2 does not show a minimum and rather decreases as the frequency of rotation decreases.

Bloembergen, Purcell and Pound [23] described the mechanism of relaxation in terms of molecular random motion of translations, rotations and vibrations. Rotational random motion of molecules is the one that influences T_1, T_2 relaxation times the most as translations of molecules and vibrations (happening in the infrared electromagnetic spectrum) do not strongly affect the nuclear magnetisation. Molecular rotation modulates the dipolar fields experienced by the nuclei, driving transitions between energy levels, hence leading to relaxation. Changes in the rate of molecular rotation, characterised by the correlation time, have a strong effect on the rate of relaxation. Rotation, and hence field fluctuation at the Larmor frequency is important for driving T_1 and T_2 relaxation, but T_2 relaxation is also strongly affected by low frequency motion.

1.2.2 Relaxation times

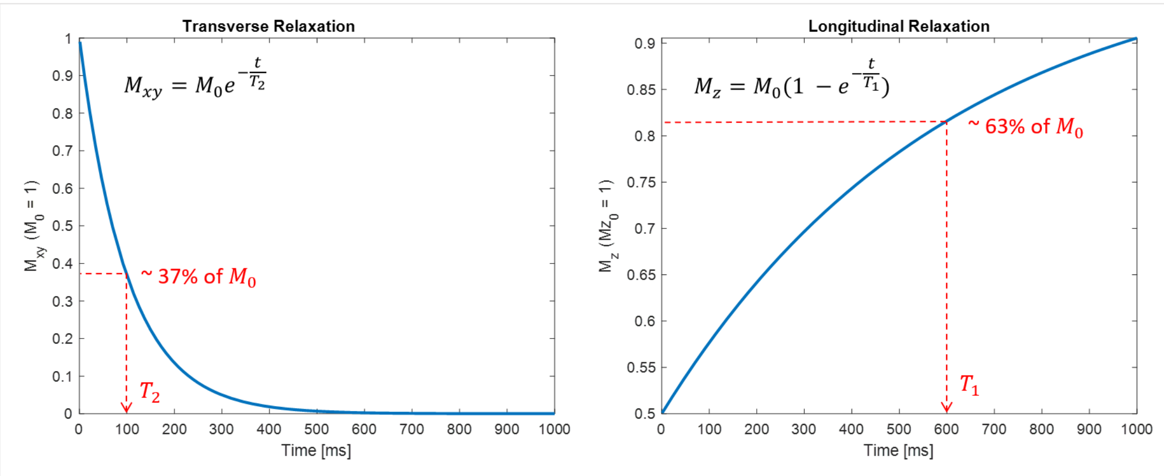

Figure 1.4: Transverse magnetization (M_{xy}) and Longitudinal (M_z) magnetization [22] for $T_2 = 100\ ms$ and $T_1 = 600\ ms$.

The relaxation of the magnetisation components is visualized in Figures 1.4 and 1.5 for different values of the relaxation times.

The *spin–lattice relaxation time* (T_1) describes the recovery of thermodynamic equilibrium, while the *spin-spin relaxation time* (T_2), characterises the irreversible loss of phase coherence of the spins: the general relation between these parameters is $T_2 < T_1$ (Figure 1.3).

T_1 and T_2 are different for different tissues (Figure 1.5) and this is exploited to produce different contrast in images produced using different magnetic resonance imaging techniques.

Spin-lattice relaxation time (T_1) The *spin-lattice relaxation time* (T_1) represents the interaction between the nuclei and experimental environment, the spin system's loss of energy to the lattice is largely driven by field fluctuations occurring at the Larmor frequency (Figure 1.3). This corresponds to the recovery of the component of $\vec{M}_z$ (Equation 1.9) along the static field (the recovery of the longitudinal magnetization).

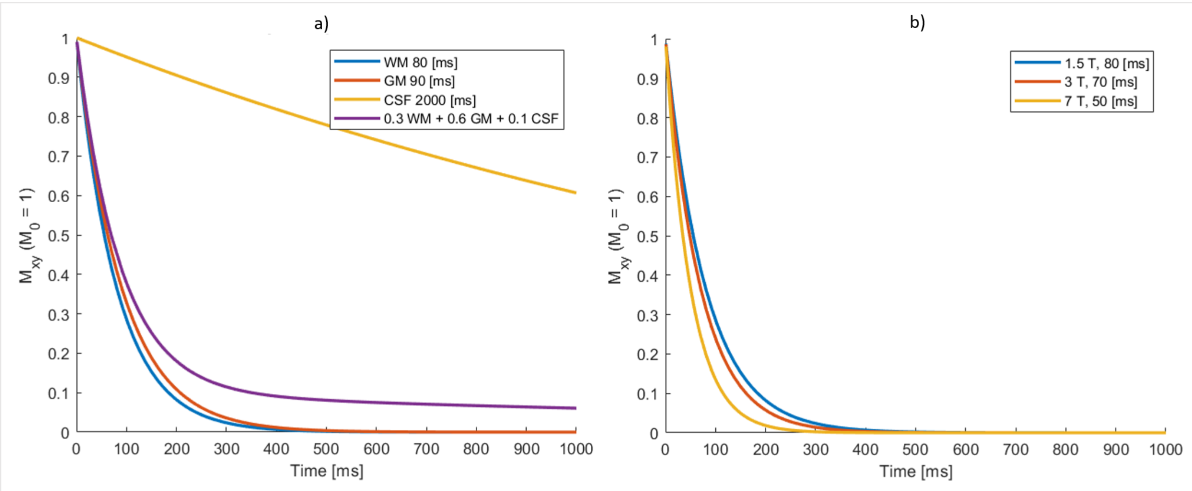

Figure 1.5: (a) Decay of transverse magnetization (M_{xy}) of different tissues in the brain. Gray Matter (GM), White Matter (WM), Cerebral Spinal Fluid (CSF). (b) Decay of transverse magnetization (M_{xy}) of the same tissue (WM) at different field strengths. In general the higher the field, the shorter the T_2 [22]

Spin-spin relaxation time (T_2) The *spin-spin relaxation time* (T_2) characterises the decay of the component of $\vec{M}_{xy}$ (Equation 1.9) transverse to the static field (the decay of the transverse magnetization). Decay is promoted by the loss of coherence in phase between spins due to intrinsic local magnetic field fluctuations caused by molecular motion (Figure 1.3). Because of inhomogeneities in the main magnetic field, the observed T_2 is shorter than the one predicted and the resulting values is known as the $T_2^\star$ ($T_2^\star \leq T_2$) relaxation time. It can be written as: [2].

$$\frac{1}{T_2^\star} = \frac{1}{T_2} + \frac{1}{T_2'} \tag{1.13}$$

[2]"Twinkle twinkle T two star" song from "muscle and Magnets" album of Greg Crowther sum up the phenomena https://www.youtube.com/watch?v=uu7Ph25EhLQ

where the relaxation time due to the inhomogeneities is approximately given by the inverse of the range of precession frequencies due to the magnetic field inhomogeneities ($1/T_2' = \gamma \Delta B_i$).

Relaxation times in tissues Biological tissues cannot be modelled as either solid or liquid due to the complex interaction of macro-molecules and water. However, the BPP theory can nicely explain the relaxation times of protons in water in tissues when considering the spread of molecular tumbling frequencies in the tissue. For example, T_1 in CSF (liquid, 'free' protons tumbling) is long (of the order of a second[24]) because of the very rapid tumbling of the water molecules leading to a relatively low field fluctuations at the Larmor frequency. Likewise, T_2 is long (order of magnitude of the second[24]) because of the small contribution to field fluctuations at low frequency. Body tissues where water molecules are neither 'free' nor 'bound', have more efficient spin-lattice interactions (short T_1) as there is a larger contribution to field fluctuations at the Larmor frequency. Spin-spin interactions T_2 in structured materials are weaker than in 'bound' ones (such as bones), where the tumbling motion limited by the molecular binding leads to very short T_2. Bound materials are also characterised by long T_1 as spin-lattice interaction (that provides energy for the $\vec{M}_z$ recovery) is not favoured by the binding. Typical range of values of relaxation times are reported in Table 1.1.

Relaxation times	Free protons (Body fluids)	Structured protons (Water-based tissues)	Bound protons (Fat-based tissues)
T_1	$1.50 \div 2.00\ s$	$0.40 \div 1.20\ s$	$0.10 \div 0.15\ s$
$T_2 (< T_1)$	$0.70 \div 1.20\ s$	$0.04 \div 0.20\ s$	$0.01 \div 0.10\ s$

Table 1.1: *relaxation times.* Example of typical relaxation time values for body tissues. Values are given as approximate ranges as they strongly depend on the field strength [24]

1.3 Magnetic resonance imaging (MRI)

Magnetic resonance imaging (MRI[3].) is an imaging technique based on the NMR phenomenon that can be used to investigate the body of a patient. Research in this field is now moving towards the investigation of the use of *Ultra High-Field* scanners. The achievable spatial resolution of MRI increases with the strength of the magnetic field. Subject movements which can be tolerated at lower field are not acceptable in high spatial

[3] "The MRI song" Matt Wall sum up the phenomena https:https://www.youtube.com/watch?v=zfYINee1VA4

resolution imaging at ultra high field, since they create artefacts that can invalidate images. The movements break the correspondence between the spatial position of the nuclei and their magnetic resonance signal, which is fundamental to the MRI technique. The artefacts can be corrected when the movements of the head during the scans are known, this is the idea of *Motion Correction*.

1.3.1 MRI technique

MRI produces very clear images of the inner parts of the human body. The major advantage of MRI is that it is non-invasive for the patient because it does not use any ionising radiation. Moreover, MRI provides better soft tissue contrast than other medical imaging techniques, such as X-Ray computed tomography.

MRI uses radio frequency irradiation to stimulate the nuclear magnetisation arising from the nuclear spin of hydrogen nuclei in water molecules in the body [4]. In MRI, the signals originating from this magnetization are measured in the presence of magnetic field gradients and processed to obtain pictures of the human body.

Magnetic susceptibility (χ). The presence of the patient causes magnetic field variations that depend on the magnetic susceptibility of the tissue. Typical values [26] are: $\chi_{Fat} = -7.79 \cdot 10^{-6}$, $\chi_{Bone} = -11 \cdot 10^{-6}$, $\chi_{Water} = -9.00 \cdot 10^{-6}$. Equation 1.2 becomes: $\omega = \gamma(B_0 + \Delta B)$, where $\Delta B \approxeq \chi_m B$ depends on the spatial distribution of χ. Hence, the frequency of precession depends slightly on the anatomy.

Fields used in MRI. Three different electromagnetic fields are used in MRI:

- **Static Magnetic Field (B_0)**: This aligns the magnetic moments of the hydrogen nuclei to generate a net magnetization vector ($\vec{M}$).
- **Gradient Magnetic Field**: Gradients are used for the spatial localization of the signal (G_x, G_y, *or* G_z, depending on the direction of application). The gradient changes the value of the magnetic field in space. So, the resonant frequencies of the protons depend on their position in space ($\vec{r}$).

$$B = (B_0 + G \cdot \vec{r}) \longrightarrow \omega(\vec{r}) = \gamma(B_0 + G \cdot \vec{r}) \tag{1.14}$$

  The equation shows that the gradient characterises a linear variation of the z-component of the field (defined by the direction of B_0) with spatial position

[4] 70% of the human body is composed of water (H_2O). The spins of the hydrogen nuclei are influenced by applied magnetic fields. For fields from 1 to 23 Tesla, the frequency of precession of hydrogen nuclei varies from 42 MHz to 1 GHz [25].

- **Radio Frequency (RF)**: It is usually centred at the proton resonant frequency (equation 1.2) and it rotates the net magnetization vector away from the direction of the static magnetic field. The flip angle is changed by varying the duration or the intensity of the applied RF pulse. After the perturbation, the transverse magnetisation precesses and the net magnetization vector gradually returns to its equilibrium state (magnitude of M_0, aligned with the static magnetic field). The time-scale of the relaxation processes depend on the properties of the tissue and is characterised by T_1 and T_2.

1.3.2 Overview of an MRI scanner

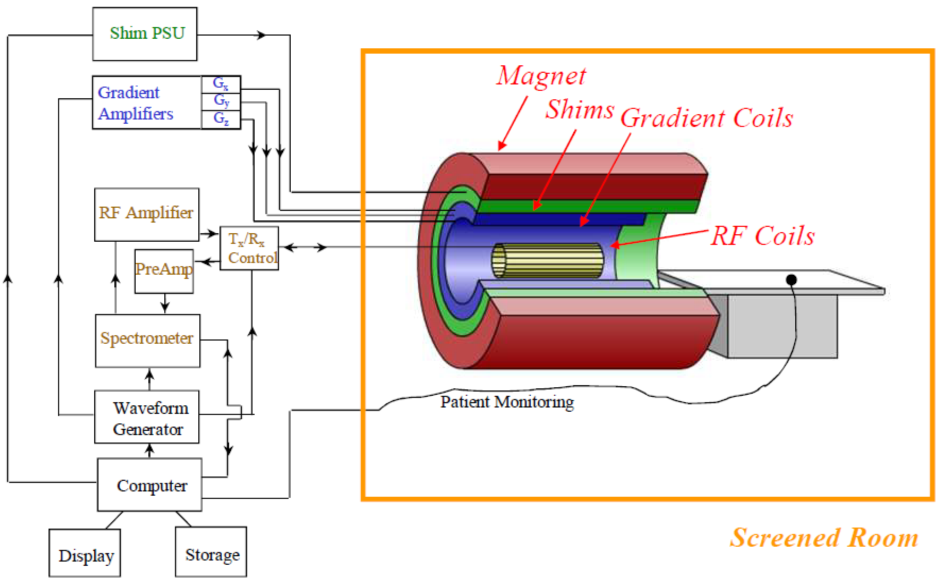

Figure 1.6: ***MRI System***. *[Picture made by Richard Bowtell, MRI class 2018]*

- **Magnet.** MR techniques need a static magnetic field (B_0) that must be spatially homogeneous and time invariant. The strength of the field must be high and is linked to the resolution of the image. The static magnetic field can be generated via magnetic material (*permanent magnet*) or high electrical current flow (*resistive* or *superconductive* magnets). In our system, $B_0 = 7\ T$, is aligned along the z axis ($B_0 = B_z$) and generated by a superconductive magnet.

- **Shim coils.** Shim coils are necessary to correct spatial variation in the main magnet field B_0. They generate a spatially varying magnetic field parallel to the static magnetic field ($B_z(r)$). These fields can also be generated using magnetic material or current flow in wires. The field is modelled on the installation of the scanner and also changed on a per-subject basis during scanning.

- **Gradient Coils.** MRI techniques exploit magnetic field gradients generated by three gradient coils, one for each spatial direction (G_x, G_y, G_z). The gradients are varied in time, depending on the sequence applied.
- **Radio Frequency (RF) Coils.** RF coils generate a radio frequency field, orthogonal to B_0, which is linearly or circularly polarised. They are tuned to the NMR frequency. RF transmitter coils generate an uniform field over a large region and are used for signal excitation. RF receiver coils produce a localised field and are used for signal detection.
- **Screened Room.** Usually the MRI scanner is housed in an RF screened room to reduce interference between the MRI unit and other electronic devices.
- **Electronics.** Each element of the scanner has a dedicated cluster of controllers placed in the equipment room.

1.3.3 Spatial frequency space (k-space)

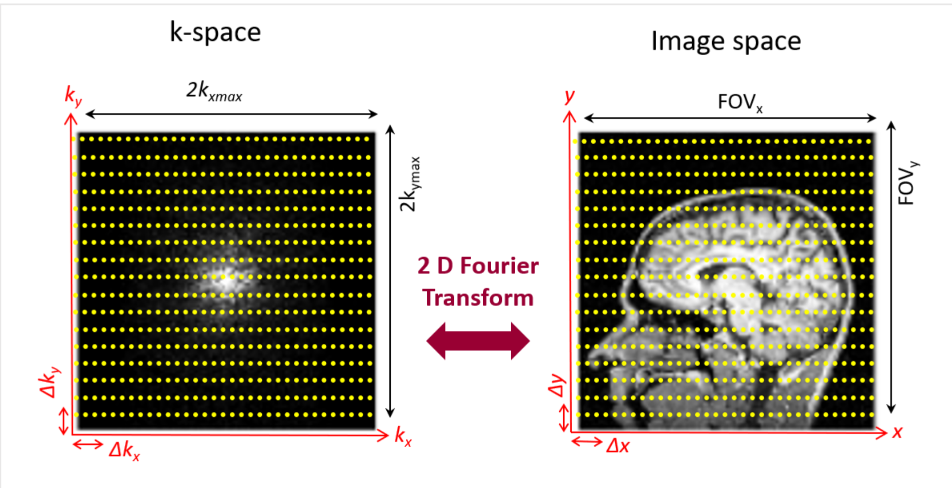

Figure 1.7: *k-space and 2D space.* The k-space representation (left) can be used to describe the signal acquired during MRI scanning. It is processed by Fourier Transformation to obtain the MR image (right). The spatial resolution of the image is inversely proportional to the gradient amplitude (G) and the duration (t). Hence, to have a high spatial resolution it needs a large $G \cdot t$ product. [Picture made by: Bowtell Richard, University of Nottingham, MR classes, 2016].

MR image formation is based the process called *spatial encoding* that is used to encode the spatial information in the NMR signal produced by the nuclear spins of the

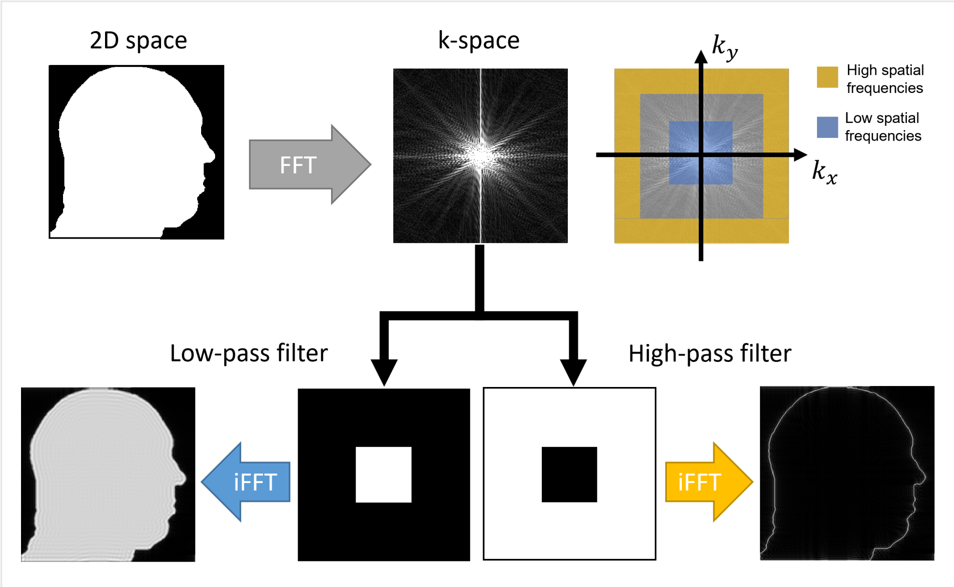

Figure 1.8: *Analysis of the k-space.* The Fourier spectrum of a Boolean 2D human-like picture has been filtered to highlight correspondence between spatial frequencies space (k-space) and the 2D space representation. Rapid changes with spatial position (head's edge) are represented by high spatial frequencies, while flat regions (head) are represented by low spatial frequencies. Band pass filters have been applied.

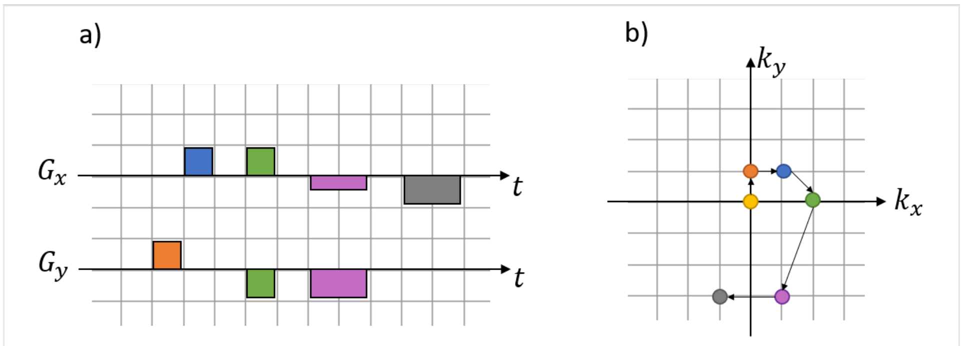

Figure 1.9: *Trajectory in 2D k-space.* (a) Illustrative gradient waveforms, and (b) the concurrent movements in k-space. Starting from the centre of the k-space (no excitation, yellow) (orange) $G_y > 0$ creates a trajectory towards $k_y > 0$, same effect for $G_x > 0$ (blue) along $k_x > 0$. (green) $G_x > 0$ and $G_y < 0$ lead to encode in a diagonal direction. (purple) As the integral (area) of the gradient determine the new coordinates in the k-space, and in this case $2A_{Gx} = A_{Gy}$, the end of the trajectory. (grey) $G_x < 0$ move backward to $k_y < 0$.

sample.

Considering Figure 1.7, the coordinates of the signal are the frequency and the phase encoding directions that characterise the 2D k-space. Using varying magnetic fields gradients allows the signal to be measured at each point of k-space ($k_x,\ k_y$).

The spatial encoding process relies on *frequency encoding*, *phase encoding* and *selective excitation*. Frequency is used to encode one dimensional information. A magnetic field gradient produces a linear variation of magnetic field with position, and thus the frequency also varies linearly with position. The precession frequency (equation 1.2) in the presence of a field gradient (ΔG) added to the B_0 field ($B = B_0 + \Delta G = B_0 + G \times x$) becomes: $\omega = \gamma B = \omega_0 + \gamma G x \quad [Hz]$. Gradients that change the phase of the signal are used to encode two, three or higher dimensional information.

In 2D space for example (Figure 1.7), the x position can be encoded in frequency and the y position is encoded in phase. The phase is related to the gradient by: $\phi = \gamma G_y y \tau$ where G_y and τ are the intensity and the duration of the applied gradient. Furthermore, for 2D MR imaging it is necessary to select a slice of the sample to scan. The equation 1.2 becomes: $\partial\omega = \gamma G \partial s$. Sending a gradient G centred on the frequency $\omega_a = \frac{\omega}{2}$ selects the slice ∂s. In 3D space, slice selection involves applying an RF pulse that contains a finite range of frequencies ($\Delta\omega$). When this is applied in conjunction with a slice select gradient it excites magnetisation across a finite range of positions.

Figure 1.8 reports an example of k-space corresponding to a highly simplified human head image. k-space represents the distribution of spatial frequencies obtained by Fourier Transform of the image. Low frequencies (centre of the k-space) and high frequencies (border of the k-space) represent respectively flat regions and rapidly changing regions in the image space. By the use of spatial filters it is possible to separate those components. High spatial frequencies are given by weak signals and contain fine details. Most of the signal is characterised low spatial frequency and contains information on image shape and contrast.

Changing the order of application of the gradients (or the (k_x, k_y) points) and the timing for filling the k-space is the way to generate diverse MR sequences (Figure 1.9). The most used k-space trajectories can be divided into four main classes: standard non-EPI rectilinear (where EPI stand for Echo Planar Imaging); EPI; Radial; Spiral. The main difference is that the centre of the k-space is heavily sampled for radial and spiral trajectories.

1.3.4 From MR signal to medical imaging

The signal measured is ideally: $S(t) = M(t) \cdot exp(i\varphi(t))$. It is composed of two parts: the magnitude ($M(t)$) and the phase ($\varphi(t)$).

- **Magnitude.** The MR image represents the spatial distribution of the magnetiza-

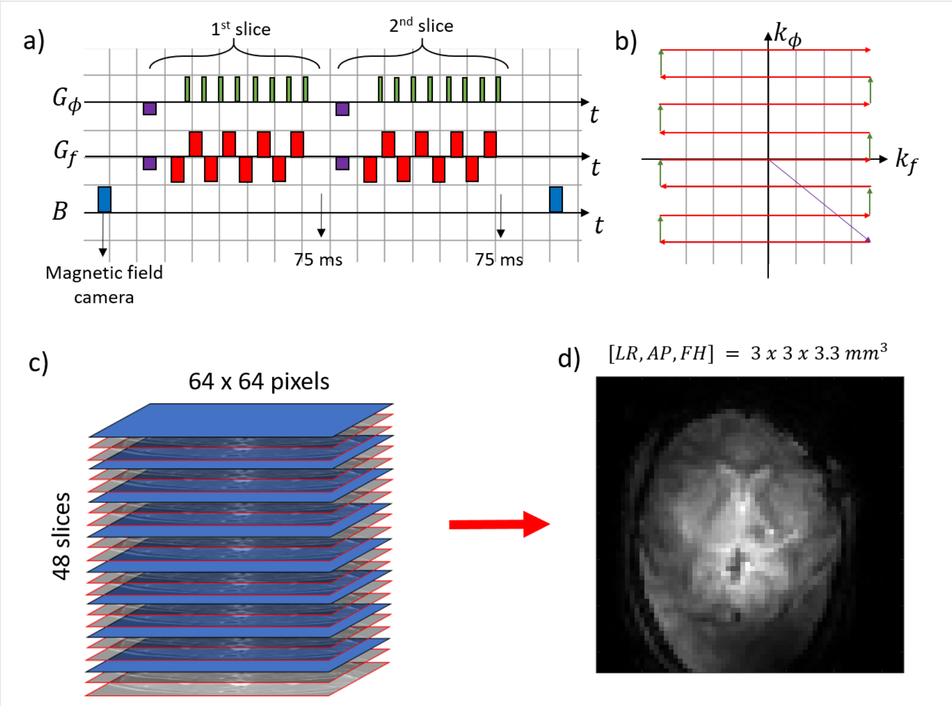

Figure 1.10: *Specific sequence.* (a) Timeline of the measurements. (b) k-space trajectory for one slice. (c) Image volume. (d) Axial slice of the MRI.

tion. The appearance depends on the physical proprieties of the tissue and on the RF pulse sequence applied.

- **Phase.** The phase contains information about all the sources of perturbation of the magnetic field, including the effects of hardware imperfections, field inhomogeneity and perturbations due to movements.

The variation of the magnetic field inside the head is correlated with the phase variation of the signal, but the magnitude signal only is usually used to produce the MR image.

1.3.5 Image artefacts

Image artefacts produce signals and structures in the image which do not correctly reflect anatomical information. On the clinical side, these tends to be more severe for paediatric and elderly patients who find it hard to keep still in the scanner. Artefacts in the image can mimic pathologies and lead to improper diagnosis. On the research side, artefacts can still exist even if the subjects are co-operative and able to remain still, and the spatial resolution may therefore be limited by motion.

Artefacts emerge for different reasons. There are inherent physical artefacts, like chemical shift artefacts due to the frequency variation of different tissues (e.g. fat and water) or magnetic susceptibility artefacts due to variations in magnetic proprieties of the tissue or implants. These artefacts can be reduced by changing the MR sequence.

Even if the whole scanner hardware is optimised not to interfere with the measurements, the interference between the MRI unit and other electronic devices inside the room can create noise patterns on the image. Furthermore, the imperfections in the static magnetic field, gradient fields and shimming can create artefacts. The magnetic field must be uniform to at least a few part per million.

If we assume the absence of hardware noise sources, the movement of the patient is the only perturbation source. It produces a shift of the region of interest (ROI) of the scanner. As explained on page 18, if the ROI shifts, the same region could be excited with different values of gradients and reconstructed at two different locations in the image. Thus, the movements of the patient introduce encoding errors.

1.4 Low/high field scanners for MRI

Ultra high field MRI scanners ($\geq 7\ T$) are a leading-edge technology growing fast in the last decade, that comes with technical challenge and many medical benefits [27]. The benefits include the capability to visualise anatomical details with high resolution, which may lead to improve planning of treatment to prevent or slow down various disease developments in the future. Table 1.2 summarises how the main scanning parameters scale with the field strength. Thus, it is natural to wonder what is the gain compared to low field MRI scanners ($\leq 3\ T$):

- The size of the *footprint* around the scanner, so how the magnetic field decrease with distance from the scanner bore, mostly depends on the shielding [28]. The force that an object can feel is proportional to the spatial variation (rate of change of the magnetic field): $F \propto B_0 \frac{dB_0}{dz}\ [T^2 m]$. This also increases the risk of the projectile hazard.
- UHF provides higher *Signal to Noise Ratio (SNR)* [29]. This improves the resolution of the image and reduces the scan time. Higher SNR also allows the recording of signals from other nuclei than protons.

Scan parameters	Mathematical relationship with B_0
Signal to Noise Ratio	$SNR \propto B_0$
Spatial Resolution	$Resolution \propto SNR^{1/3} \propto B_0^{1/3} \approx 47$
T_1	$T_1 \uparrow B_0$
T_2^*	$T_2^* \downarrow B_0$
Apparent T_2	$T_2 \downarrow B_0$
Spectral separation	$\Delta\omega \propto B_0$
Susceptibility effects	$\Delta\phi \propto TE \cdot B_0$

Table 1.2: *UHF*. Summary of the relationship between MRI/MRS/MRSI scan parameters and B_0 [2]

- *Physiology* common temporary side effects on going in to a UHF scanner [30, 28] are dizziness, vertigo and metallic taste. These effects are mainly induced by motion of charges (a person that moves into the magnetic field, ion fluid moving in the vestibular system, blood) in a magnetic field [5]. Time-varying MRI gradient fields induce electric fields in the patient that can become strong enough to stimulate peripheral nerves (*PNS*), muscles, and possibly even the heart. These unwanted physiological effects significantly limit the performance of modern MRI gradient systems.

- The *Power deposition (Specific Absorbing Rate, SAR)* scales with the square of B_0. So, at UHF, the limits for sequence design (in terms of TR, flip angle and saturation) are reached faster [31].

- The *Spin - lattice relaxation time (T_1)* increases at UHF. For a saturation recovery or inversion recovery based image, this provides longer label persistence and better background suppression. However, if you want a similar contrast, you need longer TR (repetition time) and TI (inversion time) so image scan times become longer.

- The *Spin - spin relaxation time (T_2)* decreases. Shorter TE (Echo time) are needed to avoid signal attenuation. In the case of spectroscopic images, short T_2 has the effect of broadening the lines of the spectrum.

- Increasing the B_0 leads to increased *susceptibility effects* (magnetization of the tissues, susceptibility effects $\propto B_0$) and resonance frequencies (equation 1.2). This lead to larger B_0 in-homogeneity and distortion as the local magnetic field changes at tissue boundaries increase. An example of consequences of this are in fat suppression in MRI sequences. Most fat suppression methods are built on the frequency difference between water and fat. So, if field inhomogeneities are too large frequencies will be mixed up and the fat suppression will be poor. High order spherical

[5] *Effects induced by motion of charges in a magnetic field.* Motion of charges through a homogeneous field (Lorentz forces).

harmonics shimming compensation of the scanner (add field to compensate inhomogeneity) reduces the effect.

- The *Chemical Shift* differences between metabolites increase leading to a better peak separation since the resonant frequency increases linearly with the field strength (e.g. a $\Delta = 100\ Hz$ at 3 T results on $\Delta = 240\ Hz$ at 7 T). Also, the SNR increase allows the detection of low concentration metabolites [29].

- B_1 inhomogeneity increases. Resonant frequency increases with field strength (equation 1.2) and so RF field wavelength will be shorter [6]

B_0 :	$1.5\ T$	$3.0\ T$	$7.0\ T$
frequency [$\mathbf{10^6}$ **Hz**]	≈ 60	≈ 130	≈ 300
Wavelength [**cm**]	≈ 50	≈ 20	≈ 10

Table 1.3: *Wavelength of RF.* $\lambda = \frac{c}{\gamma \epsilon_r} = \frac{c}{\gamma B_0 \epsilon_r}$, $\gamma = 3[10^8\ Hz]$, hydrogen, $c \approx 3\ 10^8 [m/s]$

If the wavelength is smaller than the head diameter, RF waves will interfere inside the head. Constructive interference leads to area with high signal (and potentially, high power deposition), while destructive interference leads to signal losses. This is reflected in the flip angles perceived by the spins. So the concept of one single flip angle is no longer valid and this can create regions of poor contrast and shading artefacts. The severity of the effects depends on many parameters, but mainly head size, as smaller head are less affected by this problem. A possible solution is the use of dielectric pads that superimpose a static secondary RF field, or the use of parallel transmit technology. Parallel transmit system have multiple RF transmit whose parameters can be adjusted separately (amplitude, pulse, phase).

- *Motion Artefacts* are not specific to any field strength, but the high resolution achievable at UHF and the longer scan make them more pronounced. Motion can also induces frequency fluctuation that gives artefacts in T_2^* images.

1.5 NMR field probes

NMR probes are active probes developed for measuring the net magnetic field evolution inside the MR scanner. NMR probes measure the NMR signal using a small volume of liquid, and allow calculation of the local magnetic field.
The features satisfied by the probes are:

[6] $\lambda = \frac{c}{f}$, λ $[m]$ wavelength, $\frac{c}{\sqrt{\epsilon_r}}$ $[m/s]$ speed of light in tissue (dielectric effect), f $[m/s]$ frequency.

- In each measurement, the probes are excited by RF pulses and the individual FIDs are measured. The magnitude of the FID signal does not strongly feel the influence of external gradient fields, otherwise the probes $\vec{M}$ could be dephased. This is guaranteed if the dimension of the probes is less or equal to roughly the inverse magnitude of the maximum k-space vector of the measurements. That leads to having a diameter of less than two pixels in size ($< 2\ mm$).

- The materials surrounding the active probes do not influence their FIDs. The magnetic susceptibility of materials have to match with those of the probe.

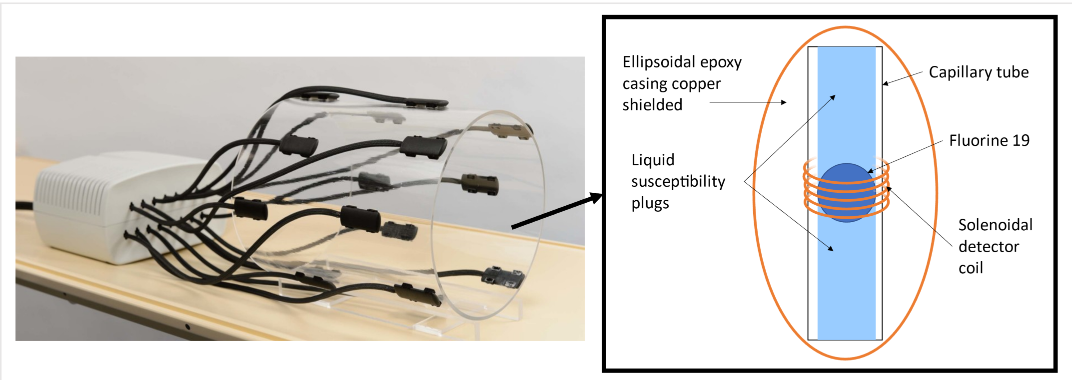

Figure 1.11: *Clip-on camera system.* The figure shows the Clip-on camera system (left) and a schematic representation of the field probe capillary (right) described in Section 1.5. The system is comprised of 16 magnetic field probes. The shape of each probe is ellipsoidal to limit field inhomogeneity due to the magnetic susceptibility of the container of the probes. The container is closed to prevent the entering of gas bubbles [32].

The probes are based on an MR-active liquid. The MR-active liquid has to exhibit a high concentration of nuclei with high gyromagnetic ratio to obtain a sufficient signal to noise ratio (SNR). The droplet exhibits a spherical shape to maximize the volume to surface ratio. The small diameter allows the measurement of the magnetic field in the presence of a large gradient. The droplet is confined by surrounding liquid to prevent movement, changes in shape and to avoid entry of gas bubbles. It should be chemically inert. The interfaces between the liquids must not give rise to susceptibility broadening. Hence, the magnetic susceptibility of the materials must be similar. The container should be a capillary with a small diameter and a long shape (like a cylinder or an ellipsoid, Figure 1.11), remain chemically stable in time and not react or mix with the droplet. A micro RF coil is wrapped around the capillary tube (solenoidal detector in Figure 1.11). The board that carries the whole system is made of a material that matches in susceptibility the copper wire, is chemically inert and non conductive.

In 2008, the prototype of the NMR probes used in this project [33] was based on *Cycloexane* (C_6H_{12}) doped with *tris(2,2,6,6-tetramethyl-3,5-heptanedionato) chromium(III)* ($Cr(III)(tmhd)_3$). A spherical droplet of the MR-active solution was confined by a solution of heavy water (D_2O) and *Manganese (II) chloride* ($MnCl_2$) in a miniature cylinder of Pyrex (1.3 [mm] diameter and 0.2 [mm] wall thickness). The detector coil was a high-purity copper wire turn around the cylinder. The whole system was surrounded by a cylinder made with *perfluorinated hydrocarbon* and it was controlled remotely using a Field Programmable Gate Array (FPGA). This probe was developed in order to define the features of the future probe system and their potential use, is measuring the k-space trajectory in a EPI (Echo Planar Imaging) sequence.

In 2008, more probes were produced and rearranged in a tetrahedral fashion [34] to better evaluate the k-space trajectory during EPI, spin-warp and spiral sequences, to inform image reconstruction. Further considerations on using a system formed by more than one probe were made, e.g. the best relative positions of the probes. In 2011, NMR probes were used to measure the entire field evolution [25] in order to correct field imperfections in the image during diffusion imaging, EPI scans on phantoms and in vivo scanning. The spatial variation of the magnetic field was measured up to the third order solid harmonics using a 16-probe system. In 2015 [35], the actual stand-alone monitoring system was designed and used for the first time to measure MR sequence k-space trajectories leading to successful image reconstruction. Further analysis of the system imperfections were made. The commercial monitoring system that was used in my work is ^{19}F ($\gamma_{^{19}F} = 252 \cdot 10^{-6}\ \frac{rad}{sT}$) based rather than ^{1}H based ($\gamma_{^{1}F} = 267 \cdot 10^{-6}\ \frac{rad}{sT}$) , which means that it is relatively insensitive to the ^{1}H RF pulses used for imaging ($\Delta\gamma \approx 6\%$). Further improvements have been recently made on making frequency-adjustable magnetic field probes [36]. The proposed field probes features a second coil that can be used to change the local resonance frequency (and so to modify the local magnetic field) in the probe. This allows the probes to be switched on and off, tuning selective excitation to a frequency that doesn't interfere with the MR image sequence.

NMR probes [35] are the magnetic field sensors used in this project. The probes that we use [25] are based on ^{19}F based MR-active liquid. They exploit the free induction decay (FID) signal of a small droplet of the MR-active liquid. The evolution of the phase of the signal from a single probe is related to the magnetic field by rewriting equation 1.2 [33]:

$$\gamma \int_0^t \mid \mathbf{B}(\mathbf{r},\tau) \mid d\tau = \phi(t) + \omega_d t \qquad \Longrightarrow \qquad \mid \mathbf{B}(\mathbf{r},t) \mid = \left(\frac{d\phi(t)}{dt} + \omega_d \right) \frac{1}{\gamma} \tag{1.15}$$

where τ represents time, $\mathbf{r}$ represents the position of the probe, ω_d denotes the demodulation frequency [7] and $\phi(t)$ is the signal phase.

[7] The demodulation frequency is the frequency of the RF used to demodulated the measured NMR

The continuous phase time course is extracted from the FIDs by a phase-unwrapping process [8]. The errors due to the unwrapping process are minimized via up-sampling the raw data and down-sampling the results [33]. The phase measurements can be used to obtain magnetic field magnitude, k-space trajectories and concurrent gradient evaluations.

Sensitivity of the field probes. The main limiting factor of the probes is the thermal noise. This arises from the solenoidal RF coil and circuits. At the MR frequency bandwidth (BW), the noise is given by:

$$\xi = SNR\sqrt{BW} \tag{1.16}$$

The probe's phase sensitivity can be obtained considering equations 1.15 and 1.16 as:

$$\sigma_\phi = \frac{\sqrt{BW}}{\sqrt{2}\xi} = \frac{1}{\sqrt{2}SNR} \tag{1.17}$$

The noise in the field measurement is given by:

$$\sigma_B(t) = \frac{\sqrt{2}\ \sigma_\phi(t)}{\gamma\Delta t} = \frac{1}{\Delta t}\sigma_\phi(t)\frac{\sqrt{2}}{\gamma} = BW\frac{\sqrt{BW}}{\sqrt{2}\ \xi}\frac{\sqrt{2}}{\gamma} = \frac{BW^{\frac{2}{3}}}{\gamma\xi} \propto T_{obs}^{-\frac{2}{3}} \tag{1.18}$$

where, in the absence of noise autocorrelation $BW = \Delta t^{-1} = n\ T_{obs}^{-1}$ (Δt represents the sampling period, n is the number of samples and T_{obs} the overall sampling duration).

Furthermore, there are minor sources of systematic errors that influence the evolution of the magnetic field. The chemical shift effect of MR-active liquid and the magnetic susceptibility of the surrounding materials causes errors of parts per million (ppm) magnitude. A constant offset is due to the magnetic susceptibility effect on the boundary of the materials. Susceptibility effects of the MR-active liquid can also lead to field inhomogeneity. The bias is the order of 10 nT for static measurements, but does not affect MR applications where relative field changes are relevant . For time-varying measurements, the influence of changes in probe temperature is evaluated as having a nT/K magnitude.

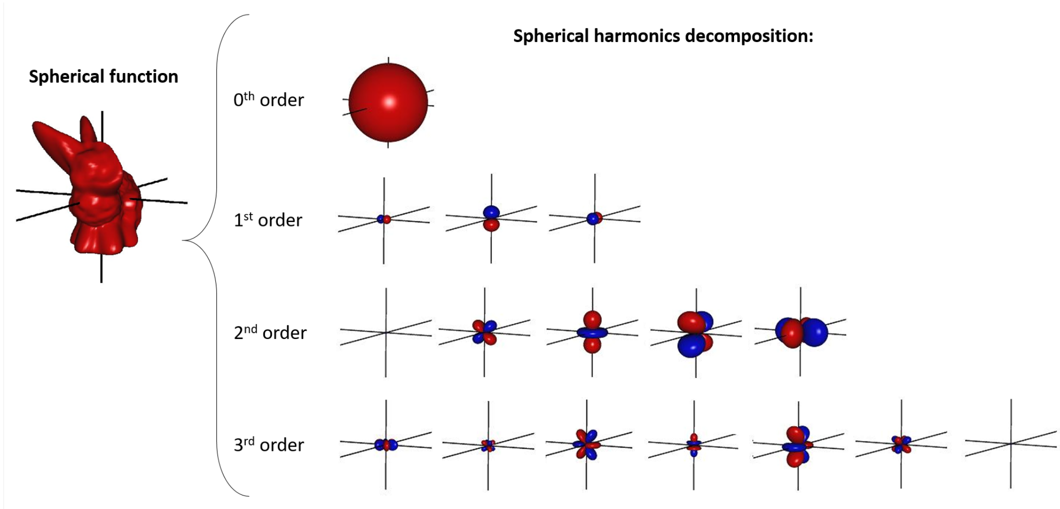

Figure 1.12: *Example of spherical harmonics decomposition.* The picture shows the solid harmonic decomposition of a general spherical function [37]. It is clear that the complexity of the harmonics increases with the spatial order.

1.5.1 Solid harmonic functions

Spherical harmonics ($\Psi_l^m(\theta, \phi)$) form a family of functions that can be used to represent a function as:

$$f(\theta, \phi) = \sum_{l=0}^{\inf} \sum_{m=-l}^{m=l} a_{lm} \Psi_l^m(\theta, \phi)$$

where θ, ϕ, l, m, represent angles, degree and orders respectively. A graphical example is shown in Figure 1.12.

Spherical harmonic equations are written based on the coordinate system chosen. Table 1.4 reports the equations based on Cartesian coordinates. Spherical harmonics assume then the name of solid harmonics. These equations are used to evaluate the spatial variation of the fields measured using an array of NMR probes.

signal.

[8]**Phase wrapping and unwrapping algorithm**. The phase is defined as a periodic continuous function in the range $[-\pi, +\pi]$. If the sampled signal exceeds the range, the phase is digitised as wrapped phase (signal that contains jumps every 2π). The unwrapping process is applied to make it continuous and usable for further analysis. The noise level of the original signal can invalidate the unwrapped phase.

Basis Nr.	Spatial Order	Basis functions
0	0	1
1	1	x
2		y
3		z
4	2	xy
5		zy
6		$3z^2 - (x^2 + y^2 + z^2)$
7		xz
8		$x^2 - y^2$
9	3	$3yx^2 - y^3$
10		xzy
11		$(5z^2 - (x^2 + y^2 + z^2)) \cdot y$
12		$5z^3 - 3z(x^2 + y^2 + z^2)$
13		$(5z^2 - (x^2 + y^2 + z^2)) \cdot x$
14		$x^2 z - y^2 z$
15		$x^3 - 3xy^2$

Table 1.4: *Solid Harmonics.* Solid harmonics basis function in Cartesian coordinates [33].

The magnetic field $\mid \mathbf{B}(\mathbf{r}, t) \mid$ is formed by *static* and *dynamic* components. The first represents the contribution due to the magnetic susceptibility of the parts of the object, so it is well defined and highly structured in space. It is evaluated during the calibration of the probes (t_{calib}). The gradient coils, the main field coil, shim elements and the perturbation due to the presence of the subject are the sources of the dynamic component. They are generally distant enough to give a spatially smooth contribution to the field. Hence, the dynamic component can often be expressed using low-order solid harmonic functions [34].

$$\mid \mathbf{B}(\mathbf{r}, t) \mid = B_{dynamic}(\mathbf{r}, t) \ + \ B_{calib}(\mathbf{r}) = \sum_{l=0}^{N_L - 1} c_l(t) f_l(\mathbf{r}) + B(\mathbf{r}, t_{calib}) \tag{1.19}$$

where $N_L = 16$ represents the total number of basis functions $f_l(\mathbf{r})$ (l the number of the basis), and the dynamic coefficients $c_l(t)$. Based on equation 1.15, the phase is evaluated as:

$$\begin{aligned}
\phi(t) =& \gamma \int_0^t \mid \mathbf{B}(\mathbf{r}, \tau) \mid d\tau = \gamma \int_0^t \left(\sum_{l=0}^{N_L - 1} c_l(t) f_l(\mathbf{r}) + B_{calib}(\mathbf{r}) \right) = \\
&= \sum_{l=0}^{N_L - 1} \left(\gamma \int_0^t c_l(\tau) d\tau \right) f_l(\mathbf{r}) + \gamma B_{calib}(\mathbf{r}) \left(\int_0^t d\tau \right) = \\
&= \sum_{l=0}^{N_L - 1} k_l(t) f_l(\mathbf{r}) + \gamma \omega_{calib}(\mathbf{r}) t
\end{aligned} \tag{1.20}$$

where $k_l(t)$ represents the coefficients of the dynamic part of the magnetic field during the MR sequence. The $k_l(t)$ coefficients are determined by sampling the phase of the signal at $N_p \geq N_L$ positions over the scanning volume.
Hence, if the Larmor frequency of the probes during the calibration are given by $\omega_{calib} = \gamma_P B_{calib}(\mathbf{r_j})$. Equation 1.20 becomes:

$$\phi_j(t) = \sum_{l=0}^{N_L-1} k_l(t) f_l(\mathbf{r}_j) + \gamma \omega_{calib,j}(\mathbf{r}_j)t \tag{1.21}$$

Using the matrix notation:

$$\phi_P(t) = [\phi_1(t), \ldots, \phi_{N_P}(t)]^T; \qquad \omega_{calib,P} = [\omega_{calib,1}, \ldots, \omega_{calib,N_P}]^T;$$

$$\mathbf{k}(t) = [k_0(t), \ldots, k_{N_{L-1}}(t)]^T; \qquad \mathbf{P} = \begin{bmatrix} f_0(\mathbf{r}_1) & \ldots & f_{N_{L-1}}(\mathbf{r}_1) \\ \vdots & \ddots & \vdots \\ f_0(\mathbf{r}_{N_P}) & \ldots & f_{N_{L-1}}(\mathbf{r}_{N_P}) \end{bmatrix};$$

This notation describes the structural features of the probes (size, positions) and the number and choice of the basis functions in the matrix $\mathbf{P}$. For any basis set $f_l(\mathbf{r})$, the phase is given by the linear system:

$$\phi_P(t) = \mathbf{P}\mathbf{k}(t) + \omega_{calib,P}\ t \tag{1.22}$$

The coefficients $\mathbf{k}(t)$ are estimated in a least-squares fashion as:

$$\mathbf{k}(t) = \mathbf{P}^+ \left[\phi_P(t) - \omega_{calib,P}\ t\right] \tag{1.23}$$

where $\mathbf{P}^+$ is the Moore-Penrose pseudoinverse of $\mathbf{P}$.

The error on the evaluation of the coefficients is related to the relative positions of the probes as:

$$\sigma_{k_l} = \sigma_\phi \sqrt{\sum_j \left(\mathbf{P}^+_{\mathbf{lj}}\right)^2} \tag{1.24}$$

where σ_ϕ is defined as in equation 1.17. In order to minimise the errors on the coefficients, the probes must be distributed evenly around the object[9] and the number of probes must be greater or equal to the number of basis functions.
Considering my work, I used an array of $j = 1 \ldots 16$ probes held by a support at positions

[9] Columns of $\mathbf{P}$ must be orthogonal or nearly linearly independent.

$\mathbf{r_j}$, so $N_p = N_L = 16$. Using the spherical harmonics as basis functions, the matrix $\mathbf{P}$ for our probe set is:

$$\mathbf{P} = \begin{bmatrix} f_0(x_1,y_1,z_1) & f_1(x_1,y_1,z_1) & \dots & f_{14}(x_1,y_1,z_1) & f_{15}(x_1,y_1,z_1) \\ \vdots & \ddots & \ddots & \ddots & \vdots \\ f_0(x_{16},y_{16},z_{16}) & f_1(x_{16},y_{16},z_{16}) & \dots & f_{14}(x_{16},y_{16},z_{16}) & f_{15}(x_{16},y_{16},z_{16}) \end{bmatrix} =$$
$$= \begin{bmatrix} 1 & x_1 & \dots & x_1^2 z_1 - y_1^2 z_1 & x_1^3 - 3x_1 y_1^2 \\ \vdots & \ddots & \ddots & \ddots & \vdots \\ 1 & x_{16} & \dots & x_{16}^2 z_{16} - y_{16}^2 z_{16} & x_{16}^3 - 3x_{16} y_{16}^2 \end{bmatrix} \tag{1.25}$$

If we define:

$$\begin{aligned} &0^{th}\text{order: } \mathbf{k}_0(t) && \text{(homogeneous component)} \\ &1^{st}\text{order: } \mathbf{k}^{(1)}(t) = [\mathbf{k}_1(t), \mathbf{k}_2(t), \mathbf{k}_3(t)] && \text{(linear component)} \\ &2^{nd}\text{order: } \mathbf{k}^{(2)}(t) = [\mathbf{k}_4(t), \mathbf{k}_5(t), \mathbf{k}_6(t), \mathbf{k}_7(t), \mathbf{k}_8(t), \mathbf{k}_9(t)] && \text{(linear component)} \\ &3^{rd}\text{order: } \mathbf{k}^{(3)}(t) = [\mathbf{k}_{10}(t), \mathbf{k}_{11}(t), \mathbf{k}_{12}(t), \mathbf{k}_{13}(t), \mathbf{k}_{14}(t), \mathbf{k}_{15}(t)] && \text{(linear component)} \end{aligned} \tag{1.26}$$

The the global phase term is represented as a sum of harmonics:

$$\phi_P(t) = \mathbf{k}_0(t) + \mathbf{k}^{(1)}(t) \cdot \mathbf{r} + \mathbf{k}^{(2)}(t) \cdot \mathbf{r} + \mathbf{k}^{(3)}(t) \cdot \mathbf{r} \tag{1.27}$$

The low order harmonics (0^{th}, 1^{st}) represent mainly the field induced by the subject of the scan. The high order harmonics (2^{nd}, 3^{rd}) of the static magnetic field component reflect imperfections of the main magnet and susceptibility effects [25]. High order field perturbations describe varying sources, such as the concurrent field, eddy currents (arising from gradient coils, shims and cryostat), thermal noise and subject motion.

1.5.2 From raw signal to absolute magnetic field values

Acquiring phase data allows the magnetic field value recorded by the NMR field probes to be evaluated. First, the data needs to be de-noised by applying a smoothing function (such as the lowess method of `smooth` MATLAB built-in function). Considering the phase signal given by $\phi = \gamma \int_0^t B(t) d\tau$, the magnetic field is obtained by:

$$B = \frac{1}{\gamma}\left(\frac{d\phi}{dt}\right) \tag{1.28}$$

where $\gamma = 251.6\ 10^6\ [rad(sT)^{-1}]$ of the ^{19}F. The derivative can be approximated as finite difference:

$$\frac{d\phi}{dt} = \frac{\phi_{t_1} - \phi_{t_0}}{t_1 - t_0} \tag{1.29}$$

The time difference between two consecutive points can be written as:

$$t_1 - t_0 = \frac{\Delta T}{N} = \frac{\Delta T}{\Delta T BW} = \frac{1}{BW} \tag{1.30}$$

where: $\Delta T = 10\ [ms]$ is the acquisition duration and $BW = 10^6\ Hz$ is the bandwidth of the acquisition for phase data, and N is the total number of data points sampled in the ΔT.

In conclusion:

$$B = \left(\frac{d\phi}{dt}\right)\frac{1}{\gamma} = \tag{1.31}$$

$$= \left(\frac{\sum_{i=1}^{10^4}(\phi_{t+1} - \phi_t)_i[rad]}{\frac{10\times10^{-3}[s]}{(10\times10^{-3}[s])\times(1\times10^6[1/s])}}\right)\frac{1}{251.6\times10^6[rad/(sT)]} \tag{1.32}$$

$$= \left(\frac{\frac{\sum_{i=1}^{10^4}(\phi_{t+1}-\phi_t)_i[rad]}{10^4}}{10\times10^{-6}[s]}\right)\frac{10^{-6}}{251.6\times10^6[rad/(sT)]} \tag{1.33}$$

$$= \frac{\sum_{i=1}^{10^4}(\phi_{t+1} - \phi_t)_i}{251.6\times10^4}[T] \tag{1.34}$$

1.5.3 Magnetic field camera

The field camera system is formed by the field probes array connected to the T/R signals and the Acquisition System (booster unit, computer desktop application) and manage the data T/R and scanner communication (trigger and synchronisation) [39]. Once the field probes are placed on the scanner bed, the system is turned on. Figure 1.13 shows the two mounting systems used in this thesis. The systems hold the probes in place during the measurements. The former holder (Figure 1.13.a) did not allow measurements to be performed with simultaneous scanning, so the latter has been developed (Figure 1.13.b). Technical challenges faced in the process were to design the holder using a material that did not interfere with the measurements, that could fit in between the receiver and the transmit coil and to reduce the risk of pulling on the cables while the scanner bed was moving.

Field camera calibration First of all, it is necessary to measure the probe positions. The accuracy is 0.1 mm and the action to move the bed to place the set-up is sufficient to detect a shift in probe positions [11]. The field camera calibration is computed at the beginning of each measurements and it is relevant for the accuracy of phase data, k-space data, and field data. It consists of the measurements of the off-resonance FIDs values of the field probes and field probe positions in the scanner frame. The off-resonance

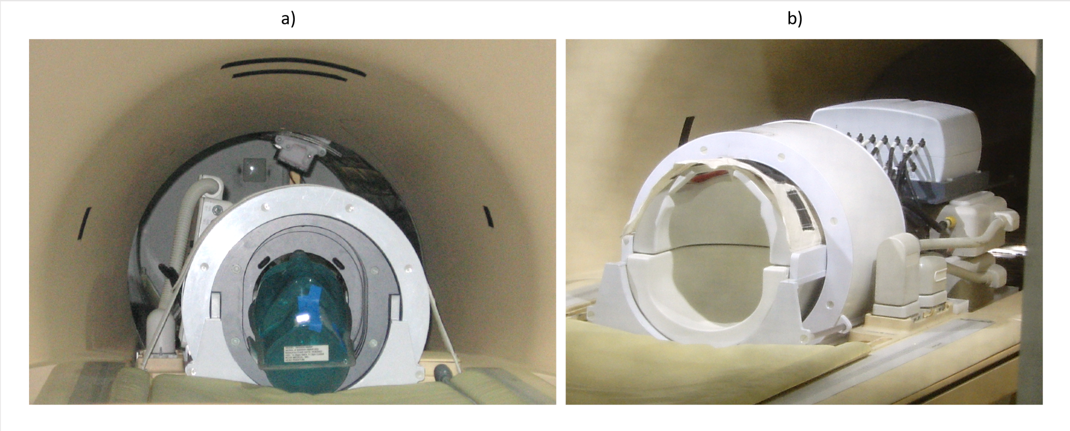

Figure 1.13: *Photo of the customised mounting systems for NMR field probes.* (a) Figure shows the PVC probe-holder [38, 11], placed inside the transmit head coil. On the top of the scanner bore, the optical camera is visible. The anthropological phantom used for developing the mounting system was placed inside the mounting system. The set-up has been improved to allow measurements of the magnetic field with simultaneous scanning. Figure (b) shows the Cloth probe-holder [12, 13], placed in between the transmit and receiver head coil. The transmit coil has been slightly pulled back for the purpose of this picture only. To avoid cables pulling while the bed is moved, a PVC plastic tray has been added to hold the T/R box of the magnetic field camera system on top of the scanner's receiver boxes. Neither mounting system was commercially available.

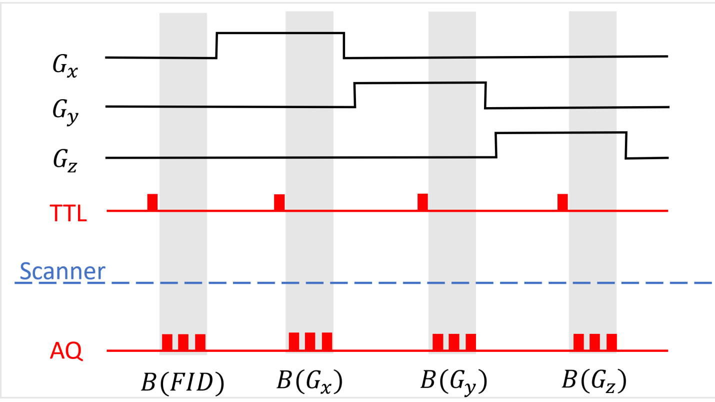

Figure 1.14: *Sequence of Skope Calibration.* The sequence played out in the scanner involves acquiring four sets of FIDs from the probes. The first FID is used to estimate the frequency offset at each probe. During the 2nd to the 4th FID only, the scanner applies an external field gradient on the X, Y and Z axes with an amplitude of ($2.5mT\ m^{-1}$). The positions of the probes are extrapolated from the field values that the gradients create in each probe and from the known gradient strength. The TTL signal is an external trigger to manage the field camera acquisitions. The FID is acquired after a certain time from the beginning of the gradient to avoid the error due to eddy currents or mechanical gradient vibration. [39]

calibration process compensates static magnetic field inhomogeneity. Calibration of the probe positions in the scanner frame is performed by running the sequence described in Figure 1.14.

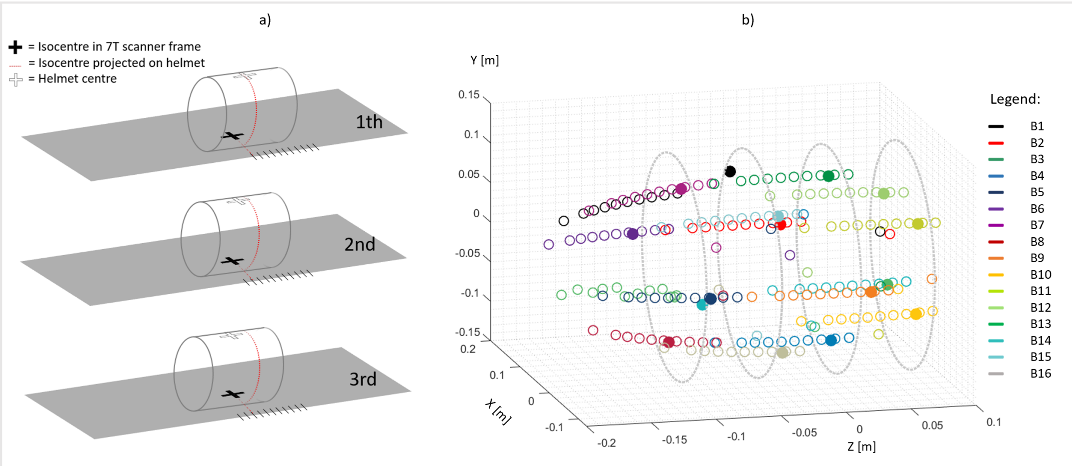

Figure 1.15: *Stability of B_0 field.* The PVC probe-holder (Figure 1.15) was shifted in 11 different positions (empty dots) respect to the isocentre (black cross). As a result, B_0 was not stable and influenced the shape of the gradients used for calibration (Figure 1.14) and led to an incorrect evaluation of probe positions.

The calibration sequence was used to test the error in probe positions in a cylindrical shape related to the stability of the B_0 scanner field relative to the distance with respect to the isocentre (Figure 1.15). The PVC probe-holder was placed in the transmit coil and the bed was shifted to 11 different positions along the foot-head direction (z). So, it is expected to measure variations along the z axis only. The calibration sequence was run at each position and compared with the PVC probe-holder position used for Motion Correction experiments (Figure 3.7).

For a perfect gradient, probe positions ($\vec{r} = (x, y, z)$) could be easily found from Equation 1.14, $\vec{(r)} = \frac{\vec{(B)}}{\vec{(G)}}$, where $\vec{(B)}$ is the magnetic field, $\vec{(G)}$ is the gradient. As the magnetic field far from the isocentre varyies (Δ_B), the positions at each step are given by: $\vec{r'} = \vec{r} + \frac{\Delta_B}{G}$. An estimation of the percentage variation with respect to the experimental set-up is reported in Table 1.5 for probes 5 and 10 as the former was getting further from the region of stability and the latter rested within it. The gradients (Figure 1.14) change shape outside the stability region of the B_0 field and lead to a mis-evaluation of the probe positions; this is particularly evident on the percentage variation of probe 5 along x and y axes.

	Probe 5			Probe 10		
	$\Delta_x[\%]$	$\Delta_y[\%]$	$\Delta_z[\%]$	$\Delta_x[\%]$	$\Delta_y[\%]$	$\Delta_z[\%]$
Pose 1	-5.296	-0.103	0.394	0.020	0.001	-0.669
Pose 2	-5.117	-0.077	0.301	0.016	-0.002	-0.527
Pose 3	-5.724	-0.054	0.207	0.009	-0.008	-0.387
Pose 4	-5.964	-0.034	0.110	0.000	-0.015	-0.245
Pose 5	-5.719	-0.016	0.010	-0.008	-0.021	-0.101
Pose 6	-5.809	-0.001	-0.092	-0.020	-0.031	0.043
Pose 7	-5.417	0.011	-0.195	-0.034	-0.044	0.188
Pose 8	-5.464	0.011	-0.195	-0.034	-0.044	0.188
Pose 9	-5.464	0.011	-0.195	-0.034	-0.044	0.188
Pose 10	-5.422	0.011	-0.195	-0.033	-0.045	0.188
Pose 11	-209.873	-1.271	-0.790	-0.286	-0.892	-0.044

Table 1.5: *Percentage variation of probe positions.* Table reports the percentage of variations of probe positions show in Figure 1.15.

Data acquisition The acquisition data is managed by computer. The software library is under the MIT licence (LUFA Library. Copyright (C) Dean Camera, 2013.) [39].
The scheme of the acquisition is shown in Figure 1.16. The external trigger signal from the 7 T scanner indicates the beginning of the measure if the system is set to be driven by the scanner, otherwise it can be started manually. Then, a RF pulse is generated by the system to excite the fluorine inside the probes and FID decays are measured with a minimum of 5 ms delay [39]. The data used to evaluate the magnetic field are taken in the first 5 ms of the the FID of the probes. The frequency of the signal is sensitive to the local magnetic field.

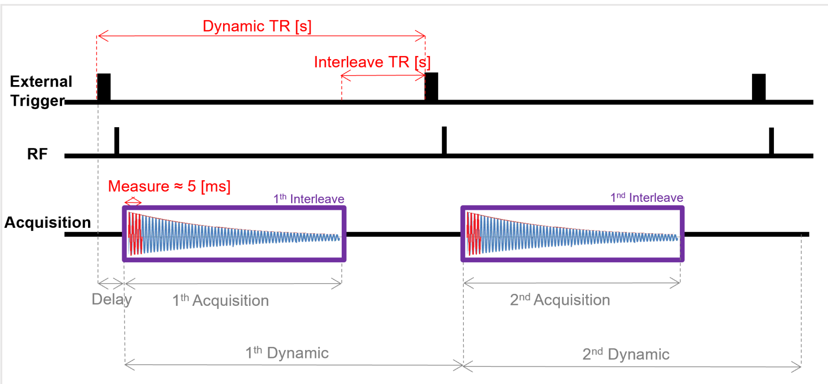

Figure 1.16: *Time scheme of the parameters for the acquisition.* Note that each acquisition is preceded by an RF pulse for field probe excitation.

Scan Parameters	Description	Values
Nr Acquisition	(Nr Dynamics $\times$ Nr Intervals)	$1 \div 10$
Aq Duration	(Interleave TR $\times$ Nr Intervals)	$150\,[ms]$
Nr Dynamic	The number of acquired dynamics.	$30 \div 4000$
Dynamic TR	The repetition time between each dynamic.	$150\,[ms]$
Nr Interleave	The number of intervals for each Dynamic.	$1 \div 24$
Interleave TR	The repetition time between each Interval.	(Varying)
Aq Delay	Delay of acquisition start	$5 \div 30\,[ms]$

Table 1.6: *Magnetic Field camera Parameters.* Scan parameters set for the acquisition of data shown in this Thesis.

Field camera parameters Parameters to set-up to perform measurements are reported in table 1.6. The so-called *Dynamic* (Figure 1.16) is defined as being between two consecutive RF pulses, the *Time Repetition* (TR) of the camera is the length in time of a Dynamic. One or more *Acquisitions* could be acquired for each dynamic. The *Interleave TR* is the time between two acquisitions. Interleave TR coincides with TR if one acquisition is taken for each Dynamic, otherwise needs to be set as a submultiple of TR. Both the cases have been used to acquire the data shows in this dissertation. TR is limited as $\geq 100\ ms$ by the NMR probes flip angle (constant).

1.6 Conclusion

UHF MRI scanner solutions allow an increase in image accuracy and resolution of MR images (Section 1.4). However, their implementation leads to multiple additional challenges, including B_0 homogeneity and motion sensitivity.

The field camera system (Section 1.5) probes the magnetic field inside the scanners (operating at up to 11 T). These measurements could be used for facing those challenges. In this dissertation, the field camera system has been used in a brand new approach for developing motion tracking systems (Chapter 3).

Chapter 2

Ameliorating the effect of motion in MRI

Motion-related problems in MRI and MoCo (Motion Correction) techniques already developed to ameliorate the effect of motion in MRI are summarised in this chapter (Section 2.2). MoCo techniques include motion prevention, and marker-less and marker-based motion tracking. Effects of motion on the MR image acquisition process and the need to modify the MR imaging sequence for better implementation of motion correction are also discussed.

2.1 Effect of motion in MRI

The MRI technique is a slow (at best ≈ 50 Hz frame rate for two-dimensional imaging) and low resolution (4 MP per two dimensional image) imaging modality compared to modern optical imaging methods (up to 8 MP and 3×10^4 Hz in optimal light conditions) [40, 3]. Nevertheless, both techniques suffer from motion artefacts (Figure 2.1). MRI is susceptible to motion due to the long scan times necessary to acquire images compared to the time-scales of relevant physiological phenomena. For example, the breathing cycle is repeated approximately every 3 s causing the motion of the chest and so of the head, but to acquire a MRI image could take several minutes or more. Furthermore, even collaborative subjects struggle to remain still and control motion during longer scan sessions, while non-collaborative subjects may perform unpredictable motion even during short scans.

Motion can be involuntary (such as the muscular contraction of the heart and diaphragm) or voluntary. In both cases, motion may lead to corruption of the image and show motion artefacts (e.g. ghosting, blurring) and in the worst case scenario can result in non-diagnostic images or false quantitative results in clinical and scientific studies.

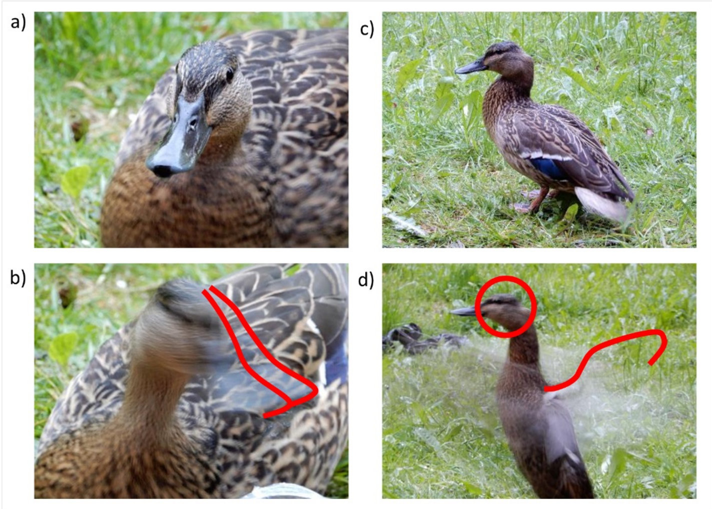

Figure 2.1: *Example of motion artefacts in co-operative and non co-operative subjects.* These pictures illustrate artefacts due to motion during MRI scans by making an analogy with optical methods. While images a,c show all the anatomical parts of the subject of the picture, images b and d show that in the presence of motion, images can show multiple versions of an anatomical structure (two beaks), not record a structure at all (wings are missing) or resolution loss due to blurring (top of the head). [Duck pictures made by Federico Venturi, University of Nottingham - The duck was well fed to assure no complaint about the pictures being taken]

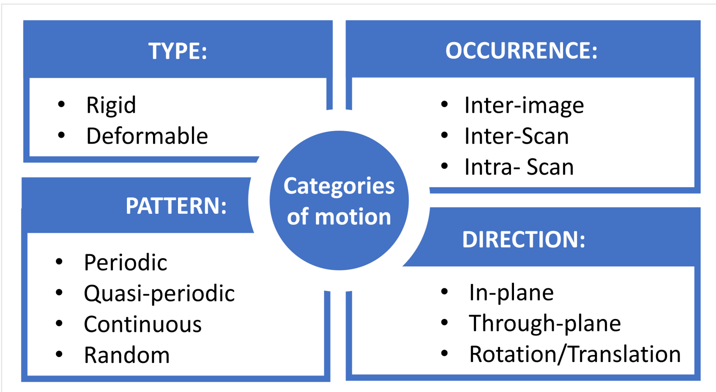

Figure 2.2: *Motion Categories* [3]. In general, it is relevant to evaluate the spatial resolution in relation to the amount of motion occurring during a given time period to evaluate the effect of that motion. The type of motion can be categorised based on the transformation (rigid, if spatial relationships between points are maintained, or non-rigid if they are not); occurrence (if motion occurs between acquisitions of volumes, inter-image, between excitation pulses within a volume, inter-scan, or during a signal acquisition and signal excitation, intra-scan); timing of the motion (random, quasi-periodic, periodic). It is called in-plane motion the type of motion that happens within the excited slice plane, while the motion happens perpendicular to the slice is called through-plane motion motion.

Reducing scan times by using faster imaging sequence reduces the motion artefacts, but this approach has limitations in terms of resolution and image quality. Motion is a practical problem that can lead to incorrect or false diagnosis and the need to repeat the scan, hence imposing additional costs on health systems (Figure 2.3) [41, 42].

A study in 2015 estimated an increased cost of 600 US dollars per hour of scanning due to motion. The study involved patients across medical evaluation programmes and emergency departments. The MR examination was repeated in the 20% of the cases (on average [41]). This leads to increased stress for the patient and additional challenges for radiographers, as the duration of the examination becomes longer or it is necessary to repeat scans in a additional sessions. It also leads to an increase in the cost of the technique (on the order of magnitude of billions of dollars per year) and to a greater impact of the technique on the environment.

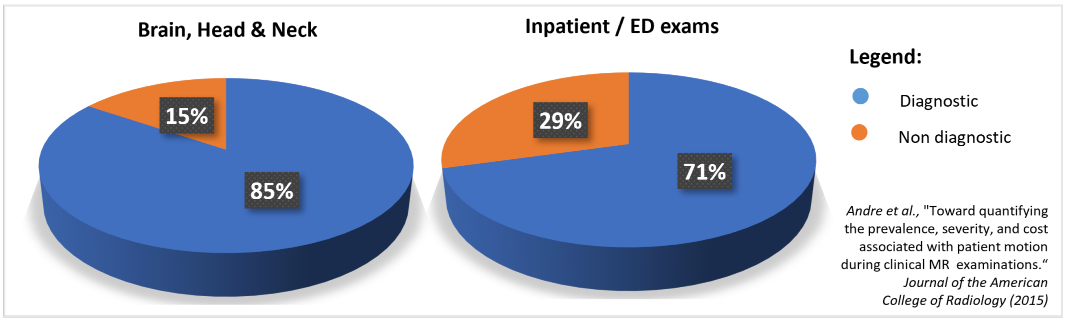

Figure 2.3: *Estimating the increased costs of MRI due to motion-induced image corruption.* An evaluation of the cost increase of the MRI technique in the clinical environment has been found to be 600 US dollars per hour of scanning, in a study involving both in-patients and patients admitted to the emergency department that were in need of a diagnosis on neck and head (brain) body parts (1.5 T scanner)[41]. Images were evaluated by radiographers as diagnostic (blue) or non diagnostic (orange). In most cases, motion artifacts were not/barely detectable or noticeable and examinations remained diagnostic in quality, while on average 20% of MR examinations were marginal in diagnostic quality and were repeated.

A model-based retrospective study (not yet prospectively validated) has been conducted in 2020, with assumptions on the daily use of the scanner and financial costs to consider. Patient categories of the study were targeted among those considered the most challenging. The study involved PET/MRI examinations on patients affected by dementia (76%) and paediatrics patients (24%) and showed that the need for repeating the scan is common in paediatric patients. The benefits of the use of motion correction techniques are to reduce the use of anaesthesia and the associated risks of side effects, and reducing financial costs.

Motion correction in magnetic resonance imaging is consequently an important research field which has a long history. Few methods for motion correction have entered clinical routine, but a number of approaches have the potential for broader application [1].

2.1.1 Limit the effect of motion in MRI.

There are a series of factors to consider in order to reduce the effect of motion in MRI.

Common standard clinical practices aiming for *motion prevention* have been established over the years. Informing the patient on the MRI procedure affects the extent of motion recorded during the procedure. The effect of reducing motion artefacts by providing a pamphlet, describing the procedure and visually showing and emphasising the importance of staying still, has been proven[43]. The practice to provide exhaustive information on the procedure also reduced anxiety related to the MRI examination and so reduced motion artefacts [44]. The immediate call of the radiologists would also prevent to complete study that would need to be repeated [45]. Respiratory or cardiac gating can provide external triggers to the MR image acquisition and lead to improvements in the contrast and spatial resolution of the image. Breath-holding and padding the body part can be used to reduce movements, but in extraordinary cases sedation or anesthesia may be necessary (this comes with other risks).

The MRI sequence length affects patient comfort. This often leads to increased motion related artefacts as patient discomfort get worse with time. In general, the longer the examination is, the harder it is for the patient to hold still (even for co-operative subjects). A good planning of where the MRI sequence falls in the overall scan time can then reduce motion artefacts. Reducing the scanning time by using *faster scanning sequences* can also reduce motion artefacts, but may lead to reduced spatial resolution and signal-to-noise-ratio (SNR). Also, suspending data acquisition during periods of head motion can help to control motion artefact levels [46]. Tracking the head position allows scanning to be divided over several sessions (up to a total of 7 hours in one case [47]).

Another important factor is to consider the inherent motion sensitivity of the sequence, which might depend on phase encode ordering, flow compensation, and the presence of non-motion related artefacts (e.g. fat/water shift). *Motion robust* image acquisition sequences may also be used.

Finally, based on the clinical purpose of the scan, a certain level of motion artefacts can be tolerated, but other scans may need higher image quality. For example, higher quality may be required to image small body parts having weak contrast.

Nevertheless, it may be necessary to *to repeat the scan* if it is not possible to correct the motion.

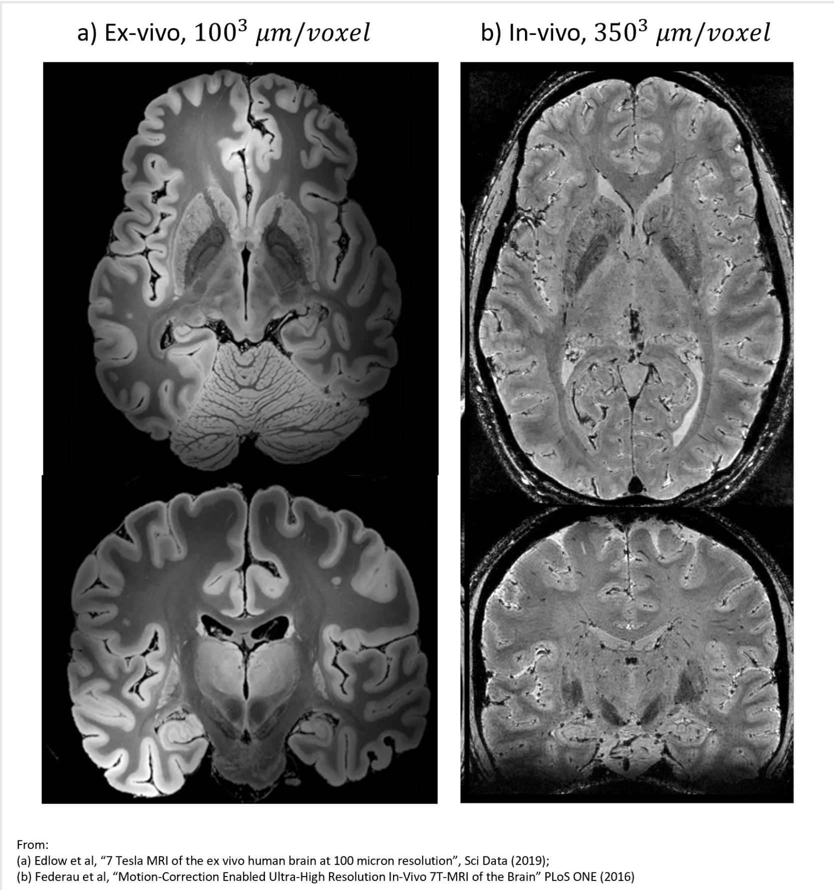

Figure 2.4: *High resolution MR image.* High resolution MR imaging is achievable with 7T scanners. Figures show (a) ex-vivo and (b) in vivo anatomical brain images. Isotropic resolution, scanning sequence and scan time were (a) 100 μm, FLASH (flip angles varying between 15 and 30 degrees in step of 5 degrees, each steps takes 25 hours) and 100 hours [48] (b) 350 μm, GRE and 2 hours [49] (total acquisition time 42 mins). In-vivo scans benefit from the use of an optical tracking device that allows tracking of motion and consequently the correction of motion artefacts [47].

2.1.2 A brief history of MoCo techniques.

Artefacts in MRI due to head motion are still an unsolved problem after 30 years of brain imaging [50]. The first motion correction technique was developed for abdominal imaging [51]. It was based on scaling the object by updating the phase encode gradient strength during a scan. The actual *prospective motion correction* name was used for the first time ten years later [52]. The next step was to compensate the acquisition for respiratory motion during a free-breathing acquisition [53]. Then, an external tracking system to detect head motion was used for real time correction in brain imaging [54, 55]. This system was independent from the MR sequence used and it emerged that six-degrees-of-freedom correction is necessary for brain imaging. A further step was the use of small RF coils as the basis of a tracking method [56]. Scanner geometry was updated based on subject motion, identified by locating three RF coils rigidly assembled and coupled with the skull. The first image-based motion correction technique was developed for brain image correction during fMRI [57]. In 2002, the 3D spherical navigator echo sequence was used to correct head motion up to 1 mm translations and 0.2° rotations. A prospective rigid-body motion correction in all six-degrees-of-freedom using an external optical camera was then successfully implemented [8] in a 3T scanner. The cross-calibration of the optical system required 30 minutes and achieved an accuracy below 1 mm, 1 °. Head motion up to 10 mm translations and 8° rotations, that represented the maximum range of motion achievable in the restricted space inside the head coil, were successfully corrected. Prospective motion correction with a motion rejecting threshold of 0.3 mm and 0.3° was also tested. In 2011, an optical marker-less motion correction technique [58] was successfully used in a Siemens mMR Biograph hybrid PET/MRI scanner (3 T). In 2014, a brain MR image with isotropic resolution lower than 14 μm was achieved by weighting the k-space acquisition to enhance the centre of the k-space [59] instead of implementing a motion correction technique. Between 2015 and 2019, an MR image of micro-structural anatomy of human brain using 7 T MRI scanner in an ex-vivo study [48] and in-vivo study [47, 49] was visualized (Figure 2.4). A post-mortem, motion-free study achieved up to 100μm isotropic resolution as time constraints (up to 100 hours) and motion are not limiting the data acquisition. In-vivo brain studies necessitate the use of MoCo techniques to achieve the same order of magnitude of resolution. In 2015, 400 μm [47] resolution was achieved in a non-consecutive 7 hour scan using optical external device-driven PMC. In 2016, a 350 μm resolution has been achieved in 2 hours scan time (subdivided in 2 sessions)[49] using the fatNav PMC technique. In 2018, a prospective motion correction technique was applied in a 7T Philips Scanner using an external tracking device [20] and integrating the B_0 map information to perform the correction. Recently, improvements in NMR field probe design [4] have allowed these probes to be used as head-mounted markers, specifically by placing three NMR probes on a pair of plastic glasses [60]. In 2019, the same research group upgraded the method by using two sets of NMR field probes. The extra set of NMR probes was fixed in the scanner's reference frame in order to evaluate the displacement of the marker-probes attached to the head and to reach the full accuracy allowed by this technique ($10-30$ μm) in a rest condition (3 mm and 3° of translation and rotation). Further and more recent techniques involve the use of deep learning and machine learning [61, 62]: these will be described later in this chapter.

2.2 Motion Correction (MoCo)

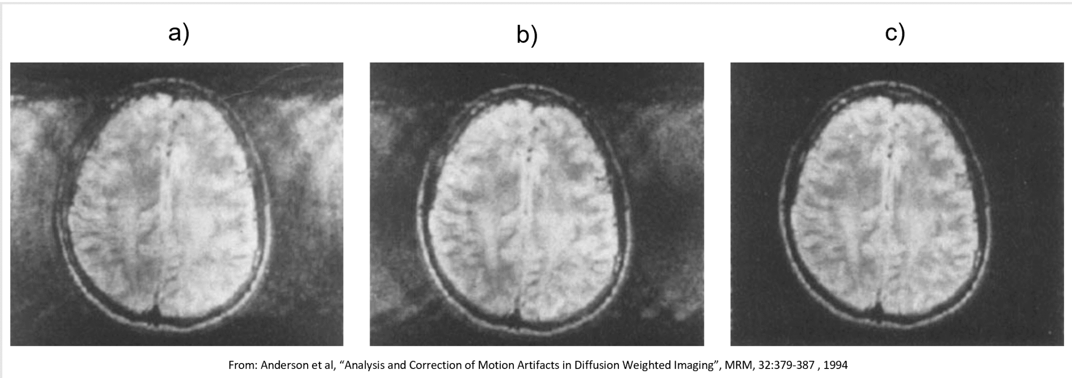

Figure 2.5: *Motion correction.* Diffusion Weighted Image (DWI) brain MR image (a) uncorrected, (b) corrected only for translations and (c) corrected for both rotation and translation [63] using Navigator technique during the image acquisition. Diffusion encoding gradient pulses were applied in the left/right direction (phase encode direction in the sequence used). Navigator phase corrections were able to remove ghosting artefacts, clearly visible in the non-corrected and partially corrected MR images. Image (c) results free of bulk motion artefacts.

The idea of *Motion Correction* is to correct the k-space data based on the pose of the patient. Pose is measured by evaluating the motion parameters, translation (T) and rotation (R) around the 3D axes ($[T_x\ T_y\ T_z\ R_x\ R_y\ R_z]$).

To quantify the rigid body motion of the patient, the body centred coordinate system (that moves with the patient) and the scanner frame coordinate system (set by the read-out, phase encode, slice select gradient directions) are defined [63]. Unit vectors of the spaces are $[\hat{X}, \hat{Y}, \hat{Z}]$ and $[\hat{x}, \hat{y}, \hat{z}]$ respectively. At the beginning, the origins of the reference frames coincide: $[X_0, Y_0, Z_0] = [x_0, z_0, z_0]$. Any point in the space can be specified in the two reference frames: $\vec{R} = X\hat{X} + Y\hat{Y} + Z\hat{Z}$, $\vec{r} = x\hat{x} + y\hat{y} + z\hat{z}$, related by: $\vec{R} = (X_0\hat{X} + Y_0\hat{Y} + Z_0\hat{Z}) + \vec{r}$. The equation in six parameters (translations and rotations around x, y, z axes) that describes the rigid body motion can be derived by considering a small displacement in patient position. A change in position of the patient can be described by a translation ($\vec{R}_0(t)$) followed by a rotation ($\theta(\vec{t})$) of the body centred coordinate system ($\vec{R}$) with respect to the scanner frame ($\vec{r}$): $\vec{R}(t) = \vec{R}_0(t) + \theta(\vec{t}) \times \vec{r}$. The initial position is $\vec{R}_0 = [X_0, Y_0, Z_0] = [x_0, z_0, z_0]$ as initially the two systems of reference coincide. The rotation vector $\vec{\theta} = [\theta_x, \theta_y, \theta_z]\ rad$. Here θ_x represents rotation around the anterior/posterior axis, here θ_y represents rotation around the left/right axis, here θ_z represents rotation around the head/feet axis. As the coordinates of the patient are fixed in the body frame, $\vec{r}$ is time-invariant. The transverse magnetisation (MR signal) is affected by both translation and rotation as it is recorded in the gradient reference frame. Translations produce 0^{th} order phase errors. Rotations produce 1^{st} order phase errors.

The effects in the k-space of motion in the real space is described by Fourier theorems. The effect of *translation* is to produce a phase change in k-space. Multiplying each line in the k-space by an appropriate spatially varying phase corrects the effect of translation. *Rotations* produce rotations of k-space lines. To correct them, it is sufficient to rotate each line in k-space. Figure 2.5 shows a motion-corrupted image (left) and the progressive reduction of artefacts (ghosting, blurring) when the k-space lines were corrected for translation only (center) and for both rotations and translation (right).

Effects of translation on k-space data. Using the Fourier shift theorem it is possible to explain the effect of sample translation while the k-space is scanned. The theorem states that: shifting a object in the real space (f) by amount T_v, produces a multiplication by $e^{i\pi(T_v K_v)}$ in the k-space (F). For example, for translations T_x, T_y in 2D xy-plane:

$$f(x, y) \to F(k_x, k_y) \tag{2.1}$$

$$\begin{bmatrix} T_x \\ T_y \end{bmatrix} = \begin{bmatrix} x - x_0 \\ y - y_0 \end{bmatrix} \to e^{i\pi(T_x k_x + T_y k_y)} \begin{bmatrix} k_x \\ k_y \end{bmatrix} \tag{2.2}$$

Effect of rotational movements on k-space data. Using the Fourier rotation theorem it is possible to explain the effect of sample rotation while the k-space is scanned [64]. The theorem states that: a rotation θ of the object in the real space (f), will produce a rotation of the same amount in the k-space (F). For example, for counterclockwise rotation (R_V) in 2D xy-plane:

$$f(x, y) \to F(k_x, k_y) \tag{2.3}$$

$$R_V = \begin{bmatrix} cos\theta & -sin\theta \\ sin\theta & cos\theta \end{bmatrix} \begin{bmatrix} x \\ y \end{bmatrix} \to \begin{bmatrix} cos\theta & -sin\theta \\ sin\theta & cos\theta \end{bmatrix} \begin{bmatrix} k_x \\ k_y \end{bmatrix} \tag{2.4}$$

Considering the situation where the patient rotates their head halfway through an MR scan of the brain. The pre-rotation and post-rotation parts of the scan data will now not align. To correct the image, it would be sufficient to re-align the rotated k-space lines (however this may lead to missed or double sampled k-space lines). The same theorem can be applied in 3D space.

Tracking data quality: assessment parameters. The quality of tracking data is defined by three parameters [50]:

1. *Precision:* The precision describes the level of jitter or the level of noise.

2. *Accuracy:* The accuracy describes the discrepancy between the true pose and the measured pose.

3. *Latency:* The latency is the delay between the measurement and arrival of the data on the computer or, in prospective motion correction, on the scanner. Latency is due to the physical transmission of the data and the analysis data method used to reconstruct the pose. It depends also on the magnitude of the subject motion.

The required accuracy of the motion monitoring is linked to the resolution of the image.

2.2.1 MoCo techniques

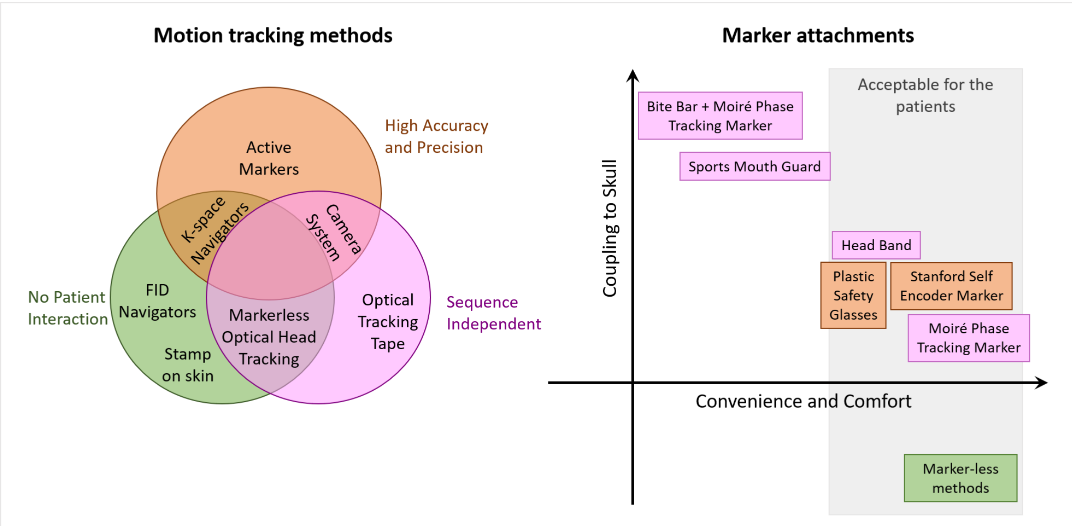

Figure 2.6: *Tracking System.* On the left, the tracking systems are divided according to the physics phenomena used and the precision of the measurement, interaction with the patient and the dependence of the MR sequence. On the right, the plot correlates the convenience and comfort of the marker to the level of brain-skull-marker coupling. The best coupling with the skull corresponds to the least comfortable solution for the patient and vice versa. [50].

To address specific motion related artefacts, it is necessary to evaluate the motion during the MRI scan. The motion correction process can be divided into two main blocks. The first involves detection of the motion. The second involves the correction of the motion to eliminate artefacts from the images.

Motion measurement techniques for brain imaging in MRI are generally based on the assumption of rigid body motion - i.e. that the brain moves in coherence with the skull. This rigid body motion can be described by 6 degrees of freedom (3 rotations and 3 translations). Pulsatile motion of the brain [65, 66] has been discussed as a residual source of non-rigid-body motion, but as long as the skull is closed, the incompressibility of the brain and cerebral spinal fluid (CSF) limits the magnitude of this type of motion. For example, phase contrast MR methods have been used to determine brain pulsation to be on the order of 100 μm and even less in the cortex. Hence, assuming rigid body motion has been a successful strategy in correcting most motion artefacts in MRI of the brain, where the typical spatial resolution is ≥ 100 μm

Motion detection techniques may require imaging sequence modifications to be made. This is definitely the case for methods that estimate the motion from MRI measurements (*self-navigation*), and can be the case with other external measurements that interact with the image data acquisition (*navigator*). Some motion measurement techniques may require additional hardware that needs to be integrated into the scanner (*external sensor based*) or specific software (*data-driven estimator*).

2.2.2 Prospective MoCo (PMC) and retrospective MoCo (RMC)

Image data correction based on measured head motion can be applied in real time, to prevent artefacts, or in post-processing, to correct them. These methods are called *prospective motion correction* (PMC) and *retrospective motion correction* (RMC), respectively (Figure 2.7).

PMC involves tracking the subject motion and updating the image volume during the acquisition based on the motion measurement through adjustment of the gradient and RF pulses . It adapts the scanner geometry periodically in order that the region of interest (ROI) of the scan moves in the scanner's frame of reference in such a way that its position remains fixed with respect to the subject. Adjusting the imaging geometry to track the movements of the object produces 'clean' k-space data that allows standard image reconstruction. Typical times needed for the update are on the order of magnitude of tens of milliseconds. Errors in PMC can arise due to inaccuracy of the motion measurements, incorrect calculation of image geometry changes and any significant latency in the adjustment of the scanner geometry relative to the motion measurement.

RMC Retrospective motion correction involves correcting the raw (k-space information) and/or image data after the acquisition. Knowledge of the object position at each time-point allows the k-space data to be manipulated to account for positional changes during signal encoding.

PMC or RMC have different pros and cons. PMC provides more flexibility than retrospective motion correction. The most important advantage of the real time correction is that the image is ready immediately. Disadvantages of PMC include the effect of the

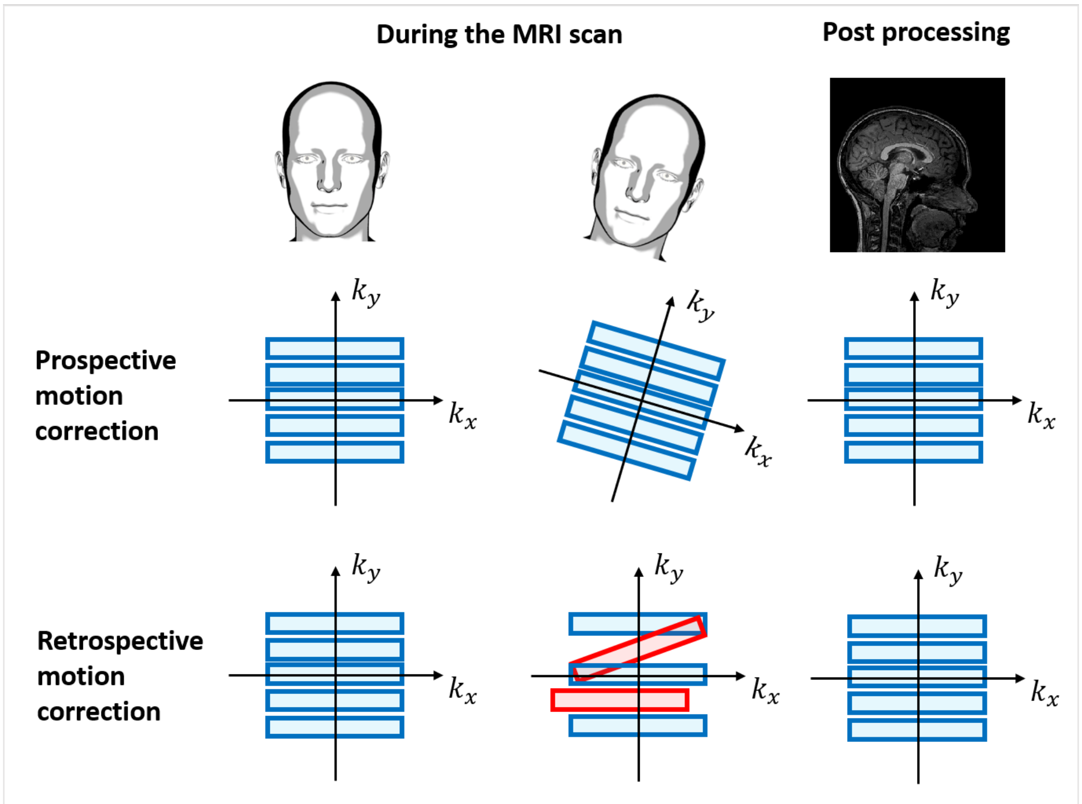

Figure 2.7: *Motion correction techniques.* Prospective motion correction techniques aim to prevent image artefacts due to movement of the head by updating the scanner coordinates during image acquisition. This approach often requires additional hardware / software. Retrospective techniques aim to reduce image artefacts due to the movement of the patient, by correcting k-space information after the acquisition. They do not necessarily require additional equipment, but additional time is needed for post processing.

motion correction cannot be easily reverse to recover data as it would have been acquired in the absence of MoCo. Combined solutions have been proposed to improve results in reducing artefacts.

2.2.3 Marker-based MoCo techniques

External devices have been employed in both research and clinical settings to provide effective motion compensation strategies. A simple categorisation of the different marker techniques is shown in Figure 2.6. Their applicability is limited by the comfort of the patient mainly and by the accuracy of the results that they produce. For example, while a solution that involves coupling the marker to the skin is generally the most comfortable, the skin isn't rigidly coupled with the skull, which makes the marker vulnerable to inaccuracies due to changes in position resulting from facial movement.

Attaching markers to spectacles/glasses. A set-up involving attachment of markers to face glasses has been successfully used in several marker-based methods [67, 4]. Glasses can be worn in the scanner by most subjects and they are quite robust to skin movement (e.g. changes in facial expression).

Wired marker systems.

- Traditional MR-based marker systems [68, 69] include RF-coil-based systems connected to the MRI scanner via traditional coaxial cables. These can be in the form of a solenoidal RF coil containing an MR-visible spherical sample (water) [70]. The water sphere is then the point that will be tracked by 3 orthogonal non-slice-selective RF pulses during the MRI sequence. The use of 3 markers integrated in a headband allows the 6 degrees of freedom of head motion to be tracked.

- *NMR field probes based system.* NMR field probes have been used as head-mounted markers by placing three NMR probes on a pair of plastic glasses [60] and an extra set of NMR probes was fixed in the scanner reference frame in order to evaluate the displacement of the marker-probes. The main advantage of using NMR field probes is to exploit the same phenomena of the MR imaging technique and so to match the measurement of the position of the head (probes) simultaneously to the MR sequence. The NMR field probes method works less well than the optical based tracking method [5], but it is more comfortable.

Wireless marker systems. The aim is to remove all mechanical connections between the markers and the MRI scanner to improve patient safety, to simplify the use and set-up for both patient and scanner operator.

- *Optical tracking system.* External optical tracking methods have been proposed in many different forms. The necessary components are an optical camera that detects one or more markers. The main advantage of this approach is that the motion monitoring method does not directly interfere with the imaging process and also allows positional updates at high frame rates. However, it is crucial to rigidly couple the marker(s) to the subject. Examples are external to the bore system [8], MPT tracking systems [5] and self-encoded markers [71, 72]. The main disadvantages of these techniques include the requirement for line-of-sight access from camera to marker, which can be a challenge in the MR scanner environment.

- *Gravity based system.* VectOrient [73] uses a magnetometer to measure the orientation of the B_0 field (pointing out of the scanner) and gravity (pointing vertically down). Orientation estimation exploits the fact that fields are orthogonal to solve the 3 degrees of freedom of the rotations only. Sensors are all encapsulated along with a micro controller mounted on the patient forehead. Evolution of this marker has lead to the development of WRAD [74] system that also measures the 3 degrees of freedom due to translation thanks to a pick-up coils which measure the gradient field. The device doesn't need to be individually calibrated for each use and frame rates up to 1 Hz are achievable.

Detecting the position of the MPT marker. In this dissertation, optical motion tracking based on a single in-bore camera with the single Moire Phase Tracking (MPT) marker [47] has been used. The system is based on an interferographic read-out and thus delivers accurate and fast motion information. This technique applied to brain imaging relies on a customised mouthpiece that is rigidly fixed to the teeth. This avoids the problem of head skin-shift due to changes in facial expression, but it needs extra preparation time involving both the subject and the operator. The marker position is obtained by integrated software that is applied to the optical image of the marker. The MPT optical camera has been used in this dissertation. It was fixed to the inside of the scanner bore and then calibrated using cross-calibration method [1] in order to identify the geometrical relationship between the frames of reference used by the scanner and the optical camera. The optical marker is rigidly coupled to the skull via a dental mould. Custom bite bars were made for each subject using thermal-setting dental plastic. On the top of dental arcade there is a plane extension to hold the holographic marker. Both of those operations required extra preparation time.
For solutions with more than 1 marker, the *correspondence problem*[1] need to be solved [69]. This problem in tackled by acquiring positions of the markers in orthogonal projections. Motion correction relies on knowing the 6- degrees of freedom transform that is needed to re-align the positions of markers in two consecutive acquisitions. Considering markers supported by glasses-like structures [70, 67]. In general, the markers are positioned in order to maximise the spatial separation along three orthogonal projections in spatial directions. Orthogonal projections are obtained by modifying the MRI sequence. In the case of wired markers, peaks that correspond to different markers are easily identified as each marker is connected to its own dedicated receiver channel. In the case of wireless markers, it is necessary to incorporate the markers at known relative locations within the glasses frame in a way that does not allow peaks to overlap or interchange when the head moves (there is then a limit on the range of movements that can be tolerated).
The correspondence problem is not a problem in the case of NMR field probe markers [60] or in the active magnetic marker system simulated in this dissertation. In the first

[1] *Correspondence problem.* Considering an image1 formed by 3 dots. If the image rotates/translates the 3 dots will lie at new position in the space (image 2). To find which of the 3 dots in the image1 corresponds to the dots in the image 2 is called the correspondence problem.

case, the position of the NMR probe-markers is found based on their relative position compared to a static set of NMR field probes. In the second case, machine learning techniques and a physical model of the system will lead to the solution, as described in Chapter 6.

Cross-calibration. Marker-based optical systems for motion monitoring in MRI are subject to a further challenge, as the position of the marker is in general measured in the camera's coordinate system of reference (r_c), while the imaging is performed in the scanner's coordinate system (r_s). The process that aims to find the geometrical transformation needed to convert measurements from the camera's frame of reference to the scanner's frame of reference ($T_{c \to s}$) is called cross-calibration: $r_s = T_{c \to s} r_c$. Traditionally, this is done by acquiring concurrent measurements of the positions of the markers and a high resolution image of a structured phantom to which the marker is attached. The procedure is repeated until a sufficient number of positions and images are acquired (up to 10) to solve the system of equations [20].

The process, if performed manually, may take up to 1 hour and needs an investigator to stay supine in the scanner bore in order to move the phantom. Alternatively, the use of cross-calibration tools can allow the calibration to be performed in tens of seconds. One example is to use the optical marker and three wireless markers [9] that can be tracked in both the camera and scanner's coordinate systems. If the optical marker and MR markers are concurrently tracked, thousands of measurements are available in a short time. This allows the transformation matrix for the cross-calibration of the optical system to be found in 10s of seconds. Substantial improvements in calibrating the MPT camera system [10] have been achieved through the development of a remote controlled system that moves both the water-based phantom and the marker in the bore.

2.2.4 Markerless based MoCo techniques

The great advantages of this approach compared to the marker-based techniques are the increment of the comfort of the patient and that the motion is measured in the scanner's frame of reference and so there is no need to calibrate the system.

Examples of this approach include:

- *Navigator Echo techniques* dynamically track the anatomic motion thanks to additional RF pulses (usually spin echo - SE - or gradient echo -GRE). It uses a scout image to describe a "pencil beam" whose echoes is used to reconstruct the motion and to trigger the scan acquisition at the same point in time of the breathing cycle (as can also be done by the use of respiratory bellows). PROPELLER [75] (Periodically Rotated Overlapping ParallEL Lines with Enhanced Reconstruction) [2] developed in the nineties as a motion reduction technique. The idea is to acquire small k-space bands (called blades) rotating around the centre of k-space. From the overlapping centre positions, low resolution images allow estimation of in-plane motion that can be considered in the reconstruction. However, the efficiency is lower than Cartesian sampling due to the redundant acquisition of many samples.

- *k-space navigator techniques.* The relevant motion information can be extracted from different k-space trajectories (sNAv) or from the un-encoded k-space center as in the case of FID (water signal)[76]. The sNav (Spherical navigator) [7, 77] technique measures rigid body motion parameters by sampling a spherical shell in k-space. Distributed and incoherent sample orders for reconstruction deblurring using encoding redundancy (DISORDER) [78] extrapolates motion information by a random sampling of the k-space line. Motion Elimination in Radial acquisition Leveraging Interleaved Navigators (MERLIN) [79] is a silent, motion insensitive, MRI technique that uses self-navigated zero echo time (ZTE) [80] imaging to correct image for rigid body motion.

- *Image phase navigators* involve repeatedly acquiring low resolution slices or entire volumes for motion estimation in addition to the main image sequence (water signal). PROMO [81] exploits three-orthogonal 2D spiral navigator sequences and a flexible image-based tracking method. Reconstruction is based on the extended Kalman filter algorithm applied to online motion measurement. Navigator methods require additional scan time and may interfere with tissue magnetization as the water signal is used for navigation. Thus, they must be incorporated wisely into sequences and different solutions are required for different sequence. This is partially addressed using the fat navigator approach. FatNav uses signal from the fat layer between the skull and the skin only and exploits this signal to determine the head position [82, 83]. Combined methods, such as combining PMC (FatNav) and RMC, have demonstrated that it is possible to correct data for small ranges of motion (root mean square of the motion: 1.08 mm, 0.34°) [82].

- *Data driven correction* algorithms are able to extrapolate motion information from data based on a given motion model. The algorithm is optimized and given an image quality metric to estimate the motion model parameters and correct the image at the same time. This is a high dimensional problem and computationally very demanding. More recent methods have exploited higher computing power

[2] Vendors have their own variations of PROPELLER named: Philips (MulitVane), Siemens (BLADE), GE (PROPELLER), Hitachi (RADAR), and Canon (JET).

and apply more sophisticated motion model. One of them is presented in this dissertation.

The pilot-tone [84] technique for 7T scanner has the potential to extrapolate motion information from the perturbation of a continuous additional RF signal sent in the scanner bore. It needs to be calibrated by an additional technique (such as DISORDER [78]).

- *Deep learning based methods* are based on training the method on data that have been artificially corrupted. The problem has been approached as an image-to-image translation problem using a conditional generative adversarial network to predict artefact-free brain images [85] and a [86] generative adversarial network to improved image quality compared to the motion-corrupted images. The main problem with these approach is that the network may create additional anatomical structure or remove area on the picture if not appropriately trained. The TArgeted Motion Estimation and Reduction (TAMER) method [87] predicts motion parameters by retrospective alignment of the 3D MRI volumes.

- *Infrared optical-based method.* The Tracoline solution (`https://tracinnovations.com/markerless-technology/`) is a motion tracker device based on computer vision technology. A vision probe is installed in the MR head coil to continuously scan the head of the subject. A cloud of points is identified based on face features and used to predict motion in real time. This solution does not interfere with the MR imaging process, and does not interact with the subject [88].

2.2.5 Benefits of applying motion correction techniques in MRI

Motion artefacts (such as blurring and ghosting) in MRI mainly affect techniques with intrinsically low signal to noise ratio (SNR), while high resolution and long scan times exacerbate the level of artefacts. Common methods for motion prevention in clinical environments are positioning the patient in a comfortable position (e.g. using cushions and padding), instructing and reminding the patient of the importance of remaining still during the acquisition of the data. Respiratory gating and skip-and-redo strategies [89] also help to ameliorate the effect of motion on the data. Reducing the MRI acquisition time can be achieved by using fast imaging techniques and require finding a good balance between the quality of the image needed (SNR) and scanning time. Non-linear k-space sampling trajectories may be less affected by motion, but the regridding process can introduce blurring artefacts. PMC techniques may be used during the acquisition. MR data pre-processing involves the use of tracking data to re-align k-space data (RMC). This section reports examples in the literature of issues due to motion affecting several diferent MR techniques.

QSM The quantitative susceptibility mapping (QSM) technique allows in-vivo measurement of the magnetic susceptibility of tissues[90, 91] by exploiting the information in the phase of the MR signal. QSM is also used to identify pathophysiological susceptibility changes in biomarkers (such as iron and calcium) [92, 93]. The main challenge involved in applying the QSM method is to solve the susceptibility-magnetic field inverse problem. The convolution between the volume susceptibility distribution (χ) and the dipole kernel (d) represents the local (position r) induced magnetic field (B) along the bulk magnetic field (B_0): $B = (\chi \bigotimes d)$. In the frequency domain, convolution is represented by a point wise multiplication making the inversion appear trivial. However, the dipole kernel, represents the magnetic field as a local dipole ($B \propto r^{-3}$) and so has a singularity at the origin in the space where the inverse problem is solved purely with algebraic inversion[92]. Several computational methods have been developed to overcome the singularity such as: Calculation Of Susceptibility through Multiple Orientation Sampling (COSMOS [94]), Morphology Enabled Dipole Inversion (MEDI [95]), Thresholded K-space Division (TKD [96]). QSM measurements benefit from the application of motion correction techniques due to the long time needed to acquire phase data. For example, PMC at 7T was successfully applied to a GRE sequence to achieve 33 μm isotropic resolution in QSM images [97].

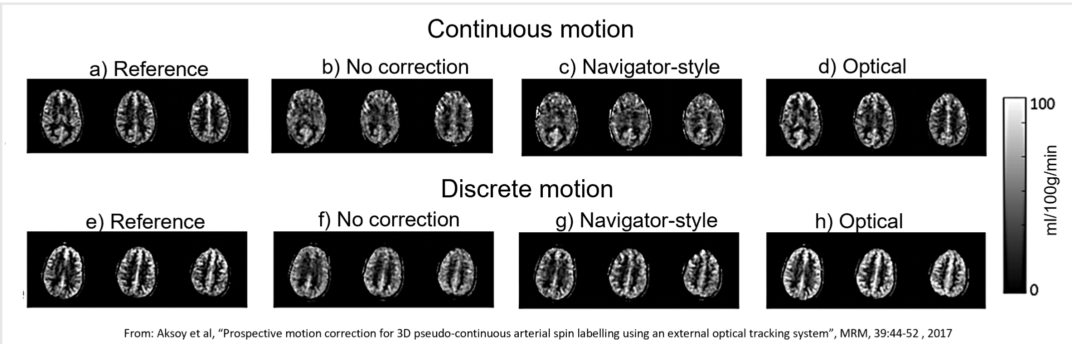

Figure 2.8: *Motion corruption due to discrete/continuous motion regime.* The PCASL (Pseudo Continuous ASL) scanning sequence in a 3T scanner has been used to obtain CBF (Cerebral Fluid) image in case of continuous motion (top row) and discrete motion (bottom row) [98]. Results using two different PMC techniques have been compared. Difference images (labelled image minus control image) in case of no corrections (second column) shows blurring on the front of the brain (where maximum displacement occurred). Navigator-style corrections (third column) the residual blurring is due to the lag of ≈ 4 s on updating the scanner geometry. Optical tracking system (last column) provided motion-free MR images in both motion regimes (lag on updating the geometry ≈ 15 ms). The Navigator approach was more comfortable for the patient, but the overall longer scan time (due to the longer latency) would not be optimal in the clinical environment.

ASL Arterial Spin Labelling (ASL) tracks tissue perfusion by using endogenous blood water as a tracer. Perfusion measurements are obtained by subtracting a control image (without the excited endogenous tracer). Bulk motion effects can be reduced by breath-holding between acquisitions or adding background signal suppression gradients to the pulse sequence [99]. MR techniques relying on subtraction of successive measurements, such as Arterial Spin Labelling (ASL), are affected by motion artefacts as MR data corruption due to motion during the acquisition propagates in the subtraction phase (when the image and the control images are subtracted). External optical tracking systems[98], spiral-navigator [81] (Figure 2.8) and a combination of affine transformation [100] have been proven to ameliorate motion artefacts in ASL images acquired using 3T scanners.

DWI Diffusion Weighted Imaging (DWI) aims to detect molecular motion of water. The order of magnitude of this motion is 10 microns, so bulk motion of this scale interferes with the measurements. Bulk motion directions and extents are random and perturb differently each measurement. Motion disrupts the acquisition process as the repetition time might be up to 10 s (roughly three breathing cycles), but it could be handled by gating[101]. Most common approaches are to reduce patient motion, to use less motion sensitive pulse sequences and to post-process the data. For non-complex motion, examples, Pulsed Gradient Spin Echo (PGSE[102]) sequences can reveal motion related phase-shifts of the imaging data by subtracting the information in phase of a control navigator image acquired ahead of the DWI image (Figure 2.5).

fMRI Functional MRI (fMRI) aims to detect neural activity by measuring the change in the MR signal due to changes in blood oxygenation and blood flow. Motion can lead to misidentification of activated areas, because of the comparison of two MR images acquired at different time points, or inducing spatio-temporal structured noise [103]. Scanning sequences that are intrinsically low in SNR (such as BOLD-fMRI [104]) require long scanning times to achieve a good measurement. Motion artefacts are likely to be disruptive in long scanning sequences because subjecs tend to become restless. Motion artefacts in fMRI, usually $\leq 2\ mm$ and $\leq 1°$, can be interpreted as neuronal activation. PMC over RMC, where motion parameters where measured using an optical device, have been demonstrated to reduce the false positive outcome [104, 57].

Body motion MR imaging of the body presents additional challenges. The rigid body motion model is not valid anymore as the internal organs in the abdominal cavity move independently. Combining multiple approaches (such as respiratory gating, MR image averaging, fat suppression and spatial pre-saturation [105, 106]) leads to a better suppression of motion artefacts. The use of drugs to prevent internal organ motility (as for the digestive system) could be used.

Cardiac MRI (CMR) has been demonstrated to be a fundamental tool for accurate diagnosis of cardiopathic patients, both for volumetric and functional assessments [107]. Respiratory motion compensation techniques (such as breath-holding and navigator-echo gated sequences) are widely used[108].

Musculoskeletal (MSK) MRI benefits from the use of motion trackers. Out-of-bore solutions (such as Digital Single Lens Reflexive camera, DSLR) have been demonstrated to be a useful tool to capture the instant and the extent of motion [109] at 1.5 T. Recently cutting edge development of printed-flexible [110], liquid-based [111], wearable [112] coil designs is providing new solutions since the coil itself will be coupled with the body parts under investigation and follows its movements.

MRS Magnetic Resonance Spectroscopy (MRS) benefits from the application of PMC due to the intrinsic low SNR, which leads to a requirement for long acquisition scan times in a homogenous B_0 field. Marker based tracking methods (optical, NMR based markers) and navigation-sequence method can achieve the submillimetre and sub degree precision required to ameliorate motion artefacts in MRS experiments in paediatrics and restless patients [113].

PET/MRI Positron Emission Tomography (PET) aims to map a radioactive tracker that targets tissues metabolites and highlights their functionality. Anatomical information is provided by an additional technique, such as CT or MRI. Ameliorating patient motion in PET/MRI combined scanners requires the use of devices that are compatible with both the techniques. PET compatibility requires placing the device out of sight of the detector. MR compatibility requires that the magnetic field is not affected by the presence of the non-magnetic device. IR marker-less devices have been successfully used for PMC in paediatric PET/MRI studies [88] ameliorating translational motion ≤ 20 mm at 3 T (Figure 2.9).

2.3 Conclusion

In MRI, artefacts due to movements (such as ghosting or blurring) may compromise image quality and lead to misinterpretation. The level of disruption can be related to the intrinsic SNR of the imaging technique (e.g. fMRI or DWI have low SNR), duration of the scan, objective of the scan (e.g. visualizing a small region) and strength of the bulk

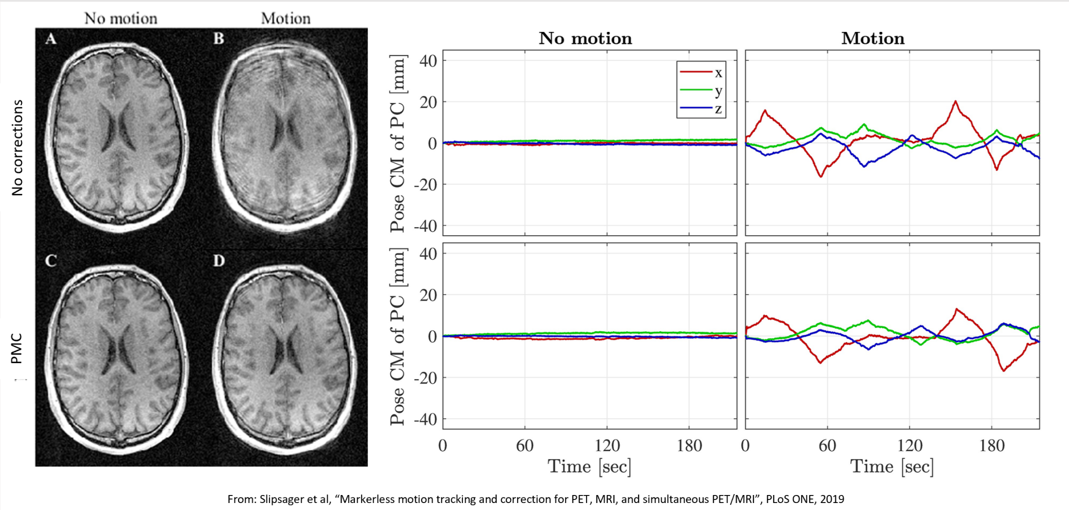

Figure 2.9: *IR contact-less motion tracking system.* 3D Fast low angle shot magnetic resonance imaging (FLASH) scanning sequence was used to acquire MR image (left) and motion data (right) at rest (no motion condition) and during repeatable motion pattern (motion condition) in paediatric subject in 3T PET/MRI combined scanner [88]. Motion data were acquired using an IR contact-less tracking system (https://tracinnovations.com/markerless-technology/). The implementation of PMC significantly reduces the motion-induced artefacts in MR image.

magnetic field. MRI performed with UHF scanners is more prone to motion artefact [89]. UHF MRI can achieve submillimetre image resolutions. The cost is an increase in motion sensitivity, also due to the long scan times required. Image quality is degraded by the motion-induced voxel displacement. The results can appear similar to partial volume effects, as voxel signal is partially assigned to a different voxel. As a results, contrast on the edges (such as brain-skull edges, sinuses-tissue edges, GM-WM edges) is blurred[115].

Metrics for comparison of image quality (such as mean squared error, SNR, structural similarity index) capture specific aspects and do not necessarily agree well with human observers. Therefore, these metrics are good to be used to compare similar images with different artefact levels, but need to be used with caution for image quality assessment of single images. An absolute reference of image quality without a reference has not been established yet. Approaches that exploit the use of 3D Convolutional Neural Networks [116] to assess the level of motion-corruption in data have recently been proposed. Robust automatic assessment of image quality remains an open issue. Images are usually assessed by radiologists[45] and a scan would likely be repeated if it is evaluated as being non-diagnostic. The need to repeat the scan affects the costs of the MRI delivery in the clinical setting[41, 42].

The extent of head motion has been estimated [89] to be of the order of magnitude of 1 *mm* at rest condition, while intra-cranial brain pulsation has been evaluated as 0.1 *mm*

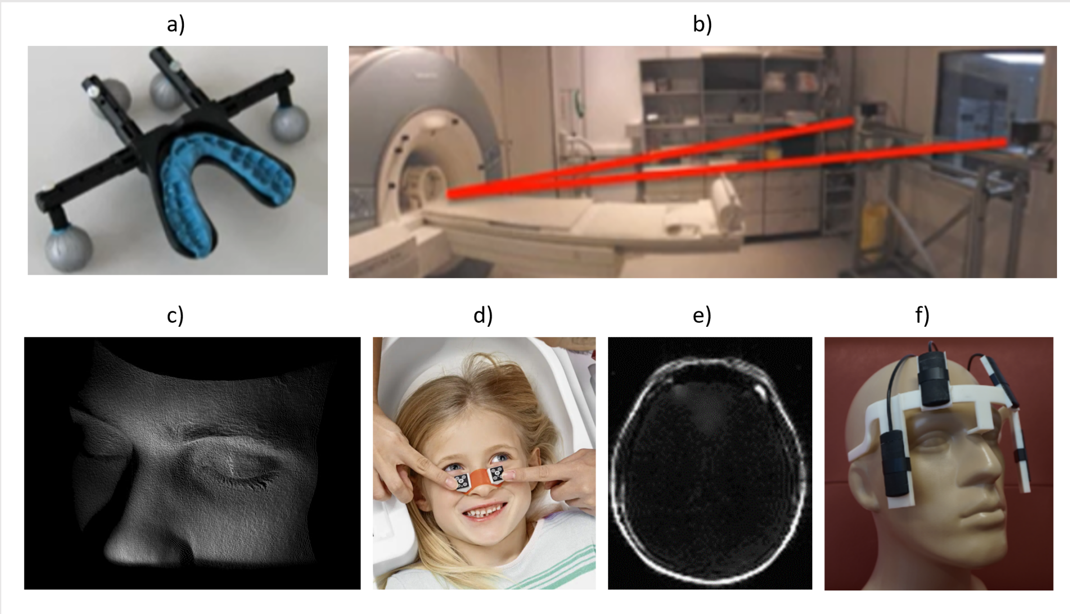

Figure 2.10: *Tracking system techniques.* (a) Customised mouth piece rigidly coupled with the teeth [8]. (b) External to the bore camera system [1]; (c) Infrared contactless (https://tracinnovations.com) in bore solution; (d) In-bore optical Moiré Phase Tracking (MPT) tracking system [114]; (e) Sequence based (FatNav) solution [82]; (f) NMR probes marker based tracking system [4]

order of magnitude, as brain-motion induced by the blood in-flow is restricted by the incompressibility of the brain tissue and CSF (Cerebral Spinal Fluid). Respiration and cardiac cycle gating can reduce the motion-induced artefacts in brain imaging. Chest movement at normal breathing (rest) condition has been estimated to be of few centimetres and it is often tracked (e.g. respiratory belt) to gate an MR imaging sequence. Arterial pulsation and cardiac motion influences brain studies as the first influences the blood flow and the second the motion [117]. Adjustments that help to limit head motion, include the use of cushions, straps and giving clear instructions to the patient.

When restless patients are scanned, the aim is often to obtain an image even if it is not the most accurate achievable with the clinical protocol. Restless patients may need to be familiarized with the scanner and be reassured on the procedure before starting the scanning [43]. A compromise between resolution and acquisition time in short image protocols helps to reduce motion-artefacts by shortening the total acquisition time which is particularly helpful with restless patients. Instructions on staying still are more effective when the patient is comfortably positioned in the scanner. The use of padding can increase the level of comfort. Reminders to remain still during the scanning sequence also help. Anaesthesia and or sedation is usually considered for difficult cases only.

Correction of motion relies on an accurate evaluation of the phenomenon that has corrupted the MR image and when it has occurred and the extent of the movement. Additional artefacts must not be introduced by the tracking method. Motion could be estimated from MR data, but a tracking sequence needs to be added to the imaging sequence and might corrupt the image acquisition. External motion tracking does not interfere with the imaging process, but might not be well-tolerated by all subjects[6].

Motion effects are reduced by applying the six-parameter (x, y, z axes rotations and translations) rigid body transformation assuming that motion happens only between entire volumes acquisition and linearly affects the image[118]. Motion might happen also within the time the volume is acquired and affect slices of the same volume differently. Motion might affect the image in a non-linear way. Currently, motion tracking and skip-and-redo strategies are the most commonly used clinical practices. In-bore and out-bore solutions are both available (Figure 2.10).

Head motion can be tackled in brain MR images by using Motion Corrections techniques based on the rigid body model (considering the brain well coupled with the skull), while motion of the body can not be considered as that of a rigid body in general. To image body parts with large intrinsic motion (such as in cardiac, lung or gastro-intestinal imaging) requires different strategies to freeze the motion (respiration gating, anaesthetics, fast imaging sequence). Small lesions are clinically important, but can be difficult to visualize[119]. Optimisation of CNR and compromising between image resolution and scan time helps to detect them. Noise reduction strategies, such as motion correction, can also usefully be applied. Accelerating imaging sequences using parallel imaging or compressed sensing allows the scanning time to be decreased, and so reducing the total scan time, but generally leads to a loss of SNR and may increase the motion sensitivity of the sequence and lead to more complicated motion artefacts [**bib:**]. Linear sampling of the k-space leads to acquisition of k-space lines that might be compromised by motion. Alternative scanning k-space sampling patterns (such as radial or spiral acquisitions) are designed to sample the centre of k-space (where most of the signal occurs) in a non-linear way. Interpolation of the non-linear trajectory in the k-space grid may create blurring artefacts [75].

Common practice in tracking head motion is to track a marker that it is rigidly coupled with the skull (attached to the patient's forehead or to a the teeth). One or more optical camera(s) record the position of the marker and recorded motion parameters are transformed into the scanner's frame of reference. Extra hardware is required (marker(s), camera(s)), and the need for line of sight access to the marker, plus additional software makes the implementation challenging. Furthermore, extra time is usually required to set-up the hardware, calibrate the system and instruct the patient. These solutions have been widely adopted in the clinical setting since they are easy to implement and have a low associated cost.

Prospective Motion Correction (PMC) aims to prevent the acquisition of corrupted k-space lines by adjusting the directions of the gradients (3D k-space grid) applied to the head during the image acquisition process. There is an intrinsic delay on correcting the image volume as it is not corrected till the movement is detected [8]. Retrospective Motion Correction (RMC) techniques aim to retrospectively correct k-space data. RMC do not correct through-plane motion [120]. RMC do not account for previous scan effects on data such as magnetic field inhomogeneities and spin history effect[117].

In this thesis, the development of a new marker-less motion tracking technique at 7 T with no need to modify the image sequence for its implementation is discussed (Chapter 3). This technique has been developed in research environment only by scanning healthy collaborative subjects. The tracking has not been tested in correcting MR image.

2.3.1 Motion Correction studies

By comparing Motion Correction studies in the literature (such as [121], [5], [122]), it is clear that a standard has not yet been established on performing MoCo studies and, in general, the choice of the movements to perform are customised for the aim of the experiment rather than to be representative of the clinical situation. The goal for the future is to standardise the experiments in a way that they could be easy to compare and more representative of the clinical environment. Motion paradigms should be defined then to describe how the volunteer moves in the scanner by detailing the body part in motion, type of motion, dynamic of motion, motion amplitude, and motion speed.

Types of motion include intentional motion, such as head shaking (left-right rotation, also called “yaw” describing rotation around the Z-axis), head nodding (top-bottom rotation, also called “pitch” usually describing rotation around physical axis X), figure of eight (in plane rotation obtained by tracing out a figure of eight with the nose, it is also called “roll”, usually describing rotation around physical axis Y), head movements due to the physical movements of another part of the body (such as the wiggle of the feet), and non-intentional motion (usually rest condition). During clinical practice, the rest condition is the most common one, but intentional motion may also occur. Motion Correction studies usually include and use intentional movements to test the motion correction technique. In presence of unintentional motion, the use of a MoCo technique does not have to disrupt the MR image.

Intentional and unintentional motion could be performed continuously or stepwise during the acquisition. The range of the motion is subject-dependent and in general not repeatable (same subject in two different sessions may perform a different motion path at different speed when the task was to repeat the same pattern as done before). To project a video showing the pattern to follow to the subject may improve the reproducibility of the motion pattern, in terms of extent and frequency (speed).

In this thesis, the subjects were asked to perform rest, head shaking, head nodding and wiggling of the feet movements (Section 3.3). Subjects were instructed to move ahead of the scan and reminded of the movement pattern when simultaneous motion-magnetic field measurements were taken. The range of movements and frequency have been retrospectively evaluated to test how they influence the data (Figure 5.16, Table B.14).

Chapter 3

Experimental set-up characterisation

This chapter's first aim is to describe and characterise the experimental set-ups used to perform simultaneous measurements of head motion parameters and the extra-cranial field changes produced by changes in head position as well as physiological signals [11, 20]. Extra-cranial magnetic field changes were evaluated using an MR-safe, in-bore, field camera comprising a set of 16, NMR field probes. Simultaneous head motion parameters were evaluated using an MR-safe in-bore optical device. A respiratory belt was used to monitor respiration.

This procedure was performed on healthy adult subjects able to make controlled head movements and to hold the mouthpiece necessary for the optical tracking system. Two different NMR field probe holders have been custom-made (Section 3.1) and characterised in terms of the influence of the material used to form the support, relative head-probe positions and Signal to Noise Ratio (SNR). The measurements that were performed are reported at the end of the chapter.

3.1 Experimental set-ups

The first set-up used for experiments is shown in Figure 3.1. It allows concurrent measurements of changes in extra-cranial magnetic field and head pose. A schematic diagram of the connections between the instruments is shown in Figure 3.2.

Sixteen NMR probes [33] were evenly distributed around the head using a custom-built former in order to sample the extra-cranial magnetic field evenly. The NMR field probe holder was designed to fit inside the Nova RF transmit head coil used on the 7T scanner with the receiver RF coil array removed. The 16 probes are mounted in 4 rings,

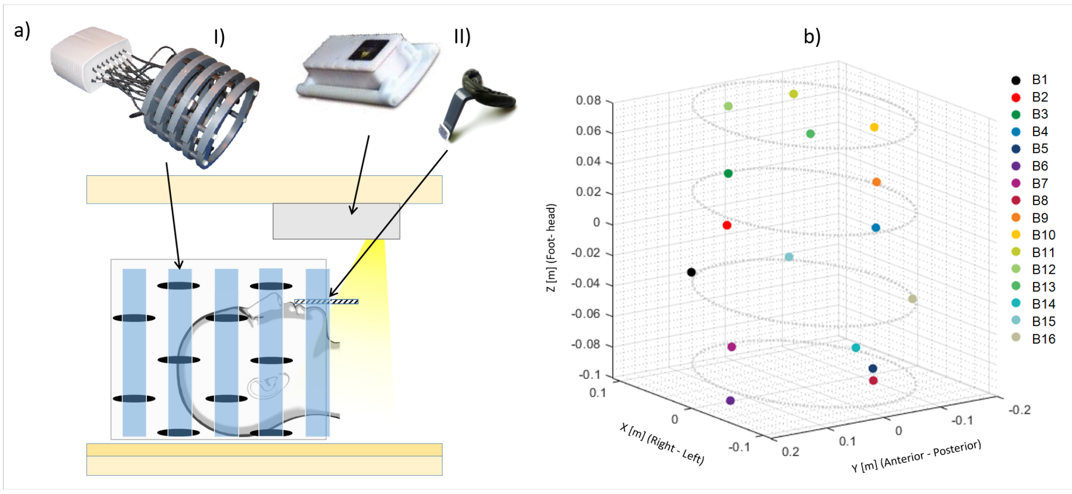

Figure 3.1: *PVC holder.* (a) A set of 16 NMR field probes (Skope Magnetic Resonance Technologies, Zurich) was held in a set of (I) four coaxial plastic (PVC) rings around the head. The system is designed to fit inside the Nova RF volume transmit head coil on a 7T Philips scanner with the receiver coil removed (Figure 1.13). The probes are sited inside the plastic rings to limit sensitivity to the magnetic field perturbations due to the PVC-air interface. (II) An optical, Moiré Phase Tracking (MPT, Metria Innovation, USA) system has been used to measure head pose by tracking an MPT marker attached to a dental mould. (b) In-bore position of the field probes during the motion correction experiment.

the fifth ring provides structural integrity. Four probes are distributed with an angular spacing of 90° in each ring. The oval-shaped rings are co-axial and connected by rods, with the probe positions on each ring rotated by an angle of 45° with respect to the neighbours. The internal measures are: minor axes equal to 190 mm and major axes 250 mm. These dimensions were chosen to keep the probes as close as possible to the head. The distances between the probes and the head depends on the size of the subject's head (except close to the crown, where the head rests on the holder) and on the movements performed.

The set-up was later improved (Figure 3.3) by using a custom-built cloth, NMR field probe holder designed to fit between the NOVA transmit and receiver RF head coils, thus allowing the 32-channel Nova receiver coil to be used for signal reception. The holder is comprised of two pieces, which together cover the whole outer surface of the 32-channel Nova receiver RF coil. The top-front part holds up to 15 probes covering the eyes and forehead. A further 4 probes can be placed in the top-back support, positioned at the top of the head at the level of the eyes in the foot-head direction. On the bottom part, up to 12 probes can be placed covering the back of the head. As the overall number of pockets available is twice the number of available magnetic field probes, this set-up allows the

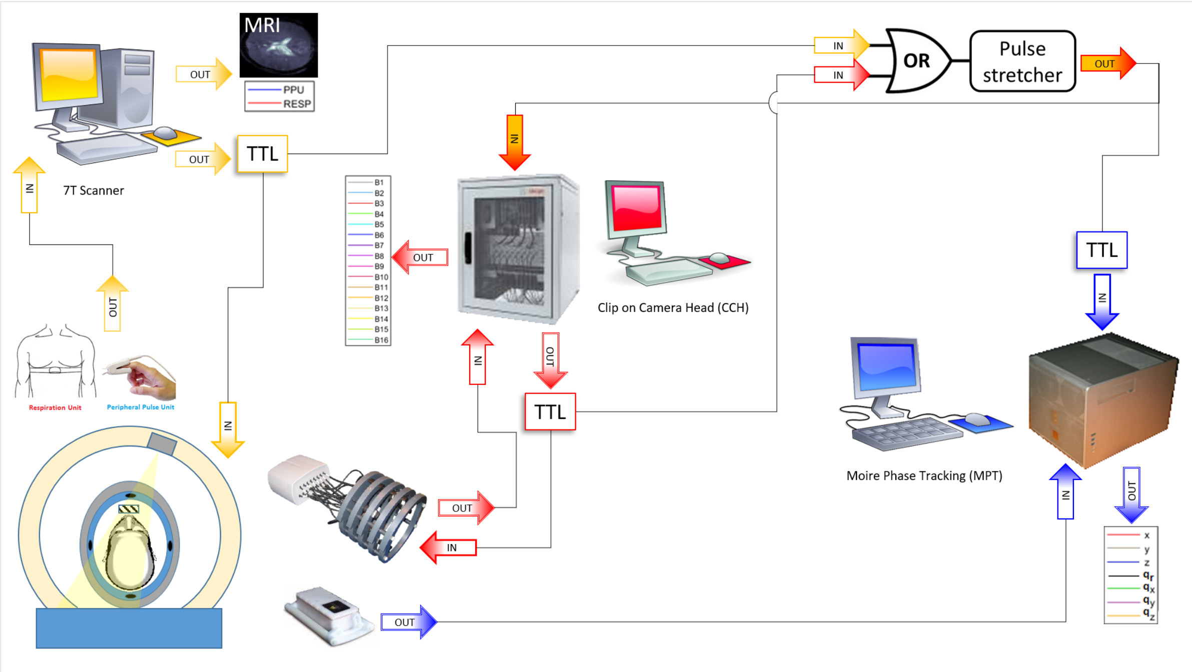

Figure 3.2: *Scheme of connection.* The picture shows how the instruments are connected in the lab to perform concurrent measurements. The TTL signals from the scanner need to be passed to both the field camera and the optical camera in order to tag the logfiles for both measurements. The TTL signal from the field camera is sent to the optical camera for the same purpose. An OR gate coupled with a pulse-stretcher ensures that the TTL signals are picked up by both devices.

positions of the probes to be adapted based on the particular aim of the measurements.

This set up allows measurements to be made while scanning using the 32-channel Nova receiver coil, which provides much greater sensitivity than reception using the transmit birdcage coil. It also allows the magnetic field to be sampled at ad-hoc positions to better characterise field changes due to physiological fluctuations and changes due to head movements. The probe holder was made from recycled materials.

For both of the set-ups described above, the MPT optical camera was fixed to the inside of the scanner bore. It is necessary to perform a cross-calibration sequence [1] in order to identify the geometrical relationship between the frames of reference used by the scanner and the optical camera. The optical marker is rigidly coupled to the skull via a dental mould. Custom bite bars were made for each subject using thermal-setting dental plastic. On the top of dental arcade there is a planar extension which holds the holographic MPT marker. We assumed that the system formed by the head and the bite-bar can be modelled as rigid body.

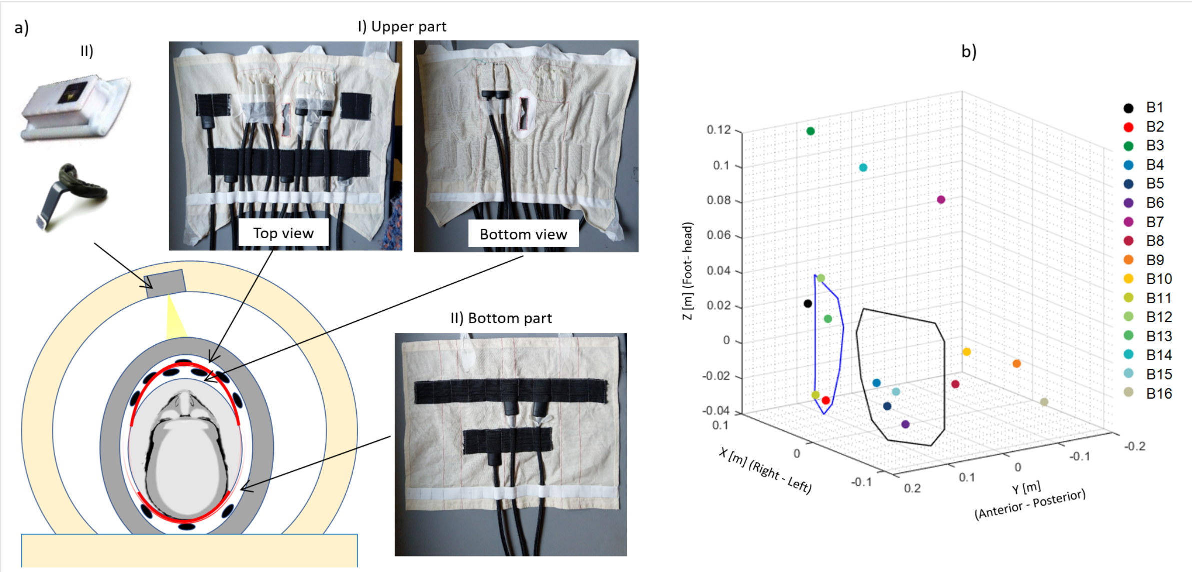

Figure 3.3: *Cloth holder.* (a) The NMR field probes were placed between the Nova transmit and the receiver RF coils (Figure 1.13). The optical camera (MPT, Kineticor) was attached to the inside of the magnet bore. The NMR field probes are held in place by elastic bands, while Velcro strips and elastic bands were used to guide the cables in the holder. The positions of the probes are shown in (b).

Physiological parameters were simultaneously measured using the scanner's physiological logging tools: respiratory bellows for respiration and a pulse oximeter worn on the finger for monitoring the cardiac cycle.

The sampling frequencies varied for each instrument, taking values of 6.7 Hz, 80 Hz, 500 Hz for the magnetic field camera, optical camera and physiological logging tool. Thus, signals were resampled at a common frequency in post-processing based on the repetition time (TR) used for the field camera measurements. The extra-cranial magnetic field was measured by the field camera and sampled every 150 ms (TR) with 1 nT of accuracy. The head movements were recorded using the optical camera with ± 0.001 mm and 0.001 $^\circ$ of accuracy for translations and rotations [20], respectively.

Probe positions in different set-ups

The probe positions used in the two different set-ups are shown in the same figure in Figure 3.4. As the PVC support was designed to fit perfectly in between the transmit and the receiver coil, the radial distance between the probes and the head does not differ much (≤ 5 cm) except for probes 10, 11, 12, 13 in the PVC holder that were placed in a smaller rings to follows the natural curve of the top of the head.

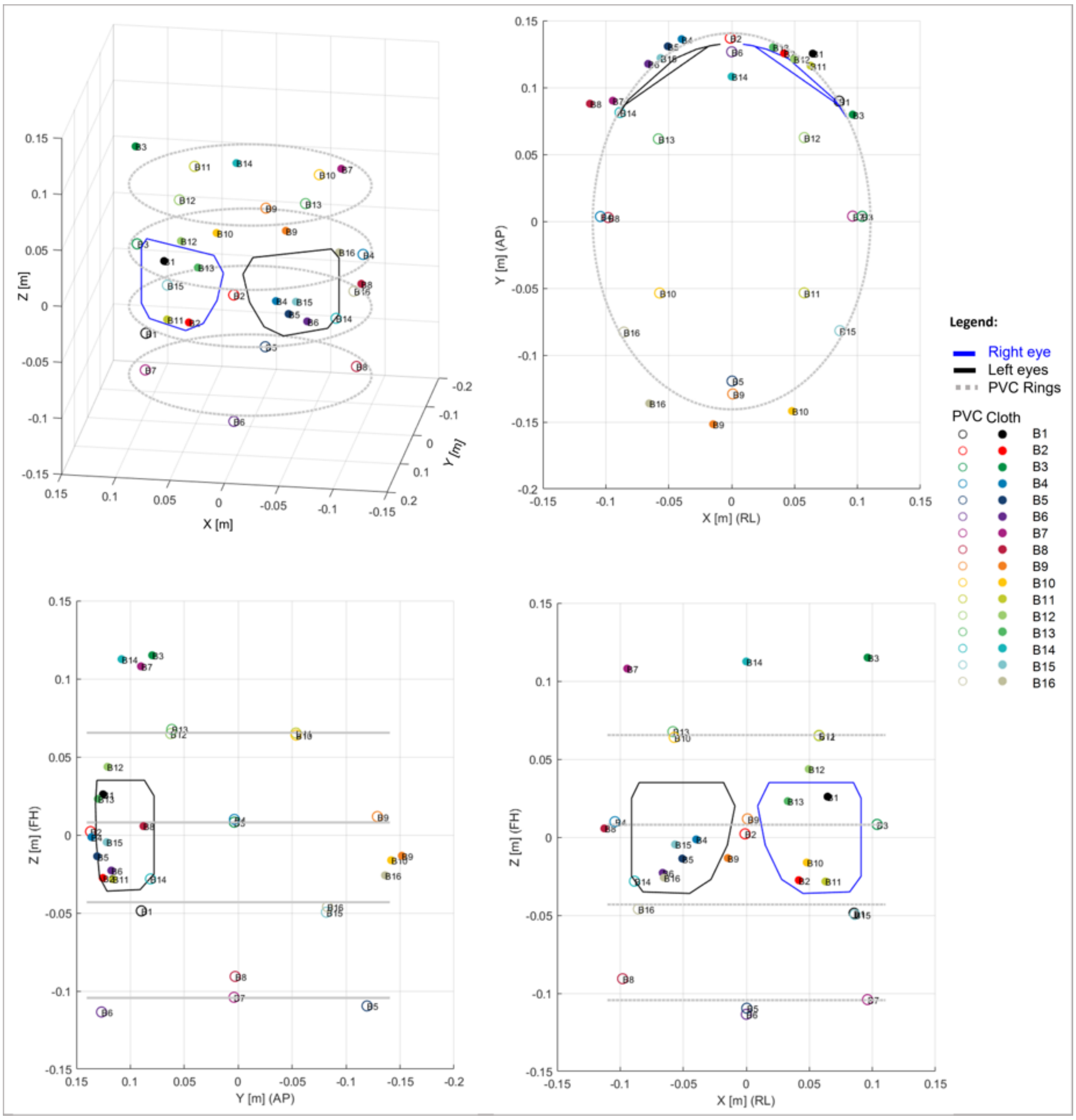

Figure 3.4: *Set-ups.* The two set-ups shown in Chapter 3 are shown in the same figure to allow them to be compared. Empty dots represent the probe positions used in the PVC set-up while the filled dots represent the probe positions used with the cloth probe holder. The PVC rings used to hold the probes in the PVC support are shown in grey. The shape of the holes at the level of the eyes on the RF receiver head coil are also shown.

The spatial distribution of the probes differs significantly for the two set-ups. While the PVC holder aims to sample evenly all around the head from the ears to the top of the head, the cloth support mainly samples the field in the area in front of the eyes. Three probes were placed on the top of the head to sample the signal in the spherical part of the head (as the top ring in the PVC support), and three probes were placed on the back to sample the magnetic field changes due to chest movement. Those six probes in the cloth support are not comparable with the position of the PVC support axially. Probe 2 on the PVC support results in a similar radial and axial position compared to the cluster of probes placed in the eyes area using the cloth support.

3.1.1 Colormap palettes for comparing magnetic field probe positions

In order to practice on the use of neural network approach, a problem with less degree of freedom compare to the regression between extra-cranial magnetic field and head motion has been solved using neural network approach. A colormap has been created to visually compare probe positions in different laboratory session. However, to represent data in this dissertation it has not been used to be consistent with the representation given by the magnetic field camera app.

The problem to solve is similar to that used to perform regression on motion data as there are a set of 16 pairs of input (probe positions in x, y, z) and 3 outputs (colours in RGB scale) whose values vary between 0 and 1. Considering the use fo the $\mathcal{P}$ space to map the positions and the $\mathcal{C}$ space for mapping the RGB colors:

$$\begin{aligned} \mathcal{P} &= \{(x, y, z) | x, y, z \in \mathbb{R} \vee [-0.1; +0.1]m\} \\ \mathcal{C} &= \{(r, g, b) | r, g, b \in \mathbb{R} \vee [0; 1]\} \end{aligned} \tag{3.1}$$

The regression involves finding a function that connects these spaces:

$$\begin{aligned} \mathbb{R}^3 \times \mathbb{R}^{+3} \rightarrow & \quad f \in \mathbb{R}^3 \\ f(x, y, z) \longmapsto & \quad (R, G, B) \end{aligned} \tag{3.2}$$

$$\mathcal{P} = [x, y, z] \in \mathbb{R}^3 \rightarrow \mathbb{C} = [R, G, B] \in \mathcal{R}^3$$

Training Data set

The training data set was simulated based on real probe positions recorded in past measurements. A total of 4 measurements of the same configuration $(16 \times (x, y, z))$ has been matched with a specific color associated to each channel (probe) on Skope software $(16 \times (R, G, B))$. This scheme is used for each of the four probe positions $(4 \times 16 = 64)$. Then, the data were repeated 10 times $([x, y, z]_{640 \times 3} \longmapsto [R, G, B]_{640 \times 3})$

and white Gaussian noise was added to perturb position and colours. White noise was generated with a normal distribution, average zero and standard deviation of 0.001 (ten times the accuracy of the measurements).

Neural Network architecture

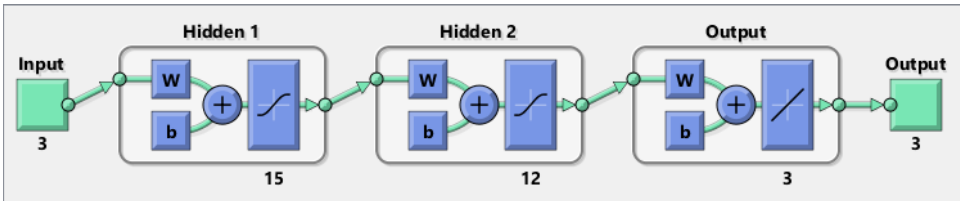

Figure 3.5: *Neural Network structure to predict probe-holder colormap*

Figure 3.5 shows the architecture of the network. A two layer feed forward architecture with three input neurons ($3 = [x, y, z]$), 15 neurons in the first hidden layer, 12 neurons in the second hidden layer and 3 output neurons ($3 = [R, G, B]$) has been chosen. The training data set comprised 1920 data point (640×3), subdivided into 75% Training, 15% Validation and 15% Test data using the *divideblock()* MatLab built-in function that subdivides the data into consecutive blocks. The activation functions of the first and second layers were the one step secant and the Levenberg-Marquardt [123] algorithm was used for training.

Results

The best results from the mapping are shown in Figure 3.6 by assigning the colours to 720 positions that s evenly span the space. Colours vary smoothly between probe positions Different architectures of the network were tested. A Neural Network with 1 hidden layer of neurons was not stable and produced very different mappings across different training runs. For a two hidden-layer network, combinations of different numbers of neurons in the first and second hidden layers where tested (12-12, 15-15, 15-12, 15-6, 12-6, 12-9), with no good results. Increasing the number of data used for the training phase did not lead to improved results. Randomly dividing the data-set (using `dividerand()`) also did not improve the results compared to dividing data in subsequent blocks. The activation function chosen has a strong effect on the results and the one-step secant function gave the best results. The output has to be $0 \leq 1$ to represents a RGB triplette.

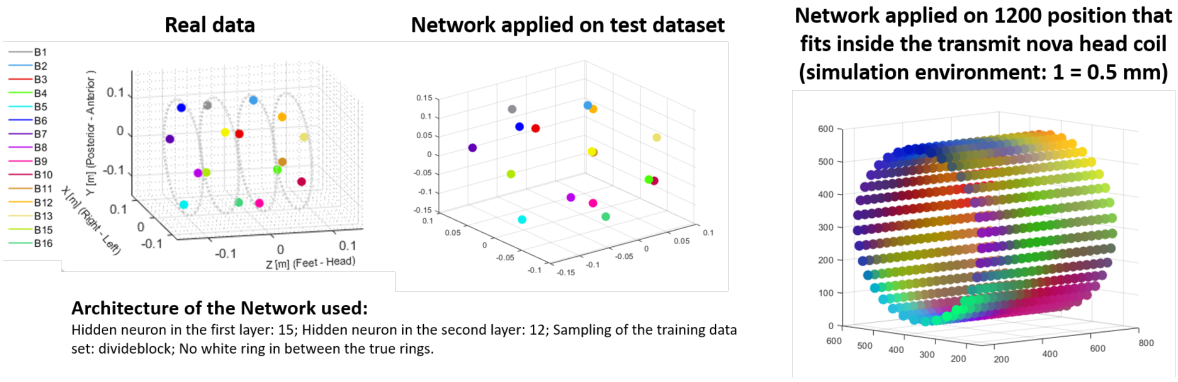

Figure 3.6: *Network data and results.* From the left: original data, test data and results over 720 different positions. The colour of the test data-set matching that of the original data. Colour over 720 positions that span the internal surface of the Nova Head RF coil varying smoothly with positions.

3.2 Field probe supports characterization

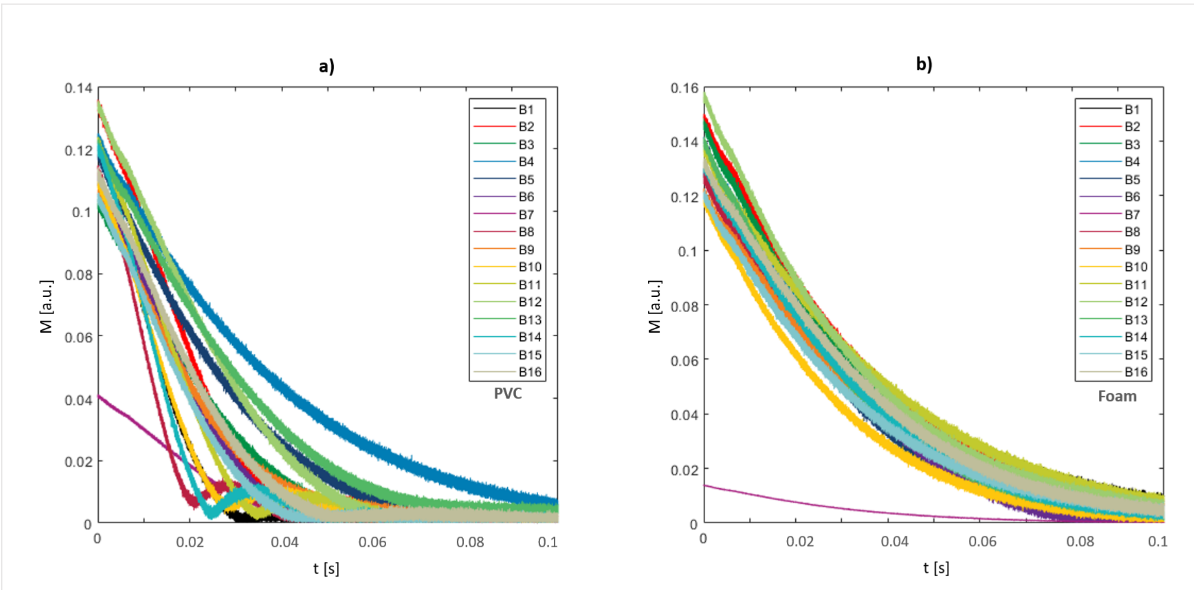

Figure 3.7: *FID - PVC.* FIDs (Free Induction Decays) from NMR probes evaluated (a) with probes mounted in the PVC support and (b) in a block of light foam using the calibration sequence (Figure 1.14). The proximity to air/PVC interfaces influences the $T_2^{\star}$ relaxation time of the ^{19}F signals from the probes. Probe 7 (dark purple line) was faulty at the time of the measurements. The other small differences in magnetization values are due to tolerances in probe manufacture and differences in position in the bore.

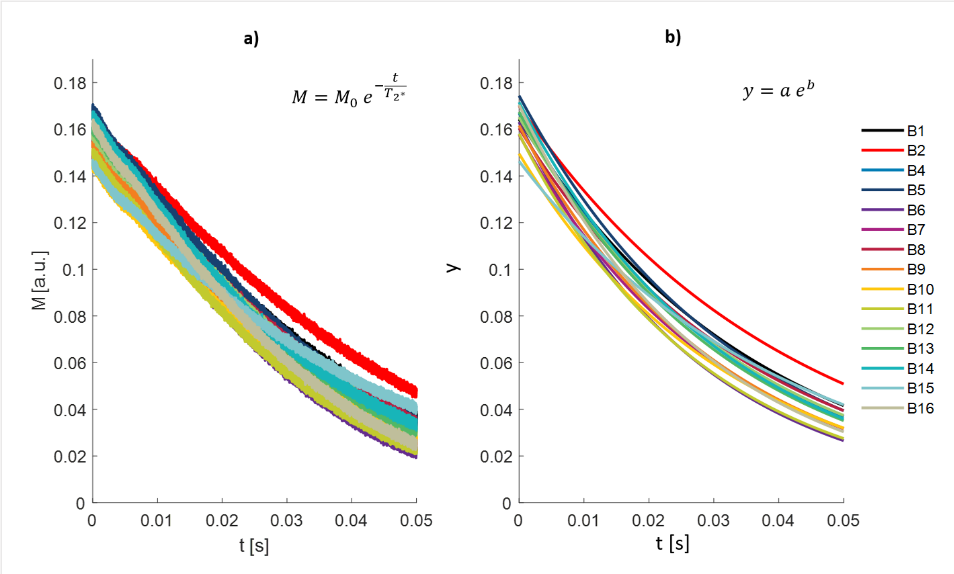

Figure 3.8: *FID - cloth.* In order to use the custom probe holder, further testing was carried out. (a) Free Induction Decays (FIDs) were acquired with the probes in the cloth holder using the calibration sequence (Figure 1.14). Probe 3 was faulty and its signal has not been reported in the the plot. The signal decay rates show that the cloth probe holder does not strongly affect the signals, with the all curves being well fitted (b) by exponential functions, with decay rates similar to those found with probes mounted in light foam (Figure 3.7).

The NMR field probes acquire raw signals (FIDs) at a fixed bandwidth of 1 MHz [39] and used a fixed number of data points to perform the fit and to obtain the magnetic field measurement. The time range (number of data points) used for the B-fit could be adjusted: a value of 0.005 s was used for all the measurements acquired for this dissertation. The NMR signal strength and T_2^* decay define the accuracy of the field measurements. The positions of the probes in the magnet bore can influence the rate of signal decay. Probes should be placed in a holder that doesn't interfere with the rate of decay of the signal. Interference may arise from the interfaces between the material used to build the probe holder and the surrounding air. In this section, the effect of different materials has been characterized. A light foam holder (whose magnetic susceptibility is similar to air) has been considered as the reference for other materials, PVC (whose magnetic susceptibility is similar to water) and cotton.

The field camera uses measurements of ^{19}F NMR signals from the probes whose decay is well described by the expression:

$$M = M_0 e^{(-\frac{t}{T_2^*})} e^{i(\omega t + \phi)} \tag{3.3}$$

where M represents the spin magnetization, M_0 represents M at $t = 0$ s, t represents the time, ω the angular frequency off set, ϕ is the time-independent phase offset and T_2^* represents the transverse relaxation time.

The exponential signal decays were well recorded using a square block of foam, the PVC support and the cloth holder as a support for the probes. Figures 3.7 and 3.8 show the absolute value of the complex MR signal measured for the different materials.

Data acquired with different holders were fitted using the exponential model provided by MATLAB:

$$y = a \cdot e^{b \cdot x} \tag{3.4}$$

Comparing equations 3.3 and 3.4, the fit parameters gave the decay parameters values:

$$M_0 = a; \qquad T_2 = -\frac{1}{b} \tag{3.5}$$

The signal from each probe was fitted to Eq. 3.3 and the results (M_0 and T_2^*) are reported in Table 3.1.

The FIDs obtained with the probes mounted in the PVC support are not well fitted by an exponential decay. This hypothesis is confirmed by the R^2 values of the fits. The curves are possibly better represented by a $sinc()$ function which would explain the bump obtained at the time of 0.02 s. However, this should not have greatly influenced the SNR of the data as typically only the first 0.005 s of the signals are used by the instrument's built-in algorithm to calculate the magnetic field value. The investigation was repeated for the cloth holder. The signal decays and fits are shown in Figure 3.8, and the fitting parameters are reported in Table 3.1.

To conclude, the FIDs are well characterised by exponential decays in the case of the cloth holder and the measured decay times are similar to those measured using the foam holder. This is in contrast to measurements with the PVC holder where decays are more sinc-like and apparent relaxation times are shorter. The difference results from the presence of the PVC/air interfaces whose normals are along the field direction in the PVC holder.

3.2.1 Signal to Noise Ratio (SNR) for different set-ups

The magnetic field camera background noise and signal to noise ratio were characterized using the PVC support in order to sample the magnetic field evenly over the relevant space. 2000 dynamics ($TR = 150$ ms) were acquired with the probes placed in the isocentre of the scanner and the average values for each channel were then subtracted.

	PVC support			Foam support			Cloth support		
	$\mathbf{M_0}$	$\mathbf{T_2^*}$ [ms]	$\mathbf{R^2}$	$\mathbf{M_0}$	$\mathbf{T_2^*}$ [ms]	$\mathbf{R^2}$	$\mathbf{M_0}$	$\mathbf{T_2^*}$ [ms]	$\mathbf{R^2}$
$\mathbf{B_1}$	0.13	12	0.97	0.13	38	1.00	0.16	36	0.99
$\mathbf{B_2}$	0.15	18	0.98	0.16	34	1.00	0.17	41	1.00
$\mathbf{B_3}$	0.12	21	0.98	0.15	31	1.00	–	–	–
$\mathbf{B_4}$	0.13	36	1.00	0.15	31	1.00	0.17	33	1.00
$\mathbf{B_5}$	0.13	25	0.99	0.15	27	1.00	0.17	34	0.99
$\mathbf{B_6}$	0.13	17	0.98	0.14	28	0.98	0.16	28	0.99
$\mathbf{B_7}$	–	–	–	–	–	–	0.16	31	0.99
$\mathbf{B_8}$	0.13	11	0.97	0.13	31	1.00	0.16	36	0.99
$\mathbf{B_9}$	0.12	20	0.99	0.13	33	0.99	0.16	31	0.99
$\mathbf{B_{10}}$	0.13	14	0.98	0.12	27	1.00	0.15	32	0.99
$\mathbf{B_{11}}$	0.14	15	0.97	0.14	38	1.00	0.16	29	0.99
$\mathbf{B_{12}}$	0.15	23	0.98	0.16	32	1.00	0.17	34	0.99
$\mathbf{B_{13}}$	0.13	27	0.99	0.15	29	1.00	0.17	32	0.99
$\mathbf{B_{14}}$	0.14	12	0.97	0.14	31	0.99	0.17	32	1.00
$\mathbf{B_{15}}$	0.12	17	0.98	0.13	31	1.00	0.15	40	1.00
$\mathbf{B_{16}}$	0.13	19	0.98	0.14	33	0.99	0.17	29	0.99

Table 3.1: *Decay parameters obtained by fitting to signals measured with the three different supports.* M_0 and T_2 are obtained from equation 3.5, R^2 represents the goodness coefficient of determination of the fit, $RMSE$ represents the root mean squared error of the fitted data. Data were acquired on different days. Probes 7/3 were malfunctioning when signals were measured from the PVC and foam support/cloth supports.

No volunteer was in the scanner for the evaluation of the background noise. Figure 3.9 shows the Probability Density Function of the data obtained. The PDF characterize the noise due to the sum of various sources, including electronics of the field camera and field fluctuations due to the scanner system. The PDF curves have been fitted using a Gaussian function. As expected, the noise of the NMR field probes is well fitted by Gaussian distribution. Table 3.2 reports the parameters of the fit (standard deviation σ and R^2) along with the signal to noise ratio (SNR) of the probes. Differences in the μ and σ are due to the different displacement of the probes in the bore and reflects the small B_0 differences around the isocentre. All the probes shows that the background white noise should be of the order of magnitude of 10^{-8} T.

The SNR ratio has been evaluated by acquiring 2000 dynamics of magnetic field changes when Subject 4 was in the scanner in a resting condition. The ratio between the Root Mean Squared error (RMS) of the data recorded with, and without, the subject present represents the SNR. SNR is influenced by the position of the probes relative to the head and the head size and shape, and so it changes for each subject, and for different head movements and probe positions. The case chosen here represented the lowest limit of the SNR expected, as the chosen subject has the largest head-probe distances and made the smallest head movements. Probes closer to the head (Figure 3.9) showed the

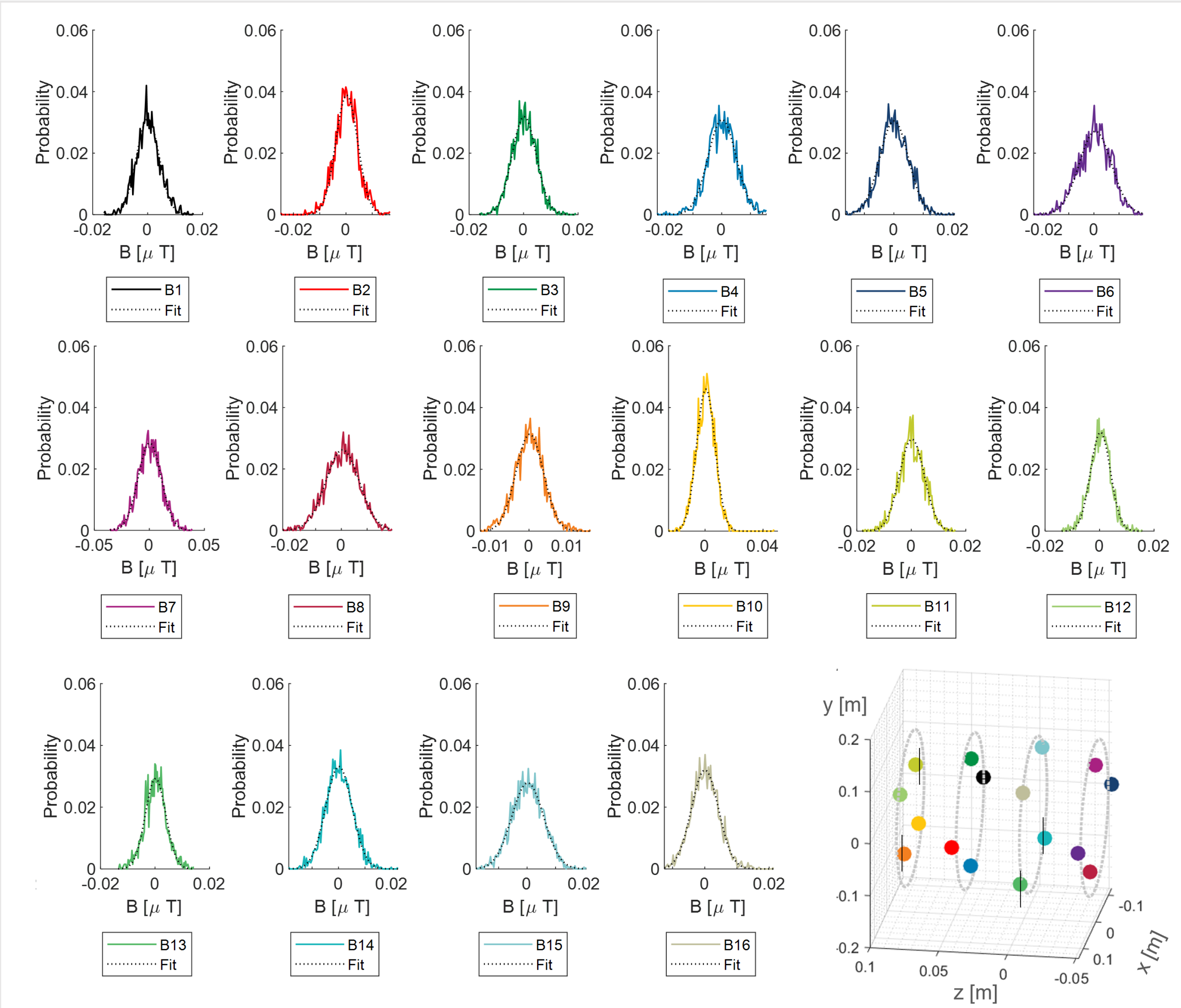

Figure 3.9: *Background noise evaluation.* Plots shows the probability density functions (and the Gaussian fit to them) of the noise recordings from the 16 channels of the magnetic field camera and the probe position in the scanner. Differences in the peaks are due to the different positions in the scanner. Statistical parameters are reported in Table 3.2.

highest SNR.

As the experimental data results were coherent over subjects, range of movements, probe positions and scanner sessions, the evaluation of the noise was not then repeated for other cases considered in this dissertation.

PVC	Gaussian Fit		SNR
	σ [μ**T**]	$\mathbf{R^2}$	**SNR**
$\mathbf{P_1}$	0.010	0.959	6
$\mathbf{P_2}$	0.012	0.966	4
$\mathbf{P_3}$	0.010	0.965	12
$\mathbf{P_4}$	0.011	0.954	10
$\mathbf{P_5}$	0.011	0.963	6
$\mathbf{P_6}$	0.013	0.933	3
$\mathbf{P_7}$	0.022	0.961	3
$\mathbf{P_8}$	0.012	0.959	7
$\mathbf{P_9}$	0.008	0.962	13
$\mathbf{P_{10}}$	0.021	0.977	12
$\mathbf{P_{11}}$	0.010	0.942	16
$\mathbf{P_{12}}$	0.009	0.971	17
$\mathbf{P_{13}}$	0.008	0.937	10
$\mathbf{P_{14}}$	0.012	0.977	7
$\mathbf{P_{15}}$	0.011	0.960	5
$\mathbf{P_{16}}$	0.010	0.973	5

Table 3.2: *Gaussian Fit and SNR values for the NMR field probes shown in Figure 3.9.* σ [μ**T**] and $\mathbf{R^2}$ values have been rounded to three decimal places. Magnetic field probes changing time series was a zero-average time series, so all the curves are centred on zero $\mu = 0$ [μT]. The standard deviation of different probes results comparable.

The study of the background noise of the optical camera has been conducted in another project [20] and so is not repeated in this dissertation. The results showed that the optical measurements are influenced by the scanner vibration, but not on a level that disrupts the measurements of head movements ($\leq$ 0.001 mm or $^\circ$) and, in the case of long measurements, could be affected by thermal drift.

3.3 Experimental measurements

During the experiments, subjects performed a range of different head movements, with and without concurrent imaging, in order to allow characterisation of the field changes produced under different conditions (Figure 3.10). These are listed in order of the extent of the movements (order of magnitude of data has been reported in brakets): breath-holding at rest ($\Delta B \approx 50\ nT$, $\leq 1\ mm$, $\leq 1^\circ$), normal breathing at rest ($\Delta B \leq 0.5\ \mu T$, $\leq 3\ mm$, $\leq 3^\circ$), small random movements of the head produced by 'wiggling' of the feet (feet-wiggling) ($\Delta B \approx 0.5\ \mu T$, $\leq 5\ mm$, $\leq 5^\circ$), head shaking ($\Delta B \approx 1\ \mu T$, $\approx 10\ mm$, $\approx 10^\circ$) and nodding ($\Delta B \approx 1\ \mu T$, $\leq 10\ mm$, $\leq 10^\circ$) and freestyle movements that include all the conditions mentioned previously executed in an order chosen by the subject. Breath-holding and freestyle conditions have not been used for data analysis.

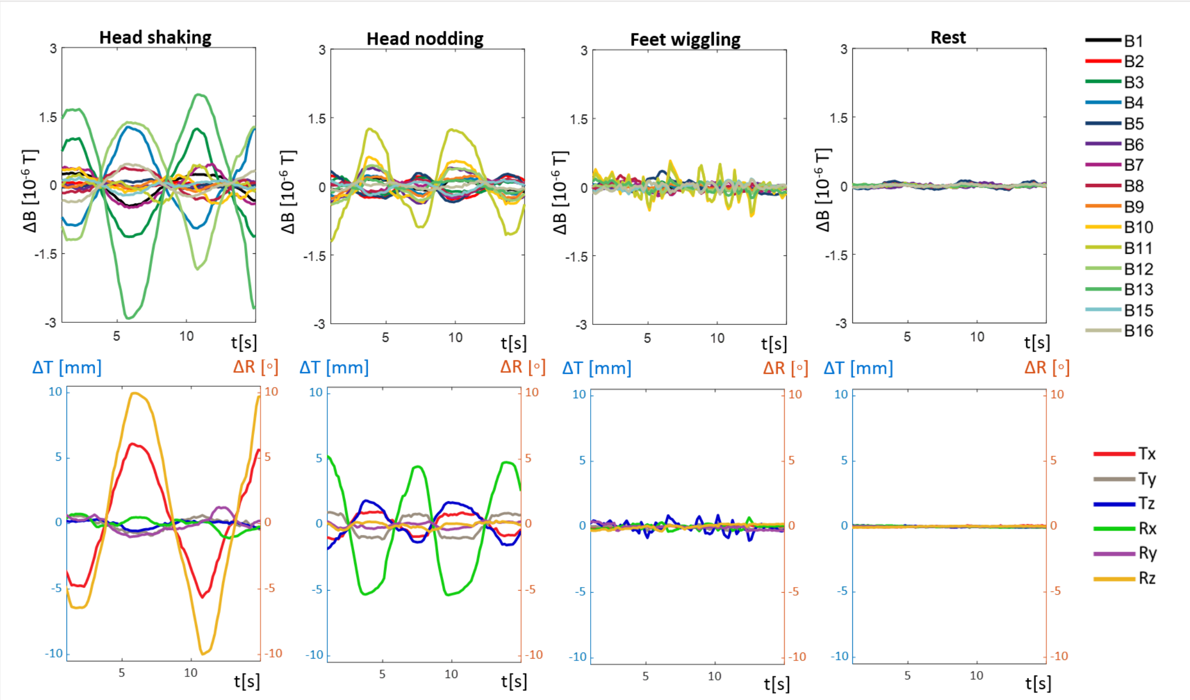

Figure 3.10: *Concomitant measurements (PVC).* The plots show examples of complete data-sets recorded while Subject 6 undertook a series of different movements inside the 7T MR scanner: head shaking, head nodding, wiggling the feet to produce small head movements and rest. The plots show zero-mean data series of field perturbation variation at probe positions, head translation and rotations time series. The order of magnitude of the magnetic field changes at the probe positions depends on the extent of the head motion. Plots show that the magnetic field changes are dominated by the effect of head movements for large head movements, while for small involuntary head movements the physiological noise dominates the magnetic field signals at the probe positions.

Data are reported in the Appendix B. Experiments with the PVC support involved Subjects 1,2,3 and 6 while with the cloth support Subjects 1,2,3,4 and 5 were studied (subject numbers agree with Figure 4.1). The head motion type and number of dynamics ($TR = 150\ ms$) involved in each experiment are reported in Table 3.3.

Analysis of the pattern of variation of the field changes using PCA (Principal Component Analysis) over the different probes, shows that the range of field variation depends on the probe position and type of movement (Figure 3.11). Also, changes in the magnetic field at the probe positions due to the chest expansion/contraction have been observed.

Set-up	Number of dynamics				Subjects
	Rest	Head shaking	Head nodding	Feet-wiggling	
PVC	1000	500	500	500	1,2,3,6
Cloth	5000	3000	3000	5000	1,2,3,4,5

Table 3.3: *Description of the experiments.* Experiments with the two set-ups involved different groups of subjects (with 3 of them studied using both set-ups). Time (or dynamics) at which the measurements with various head movement conditions were acquired varied between the experiments. As a reference, 1000 dynamics acquired at 150 *ms* time repetition corresponds to 2.5 minutes of acquisition. Data were also acquired during a breath hold condition (100 dynamics), but not considered for the analysis, as the number of dynamics was not enough to influence the results.

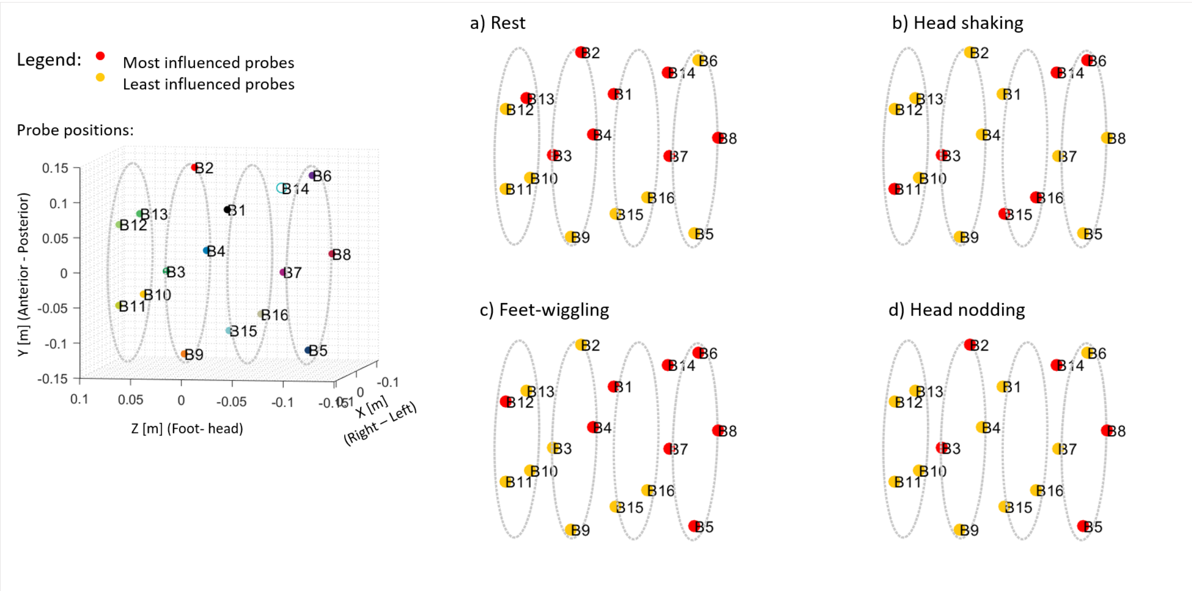

Figure 3.11: *PCA.* The figure shows sub-clusters of probes that characterise each movement condition (a,b,c,d) over 50-s of acquisition. Sub-clusters (red and yellow dots) are obtained by performing a Hierarchical Cluster Analysis in the space formed by the first two principal components obtained by Principal Component Analysis (PCA) (Section 5.1.1).

3.4 Conclusion

Two NMR probe-holders have been developed, characterised and used: neither solution was commercially available and one has been fully designed and developed by myself (Figure 8.1). Both the holder allowed valid measurements to be performed. The PVC-based one (Figure 3.1) does not easily allow simultaneous imaging, but it samples the extra cranial magnetic field evenly (Figure 3.10), while the Cloth-based one (Figure 3.3) allows simultaneous imaging and gives more degrees of freedom for probe positioning. This solution will be explored further in subsequent chapters. Example data acquired with this set-up are given in Figures 7.5 and 7.6.

The typical range of movements (Section 3.3) was limited by the available space between the head and the PVC support or the head and the helmet receiver coil array.

Each movement condition is characterized by a dominant direction of translation and axis of rotation. The first two activities, rest and the head movement due to the wiggle of the feet, represent small periodic or random movements, while periodic large voluntary head movements produce large displacements transverse or parallel to the B_0 field. Data have been reported in section B.2. The magnitude of the field measured by each probe was strongly influenced by its position relative to the head. For example, probes placed on the back of the head are more sensitive to field changes due to chest movement in respiration (Figure 3.10).

In the following chapter, magnetic field changes have been characterised further. The use of simulations allows the experiment to be mimicked in a controlled environment by superimposing sources of magnetic field changes observed (head involuntary/voluntary movements, chest expansion/contraction, and electronic noise).

Chapter 4

Mimic the experiment trough synthetic simulations

This chapter describes the implementation of customised simulations that are used to mimic the experiments in a controlled environment. Simulations were used to generate data series showing synthetic magnetic field changes which were used for various purposes in this thesis. The field simulation approach that was used here is the same approach that is used in the QSM technique (Subsection 2.2.5).

Simulations of extra-cranial magnetic field have been implemented using a Fourier Transform based method and customised head models, moved based upon experimentally measured head motion data (Subsection 4.1.1). Simulations allowed the parameters of the phenomena to be varied in a controlled environment, including investigations of the influence of physiological noise (Section 4.3), and the effects of variations in head shape and morphology on the head-probe distances and field changes (Section 4.2).

The second aim of the chapter is to better understand the relationship between head pose and magnetic field changes. This relationship should be mainly influenced by the distance between the head (closest source of perturbation of the bulk magnetic field) and the probes (where the magnetic field is sampled). Replicating the experiments in a simulated environment allows the evaluation of the influence of other parameters that effect the magnetic field changes, such as chest expansion. It allows the effects of head movement to be isolated from other sources of field perturbation and from the effects of the scanner hardware (such as vibrations due to the cryo-pumps).

4.1 Voxelated head models

The simulated environment consists of a cube of 350^3 *voxels*, each of $1 \times 1 \times 1\ mm^3$ size. The centre of the cube represents the origin of the system of reference of the scanner (isocentre), while the directions were chosen in agreement with NMR field probes' system of reference: AP as y-axis (positively oriented in the posterior direction), RL as x-axis (positively oriented towards the right side); FH as z-axis (positively oriented towards the head direction).

Hugo head model. The HUGO model is segmented into several different tissue types [26]. This allowed us to study the influence of each tissue type separately. One tissue at a time was given the susceptibility of water, rather than the pre-allocated value. As expected, the most influential tissues are largely present in the head (e.g. fat, muscle), or have a magnetic susceptibility that is different to the water one (e.g. fat), or are superficial and not so far from the probes (e.g. the lens of the eyes). However, these differences were not significant and so for the subsequent simulations all tissues were allocated the magnetic susceptibility of water. This makes the development of head models from MRI data easier, as it suggests that a non-fully segmented head model would lead to valid (for the aim of this dissertation) simulations of extra-cranial magnetic field changes.

Custom head models. Custom-voxellated models of the head and neck of 4 subjects were obtained from MRI data acquired at 3 T using an mDixon [124] sequence at $1.0\times\ 1.6 \times 2.8\ mm^3$ resolution, while models of a further two subjects were generated from MRI data acquired at 7 T using a MPRAGE [125] sequence at $1.0\times\ 1.0\times 1.0\ mm^3$. A threshold was applied to extract a binary representation of the head, corresponding to tissue and air. Then, the binary head models (with no internal cavities) were made by considering the external surface of the head and setting all voxels within this surface to have the susceptibility of water (Figure 4.1). Finally, the model was re-sampled at a resolution of $1 \times 1 \times 1\ mm^3$. This representation allows voxels to be assigned the magnetic susceptibility values discriminating between head ($\chi_{water} = -9ppm$) [26] and non-head ($\chi_{air} = -0\ ppm$) voxels (see Figure 4.2).

The head volumes can then easily be estimated and related to the mean distance between the probes and the head (see Section 4.2, and Chapter 5). To evaluate the extra-cranial magnetic field changes due to head movement, the head model was then step-by-step rotated and translated based on previously measured head motion parameters. A flat region at the base of the head model was classified as water to avoid field changes being produced by movements of the artificial boundary at the base of the head-/neck model. In order to study the influence of head-probe distance, morphology and

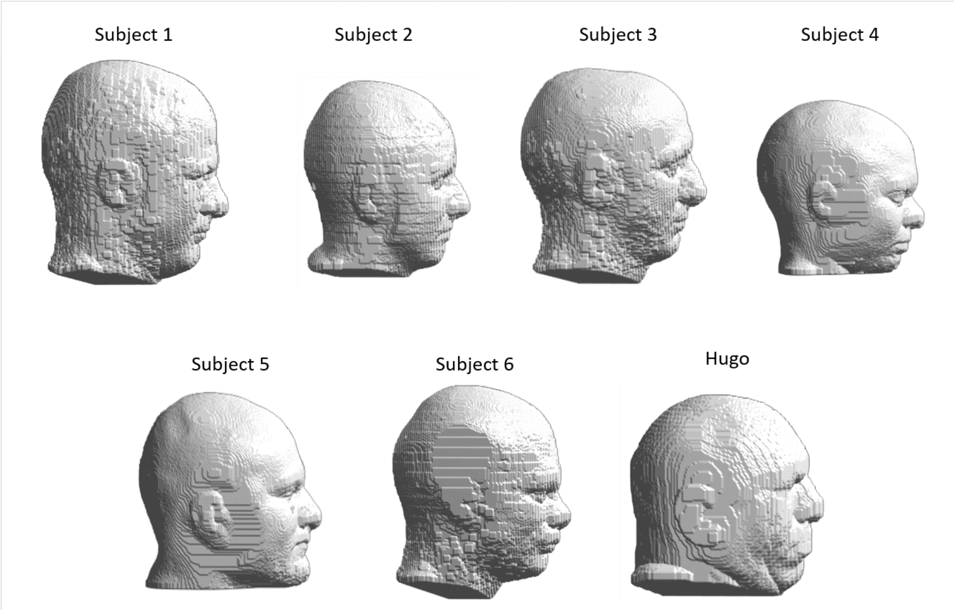

Figure 4.1: *3D head models.* Picture shows the head models (to scale) used for simulations in this dissertation. Subjects 1 to 6 are real volunteers while Hugo is a well-segmented head model ([26]). 2D projections of the head model in scale are shown in Figure 7.19.

head movement on the extra-cranial field changes, head models were scaled in size and then moved using customized motion parameters obtained by smoothing and detrending motion data acquired using the optical MPT camera from a single subject.

4.1.1 Simulated magnetic field data

Step-by-step simulation of the experiments required rotating and translating the head model using measured head motion parameters and then evaluating the magnetic field at the probe positions. The steps to simulate the time series are:

1. The simulation environment is defined. The segmented head model is placed in a matrix of $350 \times 350 \times 350$ $[1\ mm/px]^3$ (Figure 4.2, c, e). The exact position depends on the aim of the simulation. A region at the base of the model was classified as water in order to avoid field changes being produced by movements of the artificial boundary at the inferior extreme of the head/neck model (Figure 4.2, d, f).

2. The whole cube is rotated and translated in discrete steps. The range of the movements depend on the aim of the simulation.

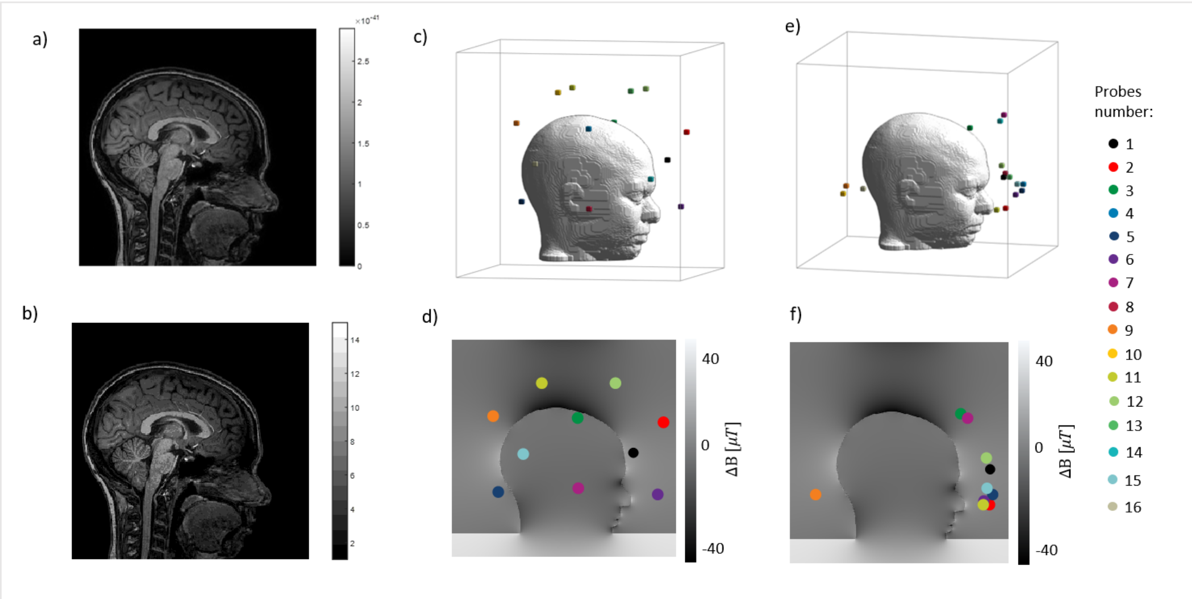

Figure 4.2: *Simulation environment.* This figure shows the steps used to build the customized simulation environment from the MR image of Subject 4. (a) Picture shows the central sagittal slice of 7T image, acquired at a resolution of $1 \times 1 \times 1$ mm^3 for a field of view (FOV) $256 \times 256 \times 256$ *voxels*. (b) Head models were produced by segmenting the MR images into 16 grey levels. Differentiation between air and 'not-air' was performed by thresholding signals above and below a level that was set by analysis of the distribution of signal intensities in the image. (c,e) As bone was also classified as air, the surface between the skin and air was used to create a water-based head model. The resolution of the head model was $1 \times 1 \times 1$ mm^3. The isocentre of the MR image corresponds to the centre of a cube of dimension $350 \times 350 \times 350$ *voxel* or $35 \times 35 \times 35$ cm^3 . Coloured squares show the probe positions in the 3D environment. (d,f) Simulation of the field perturbation produced in a central sagittal slice when the head is exposed to a magnetic field of 7T. Coloured circles show half of the field probe positions projected onto the central sagittal slice when the PVC holder was used (d) and when probes were mounted in the cloth holder (f). The region under the chin is always allocated the susceptibility of water to avoid effects of unrealistic movement of the boundary at the base of the head and neck model.

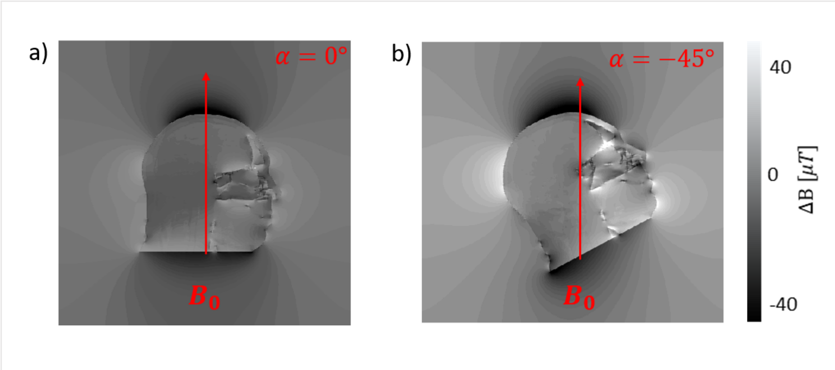

Figure 4.3: *Head model in 7T magnetic field.* (a) A simulation of the field perturbation produced in a central sagittal slice when the head is exposed to a 7T field. (b) A simple rotation of the head produces a change in the magnetic field pattern.

3. The magnetic field in the cube is evaluated using a Fourier-based method [126]:

$$\frac{B(k)}{B_0} = \left\{ \frac{k_z^2}{k_x^2 + k_y^2 + k_z^2} - \frac{1}{3} \right\} \chi(k) \tag{4.1}$$

   where B_0 is the static magnetic field at 7 T, $\chi(k)$ is the 3D Fourier Transform of the simulated three-dimensional susceptibility distribution and $k_{x,y,z}$ are the coordinates of the simulated k-space.

4. The magnetic field is sampled at the probe positions (Figure 4.2, d, f).

5. Steps 2, 3, 4 are repeated to obtain the simulated time series.

Magnetic field perturbations due to the head models were evaluated for different conditions. The 3-dimensional Fast Fourier Transform (FFT) of the model was used to evaluate the z-component of the magnetic field in the whole cube by using a Fourier-based method [126]. The original algorithm implies that the magnetic field rotates, while here the magnetic field direction is fixed and the model is rotated and translated. The simulated magnetic field has been sampled at fixed positions to mimic data from a realistically positioned array of 16 magnetic field probes. The relative positions of the head and the NMR probes were approximated by aligning the centre of the head model and the centre of the simulated environment.

The simulated magnetic field perturbation has a dipole-like shape with anomalies around the appendices of the head (Figure 4.3). After the head model was moved, field distortions due to the artificial inferior boundary of the models were successfully flattened by adding a fixed layer of water. Its contribution to the magnetic field was nulled by considering the difference in magnetic field between two consecutive movements. The head pivot was coincident with the isocentre in the 7T scanner, so the movements measured by the optical system were effectively mimicked. The head orientation and relative head-probe distances were well approximated by manually placing the probes in the simulated environment.

Simulations of the field changes produced outside the head by realistic head movements are in sufficient agreement with the measurements made for the purpose of this study (Figures 4.4 and 4.5) as the main aim was to obtain a data serie of magnetic field data that changes coherently with the changing in head position. Simulated and experimental data are reported in detail in Appendix B, Sections B.3 and B.2.

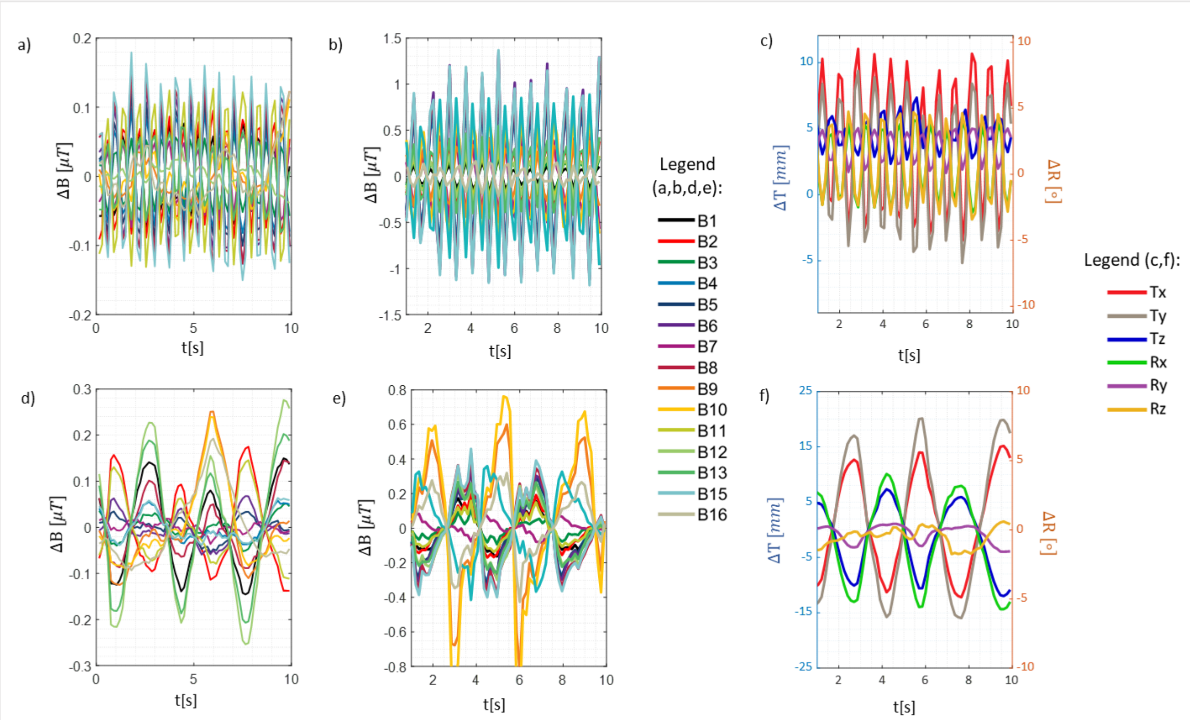

Figure 4.4: *Simulated data for Subject 4.* Measured and simulated magnetic field data due to head motion, sampled at probe positions from the cloth holder, for two head motion conditions (a-b-c head shaking, d-e-f head nodding) are reported. Simulated magnetic field data (b,e) are sufficiently coherent with measured data (a,d) for the aim of this study as they vary coherently with the change in head position. Further data are reported in Appendix B (Tables B.11 and B.18).

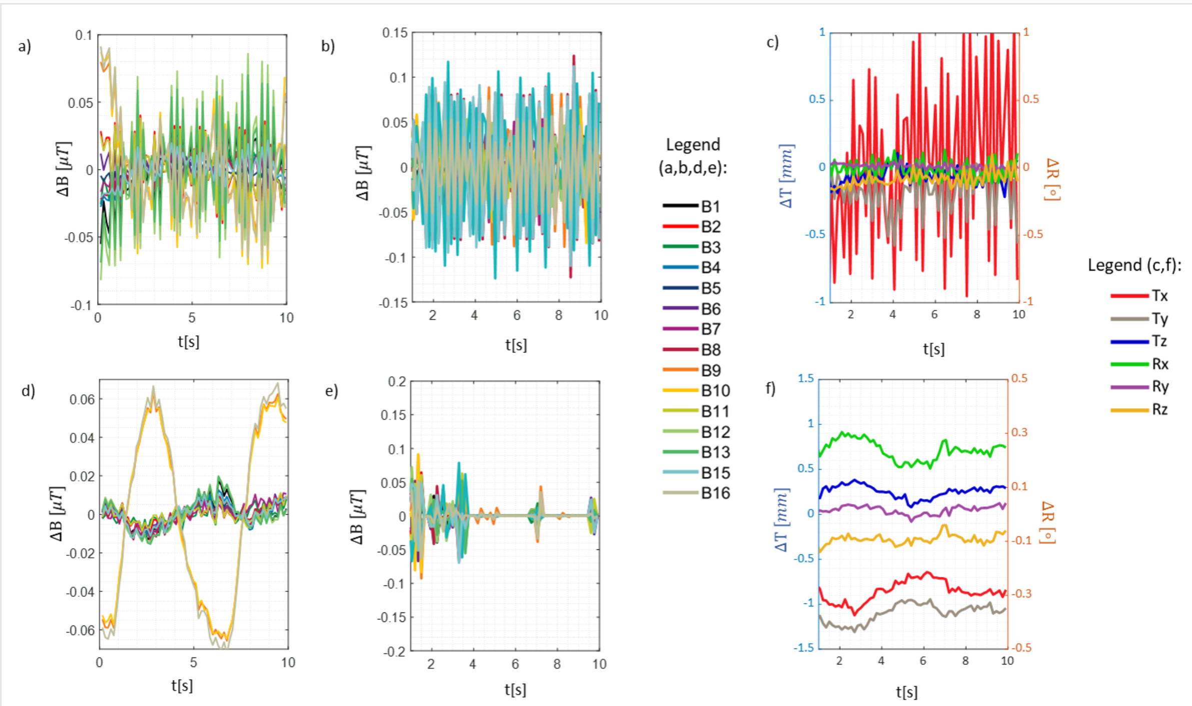

Figure 4.5: *Simulated data for Subject 4.* Simulated magnetic field data due to head motion, sampled at at probe positions from the cloth holder, for two head motion conditions (a-b-c wiggling of the feet, d-e-f rest) are reported. Simulated magnetic field data (b,e) are coherent with measured data (a,d) for the aim of this study as they vary coherently with the change in head position. Differences between (d) and (e) arise because (d) includes the effect of respiration. Data are reported in Appendix B (Tables B.11 and B.18).

4.1.2 Smoothed head motion time series

In order to create a time series of standard head movements, the motion parameters measured for subject 6 were used. Data were detrended by subtracting off the fit obtained using the built-in MATLAB function `polyfit`. The function fits the data in a least-squares approach. The degree of the polynomial chosen was 1. Then, by using the `smooth` built-in function, data were fitted. The *loess* [1] method was used with a sliding window of the size of 10% of the data in case of large movements and 2% in the case of small movements.

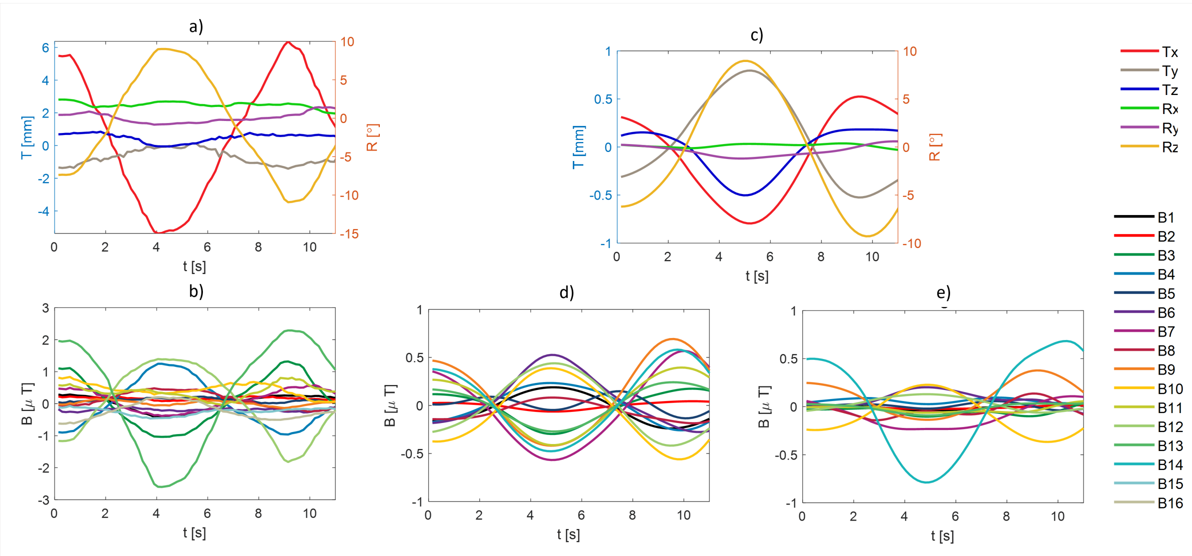

Figure 4.6: *Time series.* Simultaneously recorded (a) head motion parameters (translation T_x, T_y, T_z in mm and rotation R_x, R_y, R_z in radians) and (b) extra-cranial magnetic field changes at the 16 field probe positions (B1-B16) over 10 s of head shaking. Smoothed and detrended motion parameters over 10 s (c) used to simulate field changes at probe positions (d) from the Subject 1 model (e) and Hugo model.

An example of simulated data is reported in Figure 4.6. The process took $\approx 6\ s$ per time step on my personal laptop [2] which is a reasonable time to obtain synthetic data. The standard deviation of the motion parameters of the original time series and the processed one are reported in Table 4.1. It can be seen that the processing slightly reduced the standard deviation of data.

[1] Local regression using weighted linear least squares and a 2^{nd} degree polynomial model.

[2] Processor: Intel(R) Core(TM), i7-8550U, CPU 1.80G Hz, RAM 16 Gb

	Measured				Smoothed/detrended			
	Rest	**Shaking**	**Nodding**	**Feet-wiggling**	**Rest**	**Shaking**	**Nodding**	**Feet-wiggling**
$\mathbf{T_x}$ [mm]	0.108	3.768	0.621	0.129	0.103	3.564	0.540	0.077
$\mathbf{T_y}$ [mm]	0.096	0.770	0.665	0.158	0.068	0.499	0.578	0.119
$\mathbf{T_z}$ [mm]	0.168	0.453	0.954	0.447	0.102	0.247	0.825	0.378
$\mathbf{R_x}$ [°]	0.266	1.217	3.306	0.204	0.262	0.491	2.907	0.161
$\mathbf{R_y}$ [°]	0.096	0.761	0.372	0.167	0.089	0.617	0.184	0.164
$\mathbf{R_z}$ [°]	0.116	7.871	0.427	0.163	0.113	7.410	0.295	0.100

Table 4.1: The table reports the overall standard deviation of motion parameters (translation and rotation) in the experimental data and the smoothed/detrended data used for simulations. Values have been rounded to three decimal places.

4.2 Head-field probe distance influences on ΔB

The bulk magnetic field is perturbed by the presence of the human body in the scanner, as the body tissue is mainly formed by diamagnetic material. Voluntary and involuntary movements of the body make the magnetic field perturbation change in time. Using our experimental set-ups, the bulk magnetic field perturbations are sampled closed to the head (Figures 3.1 and 3.3) making it the main source of perturbation. By the use of synthetic data it is possible to show that head-probe distance is the main parameter influencing the perturbation. This distance changes mainly with the movement performed rather than with head morphology, both in simulated and real data. The perturbation due to chest expansion/contraction becomes relevant in the rest condition, when the head-probe distance does not change significantly over time.

4.2.1 Simulated data

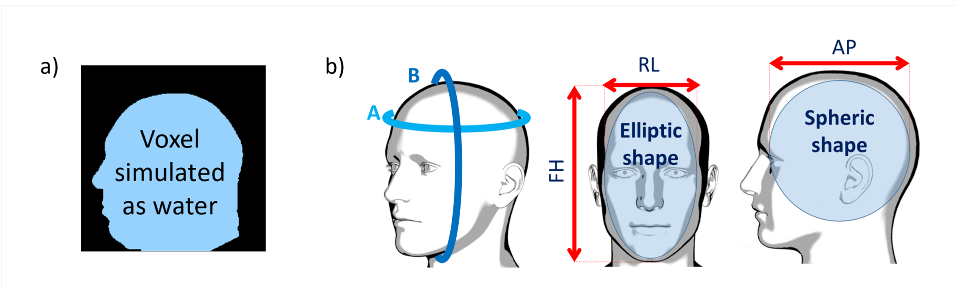

Figure 4.7: *Methods to evaluate head volume.* Schematic diagrams showing how head volume was evaluated for (a) head models and (b) real subjects. Table 4.2 reports the volumes.

To relate field changes to head size, we modelled the head as an ellipsoid as shown in Figure 4.7. Models were characterized based on the height (FH), width (RL) and depth (AP) of the head. Subjects' head circumferences were measured: A, circumference in an

	Simulation	Real measurements		
	Volume $[10^{-3}\ m^3]$	$A \pm 0.01\ [m]$	$B \pm 0.01\ [m]$	*Volume* $[10^{-3}\ m^3]$
Hugo	3.5	–	–	–
Subject 1	5.4	0.60	0.66	4.35 ± 0.06
Subject 2	3.6	0.55	0.60	3.30 ± 0.05
Subject 3	4.6	0.60	0.64	4.12 ± 0.06
Subject 4	3.5	0.55	0.58	3.09 ± 0.05
Subject 5	4.2	0.58	0.64	3.95 ± 0.06
Subject 6	4.6	0.58	0.62	3.74 ± 0.06

Table 4.2: The table reports the evaluation of the head volumes as shown in Figure (4.7). Simulated and real head volumes coincide within the experimental errors. They have been used in Figures 4.8, and 4.10

	Rest		Head Shaking		Head Nodding		Feet-wiggling	
std of:	$T\ [mm]$	$R\ [°]$	$T\ [mm]$	$R\ [°]$	$T\ [mm]$	$R\ [°]$	$T\ [mm]$	$R\ [°]$
Smoothed	0.09	0.21	0.48	4.47	0.78	1.94	0.28	0.16
Subject 1	0.05	0.08	0.98	1.74	0.64	1.44	0.18	0.15
Subject 2	0.08	0.09	1.26	2.74	0.94	3.38	0.18	0.08
Subject 3	0.30	0.23	2.15	2.57	1.15	1.99	0.27	0.27
Subject 6	0.13	0.18	2.23	4.62	0.76	1.94	0.28	0.18

Table 4.3: The table reports the overall standard deviation of motion parameters (translation and rotation) in the experimental data and the smoothed/detrended data used for simulations (Figure 4.8).

axial plane spanning the eyebrows to rear of the head and B, circumference in a coronal plane from chin to top of the head. We approximated this as:

$$RL = AP = \frac{A}{\pi} \tag{4.2}$$

$$FH = 2\sqrt{\frac{B^2}{2\pi^2} - \left(\frac{AP}{2}\right)^2} \tag{4.3}$$

$$V = \frac{4}{3}\pi \frac{FH}{2}\frac{AP}{2}\frac{RL}{2} \tag{4.4}$$

Simulations were used to evaluate the features that most strongly affect the extra-cranial field changes produced by typical head movements, including the influence of the head-probe distances and head morphology. At first, the PVC set-up was considered. In order to reduce the number of variables considered the heads were moved using an ideal time series formed by smoothing and detrending one of the motion data series acquired using the optical MPT camera during MoCo experiments. Figure 4.6b shows examples of the smoothed/detrended motion parameters and simulated field changes for two different head models during head shaking.

A further analysis of the effect of the head-probe distances has been conducted (Figure

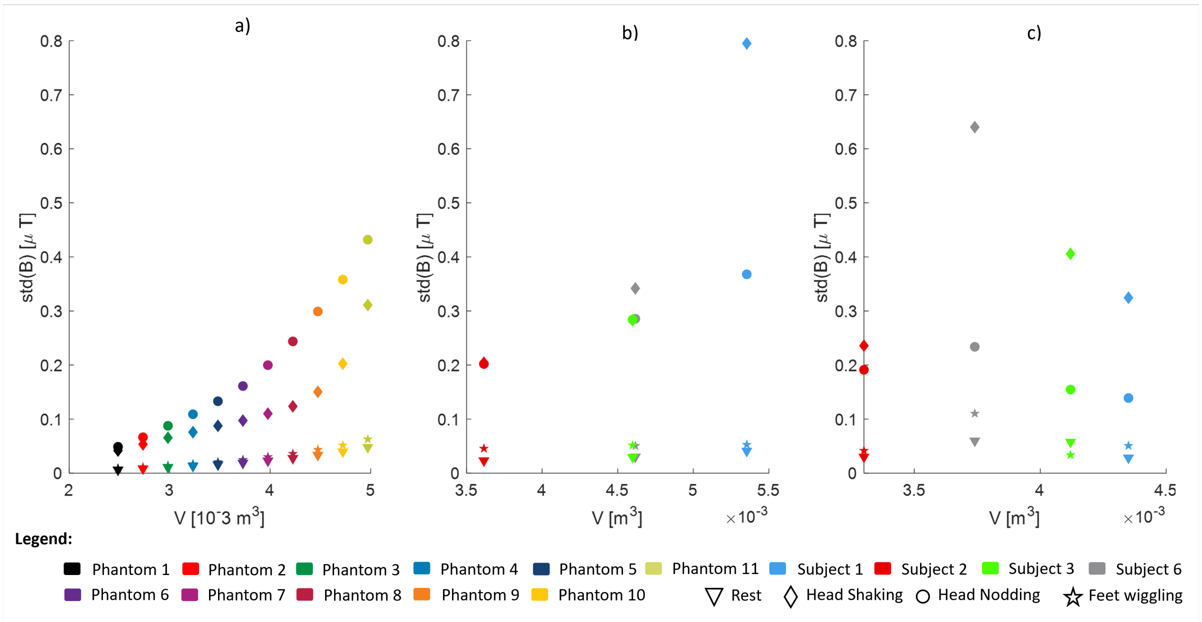

Figure 4.8: *Effect of the head-probe distances and head morphology on extra-cranial magnetic field (PVC set-up).* Variation of the average over of probes of the standard deviation of the field measurements with simulated head volumes for (a) phantoms (obtained by scaling the Hugo model) and (b) subject simulations, for different motion conditions. Table 4.3 reports the standard deviation of motion parameters in the smoothed/detrended data used for simulations (Plots a,b). (c) Variation of the average over of probes of the standard deviation of the field measurements with measured head volumes for for experimental data, for different motion conditions.

4.9). The field was sampled at two head poses only to identify the main difference in probe positions between the two set-ups. The head has been considered at the initial condition and then rotated about the z-axis by 10 degrees. The sampling on the top of the head gave similar absolute value of the magnetic field for the two head conditions as the distance between the head and the probes doesn't change significantly. By contrast, the field values on the side of the head were significantly different. To conclude, based on the relative positions of the probes with respect to the head, I expect to have a higher change in extra-cranial magnetic field due to movement when using the PVC support rather than the cloth holder because the distance between the head and probes varies more significantly over probes and head motion conditions.

PVC set-up

The configuration where probes are evenly distributed around the head was considered at first. Fifteen different voxellated water-based head models were considered, each having an isotropic resolution of 1 mm. Four models were based on MR image data acquired

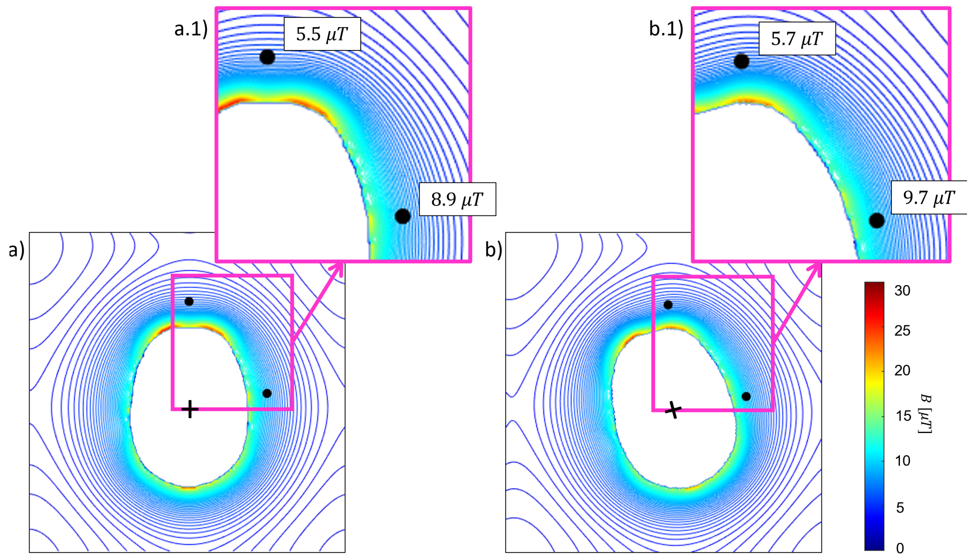

Figure 4.9: *Contour plots of the simulated extra-cranial magnetic field.* Plots show the simulated extra-cranial magnetic field for (a) head and (b) rotated head. Black dots represents where the magnetic field is sampled (by two magnetic field probes). (a.1) and (b.1) zoom on the area. Values of the magnetic field are reported and clearly show that the changes in magnetic field at the side of the head are larger than at the top of the head.

from human subjects, while 11 other models were formed by geometrically scaling the HUGO head model [26]. The latter are denoted as phantom data here. Movements were applied to these models using smoothed and de-trended motion parameters recorded over 150s from one subject in each of the motion conditions. Field changes at the probe positions were calculated by applying the Fourier method to the head models after translation and rotation at each time step.

Figure 4.8 shows how the average over probes of the standard deviation of the field measurements across different motion conditions varies with head volume for phantom and head simulations, and for experimental data (Figure 4.8). Note that the movements are the same for all simulations, but in the experimental data motion parameters are different for different subjects.
Figures 4.6 and 4.8 show that the morphology and size of the head along with the magnitude of the movement parameters strongly affect the magnitude of the extra-cranial field changes. For fixed morphology and similar movements (Figure 4.8, left), the magnetic field changes scale approximately linearly with the head volume. This behaviour likely results from the scaling of the overall magnetic dipole moment of the head with volume and also the scaling of the distance from the probes to features on the head surface

	Rest		Head Shaking		Head Nodding		Feet-wiggling	
std of:	T $[mm]$	R [°]	T $[mm]$	R [°]	T $[mm]$	R [°]	T $[mm]$	R [°]
Smoothed	0.09	0.21	0.48	4.47	0.78	1.94	0.28	0.16
Subject 1	0.50	0.16	0.34	0.11	3.64	1.59	3.68	0.80
Subject 2	2.25	0.73	0.81	0.41	11.80	7.58	12.82	4.10
Subject 3	0.52	0.39	0.50	0.13	3.74	1.81	6.72	1.83
Subject 4	1.67	0.52	0.48	0.15	7.88	3.92	7.52	1.59
Subject 5	1.60	0.50	1.48	0.40	5.17	2.11	7.63	1.76

Table 4.4: The table reports the overall standard deviation of motion parameters (translation and rotation) in the experimental data and the smoothed/detrended data used for simulations (Figure 4.10).

(which form local magnetic dipoles) with the cube-root of the volume, in conjunction with the inverse cubic dependence of the dipole field on distance. This dependence on head volume is evident, but less clear in Figure 4.8 (right) where the head morphology also varies across subjects, but the motion parameters are the same in all cases. In the real data (Figure 4.8) where the extent of movement varies across subjects (Section B.3), the dependence on head volume is obscured, as the sensitivity to the extent of head movement is greater.

Cloth probe holder

Figure 4.10 shows the results of simulations which aimed to demonstrate the complex cross influence between head volume, morphology, and extent of movement. Plots shows the standard deviation over the 16 NMR field probes and the whole time series as a function of the head volume. For fixed head movements, the distance between head and probes (Figure 4.10.a) and different heads (volume and morphology) (Figure 4.10.b) influences the linearity of the mathematical relationship between the changes of head position and magnetic field changes.

Adding a further degree of complexity by simulating the true experimental condition (Figure 4.10.c) reveals that limits in head motion due to the space available inside the head coil lead to larger magnetic field changes for smaller heads.

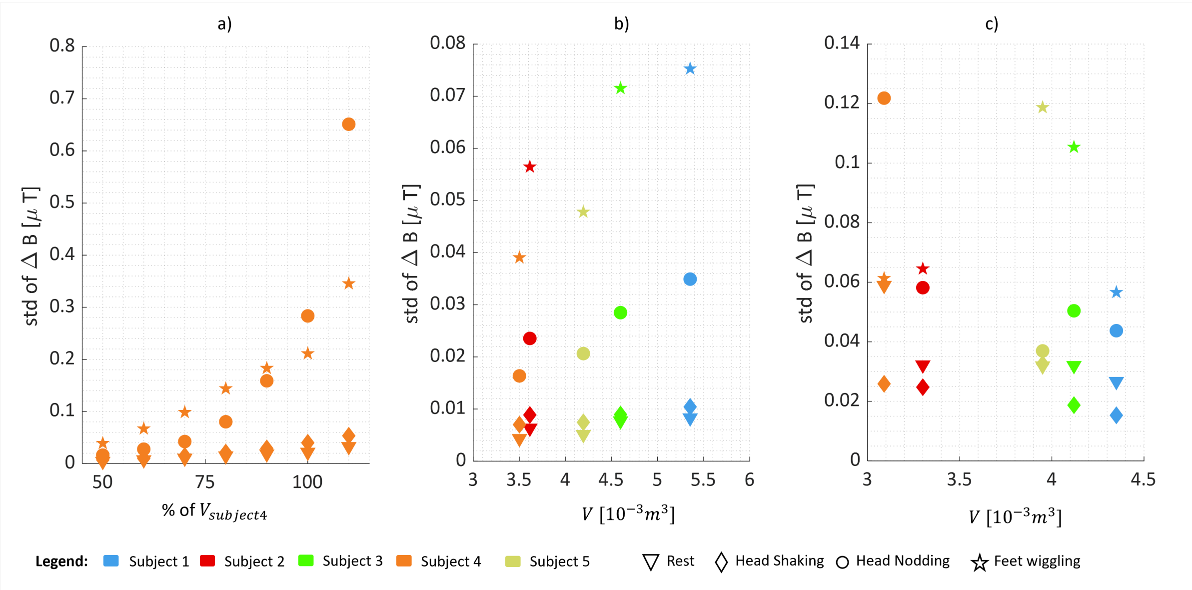

Figure 4.10: *Effect of the head-probe distances and head morphology on smoothed and detrended data (Cloth probe holder).* Variation of the average over probes of the standard deviation of the field measurements with simulated head volumes for (a) Subject 4 and (b) subjects 1 to 5 simulations, for different motion conditions. Table 4.4 reports the standard deviation of motion parameters in the smoothed/detrended data used for simulations. (c) Variation of the average over of probes of the standard deviation of the field measurements with measured head volumes for true experimental data, for different motion conditions.

4.2.2 Experimental magnetic field data

Using simulated data (see Section 4.2), it has been shown that the head-probe distance and relative positions and standard deviation of the magnetic field data (linked to the range of movements performed) influences the data the most. Here, the analysis has been repeated using experimental data from Subjects 1,2 and 3 that were involved in measurements made using both set-ups[3].

The standard deviation (STD) of the magnetic field changes measured using the PVC support was plotted as a function of the head volume in Figure 4.11a. The analysis with real data confirms the results obtained with simulated data in Section 4.2 for the three subjects considered. It also clearly shows that for the same subjects and same head movement conditions, the standard deviation of the data was larger for the PVC support. This is due to the even sampling of the field in the space around the head and the extent of motion (the larger the range, the closer the head goes to the probes). However, as the space and the comfort inside the supports differs (as reported by volunteers), we

[3]The predictions of head motion parameters data are sensitive to position of the probes relative to the head, but not to probe position relative to the scanner isocentre

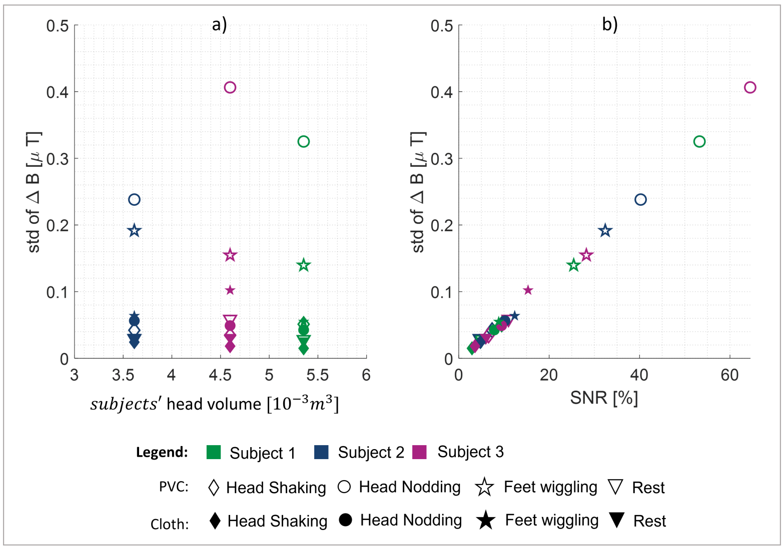

Figure 4.11: *Influence of the head-probe distance.* The influence of the head-probe distance has been analysed in experimental data for both set-ups (empty markers for the PVC holder, filled markers for the cloth holder) and for the three subjects that were studies using both set-ups. a) Results derived from simulations shown in Figures 4.10b and 4.10c have been confirmed here by using experimental data. b) The standard deviation (STD) of the data has been plotted as a function of the Signal to Noise Ratio (SNR).

cannot also exclude the possibility that this has influenced the differences in head motion range for the same volunteers.

The Signal to Noise Ratio was also measured by characterising noise as the Root Mean Square of the background measurements used to characterize the field camera (Section 3.2.1). We consider this as a standard background measurement as it has been computed by considering the magnetic field changes (the different shimming of the scanner influences the absolute values of the magnetic field measured by the probes, but not the change from the average value). The signals were the RMS of the magnetic field changes in different head conditions, for different subjects, for different set-ups.

By plotting the standard deviation of the magnetic field changes (which reflects how close the head was to the probes) as a function of the SNR[4], it is clear that: for smaller

[4]The reason why the STD and SNR are proportional could be explained by considering the equations for STD, $STD = \sqrt{\frac{1}{N-1}\sum_{n=1}^{N}|a_n - \mu_{a_n}|^2}$, and SNR, $SNR = \frac{RMS_{Signal}}{RMS_{Background}}$ (where $RMS = \sqrt{\frac{1}{N}\sum_{n=1}^{N}|a_n|^2}$). a_n is a generic time series ($n = 1, \dots N$) and $\mu_{a_n} = \frac{1}{N}\sum_{1}^{N} a_n$ is its average value. As in our case, the time series is the change in magnetic field from the average value ($a_n = \Delta B_n = B_n - \mu_{B_n}$), the squared terms in the STD equation became $|a_n^2|$ as $\mu_{\Delta B} = 0$. Also, N is always $\approx 10^3$ that making

distances between the head and the probes, and so a larger range of motion, the SNR improves due to the larger changes in the magnetic field. This is less visible in data obtained using the cloth support because the extent of the space over which the field is sampled is reduced.

4.3 Simulating field changes due to chest expansion

Movements of tissue due to physiological cycles also cause changes in the extra-cranial magnetic field . Head motion due to pulsatile blood flow across the cardiac cycle produces some small effects [127], but a more significant effect arises from the periodic chest motion involved in respiration. The physical movement of the chest produces a significant magnetic field change at the probe positions. This effect can be modelled [128] by considering a sphere of air surrounded by water sited at the position of the sternum. Field changes at the position of the head due to chest movement in respiration can be modelled by modulating the radius of this sphere across the respiratory cycle. The field perturbation at position (x, y, z) due to such a sphere centred at the origin is given by

$$\Delta B(x,y,z) = \frac{\frac{1}{3}\Delta\chi B_0 R^3(2z^2 - x^2 - y^2)}{(x^2+y^2+z^2)^{\frac{5}{2}}} \times \Delta V \tag{4.5}$$

where B_0 represents the bulk magnetic field (7 T), x, y and z represent the Cartesian components of the distance vector between the sternum and the magnetic field probes, which take values of 0, 10, 40 cm, respectively; $\Delta\chi$ represents the difference of the magnetic susceptibility between the air and tissue; R represents the radius of the sphere (8 cm) simulating the effect of the lungs [128]. The term outside the brackets represents the time series of respiration measurements normalized between 0 and 1 (ΔV). The difference of the magnetic susceptibility between the gas and the tissue was assumed to be $\Delta\chi = 9.4 \times 10^{-6}$ ppm in agreement with the literature [128]. As a result, the order of magnitude of ΔB is 10 nT, in agreement with experimental data at rest condition (Figure 3.10).

4.4 Conclusion

The simulations were based on the real experimental set-up and customised head models. Synthetic data reproduced extra-cranial magnetic field changes produced by realistic head and chest movements. Overall, there is good agreement between measured and simulated field variation, with a similar pattern of variation of field change across

the approximation $\frac{1}{N} \approx \frac{1}{N-1}$ valid. So, $RMS_{Data} \approx STD_{Data}$ and $STD \propto SNR$.

probes (Figures 4.4 and 4.5). Using the simulated data, we were able to identify the parameters which had the strongest influence on the magnetic field changes, such as the positions of the field probes relative to the head, extent of head movements and head morphology (Figures 4.8 and 4.10).

The next chapter discusses the core of the work presented in this thesis: how to predict head motion parameters from measurements of extra-cranial magnetic field changes by using two different supervised learning techniques (Section 5.1.3). The simulated data will be used to test the effectiveness of a spatial filter developed to reduce the effect of physiological body motion on magnetic field changes, and the use of a linear method (Partial Least Square) and a non-linear method (Nonlinear AutoRegressive network with eXogenous inputs) to infer head motion parameters from magnetic field data.

Chapter 5

Contact-less head motion tracking without simultaneous scanning sequence

This chapter introduces the new motion correction method developed in this thesis. It is based on using field camera measurements of the pattern of field changes produced by changes in head position to infer head motion parameters. The experimental and simulated data have been divided into large and small head movements, where large and small refer to the upper range of the movements performed. In Chapter 4, simulated data were used to show that the feature that most strongly influences the field changes is the head-probe distance. The chest expansion influence on magnetic field changes (Section 4.3) has been evaluated to be disrupting in the case of small head movements.

Under the assumption that the mathematical relationship between head motion parameters and magnetic field changes is bijective (the measured change in extra-cranial field uniquely defines the change in head position), and two different regression methods to predict head movements from extra-cranial field measurements have been tested. Section 5.2.2 shows how synthetic magnetic field data have also been used to test the performance of the regression methods chosen in order to select the pipeline for the analysis of experimental data. The PLS (Partial Least Squares) linear approach gave relatively poor results, while the NARX (Neural Network based auto regressive method) non-linear approach gave more promising results, using both simulated and real data. NARX was tested in more detail and used to predict head motion in various experimental scenarios for several subjects. This chapter describes its use in predicting head motion parameters in several subjects.

Data acquired without simultaneous scanning and simulated data have been used in this chapter. Chapter 7 shows the reproducibility of the results on magnetic field data acquired with simultaneous scanning. The method proposed has the advantages of being a marker-less, non-contact method whose use does not require significant modification of MRI sequences[60].

5.1 Implementation of the contact-less head motion tracking

Data processing involves pre-processing in terms of time alignment and denoising steps. In particular, magnetic field data have been filtered using solid harmonic functions to reduce the confounding effects of respiration (Subsection 5.1.1). The effectiveness of this step is further explored using simulated data (Subsection 5.2.2).

5.1.1 Pre-processing of Extra-cranial magnetic field data

Extra-cranial magnetic field data

The pre-processing steps that were used to select the most significant channels are shown in Figure 5.2. The change in the magnetic field was considered by subtracting the average over time from each probe time series (zero mean data series). Then, in the case of analysis of raw data series, the data are normalized, otherwise a spatial filter is applied before normalization. Normalisation is used to bring all the data into the same range. The spatial filter combined solid harmonics fitting and feature selection and was used to reduce the influence of the physiological noise and highlight those variables that best represent the data, reducing the number of time-series considered in the subsequent analysis also speed up the processing.

Channel selection. During the acquisition of the data, it is important to identify whether there are faulty channels for technical reasons (such as the NMR probe or ADC board connection being damaged) [1], we exclude channels in post-processing only. Usually, the data from such channels are not taken in account for the data analysis.

Zero mean data series. As we are interested in the relationship between the changes in magnetic field and head pose, magnetic field data time series were de-meaned, by subtraction of the average of the time series before further processing. For each channel (i):

$$\Delta\vec{B}_i = \vec{B}_i - \mu_{Bi} \tag{5.1}$$

[1] Channels may be excluded during the data acquisition process to improve SNR.

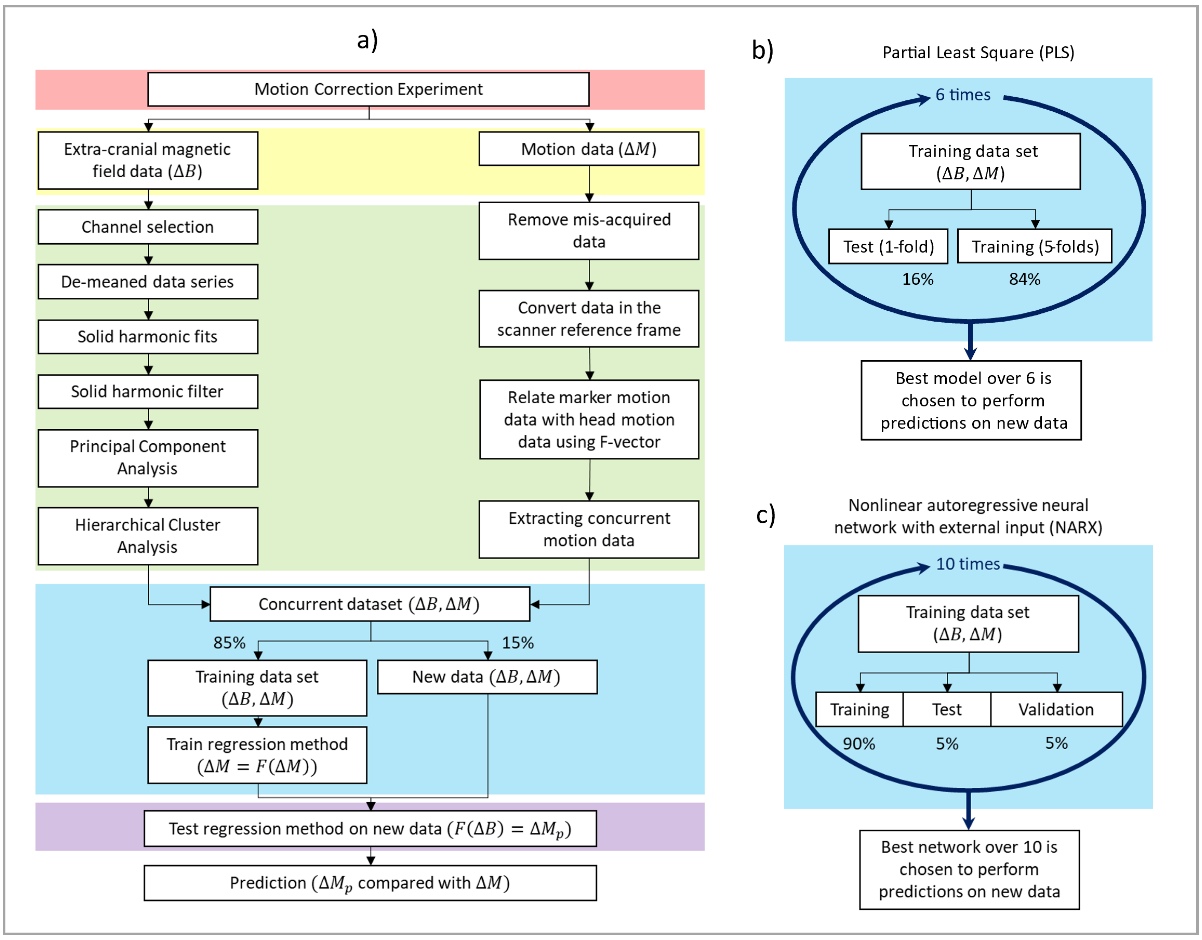

Figure 5.1: *Flowchart.* (a) The flowchart shows the steps made from the data acquisition (light red) to the prediction (light purple) described in Section 5.1. Data acquisitions (light yellow) and pre-processing (light green) are carried out before data are randomly divided into the training dataset and the new data subset. The training of the regression methods (either PLS or NARX) is further described in (b) and (c). The trained method is then applied on new magnetic field data (ΔB) to predict motion data (ΔM_p). Predicted motion data are evaluated by comparison with motion data acquired simultaneously to the new magnetic field data.

the average over the time considered (μ_{Bi}) has been subtracted from the $i - channel$ data series ($\vec{B}_i$).

Spatial filter, part I: solid harmonics fits. The field values measured at each time point were fitted to a series of solid harmonics (Table 1.4) using the `linsolve()` built-in MATLAB function. The spatial distribution of the probes determines the number and largest order of solid harmonics that can be used in the fitting [33]. An even distribution

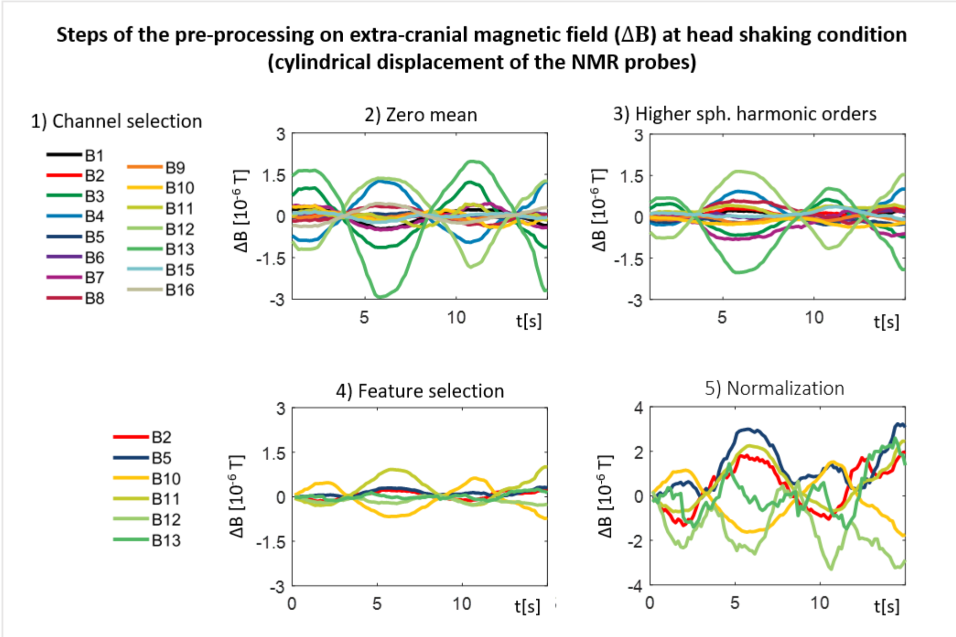

Figure 5.2: *Pre-processing steps applied to magnetic field data.* The figure shows the effect of the different pre-processing steps on 15 s of head shaking data acquired with probes mounted in the PVC holder.

of 16 probes over a spherical surface is ideal for the fitting process up to the 3^{rd} order fits (page 29). The PVC holder (Figure 3.7) provides a favourable distribution of probes, which in this case are distributed over a cylindrical surface. The cloth holder (Figure 3.3) aims to sample the signal closer to the head as far as the RF head coil allows, and so the probe positions were not evenly distributed around the head. Therefore, the fit was performed only up to the second order. The goodness of the fits was checked by evaluating the condition number using the `cond()` built-in MATLAB function. [2], ($\kappa(Matrix) = 10^k$) which can be used as an indication of the loss in accuracy [129]. As a rule of thumb, the loss in digits is equal to the order of magnitude k of the condition number. The condition number for the probes mounted in the PVC support was 5.7×10^3, while with the probes mounted in the cloth holder in between the transmit and receiver RF coils it was 4.7×10^5. While the loss of 3 digits of precision was acceptable for the former case, 5 digits loss in the latter case were not acceptable. The fit up to the second order reduced the condition number to 4.8×10^1 for the cloth holder and to 3.1 for the PVC holder.

[2] *The condition number.* The condition number measures how small changes in the input (independent variable) influence values of the output (dependent variable). A problem is well-conditioned if it has a low condition number. High condition numbers characterize ill-conditioned problems.

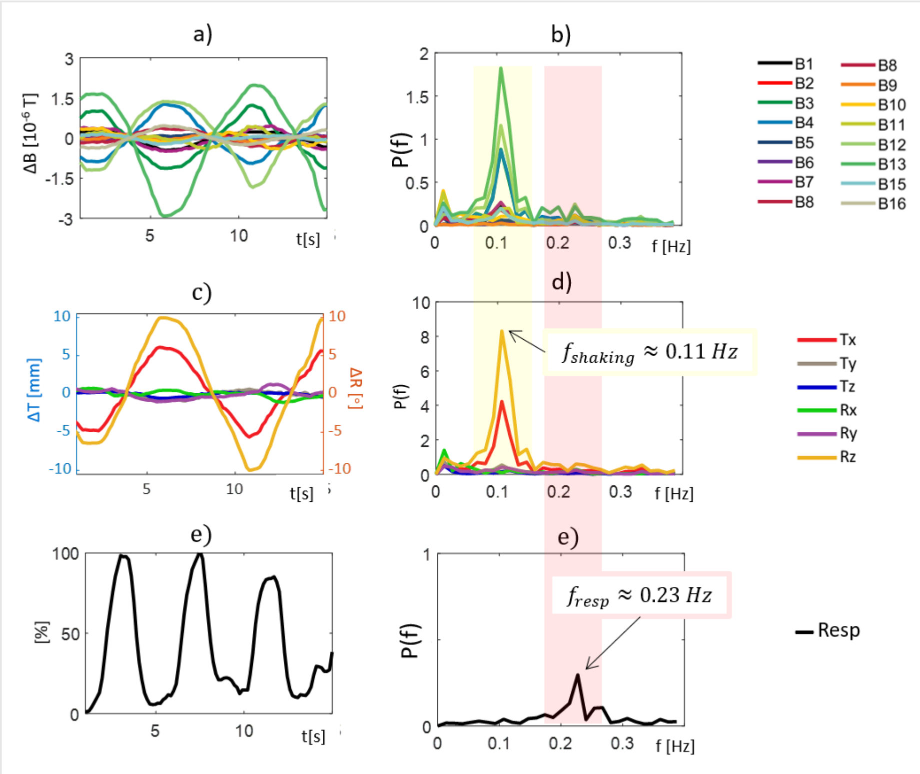

Figure 5.3: Absolute (a) field perturbations at the probe positions acquired using the PVC holder, (c) head translation and rotations and (e) physiological parameter time series during rest and head shaking conditions for *Subject6* at 7T and the associated frequency spectrum (b, d, f). Peaks show that field perturbations are influenced by both head motion and respiration.

In both scenarios, the influence of the movement of the chest in respiration on the magnetic field data decreases with increasing harmonic order, as higher order harmonics represent signal that varies more rapidly with spatial position than the lower order harmonics. This relationship has been proven by comparing the frequency spectra of the signals 5.3. An example of the analysis is shown in Figure 5.4. This shows data acquired during large head movements and the associated frequency spectrum (Figure 5.4, right). As expected, the frequencies corresponding to the head movements are clearly visible in the magnetic field data and in the motion data, while the frequencies due to the respiration are mostly visible in the magnetic field data, but also present in the motion data. So, setting a threshold to separate the effects of head movements and respiration could lead to loss of information about head movements related to the chest expansion. As head and chest movements produce magnetic field changes with different spatial characteristics, we can separate them via solid harmonic analysis. Figure 5.4 (left) shows the

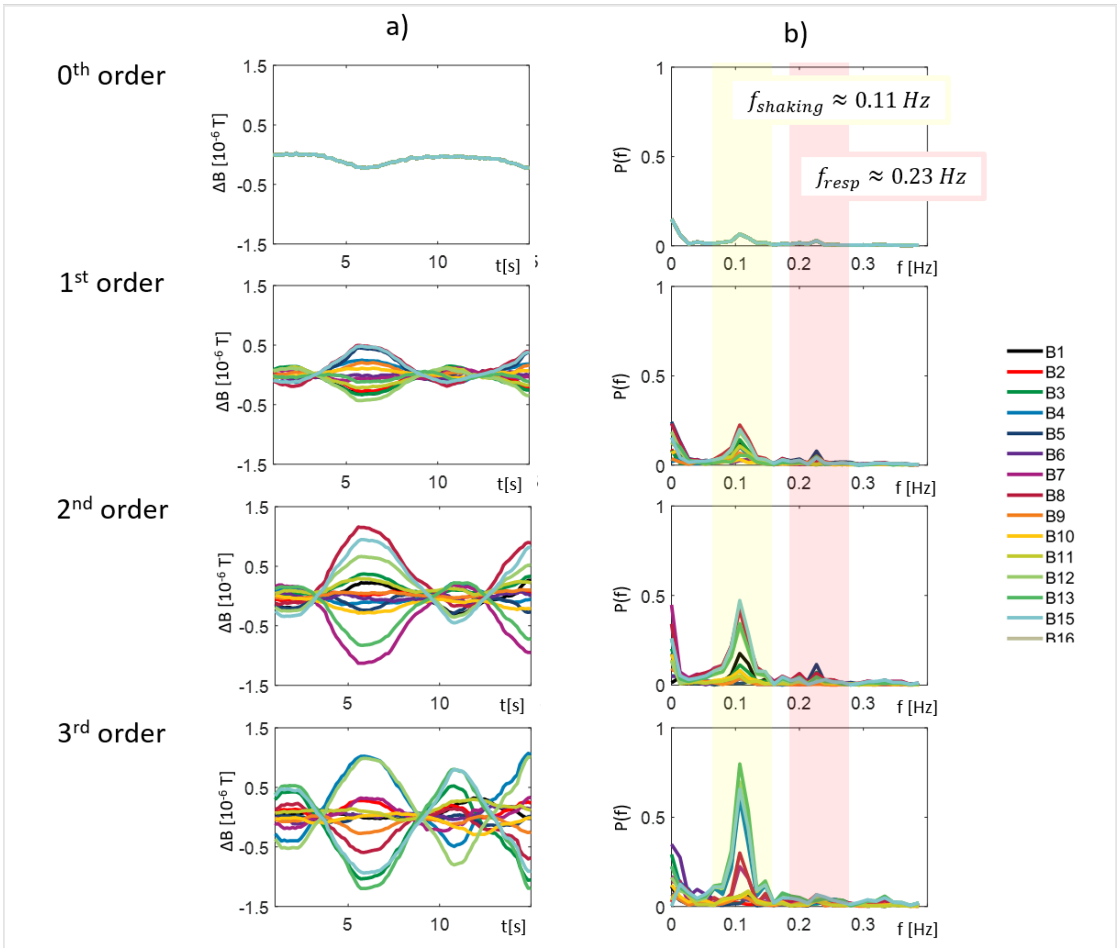

Figure 5.4: Plots show (Column a) the solid harmonic decomposition of magnetic field measurements acquired using the PVC holder (Figure 5.3.a) during large head shaking movements and (Column b) the associated frequency spectrum. The cylindrical configuration of the PVC holder allowed fitting up to the 3^{rd} harmonic order. Lower/higher order spatial harmonics best represent the effect of chest/head movements. The influences of head movement and physiological noise can be differentiated based on their different frequencies. The lower solid harmonics (0^{th}, 1^{st}) of the magnetic field data were filtered out to reduce the influence of physiological noise.

solid harmonic fits and the corresponding frequency spectra. Comparison of the spectra indicates that the influence of respiration is decreased compared with the influence of the movements in the higher order solid harmonics. Eliminating the low order harmonics (0^{th}, 1^{st}) from the field traces consequently reduces the effect of respiration compared to that of the head movements. Furthermore, the lower harmonics from the fit may be used to extract the respiration signal (section 4.3).

In the case of the PVC holder, 2^{nd} and 3^{rd} orders could be considered, while in the case of the cloth holder only the 2^{nd} order fits could be used. So, only the 2^{nd} order has been considered for comparison.

Spatial filter, part II: feature selection (PCA and HCA). Feature selection performed on $\Delta\vec{B}$ aims to select the subset of probes that carries most information about the head motion. The subset of probes was selected using Principal Component Analysis (PCA) combined with Hierarchical Cluster Analysis (HCA) [11].

PCA has been performed on normalized magnetic field signals to reduce the number of channels used for the analysis using the `pca()` built-in MATLAB function. 16 principal components (PC) were identified. The majority of the variance of the data is explained by the first three principal components. The characteristics of the principal components varied depending on the subject, the activity and the probe positions. In particular, in the case of the cloth holder, the signals from the probes at the back of the head were manually excluded from the analysis because the residual physiological noise from chest movement in respiration dominated these signals [3].

The first three principal components (PC) are used to classify the probes using the `dendrogram()` built-in MATLAB function. These are used to built a dendrogram (or hierarchical tree) based on the Euclidean distance between the probe signals represented in the PC space. So, probe signals that behave similarly in the PC space are closer and belong to the same cluster. Clusters are then defined by setting a cut-off value for the Euclidean distance using the `cluster()` built-in MATLAB function. For the analysis reported in this dissertation, the cut-off was 70% of the maximum Euclidean distance. Clusters are then sorted based on the variance of the signal of the probes and agglomerated to create a final cluster that contains ≥ 6 probes. An example outcome of the analysis is shown in Figure 5.5 and the code is reported in the Appendix at page 280.

Normalisation. The signal from each channel was normalized by:

$$\Delta\vec{B}_i = \frac{\vec{B}_i - \mu_{Bi}}{\sigma_B} \tag{5.2}$$

where μ_{Bi} is the average of each channel signal and $\sigma_B i$ is the overall standard deviation of the channel's signal computed using the `std()` built-in MATLAB function.

[3]The variance of the few probes on the back of the head dominate the choice of the principal components. This leads to a worse representation of the signal of most of the probes (≤ 12). That influences the next step of the feature selection process.

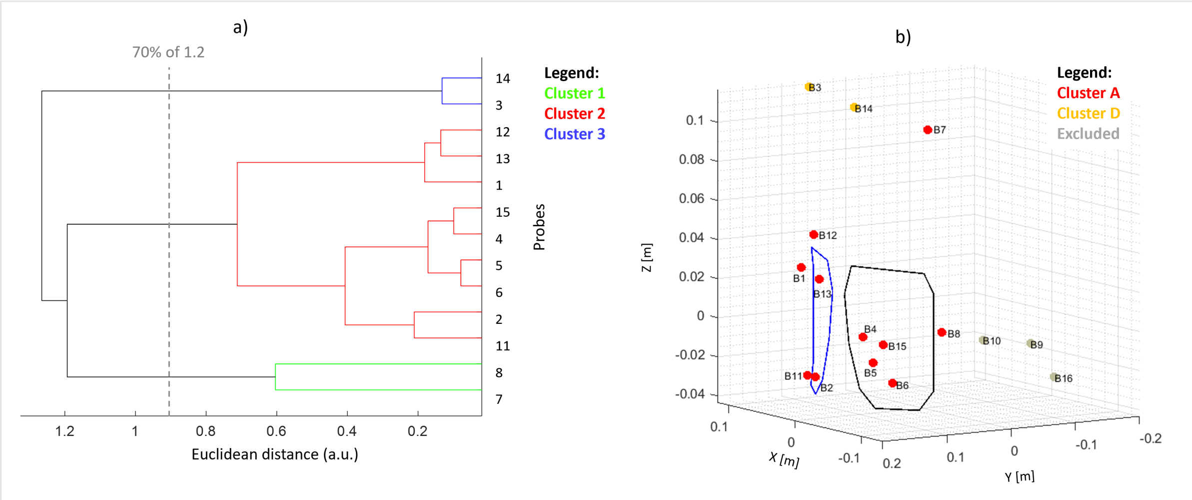

Figure 5.5: *Example of the outcome of the feature selection.* Plots show an example of the results obtained for real magnetic field data in the rest condition for Subject 5. The cloth holder was used, so signals from probes 9, 10 and 16 were removed before the analysis. (a) The dendrogram shows clusters 1,2,3 obtained by representing the probe signals in the principal component space. Clusters have been numbered based on the variance of the signals (descending order). The cut-off threshold is highlighted with a dashed gray line. It was equal to 70% of the maximum of the Euclidean distance. (b) Clusters 1-2 in (a) are then agglomerated to produce final cluster that contains $\geq$ 6 probes. Cluster A was then selected by agglomerating Clusters 1 and 2. Probes that belong to Cluster C were then excluded from the analysis.

5.1.2 Pre-processing of the head motion parameters

The raw data from the optical camera are not directly used, as the motion is recorded using quaternion algebra and referred to a system of reference centred at the position of the optical camera. The other internal parameters used for the pre-processing of motion data are called *status* (to tag data where the marker was correctly detected: $status = 1$) and the *time strings* (up to milliseconds accuracy $HH : MM : SS.sss$). The camera was set to record data at an average frequency of 80 Hz, but the actual time interval between two consecutive data points depends on the speed of the algorithm used to predict the marker position and could vary between 6 ms and 18 ms. Once motion data were calibrated and transformed to the scanner's frame of reference, concurrent head parameters measurements were extracted and data were ready to be used.

Ameliorating noise in raw motion data. The data where the marker is not correctly detected ($status = 0$) are removed from the time series. On average, the percentage of data removed was $<< 1\%$, but this depends on the extent of the movements made by the subject that may lead to the marker going out of the optical camera's field of view .

The software to record data has a bug and records the time string $HH : MM : SS.000$ as $HH : MM : SS, -01$ [4]. All the time strings (t^i) where the milliseconds part of the string assumes negative values were substituted with the average time between the previous (t^{i-1}) and the subsequent (t^{i+1}) values.

Cross-calibration of the optical camera. The optical camera is not permanently fixed in the magnet bore, and so it needs to be calibrated before or after each session assuming that during the session it doesn't move. The whole process has been developed and evaluated in a separate project. To summarize, the calibration process lasts ≈ 45 *min* and requires that a scanner operator lying prone on the scanner bed, manually moves an asymmetrical water phantom to which the MPT marker is attached [20]. A MRI calibration sequence is then performed providing concurrent measurements of phantom and marker positions. Data are analysed using a cross-calibration program that calculates the quaternion set to use for aligning the frames of reference of the scanner and optical camera.

Calibration of new motion data requires projection of the movement data from the *optical camera's system of reference* to the *scanner's system of reference*. The scanner's system of reference is defined by the MRI sequence used to scan the phantom and this sequence doesn't agree with the ones used to define the *field camera system's frame of reference*. Both systems of reference have the same origin (isocentre of the scanner), but reversed y-axis. They are left and right handed and so there is not a simple geometric transformation that can be applied to transform one into another. Thus, to make the head motion parameters measured in agreement with the magnetic field camera system of reference, the translations along the y axes are inverted ($T_y = -T_y$). Rotation measurements are not affected by the symmetry.

F-vector. As the optical camera records the movements of the marker at the marker location [5], it is necessary to apply a further transformation to obtain the actual movements of the head. So, data are shifted and rotated based on the *off-centre* and *angulation* data recorded during the planning of the MRI scan (survey).

Extracting concurrent data. The sampling frequencies of the optical camera and magnetic field camera are different, but a common trigger signal sent at the beginning of each TR period of the field camera is also recorded, allowing the measurements to be aligned in post-processing [11]. However, once the trigger is sent, the optical camera will assign the time string to the acquisition once marker position is sorted by the algorithm.

[4] My interpretation is that the 001 is interpreted as signed string of bit instead of unsigned at low level data recording in the software.

[5] The marker is rigidly coupled via a mouthpiece to the skull

Tags of the trigger and the measurements then match in time with an accuracy of $\pm 20\ ms$.

To improve the accuracy of the time alignment, the time strings of the optical camera data have been considered. Assuming that the first measurement matches between the magnetic and optical camera, a time string is created based on the TR (Δt, most common used values were 0.150 ms or 0.100 ms) of the magnetic field camera and the time of the first time-point ($t_1, \ldots, t_i + j\Delta t$) corresponding to the first triggers. The other time steps have been aligned by using the time string of the optical camera data. A locally weighted polynomial regression method (`smooth()` built-in MATLAB function, using the 'lowess' option) using sliding windows of 7% was used to smooth the motion data and perform the temporal alignment of the different time series.

5.1.3 Regression methods

In order to perform the prediction of head motion parameters ($\vec{M} = [M^1 \ldots M^6] = [T_x\ T_y\ T_z\ R_x\ R_y\ R_z]$ as defined at section 2.2) from measured changes in the extra-cranial magnetic field ($\vec{B} = [B^1 \ldots B^{16}]$), data were pre-processed to reduce the influence of the physiological noise, as described on section 5.1, and by performing a featured extraction [11] (Section 5.1.1) in order to reduce the number of input variables of the method. The signal formed using the fit to the higher solid harmonics was normalized based on each channel's standard deviation and then characterized through Principal Component Analysis (PCA) combined with Hierarchical cluster analysis (HCA) to select those $k-channels$ ($k \geq 6$) that contribute the majority of the data variance. The spatial filter applied is then formed by the combination of the solid harmonic fit, normalization and PCA.
Head motion parameters were predicted ($\vec{M}'$) from k-magnetic field data ($\vec{B}' = [B^1 \ldots B^k]$) selected: $\vec{M}' = F(\vec{B}')$, where F is a generic mapping function.

In the case of the linear model, F has been chosen as the Partial Least Square (PLS) regression model (Appendix A.2.1):

$$\vec{M}_t = F\left(\vec{B}_t\right) \tag{5.3}$$

In the nonlinear model case, F represents a single hidden layer, recurrent and dynamic neural network (RNN) based on Nonlinear Autoregressive Exogenous model (NARX). Its architecture was: $k-input$ neurons, $30-hidden$ neurons, $6-output$ neurons. At each time t, once trained, the NARX model predicts the motion parameters ($\vec{M}_{t+1}$) based on past d_{OUT} predictions and past d_{IN} inputs ($\vec{B'}_t, \vec{B'}_{t-1}, \ldots, \vec{B'}_{t-d_IN}$) and exogenous input ($\vec{B}_{t+1}$)):

$$\vec{M}_{t+1} = F\left(\vec{M}_t, \vec{M}_{t-1}, \ldots, \vec{M}_{t-d_{OUT}}, \vec{B}'_{t+1}, \vec{B'}_t, \vec{B'}_{t-1}, \ldots, \vec{B'}_{t-d_{IN}}\right) \tag{5.4}$$

d_{OUT} and d_{IN} are also called delays and for the purpose of this study they have both been considered as equal to two time steps in the field measurements (0.3 s). The network chosen will therefore predict two steps ahead.

Training, validation and test subsets of data The regression methods tested were both linear and non-linear using spatially filtered and unfiltered data. For each data-set:

- The non-linear regression models (NARX) were trained using time series formed by 85% of each data-set, saving 15% of the data for testing the model. The time correlation of the data was not considered as the training time series was further randomly divided in 90%−5%−5% to create training, validation, and test data-sets. The model that performed best over 10 training runs (where each time a random selection of subgroups is made) was selected in order to minimize the influence due to the random initialization of neuron weights and so the error on the prediction. More detail is provided in Appendix A and the code is detailed in Appendix D.2.2.

- The linear regression models (PLS) were trained using time series formed by 85% of each data-set, saving 15% of data for testing the model. The time correlation of the data was not considered as the training time series was further randomly divided to perform the k-fold cross validation ($k = 6$) to validate the prediction. More detail is provided in Section A.2.1, Appendix A (Section A.2.1) and the code is detailed in Appendix D.2.1.

The results of the regression were quantified using the mean square error (MSE), the value of R^2 and the Pearson coefficient (PC) of the fit.

Data (Table 3.3) have been divided into two subgroups for training the regression methods on two different ranges of movement; small (rest, feet-wiggling) and large (rest, feet-wiggling, head shaking, head nodding). Data were partitioned as described in Section 5.1.3. Tables 5.1.3, 5.1.3 report the number of data values used for each regression method, along with the set-up and range of movements.

	Total	**PLS** (85% – 15%) *Training*	*New*	**Training PLS** ($k - fold, k = 6$) $5 - folds$	$1 - fold$
Small (PVC)	1500	1275	225	1063	213
Large (PVC)	2500	2125	375	1771	354
Small (cloth)	8000	6800	1200	5667	1133
Large (cloth)	12000	10200	1800	8500	1700

Table 5.1: *Number of data points.* The number of data points used for training, validation and testing the linear regression methods (PLS) are reported. These numbers have been calculated following the method described in Section 5.1.3.

	Total	**NARX** (85% – 15%) *Training*	*New*	**Training NARX** (90% – 5% – 5%) *Training*	*Validation*	*Test*
Small (PVC)	1500	1275	225	1148	64	64
Large (PVC)	2500	2125	375	1913	106	106
Small (cloth)	8000	6800	1200	6120	340	340
Large (cloth)	12000	10200	1800	9180	510	510

Table 5.2: *Number of data.* The number of data points used for training, validation and testing the non-linear regression methods (NARX) are reported. These numbers have been calculated following the method described in Section 5.1.3.

The results from the previous chapter using simulated data show that the positions of the probes relative to the head influence the predictions most significantly and there is a non-linear relationship between head volume and the magnitude of the field changes (Figures 4.8 and 4.10), and thus the efficacy of a linear Partial Least Squares (PLS) method in predicting movement from field changes is limited. The non-linear method applied to pre-processed data gave the best results (Figure 5.15) and so only this method has been explored further.

5.1.4 Evaluate the prediction

Predictions were reported as plots (predicted motion data, p, as a function of the measured motion data, d) and statistical evaluation. In general, numbers have been rounded to the three decimal places. Plots, that report results over multiple subjects, have not been fitted, while predictions on single subjects have been. Results over 3 out of 6 subjects are then displayed with both plots and statistical evaluation, while plots that summarise the results over the subject do not have an associated statistical evaluation. Only relevant plots have been reported in this Chapter for clarity, Appendix C reports all the results over subjects, ranges of head motion and regression methods. Results were evaluated by plotting the predicted motion parameter (x, dependent variable) as a function of the measured motion parameters (y, independent variables). Ideal results of prediction will lead on to data lying on a straight line passing through the origin (intercept $b = 0$) and having slope equal to one ($a = 1$): $y = ax$. Data were therefore fitted using the general linear equation: $y = ax + b$. Predictions were considered to be good if

$a \to 1$,$b \to 0$. The fit was based on nonlinear least-squares fitting procedure (MatLab). The root mean squared error (R^2) of the fit was evaluated. The Standard deviation (STD) [6] of data and Mean Squared Error (MSE) [7] of the prediction compared to the fitted line were evaluated: small MSE means good prediction as predicted data are closer to the measured data. The Pearson Correlation Coefficient (PC) was also evaluated [8].

Predictions were evaluated "poor" or "good" based on how many motion parameters were close to the ideal values:

$$AND(slope \geq 0.9,\ |0 - Intercept| \leq 0.01,\ R^2 \geq 0.9,\ MSE \leq 0.01,\ PC \geq 0.9) \quad (5.5)$$

A prediction has been described as "good" when 4 or more of the 6 head motion parameters satisfied all the above conditions, otherwise "poor". The limit of 4 out of 6 head motion parameters was chosen as, in general, in the rest condition (the hardest head motion range to predict) the variation of R_y and R_z is smaller than other motion parameters because these rotations are not favoured by the position of the subject. Tables 5.3 and 5.5 summarise the findings.

How to interpret the fit Fit has been performed on predicted data (x, dependent variable) as a function of the motion data (y, independent variables). Ideal results on prediction will lead on having data lying on a line passing through the origin of the axes (intercept $b = 0$) and having slope equal to one ($a = 1$): $y = ax$. So, data were fitted using the general line equation: $y = ax + b$. Prediction was considered good if $a \to 1$,$b \to 0$. Slope ($a = \Delta y/\Delta x$,$b = 0$).

- $a \to 1$, predicted data well approximate motion measurements.
- $a > 1$, predicted data are in general overestimated compare to motion measurements ($\Delta y > \Delta x$).
- $a < 1$, predicted data are in general underestimated compare to motion measurements ($\Delta y < \Delta x$).

Intercept ($a = 1$,b).

- $b \to 0$, predicted data well approximate motion measurements.
- $b \neq 0$, predicted data shifted compare to motion measurements.

[6] $STD = \sqrt{\frac{1}{N-1}\sum_{n=1}^{N} |a_n - \mu_{a_n}|^2}$
[7] $MSE = \frac{1}{N}\sum_{n=1}^{N} (y(n+1) - \hat{y}(n+1))^2$
[8] 1 = correlated; 0 = non correlated; -1 = anti-correlated

- $b > 0$, predicted data are in general overestimated compare to motion measurements ($\Delta y > \Delta x$).
- $b < 0$, predicted data are in general underestimated compare to motion measurements ($\Delta y < \Delta x$)

Comparing sparse data with the ideal fit:

- $y = x$, predicted data well approximate motion measurements.
- $y > x$, predicted data are in general overestimated compare to motion measurements.
- $y < x$, predicted data are in general underestimated compare to motion measurements.

5.2 Tests using simulated data

Simulated data components can be combined to approximate the magnetic field changes measured during an experimental session, or can be paired wisely to mimic and test the efficacy of data analysis methods before application to real data (Figure 5.6). Simulated data have been used to select the pre-processing pipeline and regression method (PLS and NARX) that would perform best on real data.

The most significant predictions obtained using simulated data from a single volunteer are reported in this section. The random extraction used to separate the test and training data means that there may be small differences in the range of movements considered in each test, even when the data come from the same volunteer. Results were evaluated qualitatively in order to select the best workflow to be applied to real data.

5.2.1 Span of simulated data

Simulated data allow exploration of the way that measured magnetic field data are formed from the sum of different components (Figure 5.3):

$$\Delta B = \Delta B_{Head} + \Delta B_{Chest} + \Delta B_{Noise} \tag{5.6}$$

ΔB_{Head} represents the change in magnetic field due to the movement of the head. This component is well approximated by the simulated data (see Section 4.1.1). ΔB_{Chest} represents the change in magnetic field at the probe positions due to the chest expansion (see Section 4.3). ΔB_{Noise} represents the overall random noise on the measurements and it has been modelled as white Gaussian noise with std $\approx 10^{-8}\ T$.

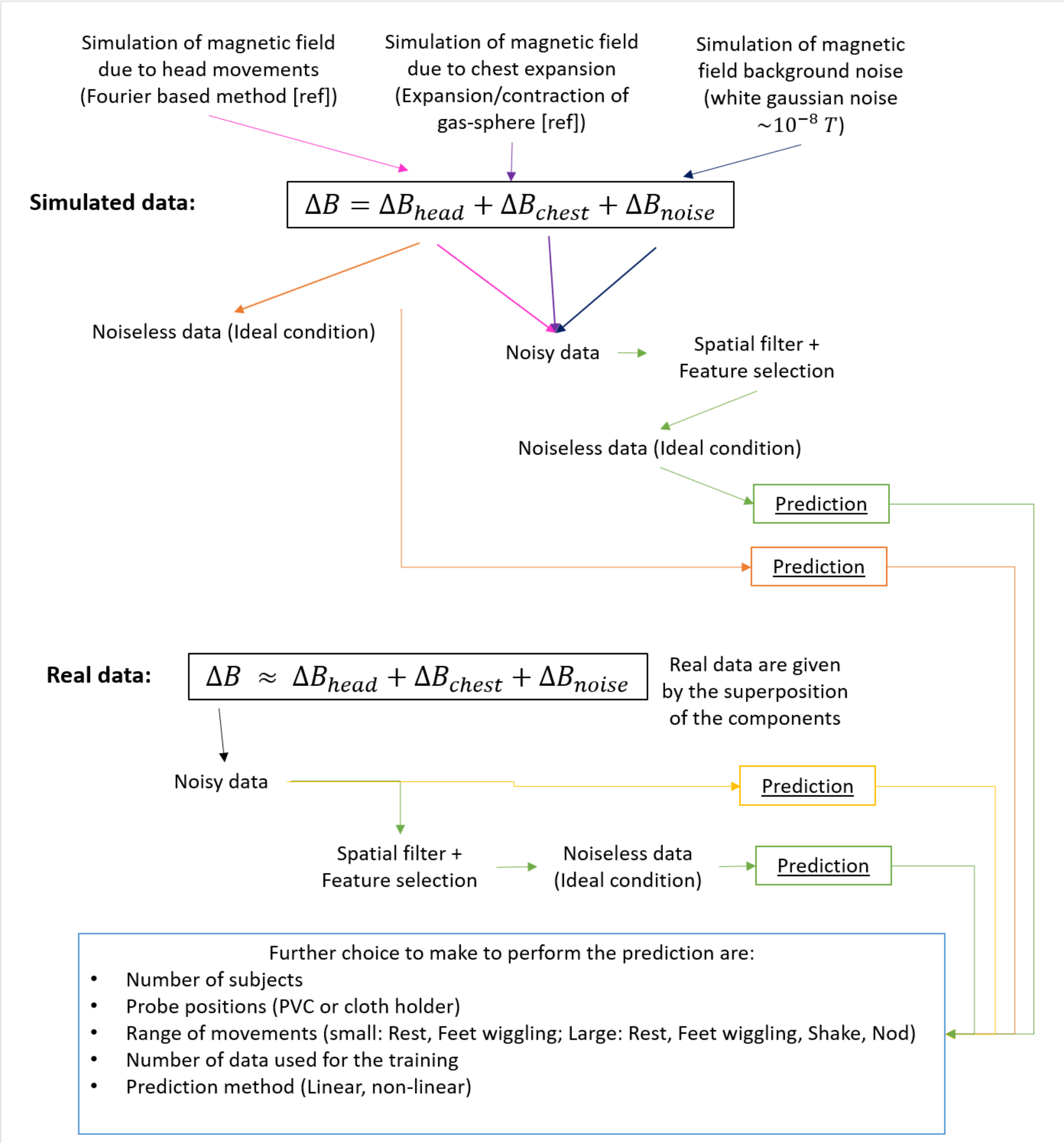

Figure 5.6: *Span of the possible data analyses.* The flow charts show the magnetic field data that can be used in the cases of simulated and real data. For example, simulated data due to head movements only correspond to pre-processed real data. Once the magnetic field data are chosen, the prediction could be carried out on data from different volunteers, probe configurations and ranges of head movements, using two different regression methods..

Figure 5.6 describes the span of the possible data analyses that can be computed on simulated data.

By using only the ΔB_{Head} component, the data represents the ideal condition where only the movements of the head contribute to the changes in magnetic field. This case is the optimal to test which regression method applied to which range of movements provides the best predictions.

By using ΔB (all the components), the data are more similar to experimental data. The spatial filtering and the feature selection (Section 5.1.1) could then be tested. Comparison between the predictions made using ΔB and filtered ΔB should give an indication of the effect of the filtering on the data.

5.2.2 Selecting the best data-analysis pipeline

Simulated data were analysed in order to identify:

- Whether the pre-processing reduces the information content of the data and/or improves the prediction (Figure 5.14 and Figure 5.15);
- The range of movements to be used in the training set to predict the most common range of movements in MRI (small head movements at rest). (Figures 5.8, 5.9, 5.10, 5.13);
- Which regression methods perform better over the range of movement previously identified (Figures 5.10 and 5.13);

Filtering field changes due to chest expansion

The simulated magnetic field changes due to chest movements in respiration have been superimposed onto simulated magnetic field changes due to head movements (Figure 4.5) in order to test whether respiratory effects can be filtered out by fitting field changes to solid harmonics and then selecting the low or high order harmonics. The simulated signal was fitted at each time point to a series of solid harmonics up to 2^{nd} order. The influence of chest movements on magnetic field data decreases with harmonic order, as higher order harmonics represent signal that varies faster with spatial position than is the case for lower order harmonics. This relation has been proven by comparing the frequency spectrum of the signals. Thus, 2^{nd} order fitting represents a signal that carries less perturbation due to chest movements. This method was tested on both simulated and real data in Chapter 5 as probes were placed ad hoc on the back of the head to better sample the effects of chest movement. In order to extrapolate respiration-like signal from magnetic field data [130], lower harmonic fit signals have been superimposed and filtered using a band pass filter centred at the respiratory frequency. The band pass width of the filter (± 0.1 $[Hz]$) was based on the subject's respiratory frequency (on the average 0.3 $[Hz]$).

Data used for prediction

An important variable that determines the outcome of the prediction is the amount of data used for training the regression methods and the head movements range considered. There were 5000 time points (750 s) in the rest condition, 3000 time points (450 s) for the feet-wiggling condition, 2000 time points (300 s) for the head shaking and head nodding conditions. So, for example, the regression method for small head movements regime (rest, feet-wiggling) uses a total of 8000 time points (1200 s) randomly divided into the training set (85% of 8000, so 6000 time points) and test set (15% of 8000, so 2000 time points).

Select the best regression method

First, the linear method (partial least squares, PLS) was tested on simulated magnetic field data including the effect of head movement only (ΔB_{Head}) where probes were simulated to be in the cloth holder set-up. This represents the optimal condition for measurements, since the probe positions allow performance of concomitant MRI acquisition using the 32-channel RF receiver coil and it exploits the regression method that is easiest to train. At first, the whole set of magnetic field data related to the whole range of head movements has been used as the training set and the test set spanned the same range of movements. Results (Figure 5.8) show that in the noiseless condition the PLS method can successfully predict the whole range of head movements. However, a closer look at the prediction accuracy for small movements (Figure 5.9) reveals that the prediction accuracy is poor for this range of movements. In conclusion, using the whole range of head movements does not train the PLS method well to predict the whole range of movements with sufficient accuracy.

We consequently evaluated the effect of restricting the range of movements represented in the training set to small head movements when using the PLS method. Figure 5.10 shows that prediction on small head movements improved significantly, but with relatively poor prediction accuracy in half of the motion parameters (T_x, R_y, R_z). Using the same range of head motion for training and test data, the non-linear method outperforms PLS (Figure 5.13). The explanation may be in the nature of the training methods. The PLS method based the training on preserving the variance of the data and for small head movements, variance over probes is small, $\sigma^2 \approx [0.01, 3]$ for small head movements and $\sigma^2 \approx [1, 80]$ for large head movements, and the method is consequently

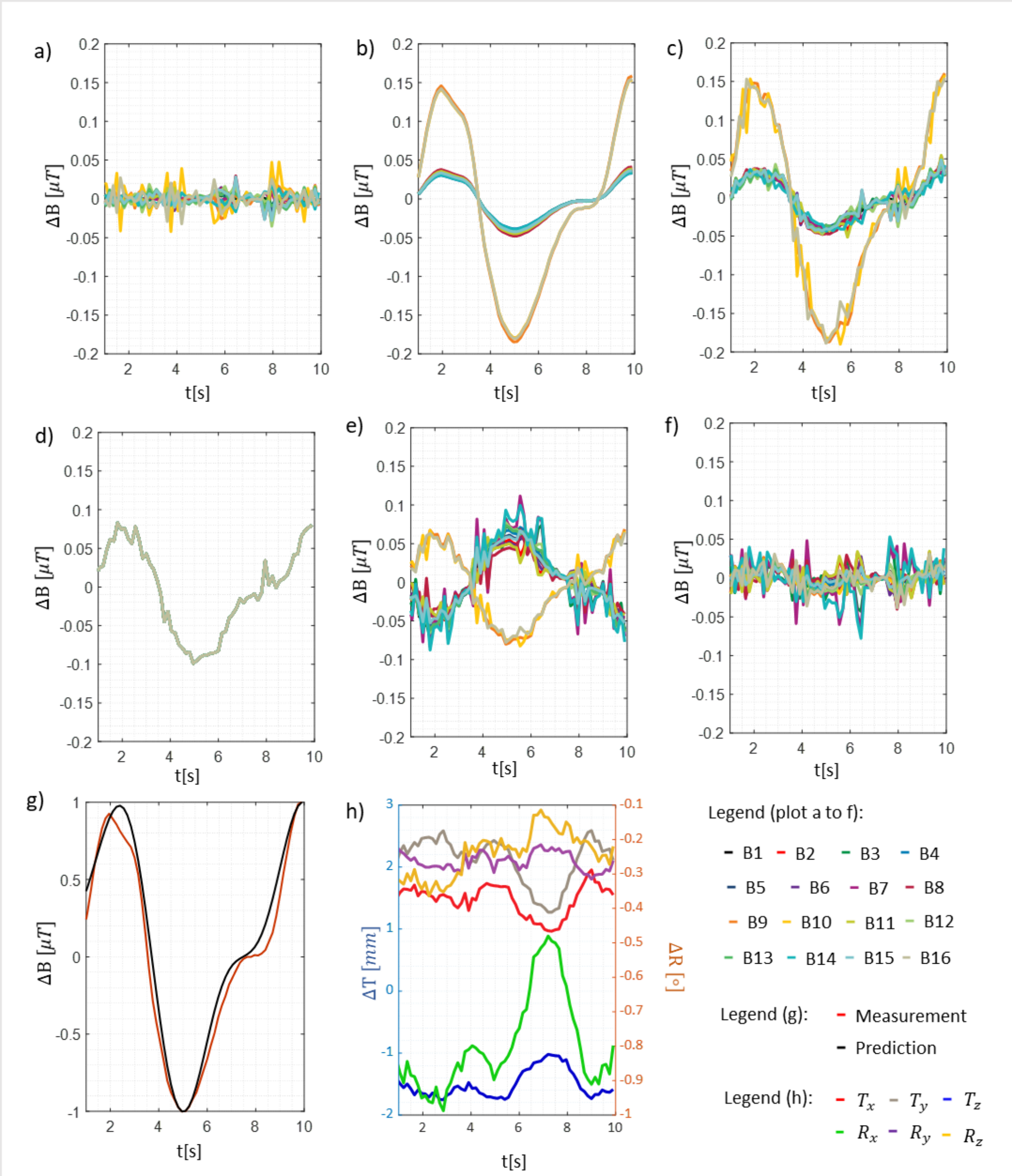

Figure 5.7: *Effects of physiological motion.* Simulated magnetic field data in rest condition (a - only due to head motion, b - only due to chest expansion, c - the superimposition of a and b) was fitted using solid harmonics up to the second order (d) zeroth, (e) first, (f) second. Only the first 10 seconds of data are shown here. Figure (g) shows the prediction of the respiration signals obtained by from the 0^{th} order fit. (h) shows the head motion parameters.

harder to train. On the other hand, the NARX method doesn't rely on the intrinsic characteristics of the data used for the prediction, but it learns from the examples and, in the training phase, adjusts the weights of the neurons. In fact, it does fail to predict large head movements (Figure 5.12) as the adjustment to make between steps is too big.

Following this, the effect of using the non-linear method to predict small head movements was further assessed by considering the magnetic field changes due to the head motion and the noise sources (ΔB). Figure 5.14 shows that the NARX approach is robust against noise sources as the prediction is not strongly affected by the addition of a realistic level of noise.

Prediction results obtained using pre-processed simulated data (Figure 5.15) were comparable to the predictions obtained using noisy simulated data (Figure 5.14) with the same regression method. Therefore, application of pre-processing to the real data did not corrupt the information about head motion that is carried by the field changes.

Qualitative evaluation of the prediction obtained with synthetic data

Results (Figures 5.8 to Figures 5.15) were evaluated by plotting the predicted data (p, dependent variable) as a function of the measured data (d, independent variables). Ideal results of prediction will lead to the data lying on a line passing through the origin of the axes (intercept $b = 0$) and having slope equal to one ($a = 1$): $d = ap$. So, data were fitted using the general line equation: $d = ap + b$. Prediction was considered good if $a \to 1$,$b \to 0$.

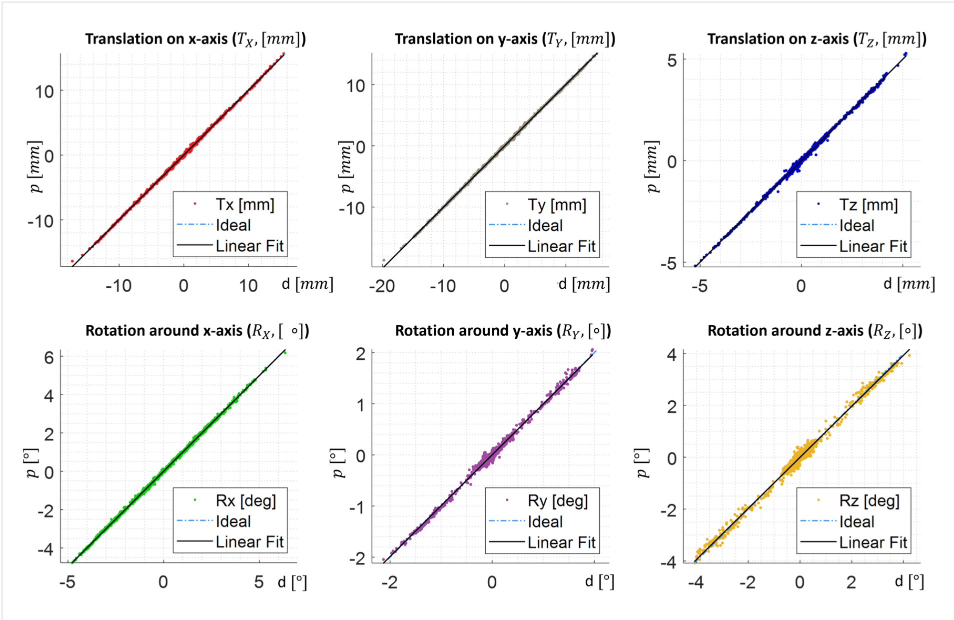

Figure 5.8: *Prediction*. Simulated magnetic field data (ΔB_{head}) due to the *whole range* of head movements have been used to train the *linear* regression method (PLS) for Subject 5. Probes were simulated in the *Cloth* holder set-up (data are reported in Table B.19). The trained method was applied to the *whole range* of head movements (test data). A qualitative analysis of the fit reveals that the trained method performs well in estimating the movements (p) in the test data (d). As the PLS method is based on preserving the variance in the data , it better predicts data with similar variance. However, the small head movements (≤ 3 mm or $^\circ$) seem to be predicted with reduced accuracy compared to the larger ones. This effect is reported in Figure 5.9.

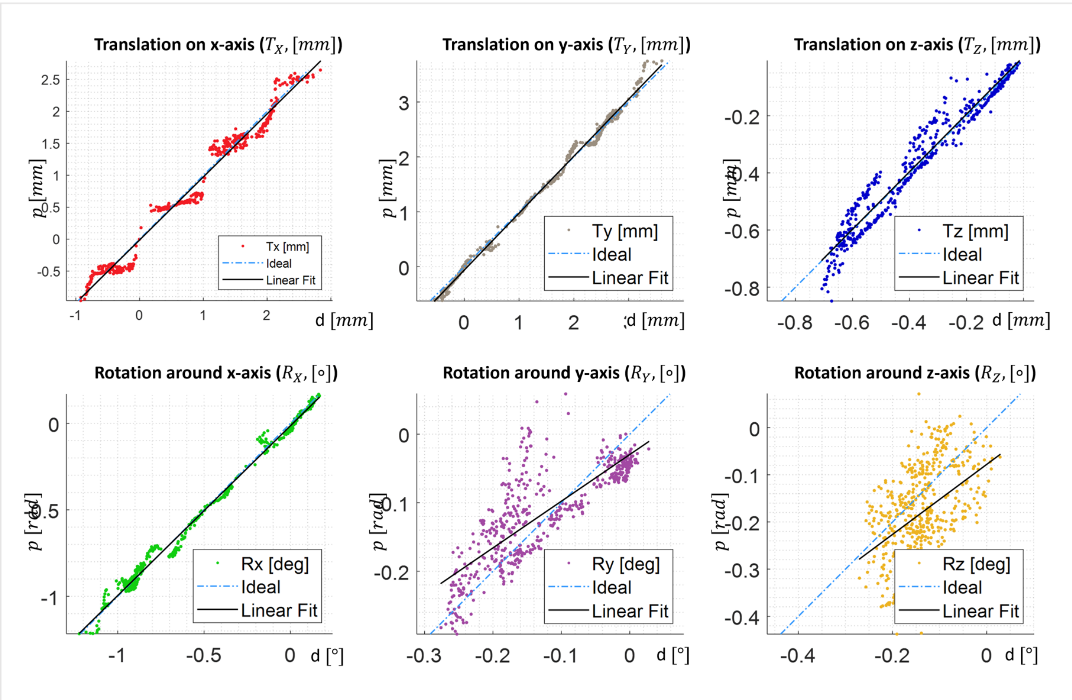

Figure 5.9: *Prediction.* Simulated magnetic field data (ΔB_{head}) due to the *whole range* of head movements have been used to train the *linear* regression method (PLS) for Subject 5 (Figure 5.8). Probes were simulated in the *Cloth* set-up (data are reported in Table B.19). The trained method was applied to the *small range* of head movements (test data). A qualitative analysis of the fit (p) reveals that the trained method perform poorly in estimating the test data (d). Further investigation is reported in Figure 5.10.

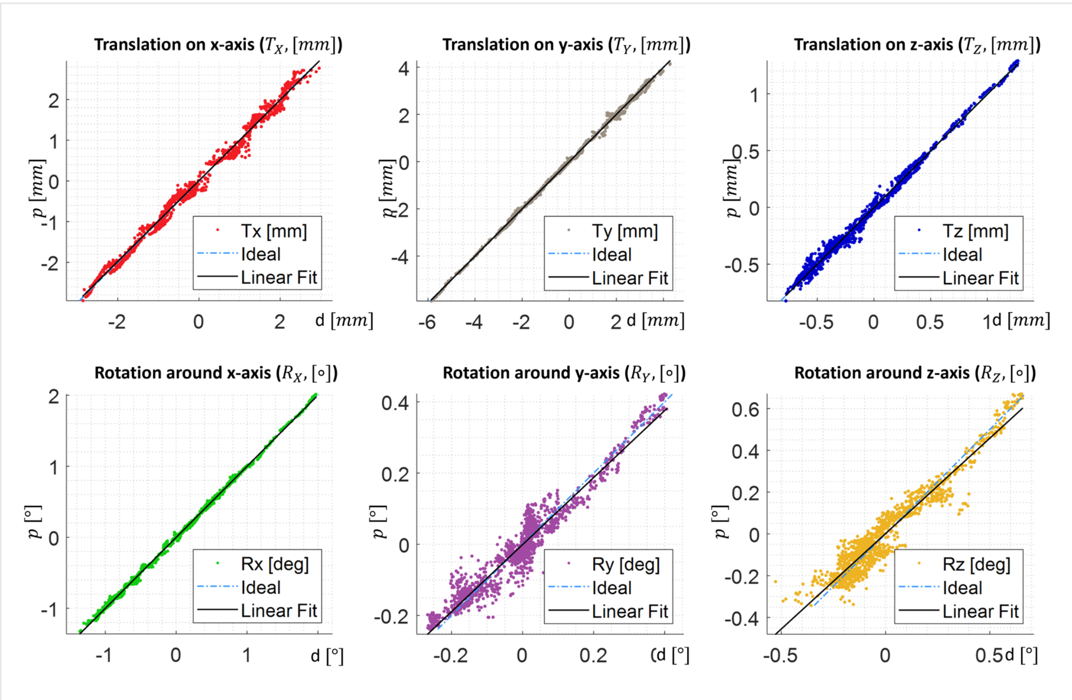

Figure 5.10: *Prediction.* Simulated magnetic field data (ΔB_{head}) due to the *small range* of head movements have been used to train the *linear* regression method (*PLS*) for Subject 5. Probes were simulated in the *Cloth* set-up (data are reported in Table B.19). The trained method was applied on the *small range* of head movements (test data). A qualitative analysis of the fit reveals that the trained method performed poorly on estimating the test data (d), but the prediction (p) was improved compare to that reported in Figure 5.9.

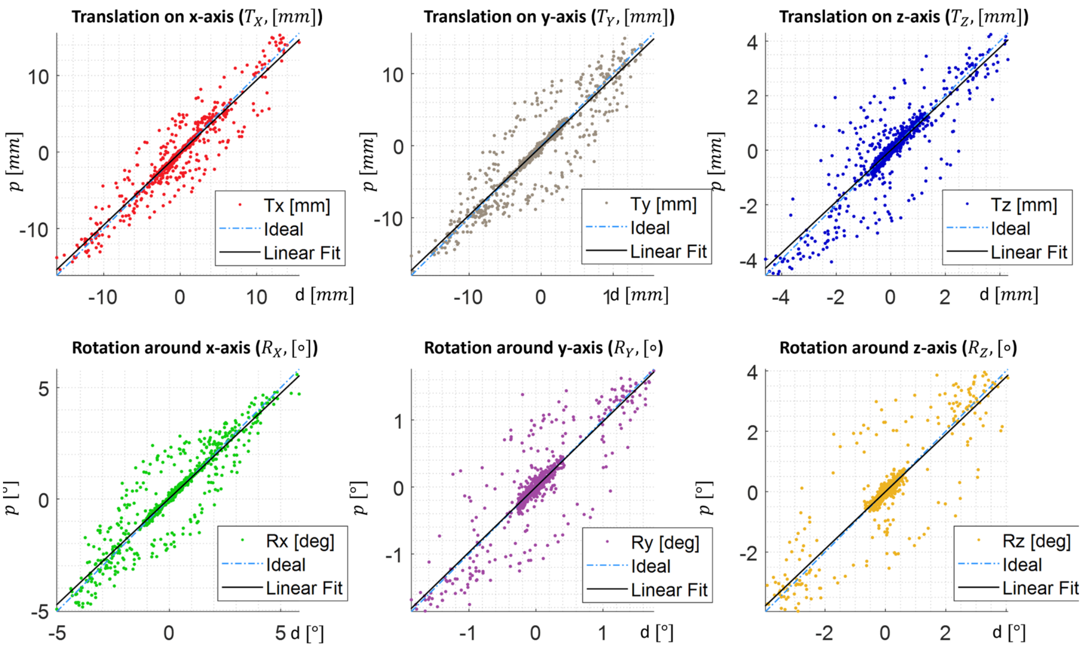

Figure 5.11: *Prediction.* Simulated magnetic field data (ΔB_{head}) due to the *whole range* of head movements have been used to train the $non-linear$ regression method ($NARX$) for subject 5. Probes were simulated in the *Cloth* set-up (data are reported in Table B.19). The trained method was applied on the *whole range* of head movements (test data). A qualitative analysis of the trained method reveals that the fit (p) estimates new data (d) with significant errors. Compared to the PLS method (Figure 5.8), the small movements are better predicted than the large ones. Changing the configuration of the probes improves the predictions (Figure 5.12).

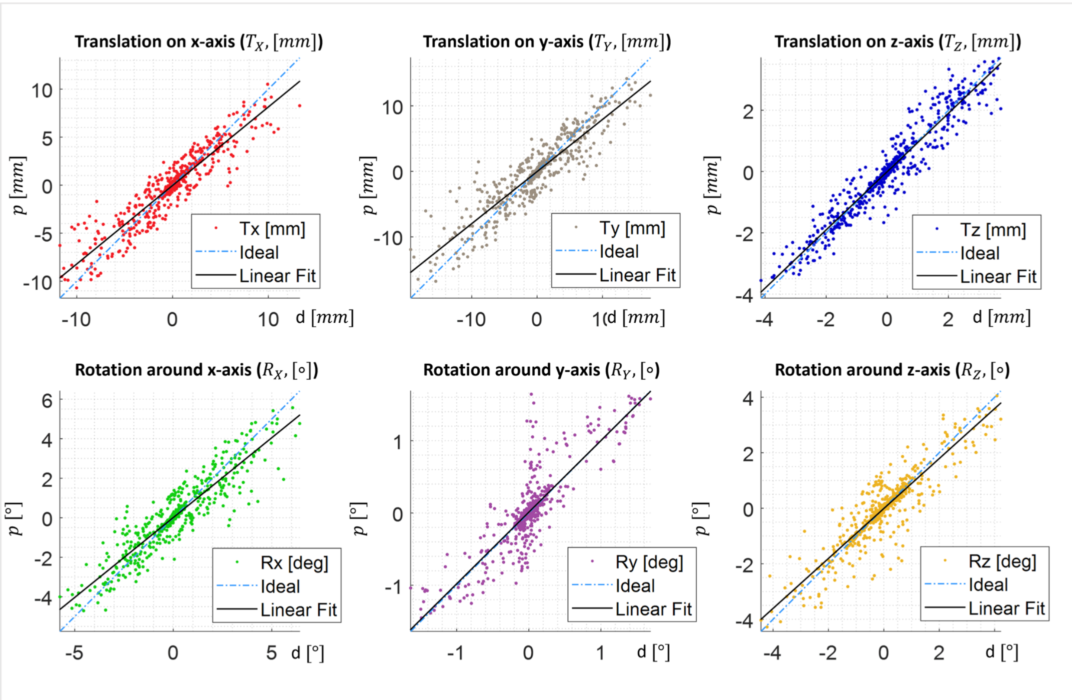

Figure 5.12: *Prediction.* Simulated magnetic field data (ΔB_{head}) due to the *whole range* of head movements have been used to train the $non-linear$ regression method ($NARX$) for Subject 5. Probes were simulated in the PVC set-up (data are reported in Table B.19). The trained method was applied to the *whole range* of head movements (test data). A qualitative analysis of the trained method reveals that the fit estimates new data with significant errors, but with slight improvements compared to the Cloth probe holder (Figure 5.11).

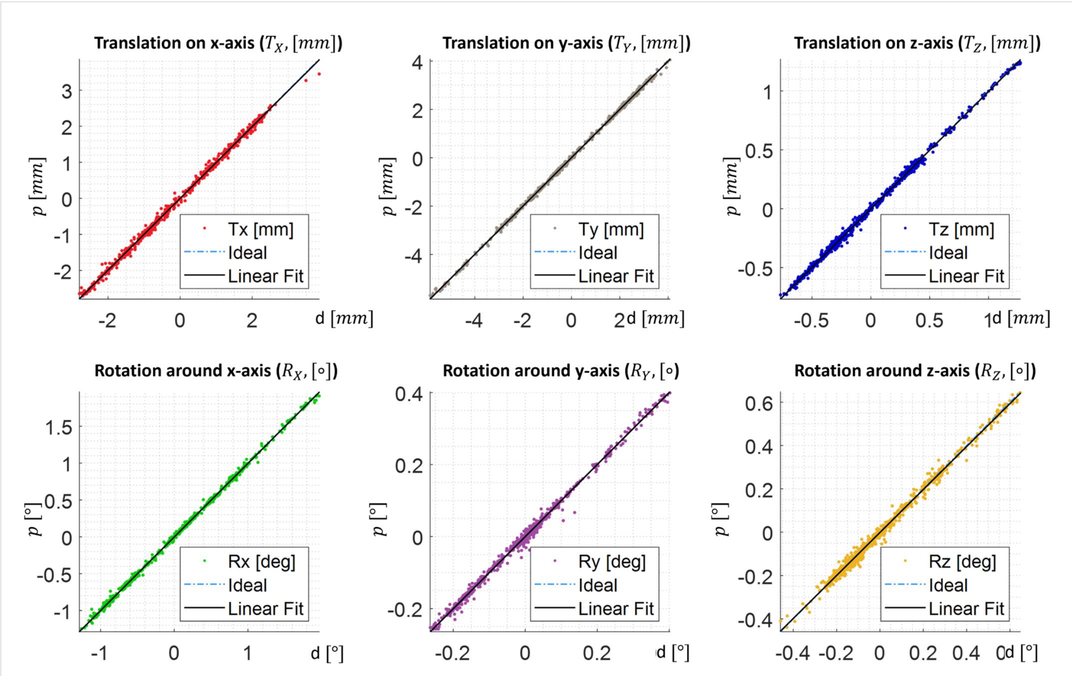

Figure 5.13: *Prediction.* Simulated magnetic field data (ΔB_{head}) due to the *small range* of head movements have been used to train the $non - linear$ regression method ($NARX$) for Subject 5. Probes were simulated in the *Cloth* set-up (data are reported in Table B.19). The trained method was applied to the *small range* of head movements (test data). A qualitative analysis of the trained method reveal that the fit estimates new data well compared to the linear method (Figure 5.10).

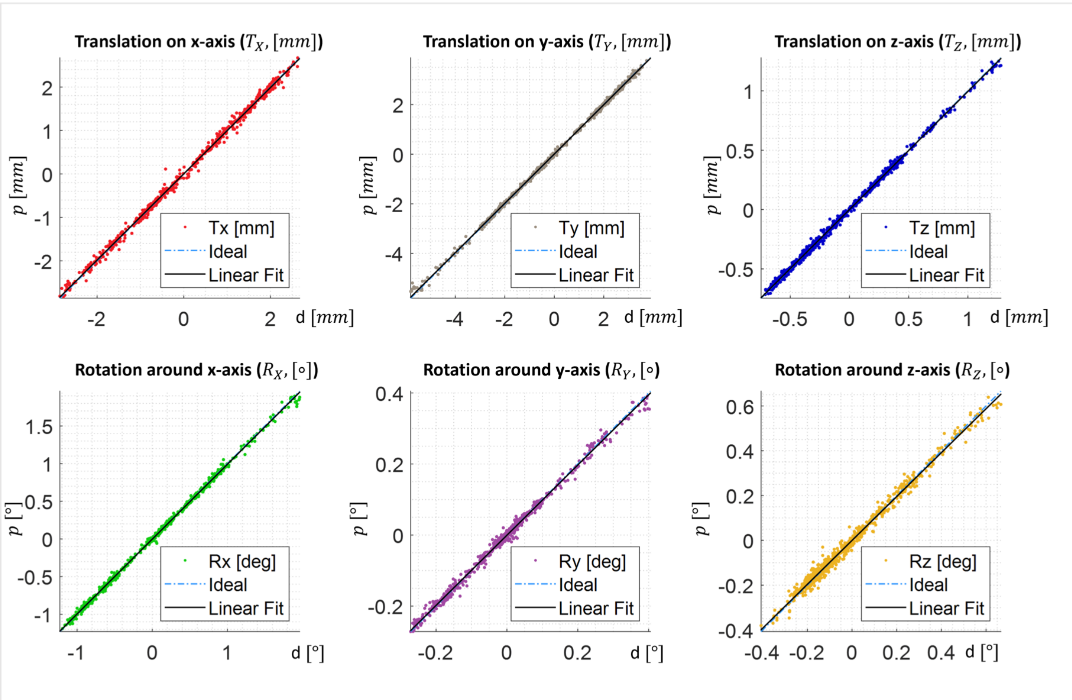

Figure 5.14: *Prediction.* Simulated magnetic field data (ΔB) due to the *small range* of head movements and the *noise sources* have been used to train the $non-linear$ regression method ($NARX$) for Subject 5. Training data were $not\ pre-processed$ to reduce the noise. Probes were simulated in the *Cloth* set-up. The trained method was applied to the *small range* of head movements (test data). A qualitative analysis of the trained method reveals that the fit estimates new data well compared to the linear method (Figure 5.10).

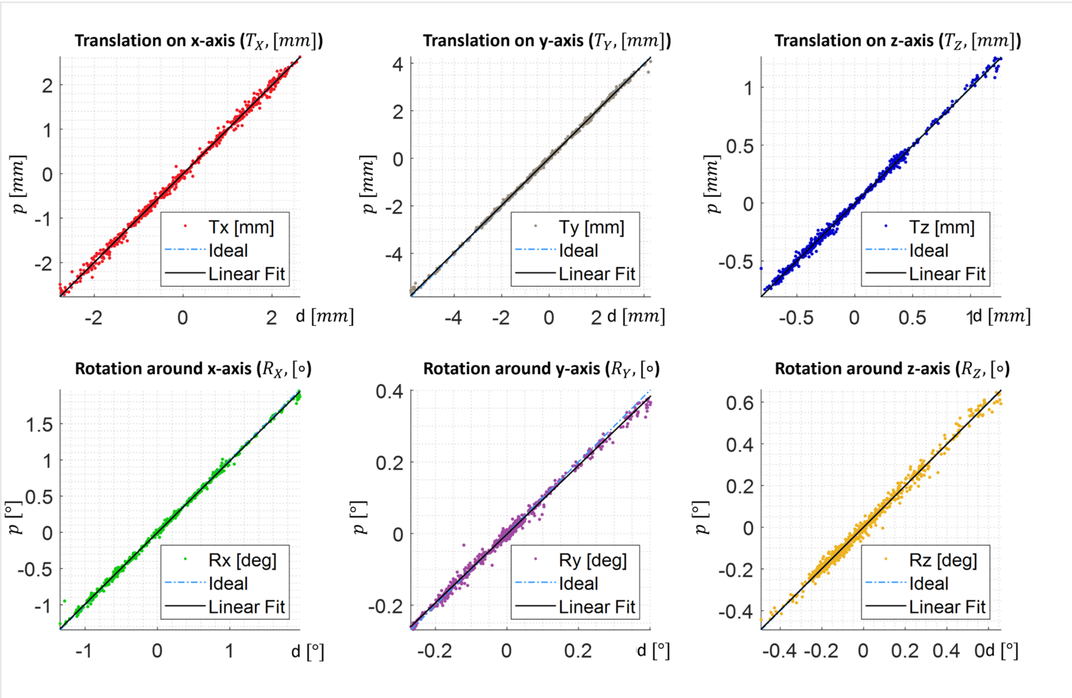

Figure 5.15: *Prediction.* Simulated magnetic field data (ΔB) due to the *small range* of head movements and the *noise sources* have been used to train the $non-linear$ regression method ($NARX$) for Subject 5. Training data were $pre-processed$ to reduce the noise. Probes were simulated in the *Cloth* set-up. The trained method was applied to the *small range* of head movements (test data). A qualitative analysis reveals that the pre-processing doesn't remove the part of the magnetic field data that represents the head motion, as the prediction results are good and comparable with the noiseless situation (Figure 5.13).

5.3 Tests using real data

In Chapter 4, simulated data have been used to identify the best way to predict head motion parameters from magnetic field changes. The influence of the probe positions relative to the head, range of movements and noise (from electrical devices and chest expansion) influences the accuracy of prediction. Both linear (PLS) and non-linear (NARX) methods (Section 5.1.3) have been applied to simulated data assuming that the probe distributions followed those used in both the PVC and cloth holders. The results showed that the most promising prediction pipeline involved using pre-processed magnetic field data from the cloth probe holder corresponding to a small range of head movements to train the non-linear method.

Here, the analysis performed on simulated data has been repeated on experimental measurements from both of the probe-holder set-ups in order to validate the results. Noiseless simulated data should correspond most closely to pre-processed real data as they were generated by considering the simulated magnetic field due to head motion only and pre-processing on real data aims to bring real data closer to this condition by reducing the influence of respiratory effects (Figure 5.6). Raw magnetic field data measurements correspond to the simulated data that considers all the sources of magnetic field change (head motion, chest expansion and electrical noise). Further comparison between predictions obtained with simulated and real data has been reported in Section 5.4.2.

For the benefit of clarity, results obtained over all the subjects (Subjects 1,2,3 and 6 for the PVC set-up and 1,2,3,4 and 5 for the cloth probe holder) are reported in the Appendix C and summarized in Tables 5.3 and 5.5. Here, results from Subject 3 have been used as a reference since the data from this subject were available for both set-ups. These results were compared with those from Subjects 5 and 6 for the two set-ups. The relevant plots are reported in Section 5.3.4.

Statistical evaluations of the fits are reported for single subjects over all the conditions tested because the fit on results on single subject may differ from the fit on the overall set of results (for example Figure 5.35 on Subject 3 and Figure C.10 that summarise measurements over all the subjects). This agreed with the fact that each data-set is unique, as the relative distance between probes and head and the exact movements are different for each subject.

Small movements refer to rest and the feet-wiggling conditions. Large movements refer to the whole range of data acquired (rest, feet-wiggling, head shaking and head nodding). Regression methods were trained and applied to the same range of movements. The numbers of data points available differ significantly for the two set-ups for the two ranges of motion (Table 3.3) because the experimental procedure evolved over time as we moved from using the PVC probe holder to the use of the cloth probe holder.

	Small range of head movements (Figure number, evaluation)					
	Raw				**Pre-processed**	
	PLS		**NARX**		**NARX**	
	PVC	**cloth**	**PVC**	**cloth**	**cloth**	**cloth (Less data)**
Subject 1	C.1, poor	C.3, poor	C.5, poor	C.7, good	C.10, good	C.11, good
Subject 2	C.1, poor	C.3, poor	C.5, poor	C.7, good	C.10, good	C.11, poor
Subject 3	5.17, good	5.23, poor	5.27, poor	5.31, good	5.35, good	C.11, poor
Subject 4	-	C.3, poor	-	C.7, good	C.10, good	C.11, poor
Subject 5	-	5.24, poor	-	5.32, good	5.36, good	C.11, good
Subject 6	5.18, poor	-	5.28, poor	-	-	-

Table 5.3: Table summarizes the outcome of the predictions reported in the indicated figures based on the criteria listed in the equation 5.5

	Small range of head movements (Table's number, evaluation)					
	Raw				**Pre-processed**	
	PLS		**NARX**		**NARX**	
	PVC	**cloth**	**PVC**	**cloth**	**cloth**	**cloth (Less data)**
Subject 1	C.1, poor	C.12, poor	C.21, poor	C.29, good	C.39, good	C.44, good
Subject 2	C.2, poor	C.11, poor	C.22, poor	C.30, good	C.40, good	C.45, poor
Subject 3	C.3, good	C.13, poor	C.23, poor	C.31, good	C.41, good	C.46, poor
Subject 4	-	C.14, poor	-	C.32, good	C.42, good	C.47, poor
Subject 5	-	C.15, poor	-	C.33, good	C.43, good	C.48, good
Subject 6	C.4, poor	-	C.24, poor	-	-	-

Table 5.4: Table summarizes the outcome of the predictions reported in the indicated tables based on the criteria listed in the equation 5.5

	Large range of head movements (Figure number, evaluation)				
	Raw				
	PLS		NARX		
	PVC	cloth	PVC	cloth	cloth (Less data)
Subject 1	C.2, poor	C.4, poor	C.6, poor	C.8, poor	C.9, poor
Subject 2	C.2, poor	C.4, poor	C.6, poor	C.8, poor	C.9, poor
Subject 3	5.19, poor	5.25, poor	5.29, poor	5.33, poor	C.9, poor
(*Fast*)	5.21, poor	-	-	-	
Subject 4	-	C.4, poor	-	C.8, poor	C.9, poor
Subject 5	-	5.26, poor	-	5.34, poor	C.9, poor
Subject 6	5.20, poor	-	5.30, poor	-	-
(*Fast*)	5.22, poor	-	-	-	-

Table 5.5: Table summarizes the outcome of the predictions reported in the indicated figures based on the criteria listed in the equation 5.5

	Large range of head movements (Table's number, evaluation)				
	Raw				
	PLS		NARX		
	PVC	cloth	PVC	cloth	cloth (Less data)
Subject 1	C.5, poor	C.16, poor	C.25, poor	C.34, poor	(qualitative)
Subject 2	C.6, poor	C.17, poor	C.26, poor	C.35, poor	(qualitative)
Subject 3	C.7, poor	C.18, poor	C.27, poor	5.33, poor	(qualitative)
(*Fast*)	-	-	-	-	-
Subject 4	-	C.11, poor	-	C.37, poor	(qualitative)
Subject 5	-	C.20, poor	-	C.38, poor	(qualitative)
Subject 6	C.8, poor	-	C.28, poor	-	-
(*Fast*)	-	-	-	-	-

Table 5.6: Table summarizes the outcome of the predictions reported in the indicated tables based on the criteria listed in the equation 5.5

5.3.1 Predicting head motion using the linear regression method (raw data)

Raw data acquired using the PVC set-up (Subject 3) were used to test predictions made using the linear method trained on small and large ranges of movements. Figures 5.17 and 5.19 and Tables C.7, C.3 report results for Subject 3. The analysis was repeated considering data obtained using the cloth holder set-up (Figures 5.23 and 5.25, Tables C.13 and C.18).

Overall, the linear method did not perform well on raw real data over for either the set-ups. Predictions of the whole range of movements were poor for all the subjects (Figures C.2-PVC, C.4-cloth). Better results were obtained by training the method over the small range of movements only (Figures 5.17-PVC, 5.23-cloth).

PVC set-up and PLS method: comparing results between Subjects 3 and 6.

Comparison of the results obtained from Subject 3 and Subject 6 could be made for the PVC set-up. In the case of prediction (and training) of the linear method on small head movements, the results on Subject 3 (Figure 5.17, Table C.3) were better than those obtained from Subject 6 (Figure 5.18, Table C.4). The most likely explanation for this finding is that the range of movements are slightly larger for Subject 3 and there is a smaller average distance between the head and the probes (as the head volume of Subject 3 is larger than that of Subject 6, respectively $4.1 \cdot 10^{-3}\ m^3$ and $3.7 \cdot 10^{-3}\ m^3$,see Table 4.2). Opposite results were obtained for the training on large head movements as Subject 6 performed a larger range of head movements in the relevant motion conditions (Figure 5.20, Table C.8).

A second possible explanation of the results relates to the rate of sampling of movements (Figure 5.16, Table B.14). All subjects were asked to perform the same movements but the rate of movement varied across subjects and experiments on the same subject. Predictions derived from data measured with "faster" movements are reported in Figure 5.21 (Subject 3) and Figure 5.22 (Subject 6) and in both cases the results were worse than the "normal" speed movements (Figure 5.19, Table C.7 for Subject 3 ; Figure 5.18, Table C.4 for Subject 6). While performing faster movements, Subject 3 also reduced the extent of the movement (so reducing the greatest proximity of the head to the probes and thus the strength of the magnetic field changes, and therefore the accuracy of prediction), while Subject 6 was more consistent in the extent of movement which they made. Considering that the sampling frequency of the magnetic field camera is constant ($\frac{1}{0.150} \approx 6.7\ Hz$), the faster the movements, the bigger the change in sampled magnetic field between consecutive measurements and the accuracy of the relationship between magnetic field change and head position is consequently reduced.

The analysis of the effect of the rate of head movement also highlights the fact that subjects may perform large head movements at a rate that is close to the respiration frequency (Table 5.7) and so magnetic field changes from two different sources (head motion, chest expansion) will happen at the same frequency. This may be an issue to consider as the pre-processing of magnetic field data aims to reduce the influence of physiological noise by removing the harmonics that carry magnetic field changes at the respiration frequency.

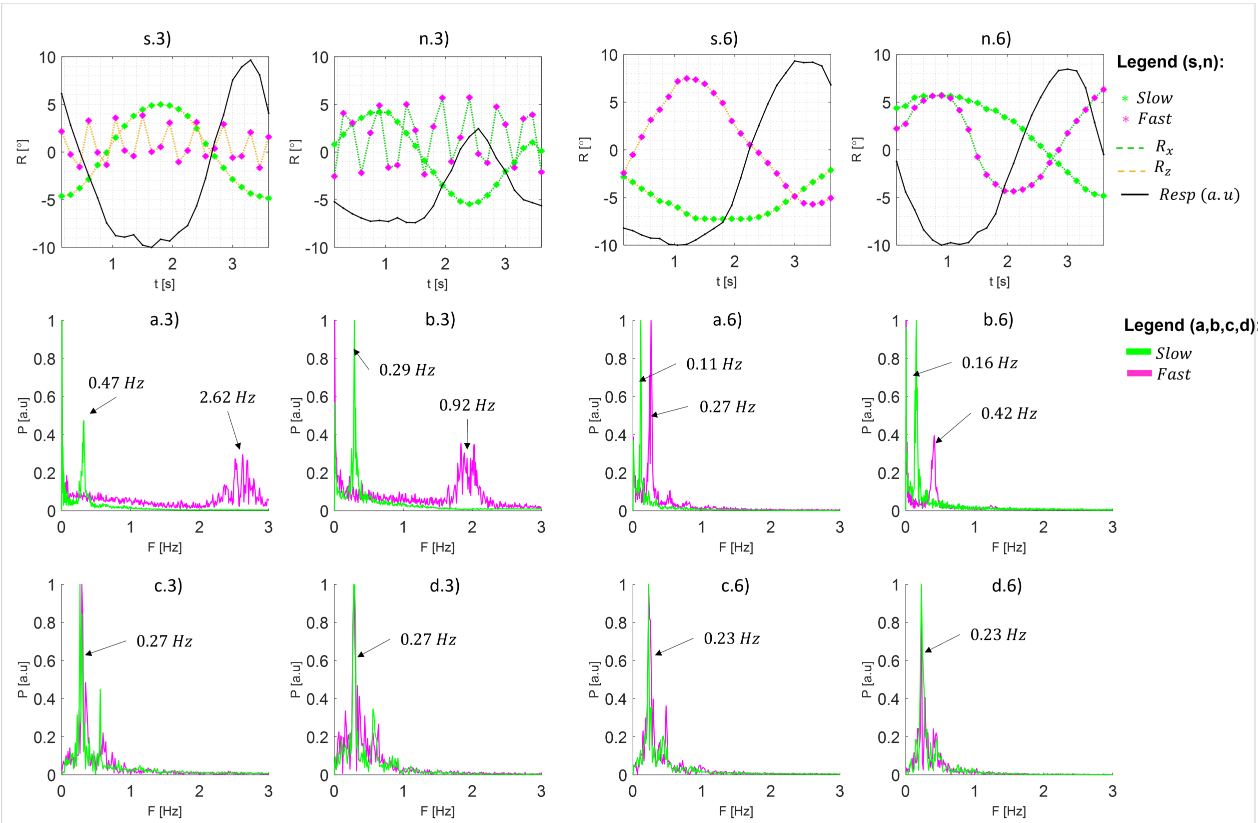

Figure 5.16: *Sampling rate of movements.* Plots reports the predominant head motion parameters for head (s.3, s.6) shake and (n.3, n.6) head nod condition (R_z and R_x, orange and green dashed lines respectively, in the scanner frame) performed at two different frequencies (Fast, Slow, tagged with green and pink dots respectively) for two subjects (3, 6) along with one respiration cycle (black). Motion and magnetic field data are reported in Table B.14. Frequency of the motion and the respiration are reported. (a) reports the frequency spectrum of the predominant head motion parameter at head shake conditions for Subject 3 (a.3) and 6 (a.6). (b) reports the frequency spectrum of the predominant head motion parameter at head nod conditions for Subject 3 (b.3) and 6 (b.6). (c) and (d) reports the frequency spectrum of the respiration signal for Subject 3 (c.3, d.3) and 6 (c.6, d.6) acquired while subjects performed the head movements listed above.

	PVC			**cloth**		
	Rest	**Shake**	**Nod**	**Rest**	**Shake**	**Nod**
Subject 1	0.30	0.43	0.30	0.24	0.49	0.49
Subject 2	0.33	0.49	0.49	0.21	0.54	0.24
Subject 3	0.28	0.32	0.29	0.23	0.72	0.20
Subject 4	–	–	–	0.28	0.34	0.32
Subject 5	–	–	–	0.23	0.50	0.76
Subject 6	0.24	0.11	0.16	–	–	–

Table 5.7: *Frequency of head movements.* The Values of the frequency of movements for all the volunteers and head movements performed. Feet-wiggling produces small random movements with a uniformly distributed frequency spectrum. So, it is not possible to identify a unique frequency to characterize the activity.

Cloth probe holder and PLS method: comparing results between Subjects 3 and 5.
Comparison of results from Subject 3 and Subject 5 could be made for the cloth probe holder set-up. In the case of prediction (and training) of the linear method on small head movements, results on Subject 3 were worse than those obtained from Subject 5 (Figure 5.24, Table C.15). The reason is that the extent of movements is slightly larger over the whole head motion parameters and this reduces the distance between the head and the probes (as head volume of Subject 3 is slightly bigger than that of the Subject 5, see Table 4.2). Predictions of large head movements were poor in both cases. Results for Subject 5 are reported in Figure 5.26 and Table C.20.

Comparing results on small head movements between the set-ups (Subject 3).
Comparison of results obtained from Subject 3 from the two different probe holders could be made by considering information in Figure 4.9. Data are reported in Table B.10. A larger change in magnetic field is found when using the PVC support because the distance between the head and probes varies more significantly over probes and head motion conditions. In fact, we see that the prediction obtained using the PLS method for data acquired using PVC probes holder (Figure 5.17) is better than that obtained using the cloth holder (Figure 5.23). In conclusion, for a similar range of movements and similar head-probe distances, we can see that the spatial distribution over which the field is sampled relative to the head motion plays a role.

5.3.2 Predicting head motion using the non-linear regression method (raw data)

Raw data acquired using the PVC set-up (Subject 3) were used to test the predictions made using the $non-linear$ method trained on data acquired with small and large ranges of movements. Figures 5.27 and 5.29 and Tables C.23, C.27 report results for Subject 3. The analysis was repeated considering data obtained using the cloth probe holder set-up (Figures 5.31 and 5.33, Tables C.31 and C.36).

Overall, the $non-linear$ method performed similarly to the linear one on raw real data over both set-ups. Predictions of the whole range of movements were worse (Figures C.6-PVC, C.8-cloth) than results obtained when training the method over the small range of movements only (Figures C.5-PVC, C.7-cloth) for all the subjects. Also, results on small head movements are better than those obtained with the linear method for the same data acquisition conditions.

PVC set-up and NARX method: comparing results between Subjects 3 and 6.

Comparison of results obtained from Subjects 3 and 6 could be made for the PVC set-ups. In the case of prediction (and training) of the non-linear method on small head movements, the results from Subject 3 (Figure 5.27, Table C.23) were better than this obtained from Subject 6 (Figure 5.28, Table C.24), but in both cases, the results were relatively poor. Predictions of large head movements were poor for both subjects (Subject 3: Figure 5.29, Table C.27, Subject 6 Figure 5.30, Table C.28).

Cloth probe holder and NARX method: comparing results between Subjects 3 and 5.

Comparison of results obtained from Subjects 3 and 5 could be made for the cloth probe holder. In the case of prediction (and training) of the linear method on small head movements, the results on Subject 3 (Figure 5.31, Table C.31) were worse than those obtained from Subject 5 (Figure 5.32, Table C.33) as for the linear method. A possible explanation for this finding is that the range of movements was larger for Subject 5 than for Subject 3. Predictions of large head movements were poor for both subjects (Subject 3: Figure 5.33, Table C.36, Subject 6 Figure 5.34, Table C.38).

Comparing results on small head movements between the set-ups (Subject 3).

A comparison of the results obtained from Subject 3 using the two different probe holder set-ups could be made considering information in Figure 4.9. The data are also reported in Table B.10. The smaller change in magnetic field obtained when using the cloth support occurs because the distance between the head and probes doesn't vary significantly for any probes for the motion conditions considered. In fact, comparing Figures 5.27 and 5.31, for similar range of movements and similar head-probe distances, where the field is sampled relative to the head motion influences the data and so the results.

5.3.3 Predicting head motion using the non-linear regression method (pre-processed data)

Analysis of head motion predictions derived from real data recorded with small and large ranges of head movements over the two set-ups and subjects indicate that the non-linear method in the cloth configuration performs best, in particular for the small head movements. In this section, this optimal choice of set-up and regression method were applied on pre-processed data to test the effect of spatial filtering on real data.

Overall, the non-linear method performed well on pre-processed real data over the volunteers (Figures C.10, Subject 3 5.35, Subject 5 5.36), but there is not a noticeable improvement in the accuracy compared to the results obtained on raw data (Figure C.7, Subject 3 5.31, and Figure 5.32, Subject 5). Further evaluation of the prediction accuracy was therefore made in terms of the timing necessary for training the network before obtaining a one time-step prediction. The number of data needed for prediction and training were also evaluated.

Timing of the prediction process. The time necessary to train a neural network depends on a few non-independent factors. First, it depends on the architecture chosen: a simpler architecture should require less time to be trained. In the case of the raw data, the architecture was always set by the number of neurons in the hidden layer which was equal to the number of channels of the magnetic field camera (16), the number of neurons in the hidden layer (arbitrarily chosen as 30, more details Section in Appendix A) and the number of neurons in the output layer, which was equal to the number of head motion parameters (6). In the case of pre-processed data, the number of neurons in the input layer is determined by the outcome of the feature selection (as explained in Section 5.1.1). The random initialization of the neurons' weights will also influence the time necessary for the training. For unfavourable values of the initial weights, the back-propagation algorithm used to optimize the weights of the neurons may take longer (e.g. because it meets a local minimum of the best fit function or goes into over-training). Numerical values of the weights of the trained network will influence the algebraic elaboration of the prediction. Last, the number of data points used for the training will strongly influence the time needed for the training as the number of iterations (to complete an epoch) necessary to train the network increases with the number of data points. The range of the head movements will also influence the time necessary for the training.

Table 5.8 reports the time (in s) necessary to train the best neural network from the more than 10 neural networks that were trained (Appendix A) and the average time (in ms) to calculate one prediction over all the subjects (for the cloth probe holder) and for raw, pre-processed data and large/small range of head motion. Comparing results for the small and large ranges of head motion, networks trained on large head movements take longer to be trained and to produce a prediction and also give less accurate predictions (Tables 5.5 and 5.3 and Figures C.8 and C.7). This reflects the larger range of field changes for large head motion (Tables B.8 to B.12) that lead to more time needed for training and more time to compute the prediction. When comparing small head motion in the case of raw and pre-processed data, the time needed for training does not differ significantly, while the time for the prediction is reduced by one order of magnitude.

Varying the size of the training data-set. Table 5.9 reports the time (in s) necessary to train the best neural network chosen from the more than 10 neural networks trained (Appendix A) and the average time (in ms) to calculate one prediction over all the subjects (cloth probe holder) and for raw, pre-processed data and large/small range of head motion. The number of data points used for the training was significantly reduced compared to the number of data points used for the PVC set-up (compare values reported in Tables 5.1.3 and 5.1.3). This, other than reducing the time necessary for the training, would also test whether the network went into over-training (especially for large head movements as predictions were poor). Predictions on pre-processed data (Figure C.11) were poor for all the head motion parameters.

	Raw					**Pre-processed**		
		Small		**Large**			**Small**	
	A	**T** [s]	**P** [ms]	**T** [s]	**P** [ms]	**A**	**T** [s]	**P** [ms]
Subject 1	$13-30-6$	87	0.82	120	0.11	$7-30-6$	100	0.09
Subject 2	$13-30-6$	67	1.47	179	0.08	$11-30-6$	82	0.09
Subject 3	$13-30-6$	57	1.11	182	0.08	$10-30-6$	56	0.08
Subject 4	$13-30-6$	91	1.05	149	0.08	$10-30-6$	53	0.09
Subject 5	$13-30-6$	63	1.25	220	0.08	$7-30-6$	47	0.09

Table 5.8: The table reports the architecture (A) of the networks (number of neurons in the input - hidden - output layer), time in seconds to train the best network of the 10 networks trained (T [s]), time in milliseconds to obtain 1 step-ahead prediction (P [ms]) for raw and pre-processed data, over all the subject, for the cloth probe holder set-up. The number of data points used for training were as reported in Table 5.1.3.

	Raw					**Pre-processed**		
		Small		**Large**			**Small**	
	A	**T** [s]	**P** [ms]	**T** [s]	**P** [ms]	**A**	**T** [s]	**P** [ms]
Subject 1	$13-30-6$	11	0.26	24	3.52	$7-30-6$	10	0.25
Subject 2	$13-30-6$	13	0.24	30	2.21	$11-30-6$	10	0.26
Subject 3	$13-30-6$	22	0.12	26	1.53	$10-30-6$	12	0.26
Subject 4	$13-30-6$	10	0.24	35	1.98	$10-30-6$	9	0.25
Subject 5	$13-30-6$	15	0.26	27	0.25	$7-30-6$	12	0.25

Table 5.9: Table reports the architecture (A) of the networks (number of neurons in the input - hidden - output layer), time in seconds to train the best network from the 10 networks trained (T [s]), time in milliseconds to obtain 1 step-ahead prediction (P [ms]) for raw and pre-processed data, over all the subject, for the cloth probe holder. The number of data values used for training were equal to the number of data values used to train the linear method (Table 5.1.3).

5.3.4 Plots of predictions shown in section 5.3

PVC set-up and PLS method (Subjects 3 and 6).

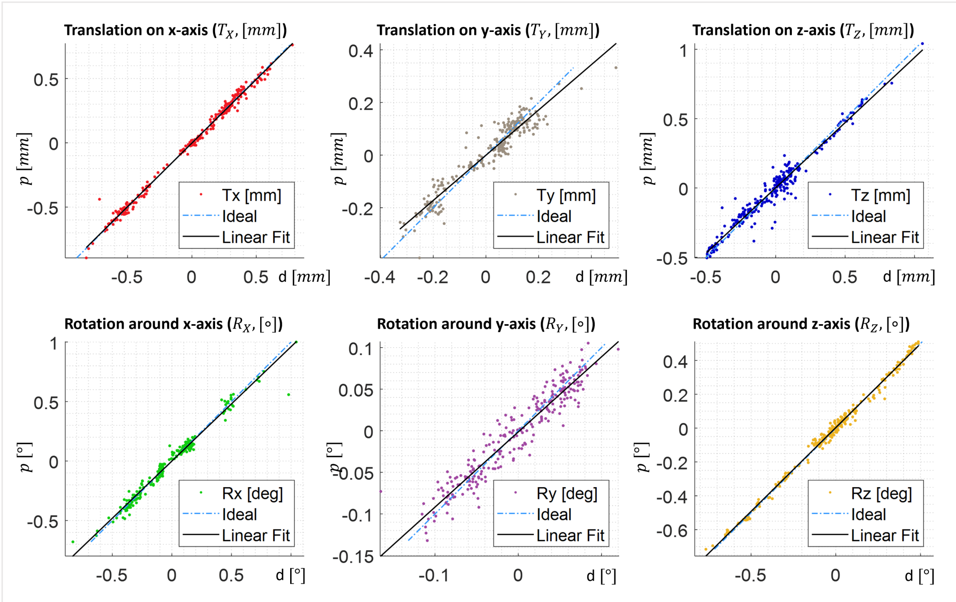

Figure 5.17: The figure shows results obtained for *small* head movements, sampled using the *PVC* probe-holder set-up for *Subject* 3, using *rawdata* for training the *linear* regression method (Table 5.1.3). Prediction results are *good* (equation 5.5). Statistical evaluation of the results is reported in Table C.3.

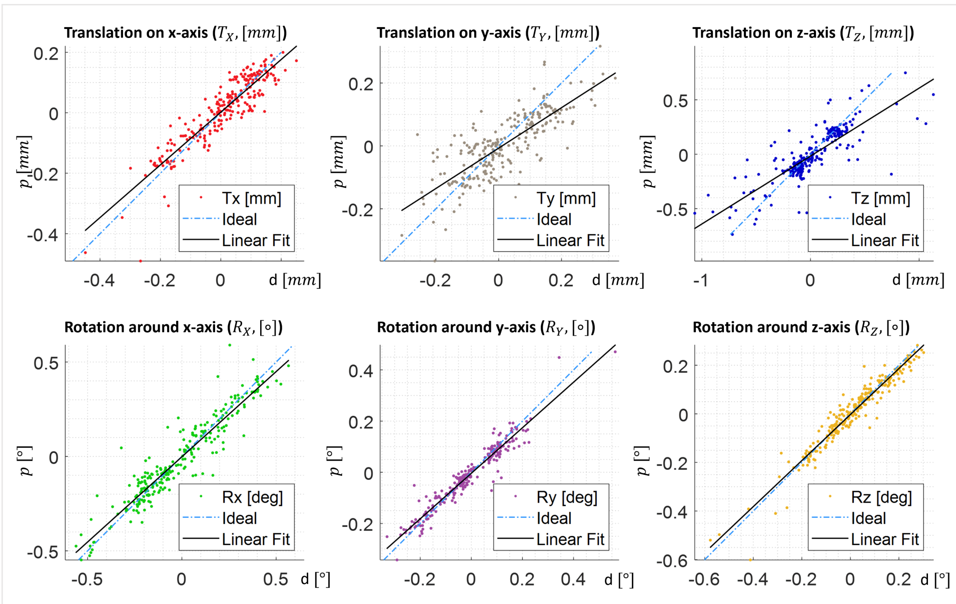

Figure 5.18: The figure shows results obtained for *small* head movements, sampled using the *PVC* probe-holder set-up for *Subject* 6, using *raw* data for training the *linear* regression method (Table 5.1.3). Prediction results are *poor* (equation 5.5). Statistical evaluation of the results is reported in Table C.4.

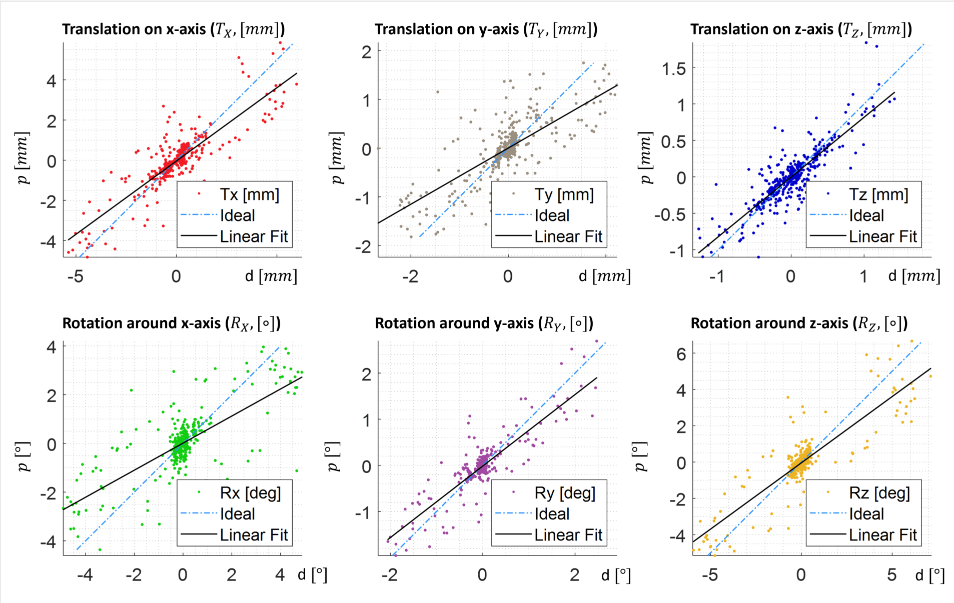

Figure 5.19: The figure shows results obtained for *large* head movements, sampled using the *PVC* probe-holder set-up for *Subject* 3, using *raw* data for training the *linear* regression method (Table 5.1.3). Prediction results are *poor* (equation 5.5). Statistical evaluation of the results is reported in Table C.7.

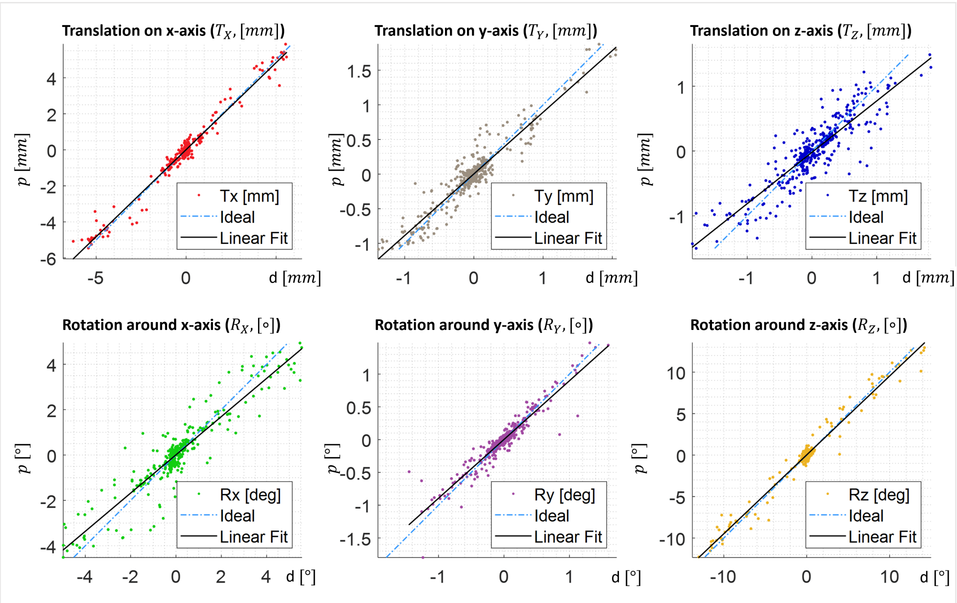

Figure 5.20: The figure shows results obtained for *large* head movements, sampled using the *PVC* probe-holder set-up for *Subject* 6, using *raw* data for training the *linear* regression method (Table 5.1.3). Prediction results are *poor* (equation 5.5). Statistical evaluation of the results is reported in Table C.8.

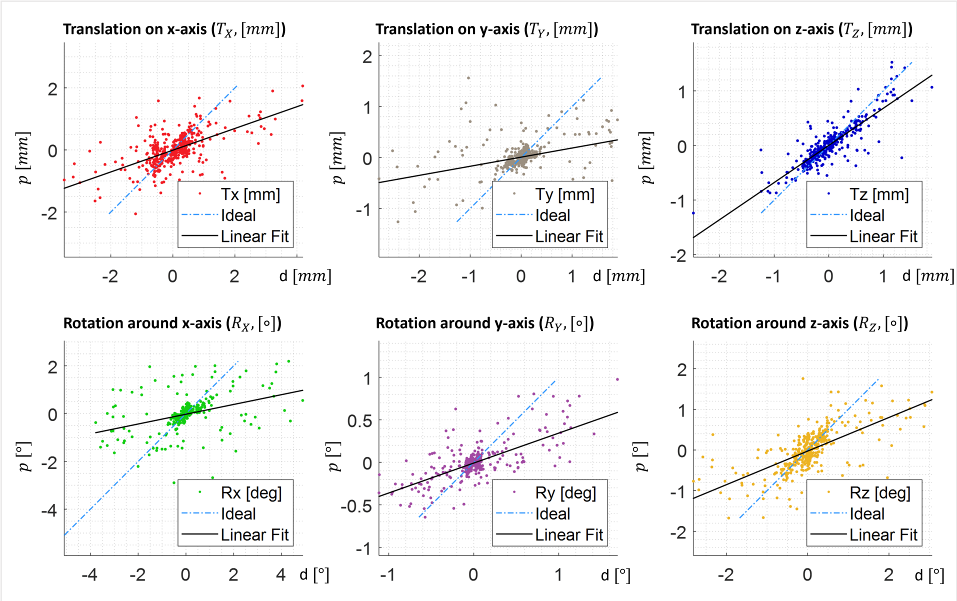

Figure 5.21: The figure shows results obtained for *fastlarge* head movements, sampled using the *PVC* probe-holder set-up for *Subject* 3, using *raw* data for training the *linear* regression method (Table 5.1.3). Prediction results are *poor* (equation 5.5). Statistical evaluation of the results is reported in Table C.9.

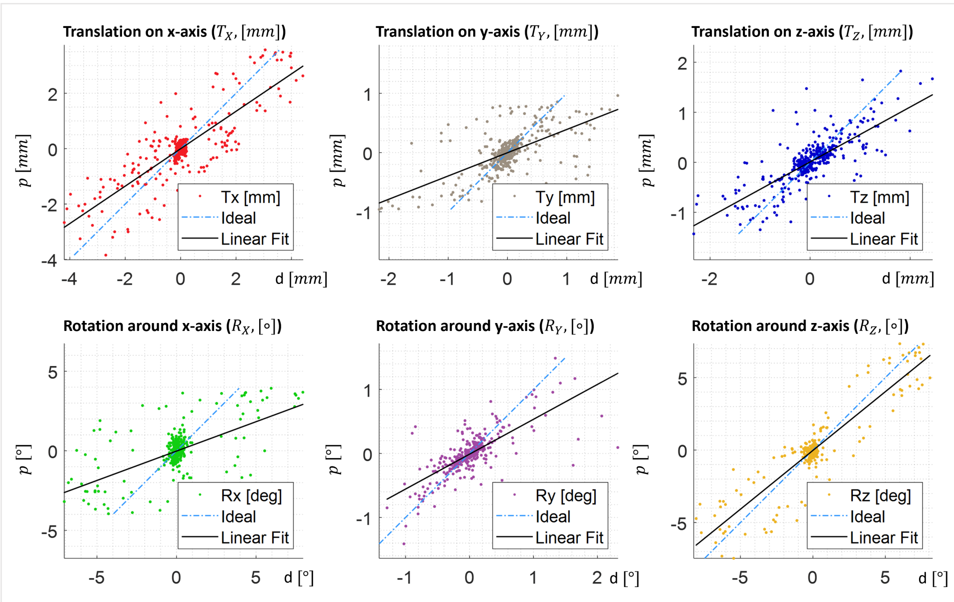

Figure 5.22: The figure shows results obtained for *fastlarge* head movements, sampled using the *PVC* probe-holder set-up for *Subject* 6, using raw data for training the *linear* regression method (Table 5.1.3). Prediction results are *poor* (equation 5.5). Statistical evaluation of the results is reported in Table C.10.

Cloth probe holder and PLS method (Subject 3 and 5).

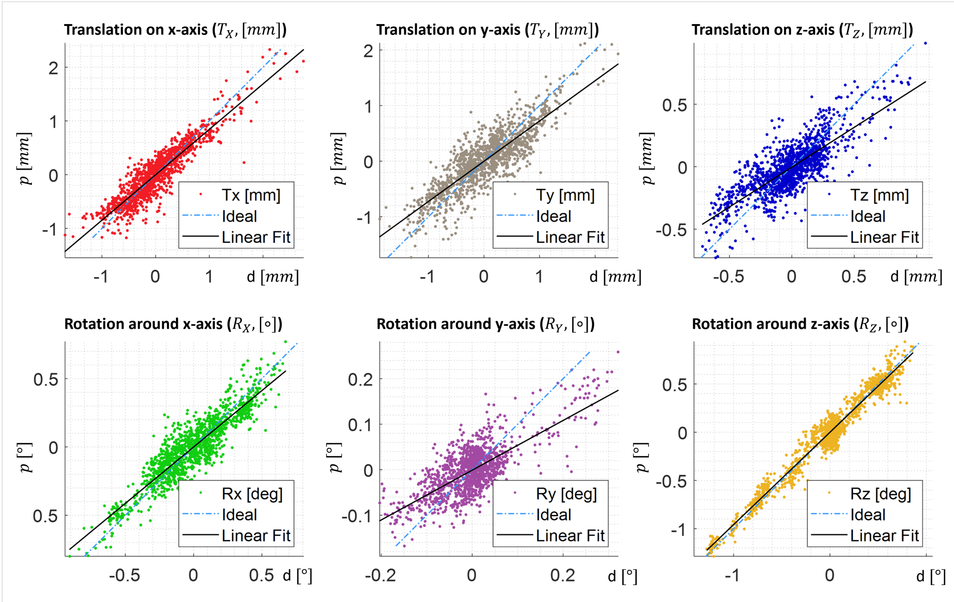

Figure 5.23: The figure shows results obtained for *small* head movements, sampled using the *clothprobe − holder* set-up for *Subject* 3, using *raw* data for training the *linear* regression method (Table 5.1.3). Prediction results are *poor* (equation 5.5). Statistical evaluation of the results is reported in Table C.13.

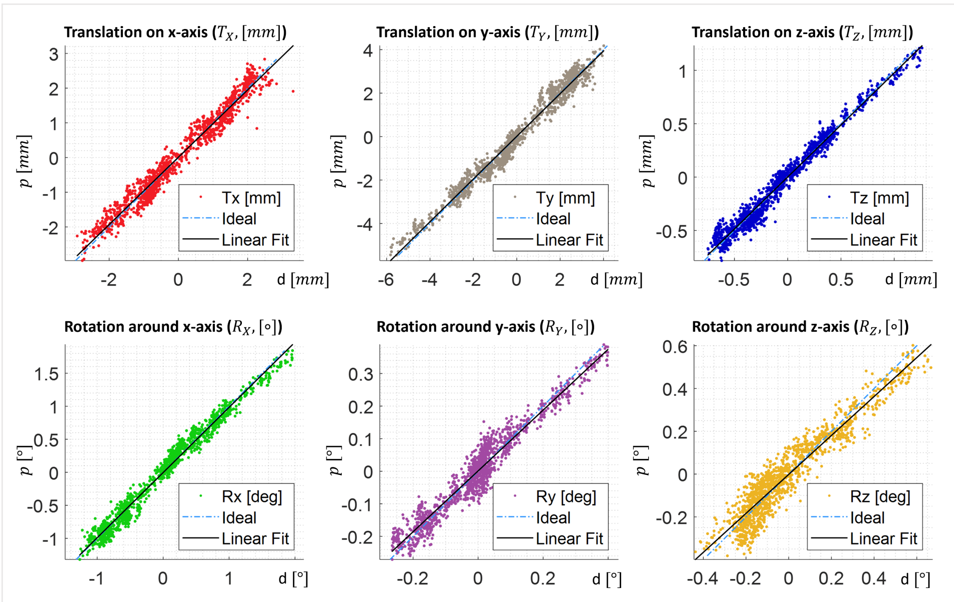

Figure 5.24: The figure shows results obtained for *small* head movements, sampled using the *clothprobe − holder* set-up for *Subject* 5, using *raw* data for training the *linear* regression method (Table 5.1.3). Prediction results are *poor* (equation 5.5). Statistical evaluation of the results is reported in Table C.15.

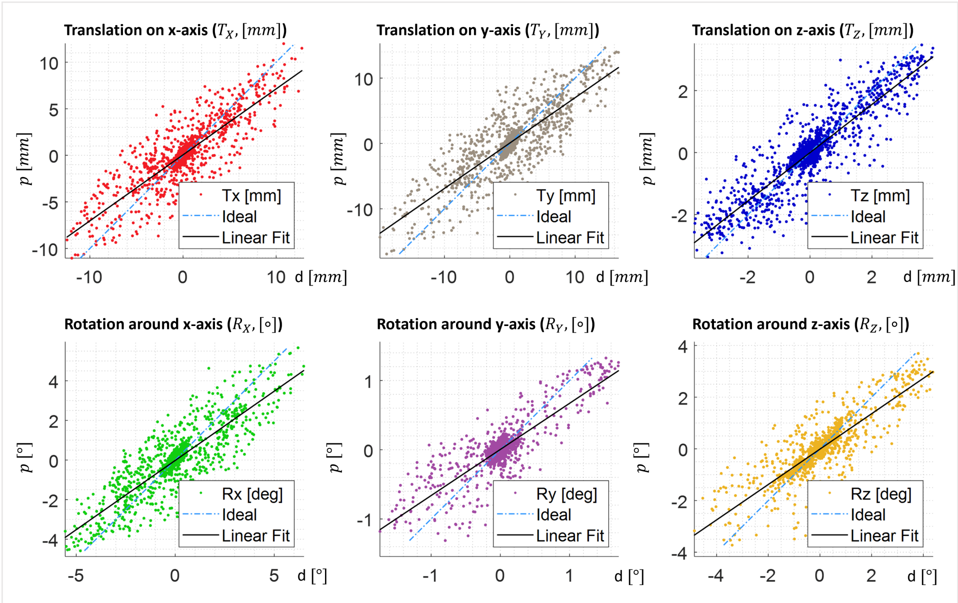

Figure 5.25: The figure shows results obtained for *large* head movements, sampled using the *clothprobe − holder* set-up for *Subject* 3, using raw data for training the *linear* regression method (Table 5.1.3). Prediction results are *poor* (equation 5.5). Statistical evaluation of the results is reported in Table C.18.

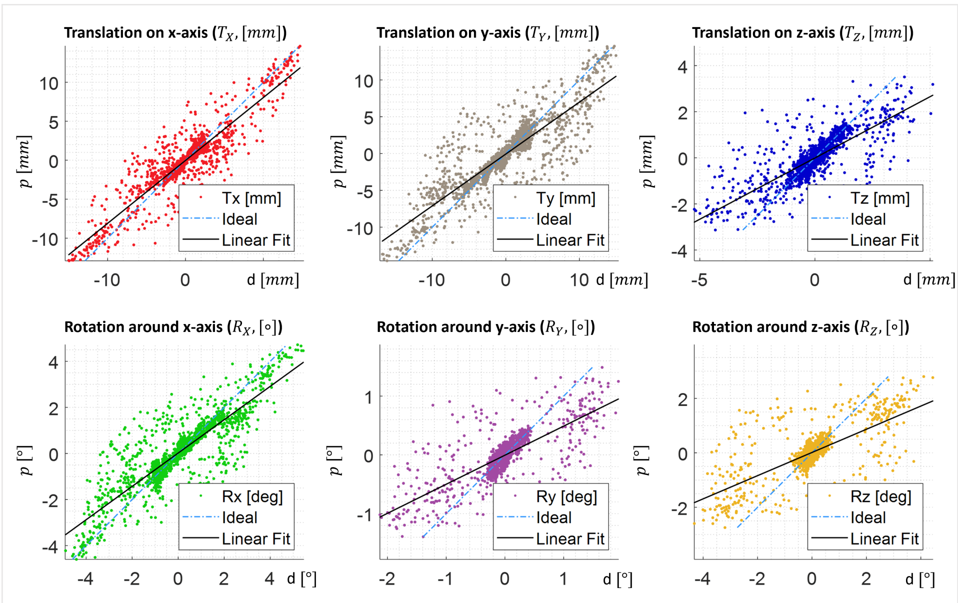

Figure 5.26: The figure shows results obtained for *large* head movements, sampled using the *clothprobe − holder* set-up for *Subject* 5, using *raw* data for training the *linear* regression method (Table 5.1.3). Prediction results are *poor* (equation 5.5). Statistical evaluation of the results is reported in Table C.20.

PVC set-up and NARX method (Subject 3 and 6).

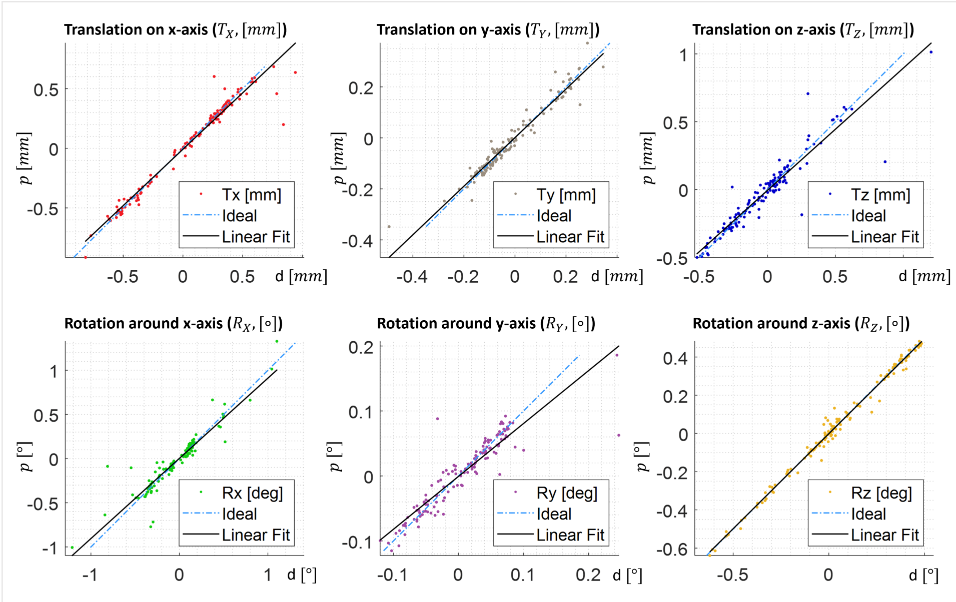

Figure 5.27: The figure shows results obtained for *small* head movements, sampled using the *PVC* probe-holder set-up for *Subject* 3, using *raw* data for training the *non − linear* regression method (Table 5.1.3). Prediction results are *poor* (equation 5.5). Statistical evaluation of the results is reported in Table C.23.

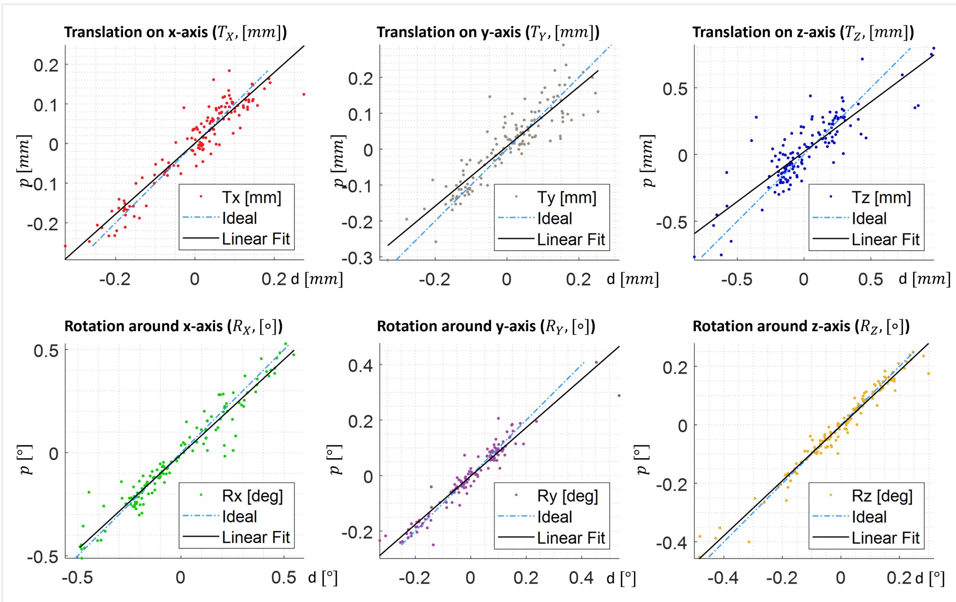

Figure 5.28: The figure shows results obtained for *small* head movements, sampled using the *PVC* probe-holder set-up for *Subject* 6, using *raw* data for training the *non − linear* regression method (Table 5.1.3). Prediction results are *poor* (equation 5.5). Statistical evaluation of the results is reported in Table C.24.

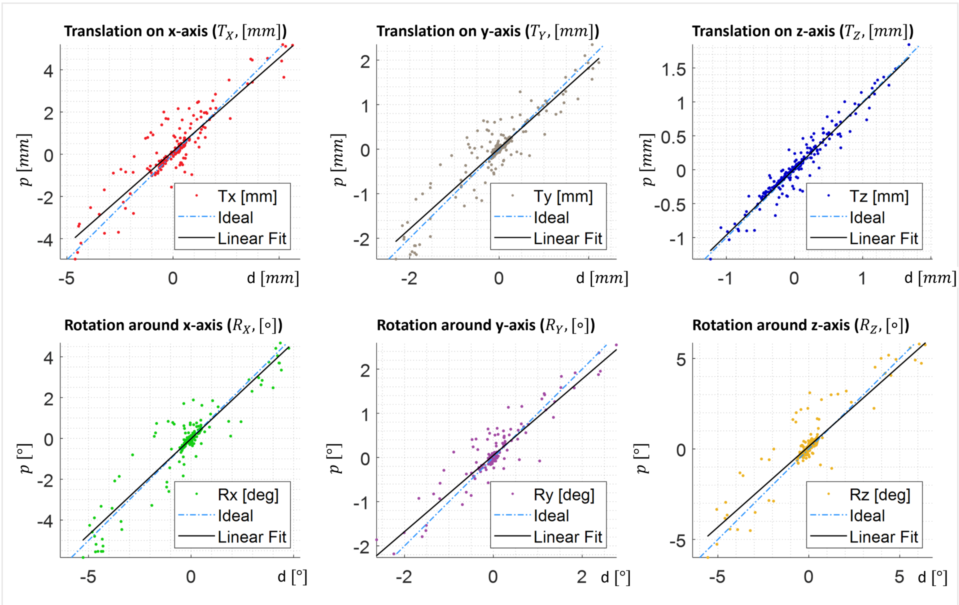

Figure 5.29: The figure shows results obtained for *large* head movements, sampled using the *PVC* probe-holder set-up for *Subject* 3, using *raw* data for training the *non − linear* regression method (Table 5.1.3). Prediction results are *poor* (equation 5.5). Statistical evaluation of the results is reported in Table C.27.

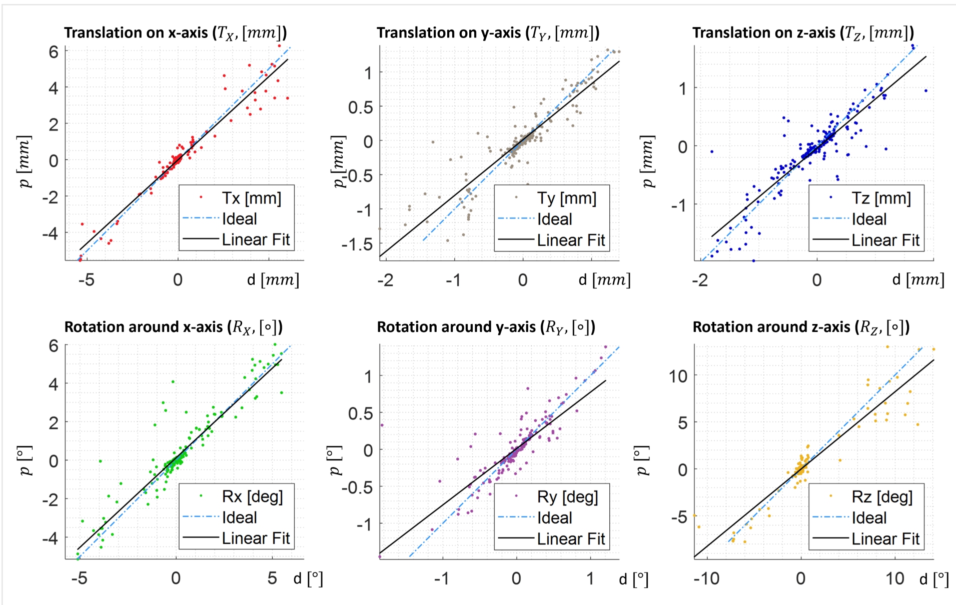

Figure 5.30: The figure shows results obtained for *large* head movements, sampled using the *PVC* probe-holder set-up for *Subject* 6, using raw data for training the *non − linear* regression method (Table 5.1.3). Prediction results are *poor* (equation 5.5). Statistical evaluation of the results is reported in Table C.28.

Cloth probe holder and NARX method (Subject 3 and 5).

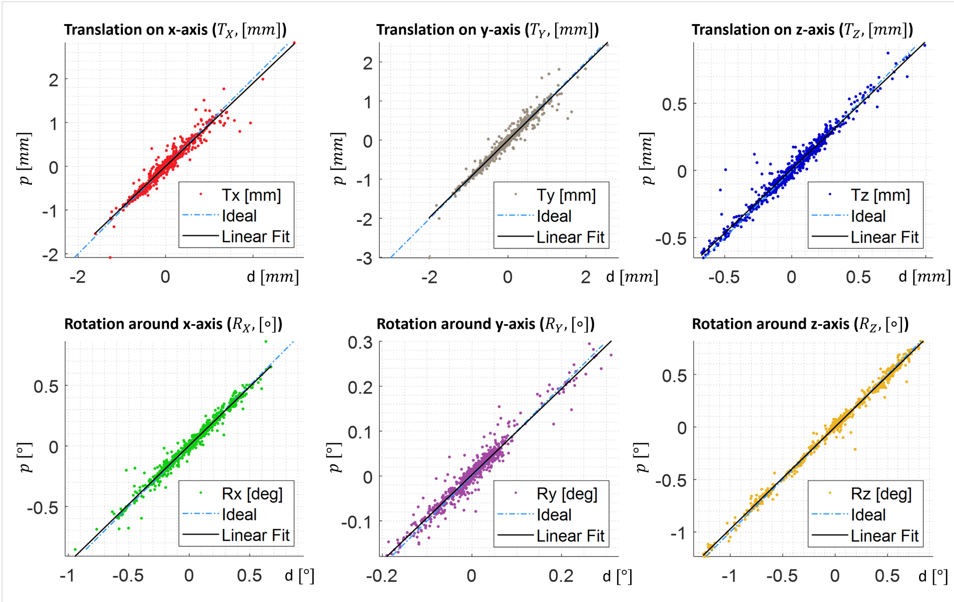

Figure 5.31: The figure shows results obtained for *small* head movements, sampled using the *clothprobe − holder* set-up for *Subject* 3, using *raw* data for training the *non − linear* regression method (Table 5.1.3). Prediction results are *poor* (equation 5.5). Statistical evaluation of the results is reported in Table C.31.

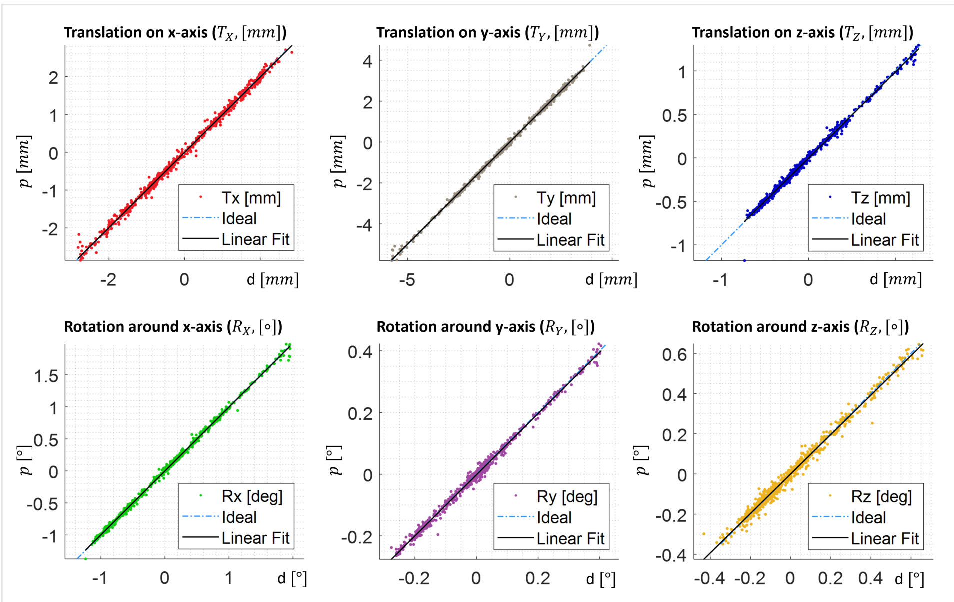

Figure 5.32: The figure shows results obtained for *small* head movements, sampled using the *cloth* probe-holder set-up for *Subject* 5, using *raw* data for training the *non − linear* regression method (Table 5.1.3). Prediction results are *good* (equation 5.5). Statistical evaluation of the results is reported in Table C.33.

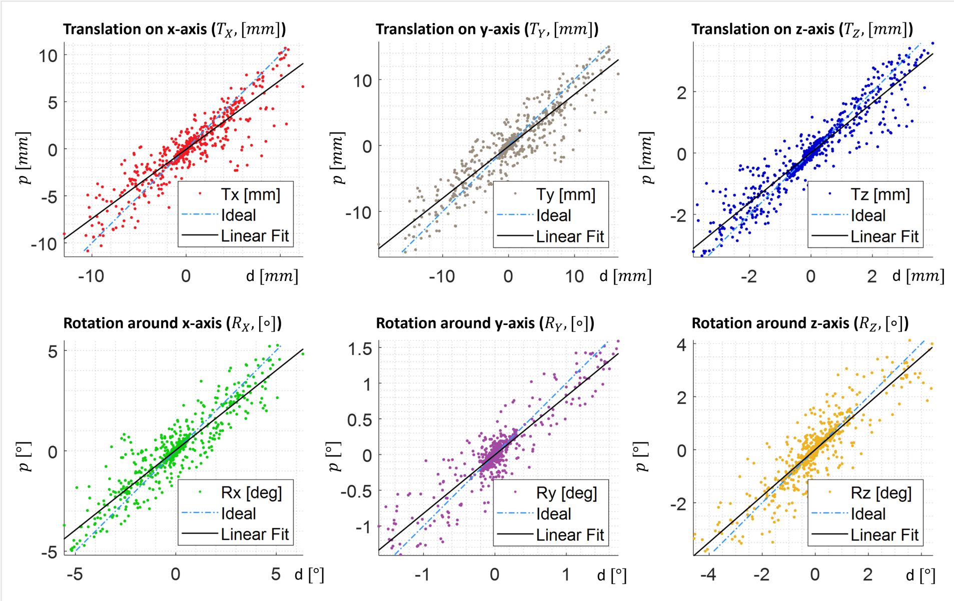

Figure 5.33: The figure shows results obtained for *large* head movements, sampled using the *cloth* probe-holder set-up for *Subject* 3, using *raw* data for training the $non - linear$ regression method (Table 5.1.3). Prediction results are *poor*equation 5.5). Statistical evaluation of the results is reported in Table C.36.

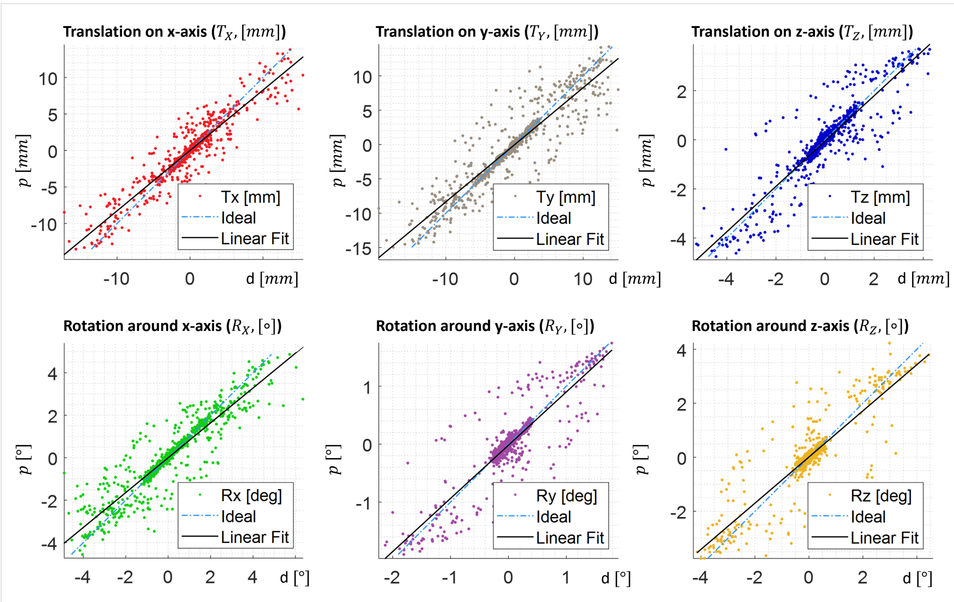

Figure 5.34: The figure shows results obtained for *large* head movements, sampled using the *cloth* probe-holder set-up for *Subject* 5, using *raw* data for training the $non - linear$ regression method (Table 5.1.3). Prediction results are *poor* (equation 5.5). Statistical evaluation of the results is reported in Table C.38.

Testing the pre-processing.

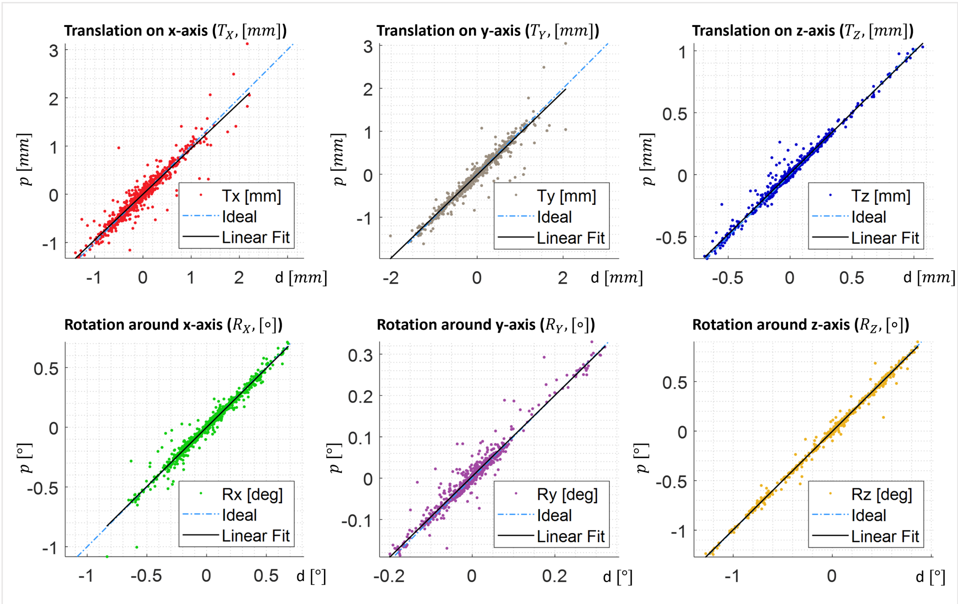

Figure 5.35: The figure *shows* results obtained for *small* head movements, sampled using the *cloth* probe-holder set-up for *Subject* 3, using *pre−processed* data for training the *non−linear* regression method (Table 5.1.3). Prediction results are *poor* (equation 5.5). Statistical evaluation of the results is reported in Table C.41.

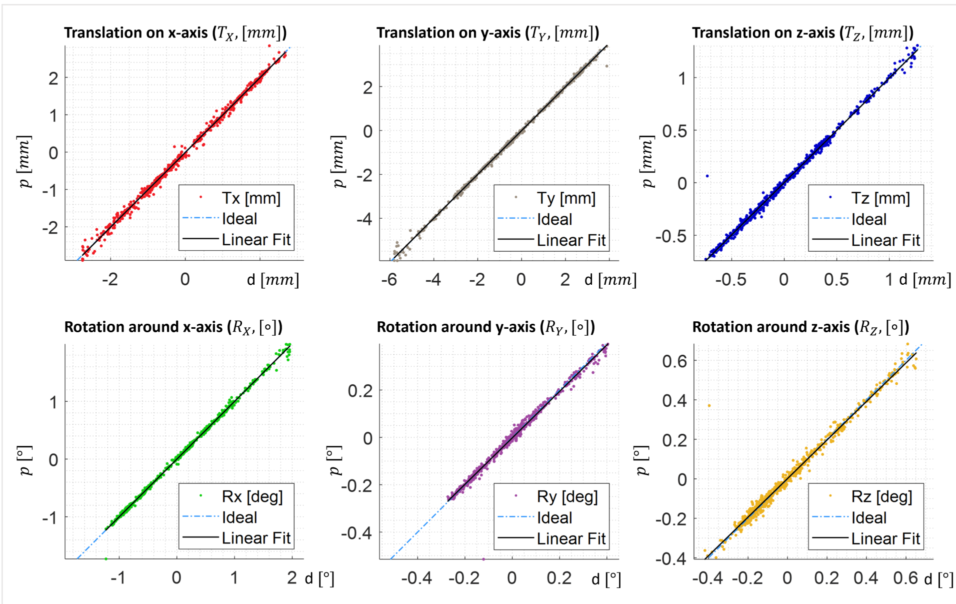

Figure 5.36: The figure shows results obtained for *small* head movements, sampled using the *cloth* probe-holder set-up for *Subject* 5, using *pre−processed* data for training the *non−linear* regression method (Table 5.1.3). Prediction results are *good* (equation 5.5). Statistical evaluation of the results is reported in Table C.43.

5.4 Conclusion

Experimental magnetic field data acquired using different set-ups have been characterised (Subsection 4.2.2). Predictions of head motion parameters obtained using both regression methods have been made using data from all of the 6 subjects involved in the measurements performed without simultaneous scanning (Section 5.3). By comparing results between subjects, set-ups, and regression methods, the best pipeline to perform accurate predictions on small range of head motion is to pre-processed magnetic field data and to train the non-linear regression method. The code is reported in Appendix D.

In the future, the use of simulated data (instead of real data) to train the regression method might provide a further development of the technique. Improvements on the simulation program would involve further optimisation (e.g. parallel programming) to reduce the time necessary to produce a ≈ 1000 data point time series (equal to ≈ 2 hours with the system used) and a better approximation of the magnitude of the data (e.g. by acquiring the MR image to obtain the head model and the probe positions in the same scanning session and frame of reference).

5.4.1 Simulated data

This chapter has reported the analysis of synthetic magnetic field data which have been shown to be coherent enough with real data to be used to meet the aims of this study (Section 4.1.1). Changes in extra-cranial magnetic field mainly depend on head-probe distances and relative positions (Section 4.2). The mathematical relationship between head motion parameters and extra-cranial magnetic field changes has been studied also considering the effect of noise sources. Magnetic field changes due to respiration (Section 4.3) can be successfully ameliorated with the proposed spatial filter and the filtered signal can then be used to predict respiration-like signals in a non-contact fashion (Figure 4.5). The prediction of head motion parameters can be performed using either the linear or the non-linear regression method (Section 5.2.2). The use of simulations allows predictions to be performed using noiseless magnetic field data due to head motion only (Figures 5.8, 5.10, 5.11, 5.12). This has allowed the identification of the non-linear method as the best method to perform predictions (Figure 5.13). Then, the robustness of the prediction has been tested by adding (and filtering) noise sources (Figures 5.14, 5.15). Conclusions and observations on results obtained on simulated data form a starting point for analyses on real data presented in Chapter 5.

			Simulated		Real	
Support	**Range**	**Method**	**Data**	**Figure**	**Data**	**Figure**
Cloth	Large	PLS	ΔB_{Head}	5.8	ΔB	5.26
Cloth	Small	PLS	ΔB_{Head}	5.10	ΔB	5.24
Cloth	Large	NARX	ΔB_{Head}	5.11	ΔB	5.34
PVC	Large	NARX	ΔB_{Head}	5.12	–	–
Cloth	Small	NARX	ΔB_{Head}	5.13	–	–
Cloth	Small	NARX	ΔB	5.14	ΔB	5.32
Cloth	Small	NARX	ΔB (pre-processed)	5.15	ΔB, (pre-processed)	5.36

Table 5.10: The table lists the data analysis that involved data (real or simulated) from Subject 5 for various set-ups (Support), range of head movements (Range), regression methods (Method), noise level on the data (Data) in agreement with Figure 5.6. Figures 5.14 and 5.32, Figures 5.15 and 5.36 could be used to test the effectiveness of the results.

5.4.2 Comparison between predictions made using simulated and real data

The aim of generating synthetic data was not to accurately reproduce real extra-cranial magnetic field changes, but to obtain a time series that would allow the main features of the phenomenon to be studied in a controlled environment (Figure 5.6). These are: changing coherently with head motion (Figures 4.4 and 4.5), head-probe distance (Figures 4.4 and 4.5), influences of magnetic field changes due to chest expansion (Figure 5.7) and general background noise level.

As all these parameters can be controlled in the simulated environment, simulated data have been further used as a proof of concept to identify the best way to obtain good predictions of head motion parameters. The simulated data that were considered were produced from one data series, one head model (Subject 5), and considering probe positions in a Cloth-like set-up. PVC-like sampling was used only to further test the influence of probes displacements in one case.

Table 5.10 lists the analysis made either for simulated or real data. At first, simulated data generated by the simpler simulation model (where magnetic field changes are due only to head motion) and the linear regression method have been used to compare predictions for large and small ranges of head movement. These results (Figures 5.8 and 5.10) cannot be compared with similar results obtained with real data (Figures 5.26 and 5.24) because noise sources have not been considered. Similar considerations hold for Figures 5.11 and 5.34. Subject 5 did not attend a scanner session when the PVC holder was in use, so Figure 5.12 does not have a real data counterpart. However, this analysis shows that a more even sampling of the field would lead to better predictions. So, the position of the probes in the Cloth holder has been slightly modified for the session with simultaneous scanning.

Simulated data have been used to establish that a small range of movements and the use of the non-linear method for prediction, when probes are in the Cloth-like set-up, is the best combination to obtain accurate predictions, even in the presence of noise sources (Figure 5.14) as confirmed with real data (Figure 5.32). The pre-processing pipeline and the spatial filter have then been tested with simulated data (Figure 5.15) and results have been confirmed with real data (Figure 5.36).

Chapter 6

Pilot studies on improving the prediction of the head motion parameters

In Chapter 5 the core of the work presented in this thesis was discussed in detail, showing how to predict head motion parameters from measurements of extra-cranial magnetic field changes using two supervised learning techniques (Subsection 5.1.3). This chapter reports pilot studies involving future solutions that, if fully implemented, could improve the motion predictions and the associated corrections of the MR image.

In the work described in Chapter 5, it has been chosen to limit the range of movements predicted ($\leq 5\ mm$, $\leq 5°$) in favour of achieving greater accuracy. K-space lines acquired simultaneously to head movements outside this range cannot be accurately corrected. To solve this issue, a retrospective pilot study (Section 6.1) has been conducted on magnetic field data. Exaggerated head movements have been identified by thresholding magnetic field data. Two approaches have been tested. First, the threshold was unique over the channels of the NMR field camera, then, it was customised for each channel. The probes act as a sensor that provides a trigger when exaggerated movements have occurred. In its future implementation, this trigger could be linked to the imaging acquisition process (skip-and-redo strategy [89]).

In Section 2.1, common standard clinical practices aiming for motion prevention were listed. Respiratory gating can provide external triggers to the MR image acquisition and is usually implemented using a respiratory belt. Section 6.2 reports a pilot study on using the 0^{th} order solid harmonic fit (Subsection 5.1.1) of the magnetic field changes to form a signal for use in respiratory motion monitoring.

The above solutions only have been further tested on data acquired with simultaneous imaging sequence. Results are reported in Chapter 7 and represents a proof of concept for future development.

The accuracy of the head motion parameters measurements from the optical camera, used for the training of the supervised regression method, limits the accuracy of the prediction and leads to a partially contact-less technique. Alternative methods that overcome the need for markers [131] or involve the use of the NMR camera only[60] are valid alternatives to explore in the future. In Subsection 6.3.1, the development of an active magnetic marker system that would augment the magnetic field changes due to the head movements is presented. The pilot study has been carried out mainly by implementing simulations. Simulated data have been used to predict head motion parameters. As the physics of the phenomena is well known in this case, a least square regression method as been used for the prediction. The active magnetic marker system plus the field camera could also be used as standalone marker-based system (like the MPT camera used in this thesis).

6.1 Flag significant head movements using magnetic field data

In this section, the possibility of using extra-cranial field measurements to flag up significant motion has been explored. This represents a first step towards the prediction of head motion parameters and it would allow the acquisition of an MR scan where the image is too corrupted from head movements to be useful to be stopped. If the level of movement is larger than the range of effectiveness of a particular MoCo technique, the image results will still be corrupted. Under these circumstances, or when no MoCo is applied, it would be useful to have a system which could indicate when head movement that is large enough to cause significant image artefact has occurred. This would potentially allow a choice to be made to reacquire all, or part of, the k-space data needed for image production, so reducing the economic and environmental cost of MR techniques and discomfort to the patient. The proposed approach allows the detection of significant head movements without requiring image sequence modification [4] nor rigid coupling of a motion marker to the volunteer's head.

Magnetic field probes were positioned evenly around the head in the PVC support (Figure 3.1), whilst head pose was simultaneously monitored using a Moiré Phase Tracking (MPT) system.

The detection of significant motion is based on a comparison of the variance of the field measurements acquired during a short time interval, to the average value of the

variance measured with the subject at rest in the scanner.
First of all, for each probe (p), normalization factors (N_p) have been evaluated on training data. Then, thresholds to discriminate each accepted movement have been defined (E_p). Finally, exaggerated motions were identified by normalising new data representing large head movements.
N_p represents the average value of the variance of magnetic field variation ($\sigma^2_(p, i)$) evaluated over n time intervals ($\Delta t = 1.5\ s$) each one equivalent to 10 field measurements:

$$N_p = \frac{\sum_{i-1}^{n} \sigma^2_{p,i}}{n} \tag{6.1}$$

Thresholds are defined by taking the maximum value of the time series. E_p values are obtained by normalizing the variance of each time $i - intervals$ for each probe:

$$E_p = max\left(\frac{\sigma^2_{p,i}}{N_p}\right) \tag{6.2}$$

The thresholds are then compared with the normalized signal over $j - time$ intervals for new data:

$$E_p \leq \frac{\sigma^2_{p,j}}{N_p} \tag{6.3}$$

Each probe for which the level is exceeded is flagged. Based on the number of probes indicating significant motion, an informed choice can be made to reacquire all, or part of, the $k - space$ data needed for MR image production.

6.1.1 Flag significant head movements using magnetic field data

A threshold method that can be applied to measured extra-cranial magnetic field data to identify large head motion has been described in Section 6.1. Here, I present the results obtained by varying the set-ups and the reference levels on experimentally acquired data.

This information could be used to make an informed decision on stopping the scan acquisition early or to flag the k-space lines that are most significantly affected by the motion and so should be re-acquired. By varying the threshold levels, it would be possible to adjust the level of movement above which a significant number of probes are classified as invalid.

Setting a single threshold for all the probe signals The plots in Figure 4.6 show the extra-cranial changes in magnetic field for different head movements for one subject where probes were fixed in the PVC support. Larger changes are measured for larger

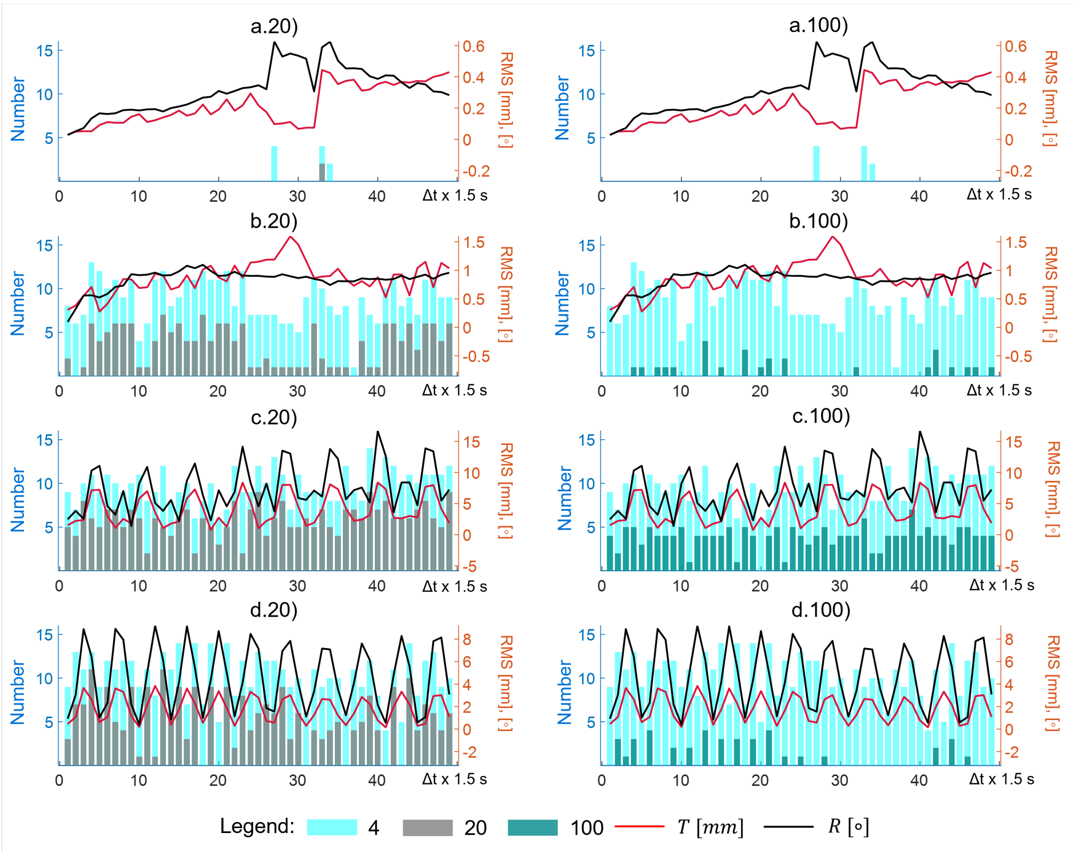

Figure 6.1: *Detection.* Example of the detection of large head movements using different reference levels defined based on the average variance measured in the resting data. a) represents data acquired at rest, b) represents data acquired during feet-wiggling, c) represents data during head shaking and d) represents data acquired during head nodding. The number of probes classified as invalid at each time-point during 50 s of recordings for different movement conditions is shown for constant thresholds over all channels of 4, 20 and 100 times the resting state value. The RMS movement parameters are shown for comparison in red and black lines. As the threshold is increased larger movements are required to produce a significant number of invalid probes.

head movements, as expected.

The threshold level was constant over the probes, so a certain number of probes will signal the exaggerated motion. The variation of the number of probes classified as invalid with time during the different movement conditions is shown in Figure 6.1 for different values of the threshold level. The concurrent variation of the RMS displacement and rotation relative to the starting position (measured using the MPT system) is also shown.

These results indicate that by varying the threshold level it is possible to adjust the level of movement above which a significant number of probes are classified as invalid. This would identify the level of motion at which a problem with MRI data is flagged to the operator.

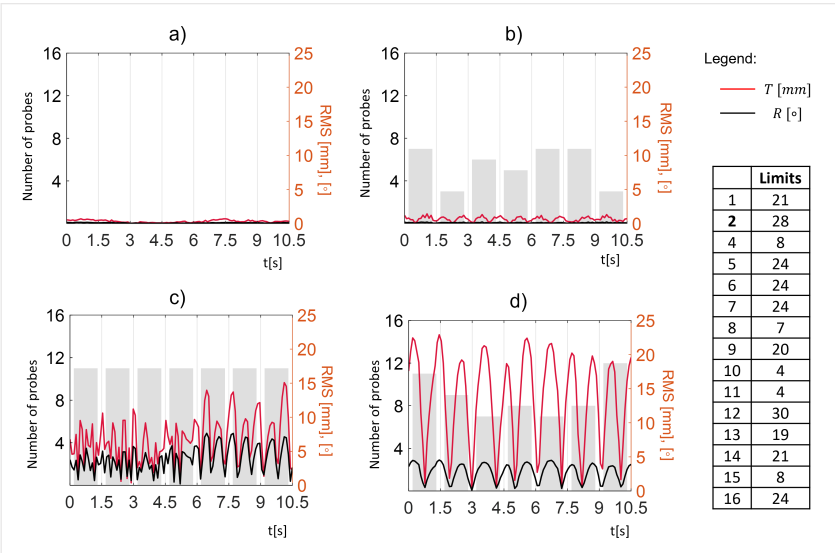

	Limits
1	21
2	28
4	8
5	24
6	24
7	24
8	7
9	20
10	4
11	4
12	30
13	19
14	21
15	8
16	24

Figure 6.2: *Exaggerated head motion detection.* Plots show examples of exaggerated head motion detection of head movements using different reference levels for different probes. The levels were defined based on the maximum variance over time intervals of 1.5 s at rest. Plot (a) shows that no probes detected exaggerated motion in the rest condition for new data over 10 s, while for (b) feet-wiggling, head (c) shaking and (d) nodding a varying number of probes did. As the range of head movements increases, the histograms show that more probes tag the head movement as exaggerated at concurrent time intervals.

Set customised thresholds for each probe Figure 6.2 shows the analysis of the pattern of variation of the number of probes (cloth support) that detect exaggerated head movements along with the concurrent measurements of head movements with a varying threshold over the probes. When the threshold is varied over probes, the pattern on the numbers of probes signalling the exaggerated motion becomes clearer. For example, comparing the head shaking condition over 10 seconds in Figure 6.1 and Figure 6.2, the number of probes showing field changes above threshold is higher and more consistent in the second case.

6.2 Respiration-like signals derived from magnetic field data

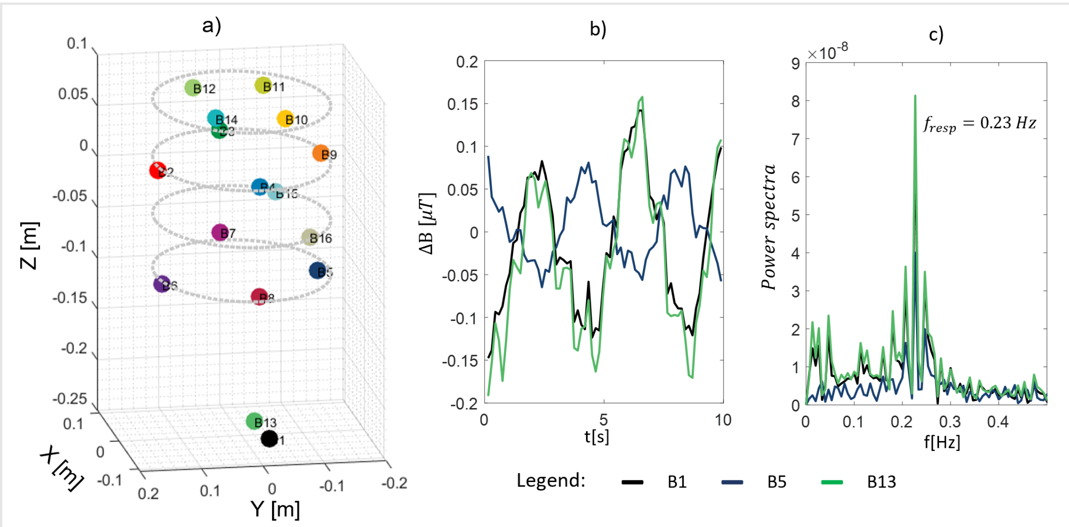

Figure 6.3: *Physiological signal from NMR field probes.* (a) Probe positions, 14 were in the PVC holder and probe 13 and probe 1 were positioned above the chest on a plastic support. The shape of the field gradient at those distances from the isocentre is not reliable (Figure 1.15), so they were localized incorrectly and the absolute magnetic field (b) is not a valid measurement. (c) Probes 1, 13 (above the chest) and 5 (approximately under the head-neck pivot) recorded a signal clearly correlated with the physiological parameters as confirmed by the peak at the respiration frequency.

It has been demonstrated that a set of 16 magnetic field probes is able to record a valid respiration signal if placed close to the chest [130]. Two plastic extensions were added to the PVC probe-holder in order to position two field probes close to the chest (Figure 6.3). This is outside the region of linearity of the scanner's gradient coils, so the positions of these probes (numbers 1 and 13) were not identified correctly and the spatial variation of the measured field from them was not valid, while the frequency analysis showed a clear correlation with the physiological parameters [11]. However, this set-up raised safety concerns in terms of the rapidity with which the subject would be able to exit the scanner in the case of an emergency and this idea was not further tested.

As probe number 5, located approximately under the head-neck pivot, shows a similar correlation with the physiological signal, it was concluded that locating more probes close to this region of the head would provide a valid signal for the analysis.
In Section 4.3, a method to derive respiratory signals from zero order solid harmonic fit of

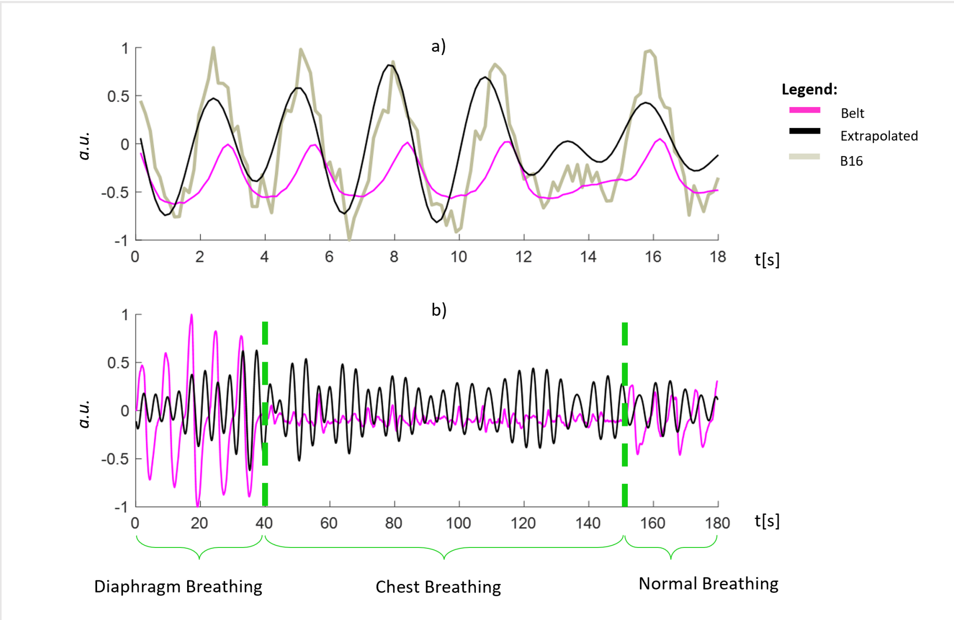

Figure 6.4: *Physiological signals.* (a) The prediction of the respiration signal obtained by filtering the 0^{th} order fit plotted along with the concurrent recording from the respiration belt and the signal directly recorded by one of the NMR probes (Subject 5). The fit has been compared with the signal from probe number 16. Signals have been normalized between minus one and one for clarity. (b) The figure shows that the signal derived from the field measurements is robust against different respiratory regimes, while the respiratory belt may fail if the pillow under the sternum is not squeezed appropriately (Subject 4).

the magnetic field data has been presented. Here, the method is tested on real data using the cloth probe-holder set-up (Figure 6.5). The signals from probes sited closer to the chest along the head-foot direction (probes 10, 9, 16) are most influenced by the effects of chest movement. Lower-order harmonic fit signals have been superimposed and filtered using a band-pass filter centred at the respiratory frequency (on average 0.3 ± 0.1 $[Hz]$) for Subject 5. Results are shown in Figure 6.4.a. To test the robustness of the method against different respiration conditions, Subject 4 was instructed to breathe by expanding the diaphragm or the chest, or to breathe normally. The pillow of the respiratory belt that is placed on the sternum is squeezed differently in different conditions and so may not accurately measure the signal, while the respiration signal extrapolated from the magnetic field change is less affected by these differences (Figure 6.4.b).

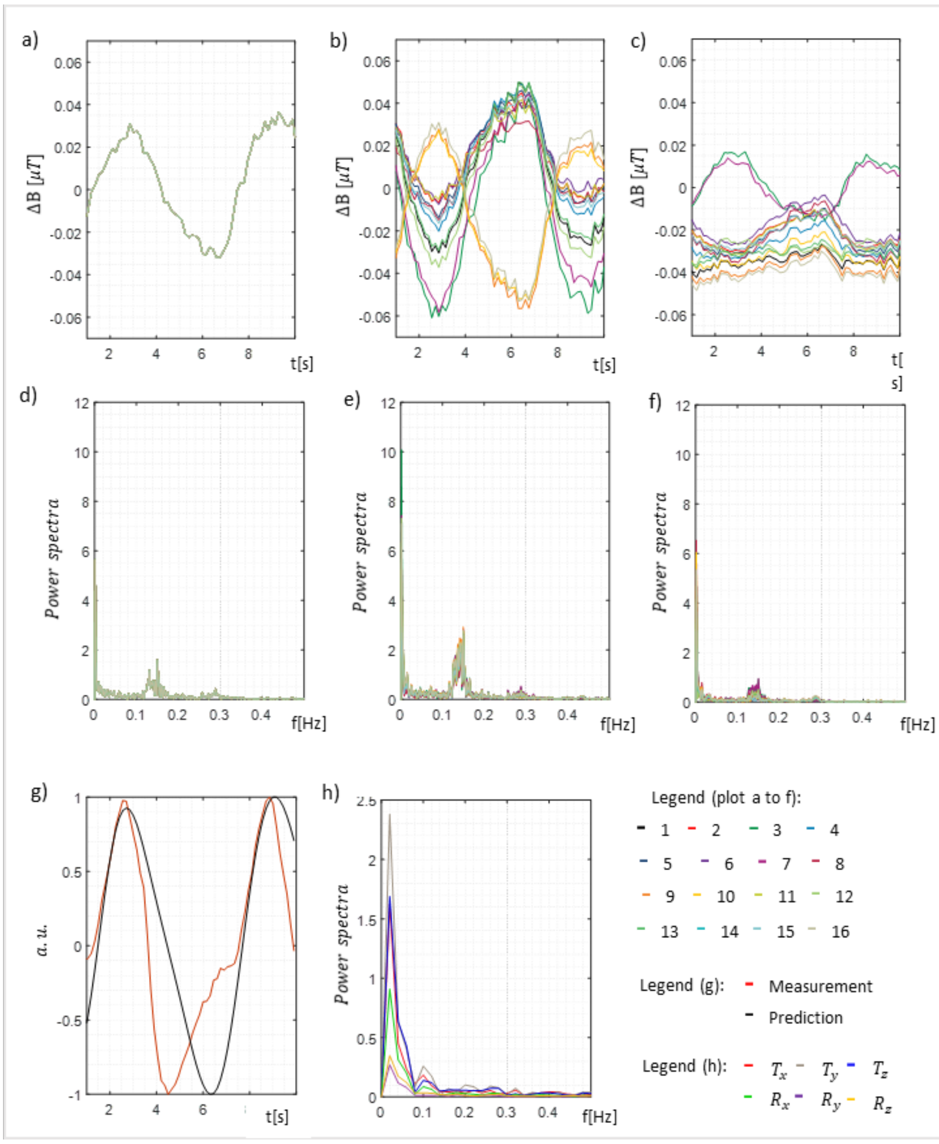

Figure 6.5: *Solid harmonic fit (real data) and physiological signals prediction.* Magnetic field data recorded during the rest condition were fitted using solid harmonic functions up to the second order (a) zeroth, (b) first, (c) second. Only the first 10 seconds are shown here. The frequency spectra (d,e,f) reveal that harmonics are influenced differently by the head motion (h) and respiration. Figure (g) shows the prediction of the respiration signal obtained from the 0^{th} order fit.

6.3 Improve the accuracy of the motion parameters data used for training the regression method

This chapter reports two pilot studies that link to the main project shown in this dissertation.

One, presents a simulation of a new head motion tracking system based on the use of active magnetic markers. The magnetic field of these markers is detected by using the NMR field probes and used to predict the position of the marker system. This has some advantages compared to other marker-based motion correction techniques as it doesn't require solution of the correspondence problem [69] to find the marker system position, does not require line of sight access to the marker [8], and could be implemented in a way that does not interfere with the imaging sequence and the paired system of markers and NMR probes is fully MRI compatible [35].

6.3.1 Active magnetic marker system for MoCo

The use of a magnetic marker to augment the extra-cranial magnetic field signal has been explored. Configurations using para-magnetic material increase the magnetic field, but since this additional field is likely also to extend over the imaging region the head and is always present, it will likely corrupt the images. A better approach is to use the additional field from active coils which can be switched on and off. Possible set-ups include: (1) a single coil solution, (2) a two-coil solution and (3) a multiple coil solution (with non-symmetrical disposition of the coils). Options (2) and (3) involve arranging the coils in a known geometry and so add extra information for the prediction of the movements. We proved that the position of the coils can be determined using a least square regression function.

To test the feasibility of the idea in the MRI scanner, two small coils were built to perform a preliminary measurement of the generated magnetic field using a customised foam-based probe-holder (without simultaneous scanning). Then, the experiment has been simulated testing a set-up feasible for scanning. Probe positions were simulated as uniformly displaced on the upper part of the internal surface of the RF transmit coil. The cross section of the internal volume is elliptical shaped with major axes equal to 28.1 cm and minor axes equal to 26.0 cm. Probes cover 22.0 cm of the height of the cylinder. Code to generate the probe positions is reported in the Appendix D.5. Our initial results show that changes in head pose can be accurately estimated from measurements of the field at 16 field probe positions due to currents pulsed in a set of small coils attached to the head.

6.3.2 Simulated magnetic field of a dipole generated by a single coil

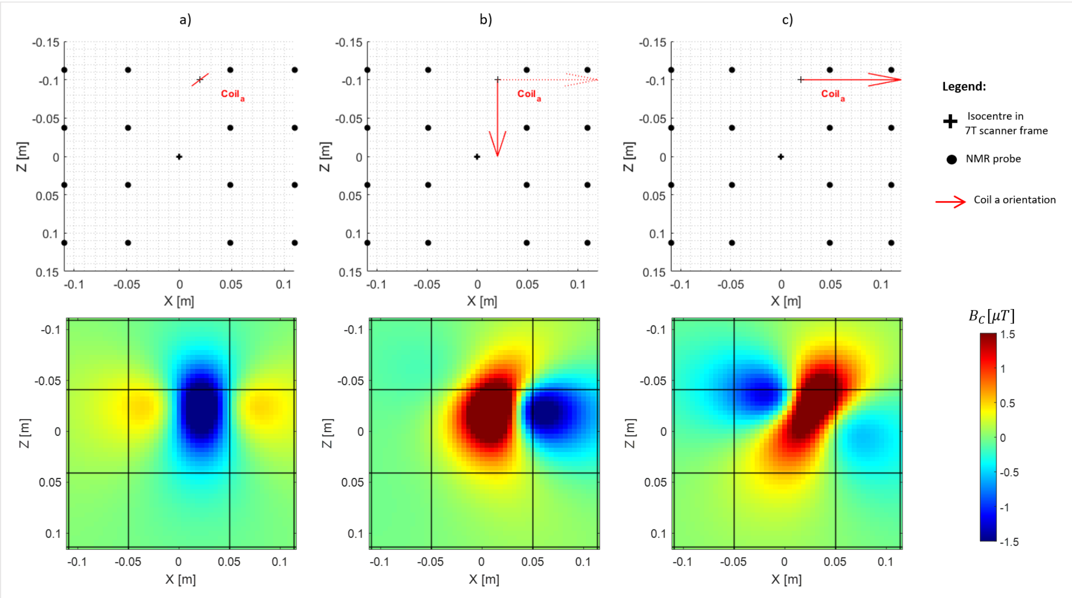

Figure 6.6: *Examples of simulated fields for single dipole.* The magnetic field generated by a magnetic dipole is well defined by equation 6.11. Coil positions (top) and z-component of the magnetic field [132] on a cylindrical surface (bottom). Probe positions are highlighted using circles (top) or line crossings (bottom). Field results asymmetric as probes lies on a cylindrical surface. The field has been evaluated for a dipole aligned along the three different Cartesian axes (a-y, b-z, c-x) positioned at $(x, y, z) = [0.02; -0.08; 0.02]m$.

The idea is to use small coil(s) in a fixed fashion rigidly coupled with the skull. The coil(s) act as active magnetic markers and measurements made using the NMR probes can then reveal the position of the markers. This idea has been simulated in Figure 6.6. Coils which could feasibly be built and operated inside an MR scanner have been simulated.

- Number of windings along the axis: 10
- Number of windings along the radius: 10
- Total number of windings: 100
- Radius of the cylindrical support: 2.6 mm
- Copper wire thickness: 0.23 mm

- Current used to drive the coils: 0.3 A

This leads to a coil which can produce fields of around 10 μT at the proximal NMR probes.

The magnetic field from a small coil can be modelled as the field from a magnetic dipole. For a general distance $\vec{r}$ from the dipole:

$$\vec{B}(\vec{r}) = \frac{\mu_0}{4\pi}\left(\frac{3\vec{r}\,(\vec{m}\cdot\vec{r})}{r^5} - \frac{\vec{m}}{r^3}\right) \tag{6.4}$$

where $\vec{m}$ represents the magnetic moment of the dipole, which is given by multiplying the number of turns (N) by the current (I) and the effective area of the coil, multiplied by a unit vector along the normal to the coil ($A \cdot \hat{s}$):

$$\vec{m} = N\ I\ A \cdot \hat{s} \tag{6.5}$$

If the coil is circular and has radius r : $\vec{A} = \pi r^2 \cdot \hat{s}$.

6.3.3 Simulated magnetic field of dipole measured by the NMR probes

The NMR field probes measure the z-component of the magnetic field $\Delta B_{Coil(s)}$. Figure 6.6 shows the magnetic field generated by a single coil at the internal surface of the standard image head coil sampled at 16 locations (as would happen with the NMR field probes in place). The magnetic field measured by a probe is described by:

$$\Delta\vec{B}(\vec{r}) = \Delta B_{Coil(s)} + \Delta B_{Head} + \Delta B_{Noise} + \ldots$$

For fixed probe, the equation 6.4 should used to evaluate $B_{coil(s)}$ as:

$$\begin{aligned} B_z(\vec{r}) = \vec{B}(\vec{r}) \cdot \hat{k} = & \\ &= \frac{\mu_0}{4\pi}\left(\frac{3\vec{r}\,((N\ I\ A\cdot\hat{s})\cdot\vec{r})}{r^5} - \frac{(N\ I\ A\cdot\hat{s})}{r^3}\right) = \\ &= \frac{\mu_0}{4\pi}(N\ I\ A)\left(\frac{3r_z(\vec{r}\cdot s r_z)}{r^5} - \frac{(s_z\vec{r})}{r^3}\right) \end{aligned} \tag{6.6}$$

Where $B_z(\vec{r})$ is the field component measured by the NMR probes, $\vec{r}$ is the distance between the coil and the probe. The $\vec{r}$ can be found by inversion of the equation 6.6. For a single coil, if we consider the distance between the NMR probe and the scanner's

	Coil 1	Coil 2
Number of windings along the axis	10	9
Number of windings along the radius	10	11
Total number of windings	100	99
Radius of the cylindrical support $[mm]$	2.66	2.55
Copper wire thickness $[mm]$	0.23	0.23
Current used to drive the coils $[A]$	0.30	0.32

Table 6.1: *Specifics of the two physical coils.* The table reports the specifics of the two twin-physical coils (Figure 6.7) tested in the 7T scanner (without simultaneous scanning). Discrepancy in the specifics are due to the manufacturing process.

isocentre is $(r\vec{_{P,a}})$ and the distance between the isocentre and the coil centre is $(\vec{r}_C(t))$, $\vec{r}(t)$ is given by:

$$\begin{aligned}\vec{r}(t) &= r\vec{_{P,a}} - \vec{r}_C(t) = \\ &= r_x \cdot \hat{i} + r_y \cdot \hat{j} + r_z \cdot \hat{k} = \\ &= (x_{P,a} - x_C(t))\hat{i} + (y_{P,a} - y_C(t))\hat{j} + (z_{P,a} - z_C(t))\hat{k}\end{aligned} \tag{6.7}$$

Where $r_C\vec{(t)}$ is the vector that provides information about the position of the head in the scanner, assuming that the coil is affixed to the head, and so can be used for motion correction. It can be evaluated by analysis of the measured fields using equations 6.6 and 6.7.
The unit vector is defined by:

$$\hat{s} = s_x \cdot \hat{i} + s_y \cdot \hat{j} + s_z \cdot \hat{k}, \qquad s_x^2 + s_y^2 + s_z^2 = 1 \tag{6.8}$$

6.3.4 Testing an active magnetic marker system (two coil solution)

Two small coils were built to perform a preliminary measurement of the magnetic field using a customised foam-based probe-holder that evenly sampled the generated magnetic field (but did not allow simultaneous scanning). Specifics are reported in Table 6.1. The set-up of the experiment is shown in Figure 6.7.

The set-up shown in Figure 6.7 has been used to acquire preliminary time series data (Figures 6.7 a,d). The coils were driven separately using alternate currents. Repetition time of the magnetic field camera was set to 100 ms resulting in the sampling of 10 data points over the period of the oscillating current. The measured magnetic field was unique for each coil due to the differences in the relative coil-probe distances. The movable disk was rotated to 8 further different positions. Thanks to two MPT markers coupled with the disk, the translations and rotations were estimated. As the aim of the experiment

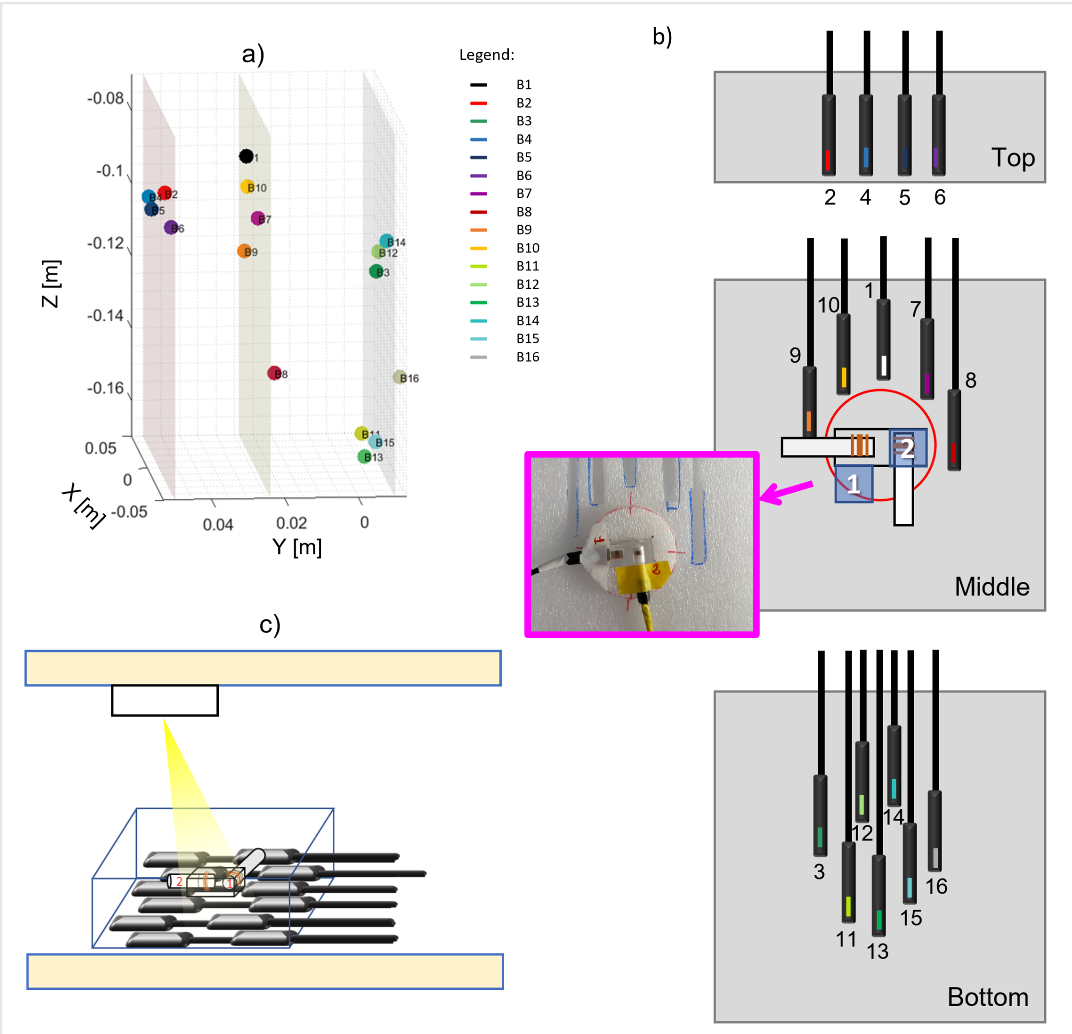

Figure 6.7: *Experimental set-up.* (a) Positions of the probes in the (b) 3 layer foam probe-holder ($\approx$ 3 *cm* thickness), a picture of the middle layer is reported. The transparent PVC support that holds the probes in a perpendicular fashion is displayed. A total of two MPT markers were placed on the PVC support and on the disk to measure the position in the optical camera's frame of reference. The foam disk is designed to be easily rotated and then to be fixed in the chosen position. (c) The set-up was placed in the scanner bore maintaining line of sight access to the optical camera.

was not to accurately measure the motion, cross-calibration was not performed ahead of the experiment, so measurements were in the optical camera's frame of reference and translations only have been reported in this thesis. The MPT camera raw data are given using the quaternion format, each time point is represented by: $[T_x\ T_y\ T_z\ q_x\ q_y\ q_z\ q_r]$. So, for non calibrated data, only translations (T_x, T_y, T_z) are measured in the metric system. The average value over the poses is shown in Figures 6.8 (c,f) and it is coherent

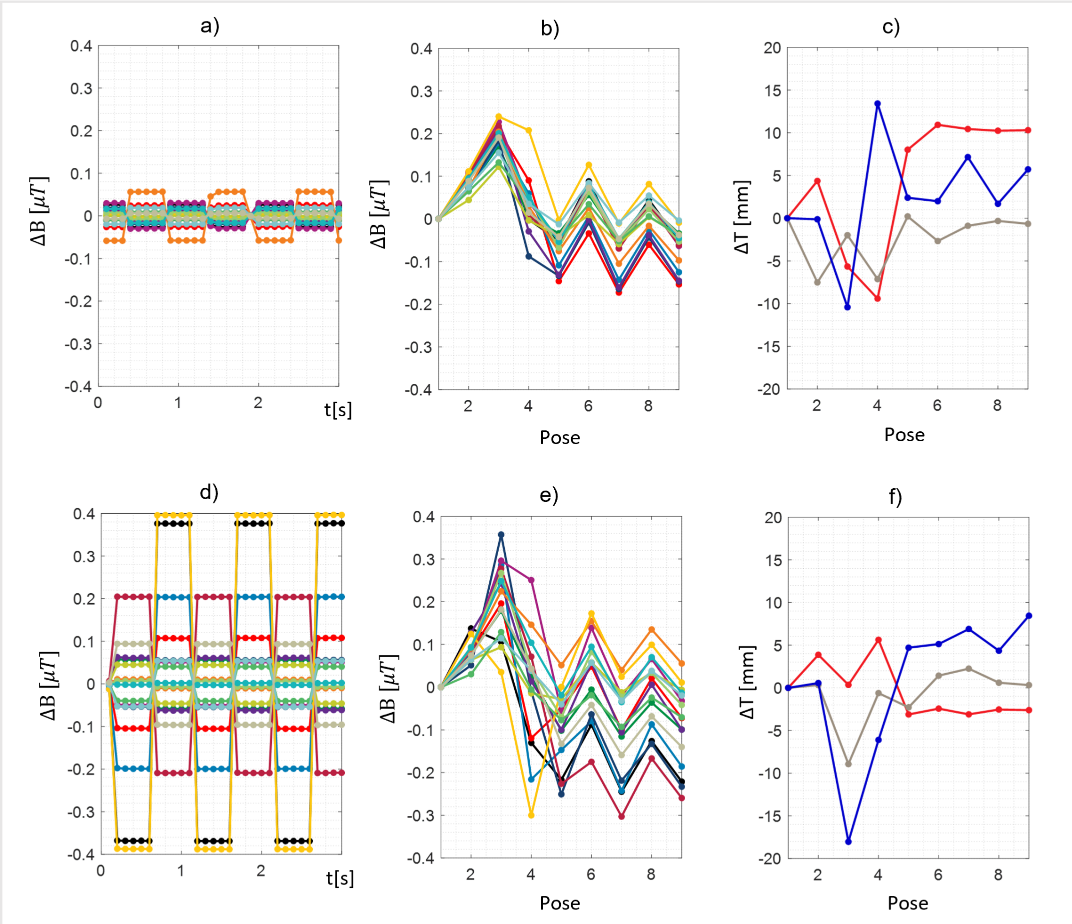

Figure 6.8: *Experimental data.* Plots (a,d) show the magnetic field time series acquired by driving Coil 1 (perpendicular to the main magnetic field) and 2 (parallel to the main magnetic field) respectively with an AC current oscillating at 1 Hz. The maximum values of the time series have been considered as measurement at first coil system position over 9 tested in total. Plots (b,e) report the difference between the maximum magnetic field value for each coil system positions and the initial one. Positions have been checked using the optical camera. The camera was not calibrated, so only translational motion parameters have been reported (c,f).

with typical head movements (Subsection 5.1).

The discrepancy of the maximum magnetic field values recorded for each magnetic field probe with respect to the initial pose (Figures 6.7 a,d) at each pose for each coil has been evaluated. Results are reported in Figure 6.7 (b,e) and are coherent with results obtained for a single coil simulation (Section 6.3.2). From Equation 6.6, considering

$\mu_0 = 4\pi 10^{-7}$:

$$B \propto NI(\pi r^2)\pi 10^{-7}\left(\frac{1}{d^3}\right) \tag{6.9}$$

and specifics given for Coil 1 (Table 6.1):

$$B \propto 100\ 0.23(\pi 0.00266^2)\pi 10^{-7}\left(\frac{1}{d^3}\right) \tag{6.10}$$

For a given distance $d \approx 2\ cm$, $B \propto 10\ \mu T$ (Figure 6.6, simulated data), while for the average distance between probes and coil in the experiment ($d \approx 6\ cm$), $B \propto 0.1\ \mu T$ (Figure 6.8).

6.3.5 Simulating real set-up and magnetic field data (two coils solution)

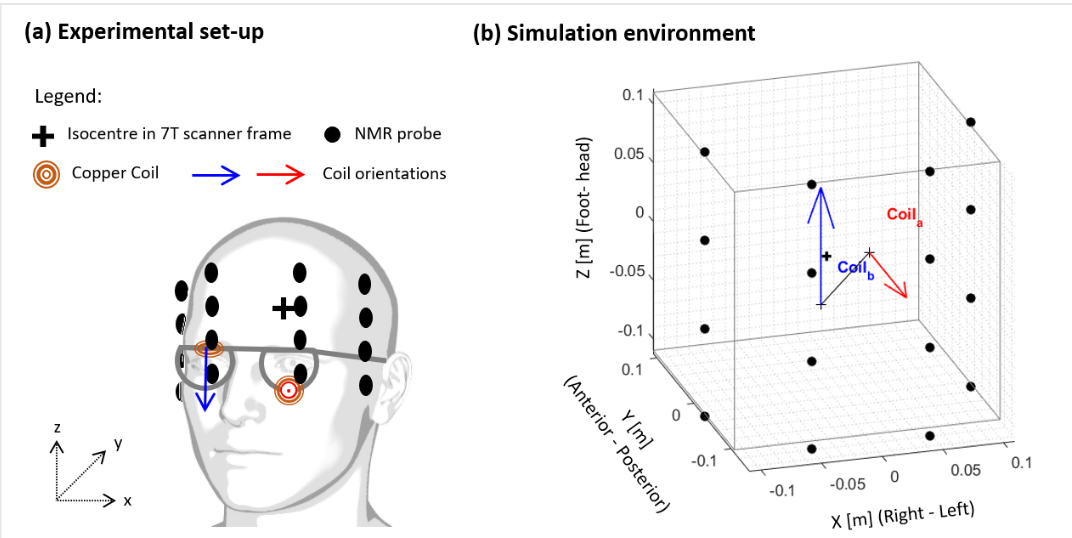

Figure 6.9: *Simulated experimental set-up.* The figure shows the simulated experimental set-up. Two coils are fixed onto the end-pieces of a pair of glasses. Each solenoidal coil was composed of 100 turns of 0.25 mm diameter wire arranged in 10 layers radially, each formed from 10 turns. The left and right coils are oriented along the y- and z-axes, respectively. The z-component of the magnetic field from the coils is monitored using 16 field probes spanning 21 cm axially and 22 cm azimuthally.

The idea behind using two coils is to create a magnetic field pattern whose shape is non-symmetric and so to add an additional constraint on the regression function as the geometrical relationship between the coils is fixed and known *a priori*.

The simulated set-up is shown in Figure 6.9. Two, small solenoidal coils (100 *turns*; internal diameter 5.2 *mm*; outside diameter 10.2 *mm*; 2.5 *mm* length) were positioned on the end-pieces of a pair of glasses. The coil orientations were chosen to be approximately along the y- and z-axes in order to create an asymmetrical pattern of magnetic field variation that would provide greater sensitivity to small head movements. The coil geometry was selected in order to give fields of $1 - 10\ \mu T$ order of magnitude at the probes when the coil was driven with a current of $10^{-1}\ A$ order of magnitude. Also, the diameter of the coils has to be small enough to be well described as a magnetic dipole and to fit on the glasses.

The z-component of the magnetic field from the coils is monitored using 16 field probes distributed over the upper part of the internal surface of the 7T Nova RF transmit coil. The magnetic fields generated at the fixed probe positions were calculated for each head position using analytic expressions for the field from solenoidal coils [132] carrying a current of 0.3 A. The *Biot-Savart* law has also been used as it is the most physically correct to describe the magnetic field generated by each infinitesimal element of the wire.

$$\mathbf{B}(\mathbf{r}) = \frac{\mu_0}{4\pi}\int_C \frac{I\ dl \times \mathbf{r}}{|r|^3} = \frac{\mu_0}{4\pi}\int_C \frac{I\ dl \times \hat{\mathbf{r}}}{|\hat{r}|^2} \tag{6.11}$$

Figure 6.10 shows the B_z field generated at the probe-surface for one head pose, and the field-changes resulting from head pose changes produced by translation of the coils along the x- and y-axes (corresponding to positional changes that might be produced by head shaking and nodding).

To test the feasibility of tracking head motion using this approach, we simulated a time-series (0.15 s time-step) of field values produced at the probes ($B_C(t)$) using head motion parameters measured previously (Table 4.1) with an MPT optical camera during motion correction experiments (Figure 6.11) [17]. The motion parameter set ($M(t)$) characterises translations and rotations related to Cartesian axes in the scanner's frame of reference. Motion parameters were then estimated from the 16 field-values recorded at each time point using the analytic field expressions.

We also evaluated the effect of adding white noise ($10^{-9}\ T$ or $10^{-8}\ T$ STD) to the simulated fields. Figure 6.11 shows the temporal variation of the motion parameters and simulated field values for 10s periods of rest, head-nodding and head-shaking.

6.3.6 Regression method to predict head motion parameters from field measurements

The prediction was performed using a Matlab function based on the Nelder-Mead Simplex optimization method [133]. The change in the magnetic field values between

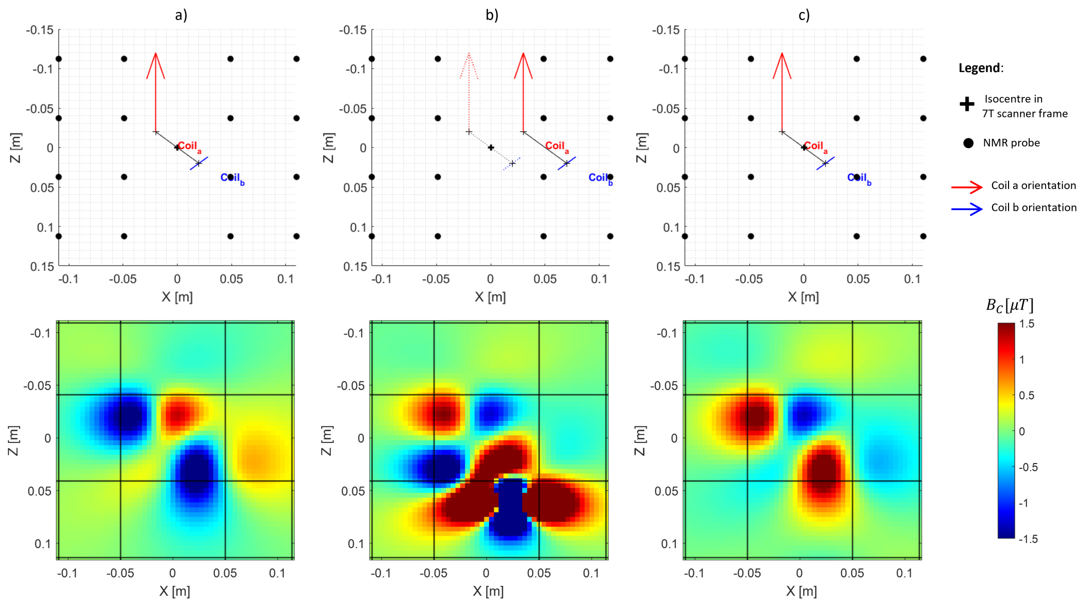

Figure 6.10: *Examples of simulated fields.* Coil positions (top) and z-component of the magnetic field [132] on a cylindrical surface (bottom, B_C) (0.3 A coil current). Probe positions are highlighted using circles (top) or line crossings (bottom). Field results asymmetric as probes lies on a cylindrical surface. (a) The field at the initial head-position is shown, along with the field changes produced by (b) translating the system along x by 0.05 m (c) and translating along y by 0.01 m. Complex patterns of field change give high sensitivity to differences in head pose.

consecutive time steps was used as the cost function. Given the value of the magnetic field at step n ($B_C(t_n)$), the value of the magnetic field at time t_{n+1} is estimated by iteratively changing the motion parameters used to move the coil system and evaluating the magnetic field, $B_P(t_{n+1})$. The algorithm converges to the predicted motion parameters ($M_p(t_n)$) once the difference between the measured and estimated magnetic field changes reaches a fixed tolerance.

The algorithm needs a starting guess for the motion parameters set ($M_0(t_n)$). For the first time step, $M_0(t_{n=1})$ was randomly extracted from a normal distribution with zero mean and deviation standard equal to the standard deviation of the motion parameters. For each subsequent time step, ($M_0(t_{n>1})$), the guess was formed using a perturbation extracted in the same way, but scaled by 0.01 that was added to the previous prediction ($M_p(t_{n-1})$).

Details of the algorithm. The magnetic field is evaluated using the known positions of the probes ($\vec{P}$) and coils ($\vec{M}$), the coil parameters (Area A, n-turns N), driving current

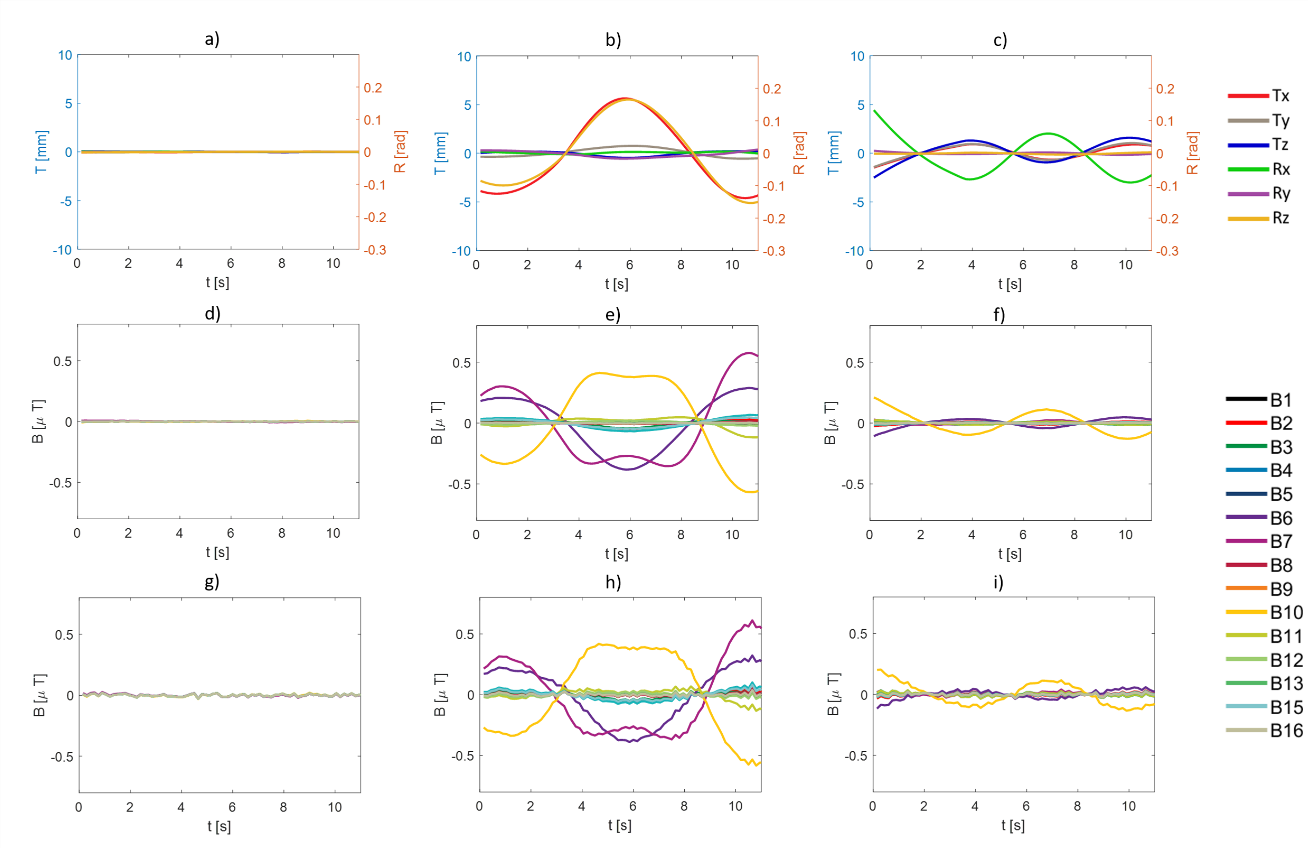

Figure 6.11: *Examples of simulated fields from true head movements.* (Top) smoothed 10 seconds time series (Table 4.1) of previously-measured head motion parameters (translations T_x, T_y and T_z in mm and rotations R_x, R_y and R_z in radiants) during (a) rest, (b) head-shaking and (c) head-nodding conditions. (Centre, Bottom) simulated field values (B_C) at the 16 field probe positions with 0.3 A current in the two coils. White noise was simulated with 1 nT (d, e, f) 10 nT STD amplitudes (g, h, i). The relationship between field and motion parameters is evident. All plots are shown with the mean values having been subtracted to highlight changes due to motion.

I: $B(P, M, A, N, I)$. As the position of the coils is the only variable that changes over time based on the motion parameter:

$$B_t(M(t)) \tag{6.12}$$

We use the `fminsearch()` MATLAB built-in algorithm to perform a step-by-step prediction of the motion parameters of the coil system $F(B) = M_P$. The algorithm F evaluates the value of the cost function that has to be fitted (C) and the initial guess of the parameters (M_G) on which the cost function depends: $F(C, M_G) = M_P$. The cost

	SNR (1 nT)			SNR (10 nT)		
	Rest	**Head shake**	**Head Nod**	**Rest**	**Head shake**	**Head Nod**
$\mathbf{B_1}$	1.9	2.7	2.7	0.2	0.3	0.3
$\mathbf{B_2}$	4.6	5.9	13.3	0.5	0.6	1.3
$\mathbf{B_3}$	6.2	6.6	12.4	0.6	0.7	1.2
$\mathbf{B_4}$	6.9	12.3	6.9	0.7	1.2	0.7
$\mathbf{B_5}$	4.7	18.1	5.3	0.5	1.8	0.5
$\mathbf{B_6}$	65.5	81.7	70.5	6.5	8.2	7.1
$\mathbf{B_7}$	65.1	78.2	75.0	6.5	7.9	7.5
$\mathbf{B_8}$	27.5	47.7	29.3	2.7	4.8	3.0
$\mathbf{B_9}$	8.5	8.6	10.9	0.8	0.9	1.1
$\mathbf{B_{10}}$	30.5	42.9	69.9	3.0	4.3	7.0
$\mathbf{B_{11}}$	13.4	30.7	45.1	1.3	3.1	4.5
$\mathbf{B_{12}}$	3.7	11.0	11.3	0.4	1.1	1.1
$\mathbf{B_{13}}$	1.8	10.1	2.6	0.2	1.0	0.3
$\mathbf{B_{14}}$	26.3	30.0	28.2	2.6	3.0	2.8
$\mathbf{B_{15}}$	20.7	27.2	20.9	2.1	2.7	2.1
$\mathbf{B_{16}}$	5.0	10.6	5.2	0.5	1.1	0.5

Table 6.2: *Gaussian Fit and SNR values for the NMR field probes.* Magnetic field changes are shown as zero-average time series, so all the curves are centred on zero $\mu = 0$ $[\mu T]$.

function is defined as the difference of the magnetic field at two consecutive time steps:

$$C = B_{ti+1}(M_{ti+1}) - B_{ti}(M_{ti}) \leq tol \tag{6.13}$$

and it defines the end of the prediction for a given time step if and only if its value is less than or equal to a given tolerance ($tol = 10^{-9}T$). The accuracy of prediction then depends on the stopping criteria of the algorithm.

Figure 6.12 describes the critical steps of the prediction process, considering the prediction of a time series of $i = 0, 1, \ldots n$ steps. At t_0, the magnetic field B_0 is generated by the coils at the initial position M_0. *fminsearch()* is used to predict M_0 from the magnetic field generated by guessed motion parameters M_G. The current estimate of the motion parameters is updated until the difference between the measured B_0 and estimated B_G is less that or equal to $tol = 10^{-9}$ T. The stopping criteria defines the goodness of the final prediction. For t_0 only, M_G was defined such that the barycentre of the system was randomly perturbed from the isocentre of the scanner by one standard deviation of typical motion parameter values (in a real scenario, it may be evaluated from an initial scout magnetic resonance image). For $t_i > t_0$, M_G is the previous prediction of the motion parameters M_{ti-1}. This choice leads to a few inaccurate predictions at the beginning of the time series before the prediction stabilizes around a more reasonable values (if $\Delta t = TR = 0.150$ ms, predictions are inaccurate for approximately). The code is reported in Appendix D.

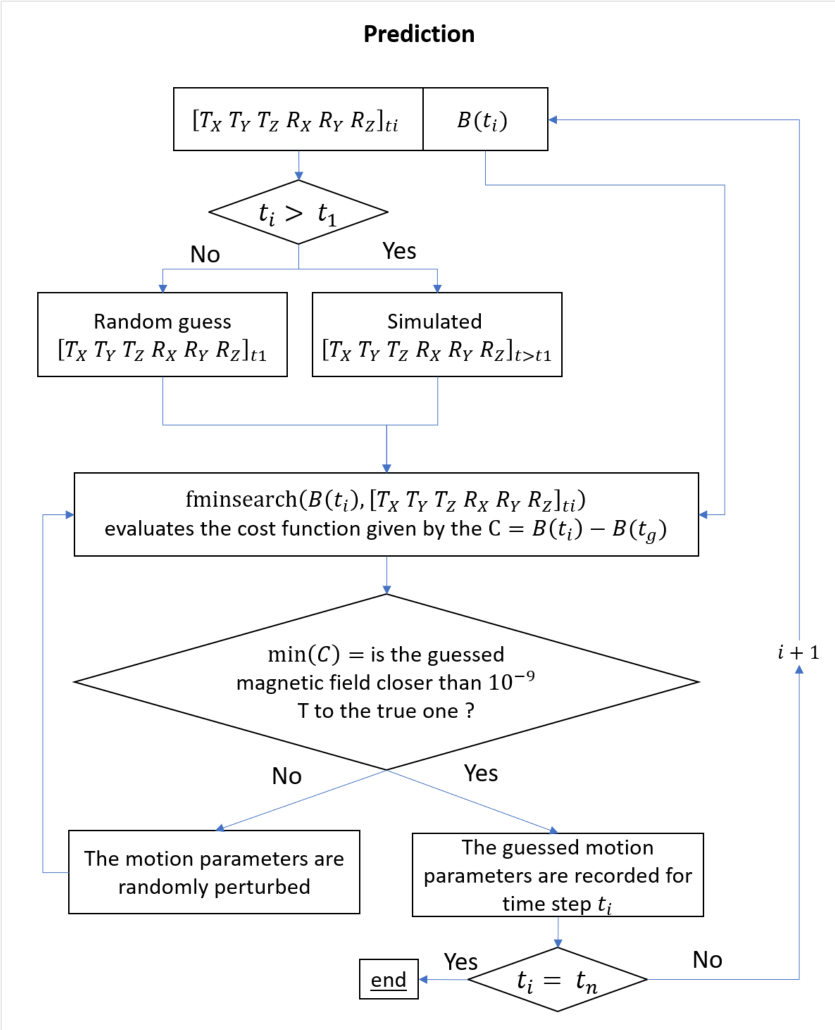

Figure 6.12: *Flow diagrams of the prediction.*

6.3.7 Prediction of head motion parameters

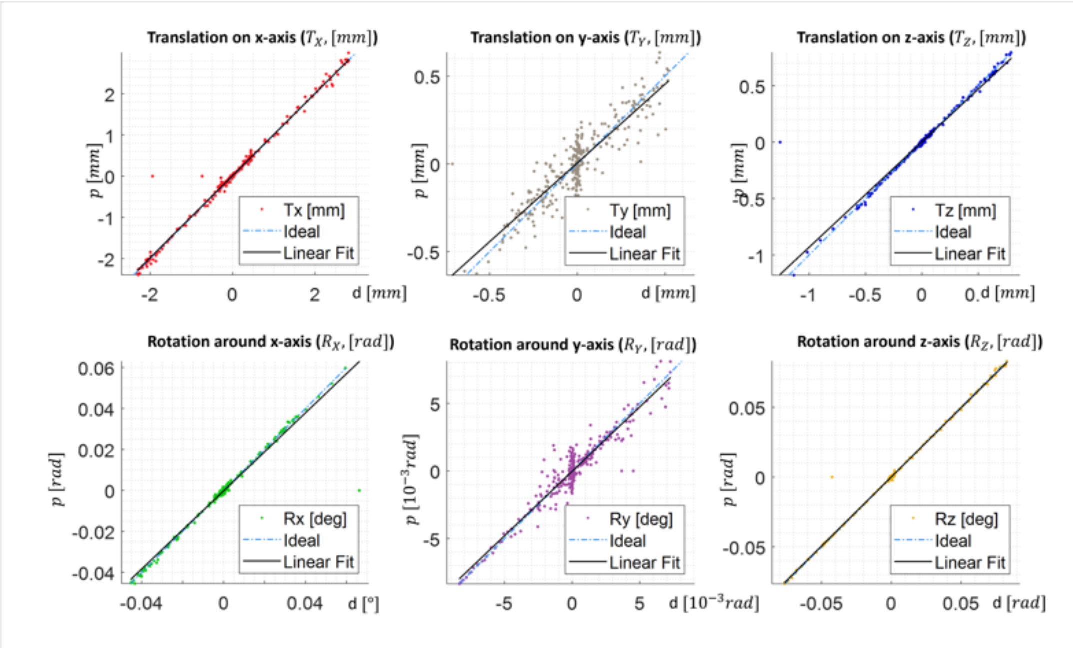

Figure 6.13: *Predicted motion parameters.* Plots of the predicted motion parameters (p) versus the actual values (d). From, the top left, plots show translation (T [mm]) and rotation (R [rad]) linked to the x,y and z axes in the scanner frame. Each plot also shows a linear fit to the data (black line) and a line of unit slope and zero intercept, corresponding to the ideal prediction (blue dashed line). Further analysis of the data plots is reported in Table 6.3. With added noise of the order of magnitude of 1 nT (1 order of magnitude less than the estimated one for the NMR field probes system, (Figure 3.9), predicted and actual values agreed nicely.

Noise level: 1 nT

	Slope	**Intercept**	$\mathbf{R^2}$	**MSE**	**PC**
$\mathbf{T_x}$ **[mm]**	0.997	0.013	0.98	0.018	0.99
$\mathbf{T_y}$ **[mm]**	0.898	0.006	0.80	0.011	0.89
$\mathbf{T_z}$ **[mm]**	0.935	0.003	0.94	0.005	0.97
$\mathbf{R_x}$ **[rad]**	0.953	< 0.001	0.95	< 0.001	0.97
$\mathbf{R_y}$ **[rad]**	0.953	< 0.001	0.92	< 0.001	0.96
$\mathbf{R_z}$ **[rad]**	0.990	< 0.001	0.99	< 0.001	1.00

Table 6.3: *Predictions.* The table shows the results of comparing the estimated and actual motion parameters on simulated data with added white Gaussian noise (average zero and deviation standard of 10^{-9} T). Values of the slope and intercept of the linear fit are reported along with the values of R^2, the mean squared error (MSE) and Pearson correlation coefficient (PC), for each of the motion parameters.

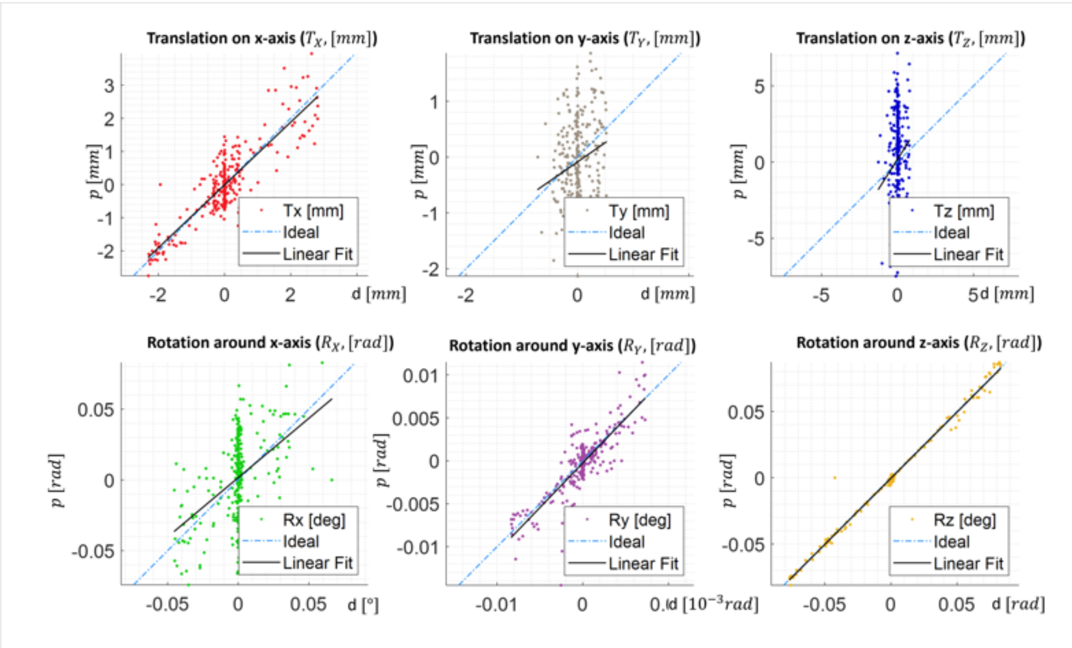

Figure 6.14: *Predicted motion parameters.* Plots of the predicted motion parameters (p) versus the actual values (d). From, the top left, plots show translation (T $[mm]$) and rotation (R $[rad]$) linked to the x,y and z axes in the scanner frame. Each plot also shows a linear fit to the data (black line) and a line of unit slope and zero intercept, corresponding to the ideal prediction (blue dashed line). Further analysis of the data plots is reported in Table 1. With added noise of the order of magnitude of 10 nT (equal to the one estimated for the NMR field probes system, Figure 3.9), the agreement between the predicted and actual values is relatively poor (Table 6.4).

Noise level: 10 nT

	Slope	**Intercept**	$\mathbf{R^2}$	**MSE**	**PC**
$\mathbf{T_x}$ **[mm]**	0.948	-0.011	0.76	0.298	0.87
$\mathbf{T_y}$ **[mm]**	0.692	-0.087	0.04	0.521	0.21
$\mathbf{T_z}$ **[mm]**	1.569	0.187	0.03	7.705	0.16
$\mathbf{R_x}$ **[rad]**	0.838	0.002	0.24	0.001	0.49
$\mathbf{R_y}$ **[rad]**	1.037	< 0.001	0.72	< 0.001	0.85
$\mathbf{R_z}$ **[rad]**	0.999	< 0.001	0.99	< 0.001	0.99

Table 6.4: *Predictions.* The table shows the results of comparing the estimated and actual motion parameters on simulated data with added white Gaussian noise (average zero and deviation standard of 10^{-8} T). Values of the slope and intercept of the linear fit are reported along with the values of R^2, the mean squared error (MSE) and Pearson correlation coefficient (PC), for each of the motion parameters.

The prediction of motion parameters from the simulated field changes was performed step-by-step on 300 data points (spanning 45 s) for each movement condition. The resulting motion parameter predictions collated from all three conditions are shown in Figure 6.14 for data with added noise. In future work, the behaviour for different noise levels and different starting positions should be evaluated.

The predicted values for each motion parameter p are plotted against the actual data values d: ideal prediction results would follow a straight line with unit slope. Table 6.3 details the results of a linear regression of the predicted motion parameters to the actual values (slope, intercept, R^2, the mean squared error (MSE), and the Pearson coefficient (PC)). Best predictions were obtained for rotational parameters. Translation along the y-axis was least accurately estimated. Lower accuracy in prediction of translations along the y-axis are likely to be due to the relative positions of the probes and coils. Adding more coils is likely to improve the accuracy of prediction, as it would increase the SNR and the asymmetry of the field. Also, adding one NMR field probe on the glasses would improve the prediction, as this would provide a measurement that is sensitive only to orientation changes since the probe coil distance would be constant.

There is a good agreement between the predicted values for all motion parameters, indicating that head motion can be tracked using the combination of two coils and 16 field probes. The best results are obtained for rotations while translation in y is least accurately estimated. The first few predictions are most influenced by the initial random guess ($M_0(t_{n=1})$) leading to greater prediction inaccuracy. The accuracy of the prediction is dictated by the choice of the stopping criteria of the algorithm and by the noise level. Inclusion of additional coils, which could be pulsed in combination with or, separately to, the initial coil pair would help to improve the localisation accuracy.

6.4 Conclusion

This chapter reports pilot studies aimed at improving the results of the main project described in this dissertation (Figure 6.15).

In this chapter, it has been proven that magnetic field data can be used to flag significant head movements (Section 6.1). Data thresholds that take into account the variability of the signals gave more stable results and will be further tested retrospectively in the next chapter. If implemented in clinical practice, this approach would reduce the need to repeat a full k-space data acquisition by excluding corrupted data a priori and inform the scanner operator if an early stop of the scan would be necessary.

The NMR field probes can provide a valid respiratory signal without requiring the

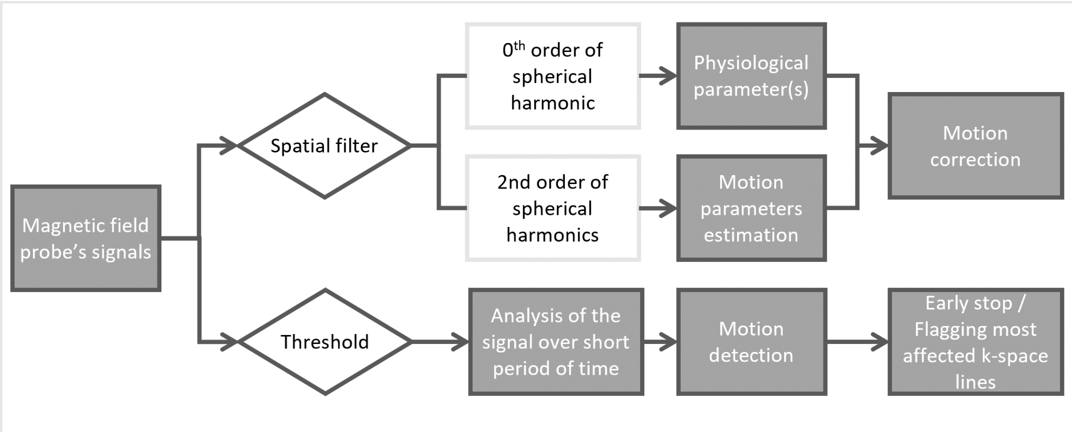

Figure 6.15: *Scheme.* The workflow represents a possible future development of the overall results shown in the thesis. Probe signals may be used to predict head motion and physiological parameters and to detect exaggerate motion to flag the concomitant k-space line affected by motion that could not be ameliorated by the MoCo technique.

attachment of any sensor to the patient. The reproducibility of the results will be tested in the next chapter. If implemented in clinical practice, it would represent a step forward in improving the comfort of the patient during MR scan.

Simulations of a new head motion tracking system based on the use of active magnetic markers has been presented. The magnetic field of these markers is detected by using the NMR field probes and is used to predict the position of the marker system. This has some advantages compared to other marker-based motion correction techniques as it doesn't require solution of the correspondence problem [69] to find the marker system position, does not require line of sight access to the marker [8], and could be implemented in a way that does not interfere with the imaging sequence. The paired system of markers and NMR probes is also fully MRI compatible [35].

The methods simulated in this chapter highlight some potential future uses of the NMR field camera in head MoCo techniques. One, uses the system to record the magnetic field produced by two small coils attached to a pair of glasses. Results show that the SNR needs to be higher to make the method robust. This system may be an alternative to the use of a marker based system (such as the MTP optical camera).

Qualitative consideration of the feasibility of bringing the new system to the market has been carried out in the frame of the "Shark Tank" Junior Fellow symposium of ISMRM 2021. The key points analysed are detailed below.

- *Comparison with existing MoCo techniques.* Major obstacles to translating a system into a clinical product are to make a system easy to be used by the scanner operator and the patient, it has to be compatible with older scanner devices and be to meet different safety standards. The marker coil system has the potential to overcome these obstacle.

- *Compatibility with existing MRI scanner.* The proposed system requires the use of wired markers, driven independently from the scanner, so the marker system would be fully compatible with any MR scanner system that has a field camera installed. To integrate the system with the magnetic field camera, modifications to the MATLAB code provided by Skope to communicate with the computer and the scanner need to be made. The motion parameters measured in this way could be used in both retrospective and prospective MoCo techniques. The approach allows the position of the head to be evaluated in the frame of the scanner, so it doesn't require calibration or the use of a training phase. In conclusion, neither the MR sequence nor other existing infrastructure would have to be modified significantly to utilise the active marker system (assuming that a field camera is available).

- *Wearability and patient comfort.* The support of the coils could be a pair of glasses worn by the subject. This configuration has been largely proved [60] to be a robust solution against marker-movement induced by patient facial expression. In non-co-operative subjects, it could mimic the use of a well known object and reduce the risk that the support is removed by the subject during the scan.

- *Time and accuracy of the prediction.* The computational time of the prediction depends on the electronic chain used to compute the prediction. It will depend on the programmable board used to drive the system, how it is connected with the computer that will calculate the prediction (same for the NMR field probes) and how this computer then communicates the results to the scanner and how much time the scanner needs to update the image geometry. The overall time should aim to be $\leq 15ms$ to be competitive with other systems (e.g. the MPT camera). Now, that the accuracy is set to be $10^{-9}T$ (stopping criteria of the least square method used) to obtain a prediction takes between 0.5 to 5 s on my personal laptop [1] – that is not particularly optimized for doing simulations. Accuracy of prediction then depends on the stopping criteria of the algorithm. Accuracy on knowing the relative position will also influence the prediction, as this information is used in the algorithm.

- *Physical phenomena that would invalidate prediction.* When the coil is energised with current it experiences a torque which acts to align the coil along the B_0 field (varies with sin of angle between coil axis and the B_0-field). The torque moment

[1] Processor: Intel(R) Core(TM), i7-8550U, CPU 1.80G Hz, RAM 16 Gb

would not be negligible for certain orientations and driving frequency and could compromise head-skull coupling. However, torque could possibly be balanced by pairing coils with opposite magnetization vectors (2 or more coils).
Alternatively, torque may be exploited to measure changes in orientation due to head movement. e.g. A coil will always try to orient itself with its magnetic dipole moment along the B_0 (z) direction. The torque will produce a rotation of a pivot sustain/squeeze a cushion next to the coil (as respiration belt works)/ other physics effect (piezoelectric sensor) whose measure lead on know which movements has been performed.

- *Induced artefacts in MR image.* The coil system will be driven to produce the magnetic fields in the quiet periods of the scanner sequence, so it shouldn't interfere with the image processing, but of course this needs to be tested experimentally. Practical considerations involve image artefacts (wires used to drive the coil(s) interact with the applied RF). The waveform to drive the coils system would be fundamental to differentiate the signal from the coils from other field variations. Possibilities for the waveform are short bursts of sinusoidal current with different frequencies(numbers of cycles) or pulses of different duration.

- *Cost.* The magnetic field camera cost is on the order of magnitude of a hundred thousand pounds, but the costs of the coil system may be an order of magnitude less (ten thousand pounds), depending on the additional tools needed (e.g. to drive the coils, a dedicated CPU to the prediction,...). The final costs need to be established once the system has been tested in the lab. To reduce costs, the field camera can potentially go down to 8 NMR field probes and still provide a good fit of the NMR signal of the probes. As the system available on the market is 16 probes, the simulation was based on 16 probes so far.

Chapter 7

Head motion tracking with simultaneous imaging and future development

In Chapter 3 a novel approach to head motion monitoring, which does not require attachment of markers to the head, line of site access for an optical camera or significant sequence modification has been presented. Two different experimental set-ups (Figures 3.7 and 3.3) have been tested: only one allows simultaneous scanning with the standard receiver coil array. The main parameter that influences magnetic field changes has been shown to be the head-probe distance (Section 4.2). The novel approach has been successfully tested with synthetic data (Section 5.2) and with real data (Section 5.3). The magnetic field data pre-processing involves time alignment and denoising steps (Section 5.1). In particular, magnetic field data have been filtered using solid harmonic functions to reduce the confounding effects of respiration (Subsection 5.1.1). The regression methods tested, a linear method (Partial Least Square) and a non-linear method (Nonlinear AutoRegressive network with eXogenous inputs), can both predict motion parameters from magnetic field data changes. The best results were obtained on pre-processed magnetic field data by using the NARX regression method to predict a small range of head movements ($\leq 5\ mm$, $\leq 5°$). In order to improve the prediction in future implementations, the use of magnetic field data in flagging significant head motion (Section 6.1) and to measure a respiration-like signal (Section 6.2) have been retrospectively tested with real data.

In Section 7.1, previous results have been extended using magnetic field data acquired during simultaneous scanning. However, the nature of the method developed was subject-dependant (the head-probe distance is not reproducible over acquisitions) and required the acquisition of a training dataset for each acquisition. A pilot study on generalising NARX over more subjects (Section 7.2) is presented.

The NARX neural network forms a good method for performing predictions of head motion parameters from extra-cranial field measurements. The mathematical assumption underlying the model is that the relationship between extra-cranial magnetic field changes and head motion parameters is described by a bijective function. This assumption only holds when we consider field measurements from a single scan session from a single subject. The aim of this section is to test whether the prediction can be performed over more subjects by adding further input parameters to the neural network. First, it is shown that grouping data from different scan sessions using the same choice of input parameters does not lead to good predictions, as would be expected. Then, by the use of synthetic data, a model that considers additional input variables has been developed and applied with promising performance to multi-subject data.

7.1 Head motion tracking with simultaneous scanning

In this section, the previous work on head motion tracking, exaggerated head motion detection and respiration-like signal generation has been extended. The main differences with the approach described in earlier chapters is in the acquisition of training data and new measurements of head movement and extra-cranial field changes. Here, the training data-set, used for the training of the regression method, is acquired without simultaneous scanning. New data, on which the trained method is applied, has then been acquired in quiet periods of a standard multi-slice EPI acquisition. The influence of eddy currents on the measured data was appropriately reduced by sampling the magnetic field at an appropriate delay from the beginning of the RF pulse. This represents a step forward in integrating the marker-less motion correction technique with standard imaging practice. Data acquisition was carried out on Subject 4 only because the approach has been proven to be subject-dependant. The cloth holder was used to hold the NMR field probes in place in between the Nova RF transmit and receiver coils. The probes were in different positions compared to the previous set-up (Figure 3.3): one additional probe was placed on the top of the head, two probes were placed on each side of the head and four probes were sited on the back of the head (Figure 7.1). Signals from the probes on the back of the head (Probes 10, 11, 15 and 16) were not used to perform head motion tracking. Results obtained by applying pre-processing, regression methods, flagging exaggerated head motion and respiration-like signals were repeated using magnetic field data acquired with simultaneous scanning.

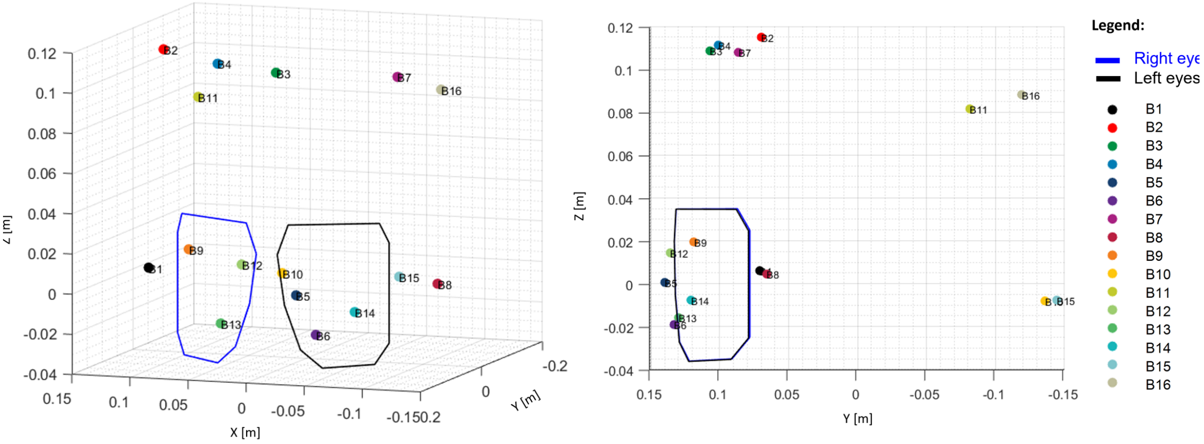

Figure 7.1: *Probe positions in the cloth holder.* The NMR field probes were placed between the Nova transmit and receiver RF coils in a different arrangement compared to that used in the previous experiments (Figure 3.4). This new arrangement allowed us to sample the extra-cranial field more evenly. Figures 7.2 and 8.1 report pictures and scheme of the holder.

7.1.1 Reducing the effect of eddy currents on magnetic field data

First, the usable timing of the acquisition of magnetic field data during the quiet period of an EPI scan was found by sampling the magnetic field at different delays (Figures 7.3 and 7.4) the minimum delay at which the probe signals are not significantly affected by the gradients applied during the image acquisitions signal was found. The delay was chosen to be 30 ms as the characteristics of the probe signals recorded at this delay time are similar to those found in the absence of scanning (Figures 7.4 and 7.3). Then, magnetic field data were acquired with and without simultaneously applying a multi-slice EPI sequence (48 $slices$, 3 mm isotropic resolution, $TR = 3.6\ s$, $TE = 20\ ms$) with a slice TR of 75 ms. The field camera was triggered to make field measurements 30 ms after the RF excitation every 150 ms (i.e. in a quiet period of the sequence after every second slice acquisition as $75 \times 2 = 150\ ms$).

7.1.2 Magnetic field data with and without simultaneous EPI

In order to test the feasibility of flagging significant head movements and head motion tracking during concurrent MRI acquisition, data were acquired without and with simultaneous EPI scanning for Subject 4. The former provided the training data sets (further divided into training, validation and test sets), while the latter formed the new data set on which the methods were applied. Both raw and pre-processed data were

Figure 7.2: *Picture of the final design of the probe cloth holder.* (a) Upper part (a.1 top view, a.2 bottom view). (b) Bottom part. Elastic band to hold the probes (32 pockets in total) were positioned to sample the extra-cranial field evenly. Elastic bands have been also placed to hold the cables. Red Velcro used to hold the cables close to the probe in order to stabilise probe positions. Dashed red lines were sewed to be used as reference lines to align the support to the head coil consistently over different scanner sessions. Plastic strings were added to the bottom part to allow it to be slid it under the transmit head coil without the need to remove it from the scanner bed.

tested. Notice that here, the spatial filter parameters were set on a training data-set (acquired without simultaneous EPI scanning) and then applied on both training and new data sets, while in the previous analysis they were evaluated on the single data-set that was subsequently divided into training, validation and testing data. A description of the data sets and the proportion of data that was used for training and prediction in the small and large head movement ranges are reported in Tables 7.1, 7.1 and 7.1. Values were evaluated in agreement with the description in Section 5.1.3. The two ranges of head motion are similar to those reported in Section 5.3. Small movements refer to the rest and feet-wiggling conditions. Large movements refer to the whole range of data acquired (rest, feet-wiggling, head shake and head nod).

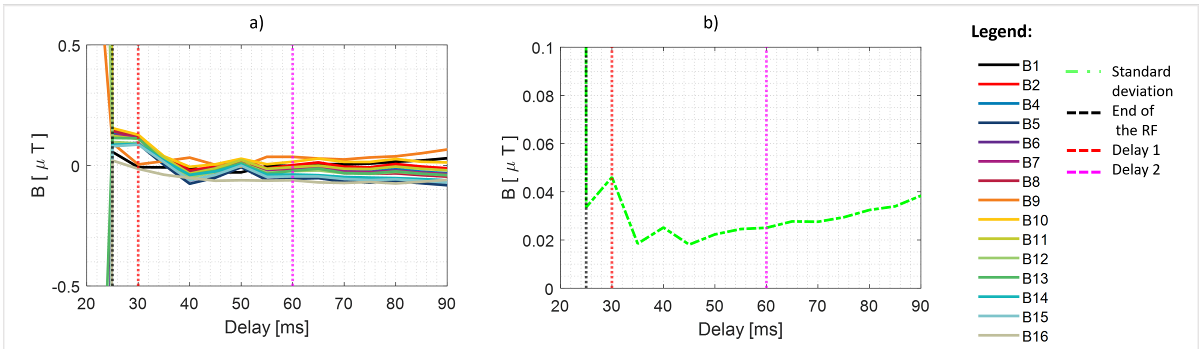

Figure 7.3: *Variation of field measurements as a function of the delay from the RF pulse of the EPI acquisition.* (a) Average of repeated 20 field measurements from different probes; (b) Standard deviation of measurements.

	Subject 4			
	Rest	**Shake**	**Nod**	**Feet-wiggling**
Training (without EPI)	5000	2000	2000	2000
New (with EPI)	1000	500	500	500

Table 7.1: Number of data points acquired for each head movement condition, with and without simultaneous EPI scanning

		PLS		**Training PLS** ($k-fold$)	
	Total	**Training**	**New**	**5-folds**	**1-fold**
Small (cloth)	8500	7000	1500	5833	1167
Large (cloth)	13500	11000	2500	9167	1833

Table 7.2: Number of data points used for training, validation and testing the linear regression methods are reported. Number have been evaluated in agreement with the description in section 5.1.3.

		NARX		**Training NARX** ($90\% - 5\% - 5\%$)		
	Total	**Training**	**New**	**Training**	**Validation**	**Test**
Small (cloth)	8500	7000	1500	6300	350	350
Large (cloth)	13500	11000	2500	9900	550	550

Table 7.3: Number of data values used for training, validation and testing the linear regression methods are reported. These numbers have been evaluated in agreement with the description in section 5.1.3.

Simultaneous measurements of head motion parameters and magnetic field changes were acquired with and without simultaneous scanning while the subject performed several types of head movement (rest, head shaking and head nodding). Example measurements are reported in Figures 7.5 and 7.6. The standard deviation and signal to noise ratio of

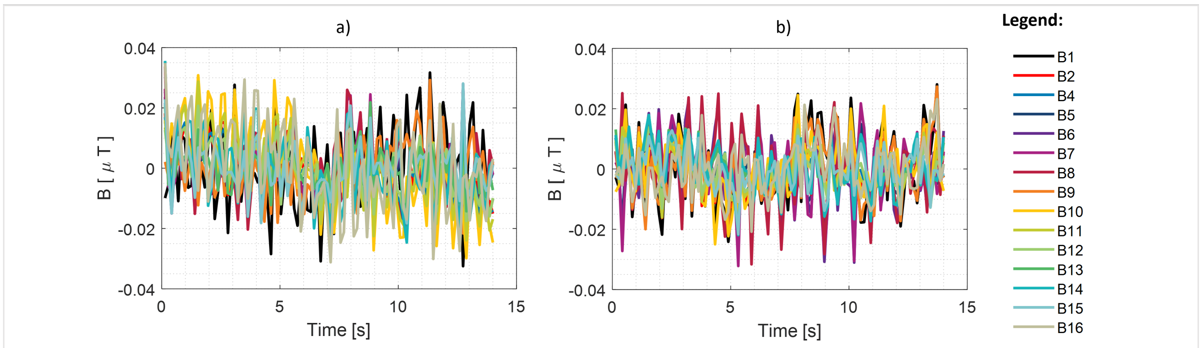

Figure 7.4: *Variation of field measurements as a function of delay from the RF pulse of the EPI acquisition.* The field was measured as a function of the delay from the RF pulse of the EPI acquisition in order to estimate the effect of any eddy currents. Plots show the variation of the average of 20 repeated field measurements from each probe as a function of the delay. (a) Data acquired over 15 ms at 30 ms delay; (b) Data acquired over 15 ms at 60 ms delay. A delay time of 30 ms was chosen as a compromise between limiting the level of field perturbation and unnecessarily extending the TR.

data acquired with and without simultaneous EPI are reported in Tables 7.4 and 7.5. Measurements acquired in the two conditions have similar STD and SNR values. This validates further that the time delay chosen (Figures 7.4 and 7.3) eliminated any significant influence of eddy currents on the field measurement data.

7.1.3 Flag exaggerated head movements using magnetic field data with simultaneous EPI

In Section 6.1, a threshold method on magnetic field data to identify exaggerated head motion has been presented and then applied using a constant threshold over all the probes (Figure 6.1) or with the threshold level varying over the probes (Figure 6.2). The second option was further tested here by evaluating the threshold on data acquired at rest acquired without simultaneous EPI and then flagging significant head motion in post-processing on data acquired with simultaneous EPI scanning.

Results of the detection are shown in Figure 7.7 and validate the previous analysis by successfully flagging conditions when there was significant head movement.

7.1.4 Deriving respiration-like signal from magnetic field data

In Section 4.3, a method to derive respiratory signal from a zeroth order solid harmonic fit of the magnetic field data has been presented. Here, the method is tested on

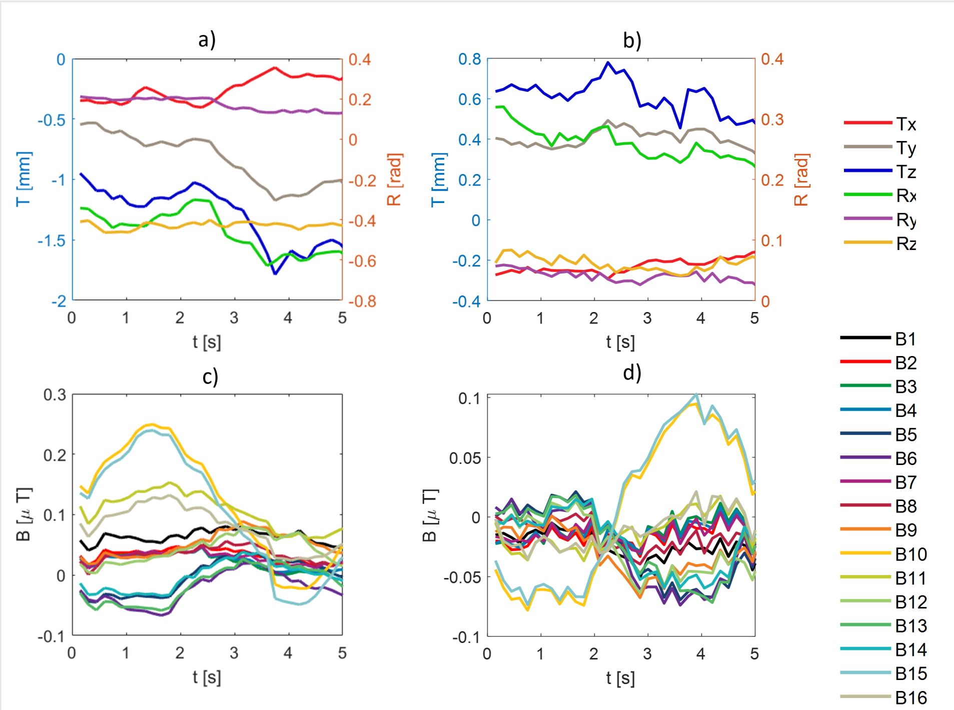

Figure 7.5: *Data training and test - example.* The plots show examples of simultaneous measurements of head motion parameters (a, b) and magnetic field (c and d). Data were recorded in the rest condition. Measurements were acquired without (a and c) and with (b and d) simultaneous EPI scanning.

real data acquired during concurrent EPI. Lower harmonic fit signals have been superimposed and filtered using a band-pass filter centred at the respiratory frequency (on average 0.25 ± 0.10 $[Hz]$). The results are shown in Figure 7.8. The day of the measurements the respiratory belt failed and so the fit has been compared with the signal from probe number 16 (that was placed on the back of the head and so is most influenced by the change in magnetic field due to chest expansion).

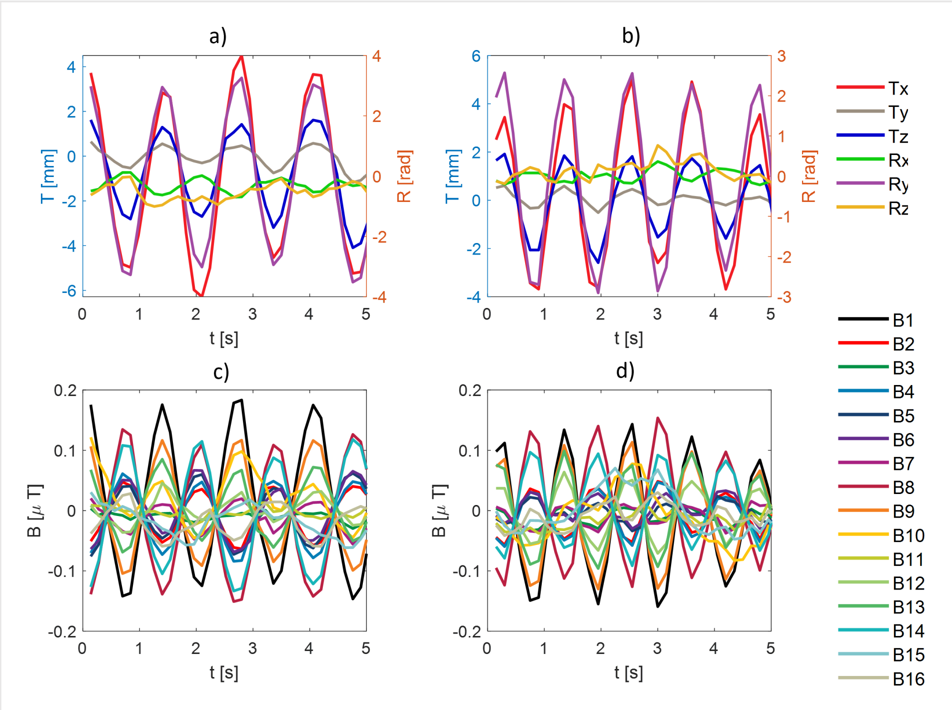

Figure 7.6: *Data training and test - example.* The plots show examples of simultaneous measurements of head motion parameters (a, b) and magnetic field (c and d). Data were recorded in the Shake condition. Measurements were acquired without (a and c) and with (b and d) simultaneous EPI scanning.

7.1.5 Head motion tracking with simultaneous EPI

In Section 5.3, data have been used to validate the best way to predict head motion parameters from magnetic field changes. Both linear (PLS) and non-linear (NARX) methods (Section 5.1.3) have been applied on data acquired using PVC-like and cloth-like probe distributions. The results show that the most promising pipeline for prediction involved the cloth probe holder, applied to pre-processed magnetic field data corresponding to small ranges of head movements (considering to flag k-space lines acquired on large head movements) to train the non-linear method (Figure C.10).

Here, the data analysis has been repeated as the nature of the data used for training and testing was different. Both regression methods and regimes of movement were considered, but only data from one subject (Subject 4) were tested. For the benefit of clarity, results are reported in the next section along with statistical evaluations of the fit. A summary is reported in Table 7.6.

STD	Subject 4							
	Without EPI				**With EPI**			
	Rest	**Shaking**	**Nodding**	**Feet-wiggling**	**Rest**	**Shaking**	**Nodding**	**Feet-wiggling**
$\mathbf{B_{1[\mu T]}}$	0.025	0.095	0.013	0.011	0.018	0.096	0.011	0.017
$\mathbf{B_{2[\mu T]}}$	0.009	0.029	0.010	0.020	0.013	0.034	0.011	0.017
$\mathbf{B_{3[\mu T]}}$	0.006	0.010	0.022	0.012	0.012	0.016	0.025	0.014
$\mathbf{B_{4[\mu T]}}$	0.006	0.039	0.011	0.014	0.012	0.033	0.014	0.013
$\mathbf{B_{5[\mu T]}}$	0.023	0.037	0.018	0.022	0.029	0.019	0.016	0.022
$\mathbf{B_{6[\mu T]}}$	0.026	0.036	0.022	0.026	0.031	0.026	0.020	0.026
$\mathbf{B_{7[\mu T]}}$	0.008	0.019	0.010	0.011	0.012	0.018	0.016	0.018
$\mathbf{B_{8[\mu T]}}$	0.017	0.081	0.025	0.013	0.015	0.089	0.028	0.012
$\mathbf{B_{9[\mu T]}}$	0.031	0.065	0.023	0.013	0.026	0.079	0.024	0.015
$\mathbf{B_{10[\mu T]}}$	0.042	0.049	0.051	0.050	0.052	0.042	0.041	0.055
$\mathbf{B_{11[\mu T]}}$	0.034	0.014	0.030	0.019	0.017	0.017	0.038	0.025
$\mathbf{B_{12[\mu T]}}$	0.023	0.020	0.020	0.017	0.023	0.040	0.022	0.018
$\mathbf{B_{13[\mu T]}}$	0.026	0.041	0.018	0.021	0.030	0.061	0.020	0.026
$\mathbf{B_{14[\mu T]}}$	0.021	0.069	0.023	0.023	0.026	0.062	0.019	0.020
$\mathbf{B_{15[\mu T]}}$	0.042	0.037	0.048	0.047	0.052	0.038	0.042	0.051
$\mathbf{B_{16[\mu T]}}$	0.026	0.027	0.031	0.023	0.017	0.022	0.039	0.029
$\mathbf{T_x}$ [mm]	0.681	2.662	2.347	0.161	0.138	3.179	2.626	0.153
$\mathbf{T_y}$ [mm]	0.762	0.399	2.463	0.386	0.210	0.496	2.752	0.505
$\mathbf{T_z}$ [mm]	1.100	1.450	4.329	0.301	0.320	1.717	4.914	0.317
$\mathbf{R_x}$ [°]	0.460	0.313	1.581	0.113	0.128	0.244	1.792	0.112
$\mathbf{R_y}$ [°]	0.114	1.860	0.220	0.031	0.015	1.918	0.206	0.027
$\mathbf{R_z}$ [°]	0.313	0.387	0.185	0.044	0.034	0.260	0.156	0.052

Table 7.4: *Data Subject 4.* The Values of the the standard deviation (STD) of magnetic field changes for the cloth probe holder set-up, for four different ranges of head movements (Subject 4) performed with and without concurrent EPI scanning. The values, which have been rounded to three decimal places, are similar in the presence or absence of concurrent scanning.

The number of data available for training and test differ significantly (Tables 7.1, 7.1 7.1), but is in agreement with data used in the previous tests using a similar set-up (Tables 3.3, 5.1.3 5.1.3). The regression methods were trained and applied on the same range of movements.

The results (Section 7.1.7, Table 7.6) confirm previous results and indicate that measurements of extra-cranial field changes made with a field camera can be used to monitor head position in a 7T MRI scanner during EPI scan acquisition. Applying the linear method on raw data gave the worst results over both head movement conditions. The non-linear method gave the best results over small head movements, however prediction of rotations around the y and z axes were poor. The reasons for this could be the larger influence of noise on small magnetic field data changes (corresponding to small head motion parameters) or numerical, as the regression method performs better on homoge-

	Subject 4							
	Without EPI				With EPI			
SNR	**Rest**	**Shaking**	**Nodding**	**Feet-wiggling**	**Rest**	**Shaking**	**Nodding**	**Feet-wiggling**
$\mathbf{B_1}[\mu\mathbf{T}]$	6	22	3	2	4	22	3	4
$\mathbf{B_2}[\mu\mathbf{T}]$	2	6	2	4	3	7	2	4
$\mathbf{B_3}[\mu\mathbf{T}]$	1	2	5	3	3	4	6	3
$\mathbf{B_4}[\mu\mathbf{T}]$	1	8	2	3	2	7	3	3
$\mathbf{B_5}[\mu\mathbf{T}]$	5	7	4	4	6	4	3	4
$\mathbf{B_6}[\mu\mathbf{T}]$	4	6	4	4	5	4	3	4
$\mathbf{B_7}[\mu\mathbf{T}]$	1	2	1	1	1	2	2	2
$\mathbf{B_8}[\mu\mathbf{T}]$	3	13	4	2	2	14	4	2
$\mathbf{B_9}[\mu\mathbf{T}]$	8	17	6	3	7	20	6	4
$\mathbf{B_{10}}[\mu\mathbf{T}]$	7	8	8	8	8	7	6	9
$\mathbf{B_{11}}[\mu\mathbf{T}]$	7	3	6	4	4	4	8	5
$\mathbf{B_{12}}[\mu\mathbf{T}]$	6	5	5	4	6	10	6	5
$\mathbf{B_{13}}[\mu\mathbf{T}]$	6	10	4	5	7	15	5	6
$\mathbf{B_{14}}[\mu\mathbf{T}]$	4	14	4	5	5	12	4	4
$\mathbf{B_{15}}[\mu\mathbf{T}]$	8	7	9	8	9	7	8	9
$\mathbf{B_{16}}[\mu\mathbf{T}]$	6	6	7	5	4	5	9	7

Table 7.5: *Data Subject 4.* Values of the signal to noise ratio (SNR) of magnetic field changes for the cloth probe holder, head ranges of movements (Subject 4) performed with, and without, concurrent EPI scanning. The values, which have been rounded to three decimal places, are similar in the presence or absence of concurrent scanning.

	Raw	
	PLS	**NARX**
Small	Figure 7.9, Table 7.9, poor	Figure 7.11, Table 7.11, good
Large	Figure 7.10, Table 7.10, poor	Figure 7.12, Table 7.12, poor
	Filtered NARX	
Small	Figure 7.13, Table 7.13, good	
	Filtered (less data) NARX	
Small	Figure 7.14, Table 7.14, good	

Table 7.6: Table summarizes the outcome of the predictions reported in the indicated figure based on the criteria listed in the equation 5.5

neous data.

Further tests on using filtered data and on reducing the number of data points used for training were made. The first, will reduce the influences of noise sources on magnetic field data, while the second will test whether the method went into over-fitting when predicting rotations around y and z axes. Results on pre-processed data were promising as the predictions (in particular on rotations around y and z axes) improved. So, for the

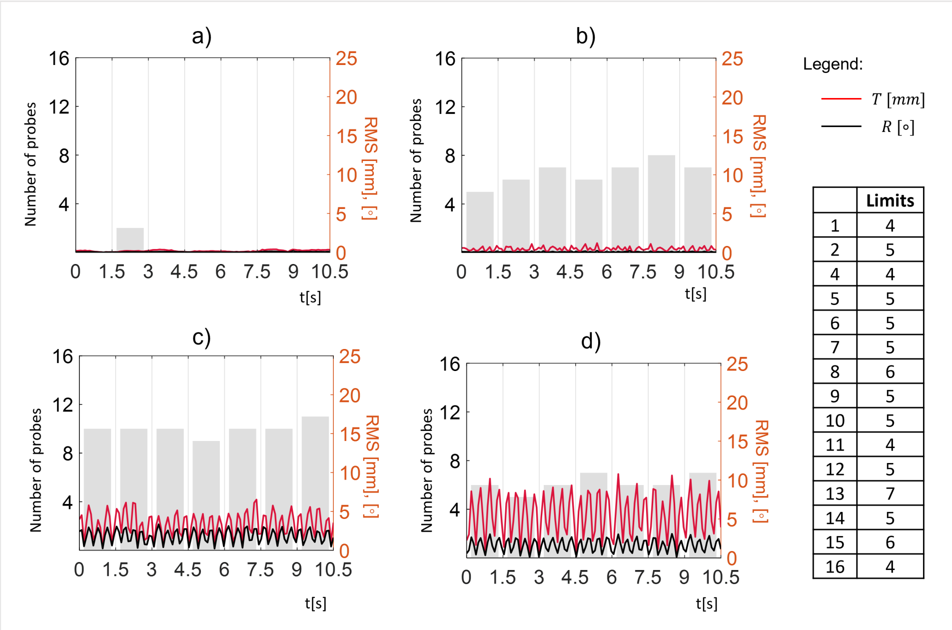

	Limits
1	4
2	5
4	4
5	5
6	5
7	5
8	6
9	5
10	5
11	4
12	5
13	7
14	5
15	6
16	4

Figure 7.7: *Exaggerated head motion detection.* Plots show examples of exaggerated head motion detection of head movements using different reference levels for each magnetic field probe signal. The threshold levels were defined based on the maximum variance over time intervals of 1.5 s at rest (without simultaneous EPI). Plot (a) show that no probes detected exaggerated motion during the rest condition for new data (with simultaneous EPI) over 10 s, while various number of probes did for (b) feet-wiggling, head (c) shaking and (d) nodding. As the range of head movements increases, the histograms show that more probes tags the head movement as exaggerated in the same time intervals.

latest tests, the number of data were reduced and the model under-fitted them.

To conclude, the non-linear method trained on pre-processed trained data, represented by $\approx$ 20 minutes of simultaneous measurements (Table 7.4) of head movement parameters[1] and field variation due to small head movements, have successfully predicted head motion parameters from magnetic field changes measured during the quiet period of a EPI scan. Results were comparable with results obtained with simulated data and the previous data-set (Figure C.10 and Table C.42).

[1]measured with a different approach, here, an optical camera and an MPT marker attached to a dental mould have been used

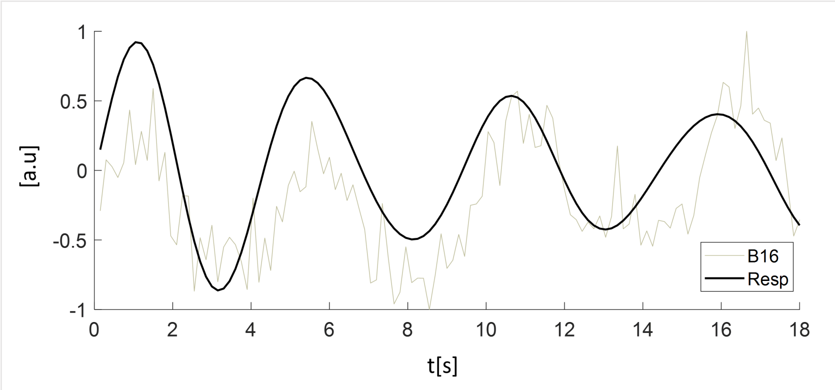

Figure 7.8: *Physiological signals.* Figure shows the prediction of the respiration signal obtained by filtering the 0^{th} order fit of field probe signals. Signal from probe 16 (B16) is reported for comparison. Signals have been normalized between minus one and one for clarity.

7.1.6 Timing of the prediction process

In order to apply the regression method during a MRI scan, it is necessary to have a clearer idea of the total timing necessary for the training phase that includes acquisition of data and to train the regression model. The former, has been evaluated as $\approx$ 20 minutes, significantly less data gave a worse prediction, but a further test can be performed with less data to find the minimum number of data to give good results. The latter has been evaluated over the training of 10 networks (Table 7.7). Number of data, range of movement and pre-processing and network architecture influences the timing. As a result, the optimal solution (based on the accuracy of the prediction) identified in the previous section is also the one that requires only $\approx$ 6 minutes to train and select the best network over 10 networks.

Furthermore, the time necessary to obtain a prediction is crucial to update the scanner geometry in the case of PMC (Prospective Motion Correction). Notice that the NARX method chosen performs a prediction ahead of the movement, allowing for adjustment of the scanner geometry. The times to obtain a step ahead prediction (Table 7.8) with all the network trained was around one micro second, this is well below the usual timing necessary for the update that is of the order of magnitude of ten milliseconds.

	Raw		Pre-processed	
	Large	**Small**	**Small**	**Small (less data)**
$NN_1[s]$	131	47	28	8
$NN_2[s]$	65	41	61	10
$NN_3[s]$	83	56	32	8
$NN_4[s]$	86	67	19	6
$NN_5[s]$	65	41	22	6
$NN_6[s]$	57	57	24	9
$NN_7[s]$	83	69	20	6
$NN_8[s]$	77	54	19	7
$NN_9[s]$	50	34	34	6
$NN_{10}[s]$	62	45	97	7
Average [s]	76	51	36	7
Total [s]	759	509	356	72
Total [min]	13	8	6	1

Table 7.7: Table reports examples of values of times necessary to train 10 neural networks (as explained in section 5.1.3), for each network, the average and the total time (in seconds and minutes) for the four head movement range presented in this section. Values have been rounded to unit. In order, the network's architectures were $11-30-6$, $11-30-6$, $7-30-6$, $9-30-6$.

	Chosen	**Architecture**	**Training [s]**	**Prediction [ms]**
Raw, Small	8	$11-30-6$	54	0.0008
Raw, Large	7	$11-30-6$	83	0.0007
Pre-processed, Small	6	$7-30-6$	24	0.0005
Pre-processed, Small, Less data	9	$9-30-6$	6	0.0007

Table 7.8: Table reports examples of values of times necessary to train the best neural network over 10 (as explained in Section 5.1.3), the chosen one (Table 7.7), their architecture and the time necessary to predict one set of motion parameters (values have been rounded to four decimal places).

7.1.7 Plots and Tables of predictions shown in section 7

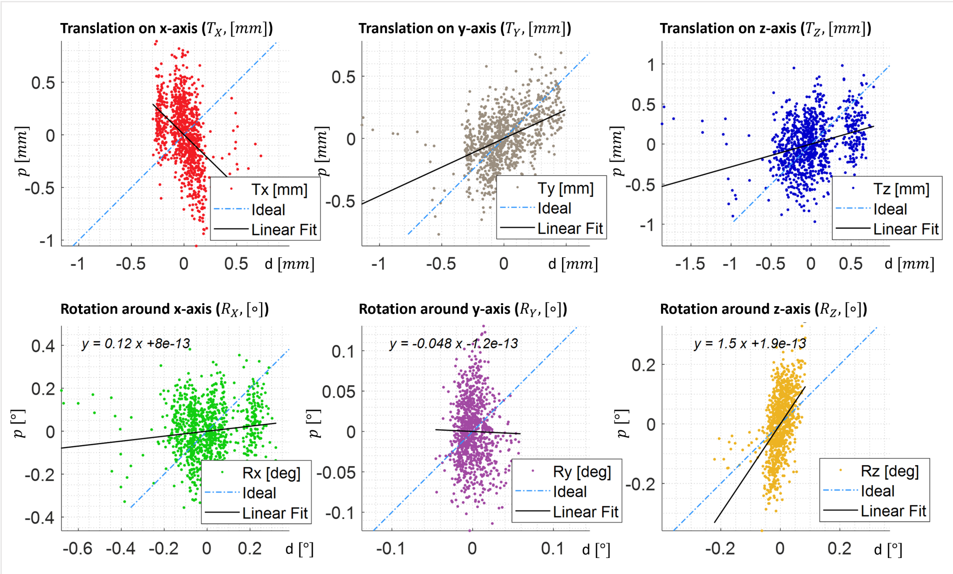

Figure 7.9: The figure shows results obtained for *small* head movements, sampled using the *cloth* probe-holder set-up for *Subject* 4, *linear* regression method (Table 7.1). Prediction results are *poor* (Equation 5.5). Statistical evaluation of the results is reported in Table 7.9.

	Slope	Intercept	R^2	PC	MSE	STD
T_x [mm]	−0.979	< 0.001	0.187	0.432	0.155	0.139
T_y [mm]	0.461	< 0.001	0.214	0.463	0.048	0.212
T_z [mm]	0.284	< 0.001	0.087	0.296	0.140	0.322
R_x [°]	0.116	< 0.001	0.015	0.123	0.028	0.129
R_y [°]	−0.048	< 0.001	< 0.001	0.018	0.002	0.015
R_z [°]	1.497	< 0.001	0.237	0.487	0.009	0.034

Table 7.9: Values of the slope and intercept of the linear fit are reported along with the values of R^2, the standard deviation (STD) and the mean squared error (MSE) and Pearson correlation coefficient (PC), for each of the motion parameters and prediction reported in Figure 7.9. Values have been rounded to three decimal places.

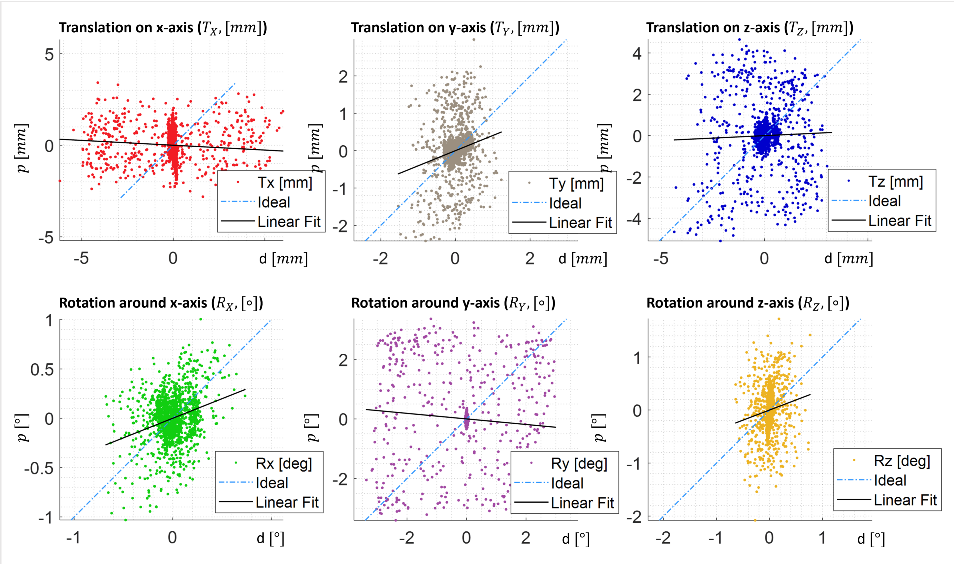

Figure 7.10: The figure shows results obtained for *large* head movements, sampled using the *cloth* probe-holder set-up for *Subject* 4, *linear* regression method (Table 7.1). Prediction results are *poor* (equation 5.5). Statistical evaluation of the results is reported in Table 7.10.

	Slope	**Intercept**	$\mathbf{R^2}$	**PC**	**MSE**	**STD**
$\mathbf{T_x}$ **[mm]**	−0.053	< 0.001	0.010	0.102	4.535	1.819
$\mathbf{T_y}$ **[mm]**	0.405	< 0.001	0.038	0.196	0.493	0.332
$\mathbf{T_z}$ **[mm]**	0.047	< 0.001	0.001	0.033	3.065	1.016
$\mathbf{R_x}$ [°]	0.397	< 0.001	0.079	0.281	0.067	0.175
$\mathbf{R_y}$ [°]	−0.093	< 0.001	0.008	0.090	2.720	1.097
$\mathbf{R_z}$ [°]	0.381	< 0.001	0.020	0.143	0.167	0.151

Table 7.10: Values of the slope and intercept of the linear fit are reported along with the values of R^2, the standard deviation (STD) and the mean squared error (MSE) and Pearson correlation coefficient (PC), for each of the motion parameters and prediction reported in Figure 7.10. Values have been rounded to three decimal places.

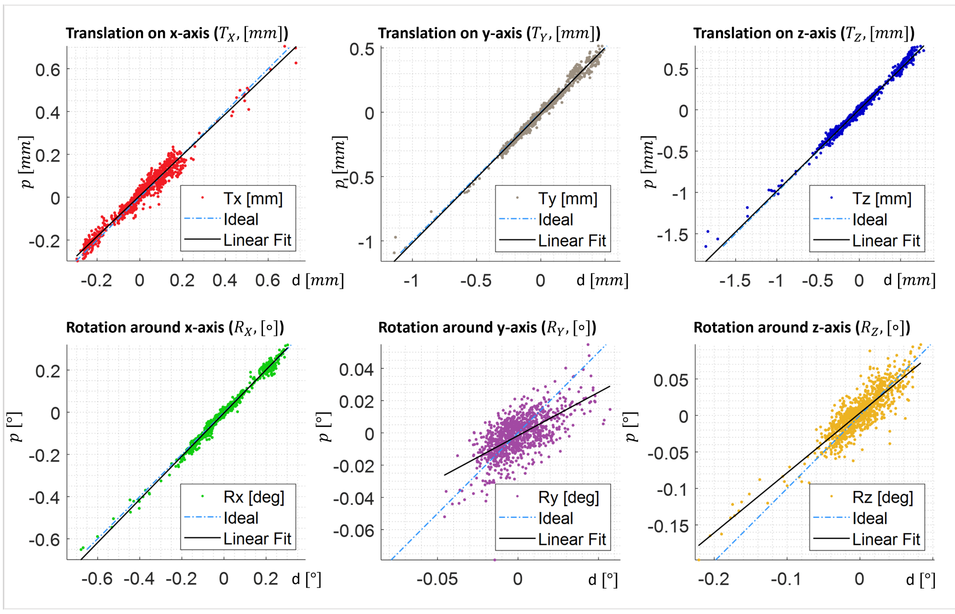

Figure 7.11: The figure shows results obtained for *small* head movements, sampled using the *cloth* probe-holder set-up for *Subject* 4, using *raw* data for training the $non-linear$ regression method (Table 5.1.3). Prediction results are *good* (equation 5.5). Statistical evaluation of the results is reported in Table 7.11.

	Slope	Intercept	$\mathbf{R^2}$	PC	MSE	STD
$\mathbf{T_x}$ [mm]	0.952	0.007	0.960	0.980	0.001	0.138
$\mathbf{T_y}$ [mm]	1.012	−0.004	0.985	0.993	0.001	0.211
$\mathbf{T_z}$ [mm]	0.987	0.003	0.988	0.994	0.001	0.321
$\mathbf{R_x}$ [°]	1.024	−0.004	0.988	0.994	< 0.001	0.129
$\mathbf{R_y}$ [°]	0.536	−0.002	0.404	0.636	< 0.001	0.015
$\mathbf{R_z}$ [°]	0.820	0.003	0.757	0.870	< 0.001	0.034

Table 7.11: Values of the slope and intercept of the linear fit are reported along with the values of R^2, the standard deviation (STD) and the mean squared error (MSE) and Pearson correlation coefficient (PC), for each of the motion parameters and prediction reported in Figure 7.11. Values have been rounded to three decimal places.

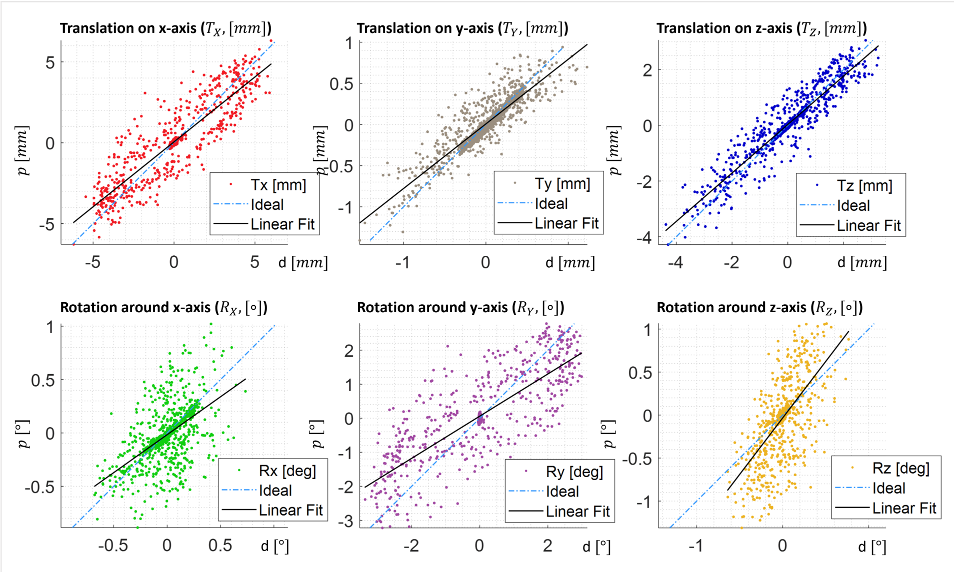

Figure 7.12: The figure shows results obtained for *large* head movements, sampled using the *cloth* probe-holder set-up for *Subject* 4, using *raw* data for training the $non-linear$ regression method (Table 5.1.3). Prediction results are *poor* (equation 5.5). Statistical evaluation of the results is reported in Table 7.12.

	Slope	Intercept	$\mathbf{R^2}$	PC	MSE	STD
$\mathbf{T_x}$ [mm]	0.803	0.056	0.778	0.882	0.742	1.821
$\mathbf{T_y}$ [mm]	0.785	0.008	0.800	0.894	0.022	0.332
$\mathbf{T_z}$ [mm]	0.869	0.028	0.869	0.932	0.136	1.017
$\mathbf{R_x}$ [°]	0.711	−0.016	0.324	0.569	0.035	0.175
$\mathbf{R_y}$ [°]	0.620	0.061	0.634	0.796	0.444	1.098
$\mathbf{R_z}$ [°]	1.313	−0.032	0.403	0.635	0.061	0.151

Table 7.12: Values of the slope and intercept of the linear fit are reported along with the values of R^2, the standard deviation (STD) and the mean squared error (MSE) and Pearson correlation coefficient (PC), for each of the motion parameters and prediction reported in Figure 7.12. Values have been rounded to three decimal places.

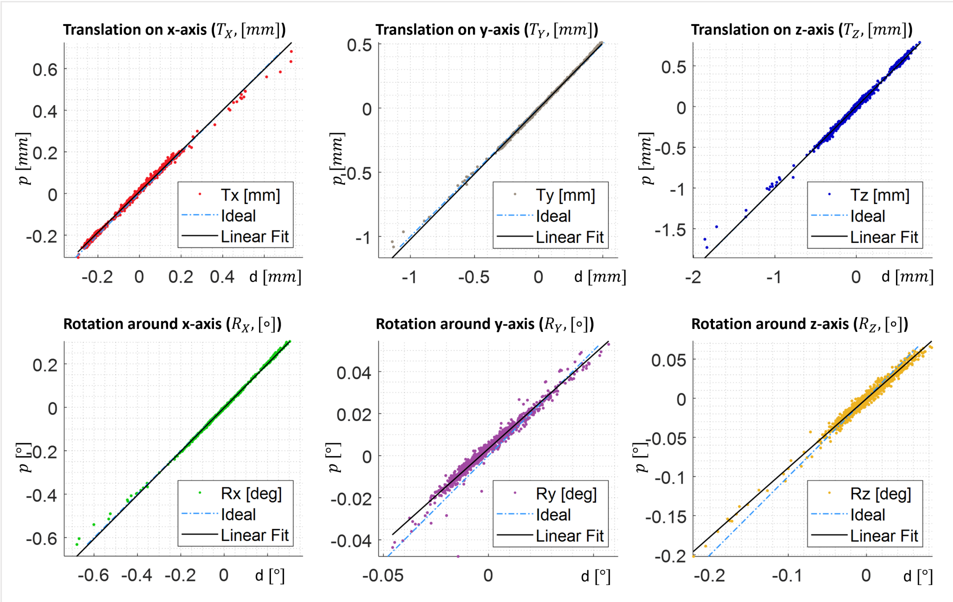

Figure 7.13: The figure shows results obtained for *small* head movements, sampled using the *cloth* probe-holder set-up for *Subject* 4, using $pre-processed$ data for training the $non-linear$ regression method (Table 5.1.3). Prediction results are *good* (equation 5.5). Statistical evaluation of the results is reported in Table 7.13.

	Slope	**Intercept**	$\mathbf{R^2}$	**PC**	**MSE**	**STD**
$\mathbf{T_x}$ **[mm]**	0.979	0.009	0.995	0.998	< 0.001	0.138
$\mathbf{T_y}$ **[mm]**	1.019	-0.003	0.998	0.999	< 0.001	0.211
$\mathbf{T_z}$ **[mm]**	0.996	-0.003	0.994	0.997	0.001	0.321
$\mathbf{R_x}$ [°]	1.008	-0.001	0.998	0.999	< 0.001	0.129
$\mathbf{R_y}$ [°]	0.895	0.003	0.967	0.983	< 0.001	0.015
$\mathbf{R_z}$ [°]	0.882	-0.001	0.979	0.989	< 0.001	0.034

Table 7.13: Values of the slope and intercept of the linear fit are reported along with the values of R^2, the standard deviation (STD) and the mean squared error (MSE) and Pearson correlation coefficient (PC), for each of the motion parameters and prediction reported in Figure 7.13. Values have been rounded to three decimal places.

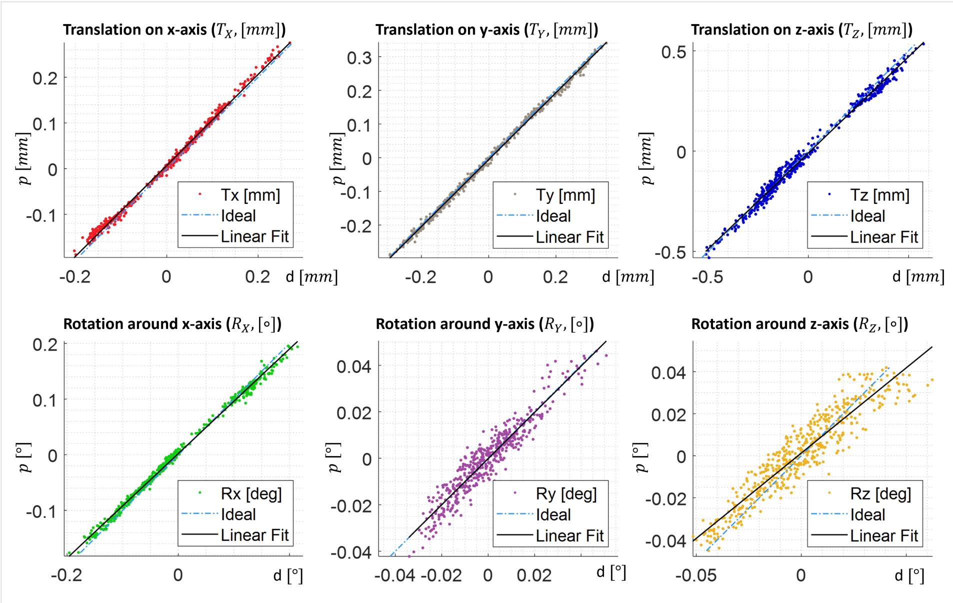

Figure 7.14: The figure shows results obtained for *small* head movements (less time point), sampled using the *cloth* probe-holder set-up for *Subject* 4, using $pre - processed$ data for training the $non - linear$ regression method (Table 5.1.3). Prediction results are *good* (equation 5.5). Statistical evaluation of the results is reported in Table 7.14.

	Slope	**Intercept**	$\mathbf{R^2}$	**PC**	**MSE**	**STD**
$\mathbf{T_x}$ **[mm]**	0.995	0.007	0.995	0.998	< 0.001	0.105
$\mathbf{T_y}$ **[mm]**	0.994	-0.006	0.998	0.999	< 0.001	0.160
$\mathbf{T_z}$ **[mm]**	0.959	-0.009	0.991	0.995	0.001	0.256
$\mathbf{R_x}$ [°]	0.940	0.002	0.996	0.998	< 0.001	0.099
$\mathbf{R_y}$ [°]	0.994	< 0.001	0.898	0.948	< 0.001	0.015
$\mathbf{R_z}$ [°]	0.811	0.001	0.875	0.935	< 0.001	0.023

Table 7.14: Values of the slope and intercept of the linear fit are reported along with the values of R^2, the standard deviation (STD) and the mean squared error (MSE) and Pearson correlation coefficient (PC), for each of the motion parameters and prediction reported in Figure 7.14. Values have been rounded to three decimal places.

7.2 Extending the markerless tracking method over subjects

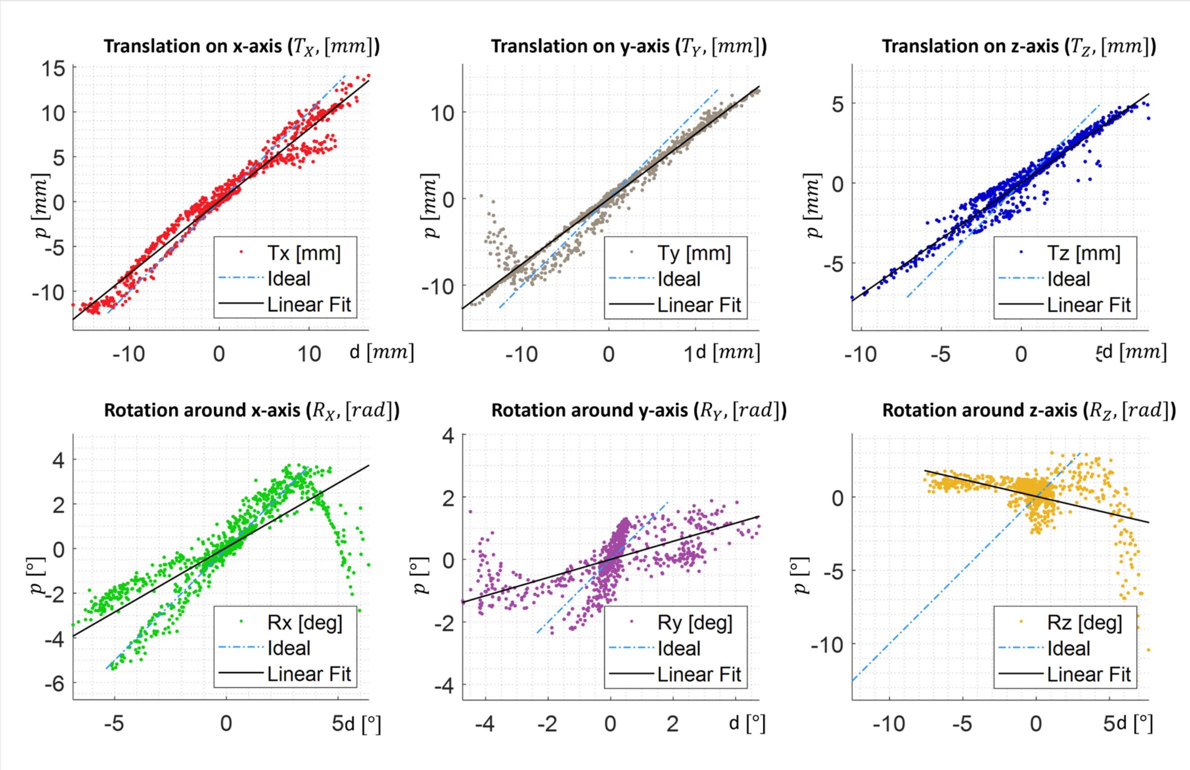

Figure 7.15: *Prediction of motion data of Subject 4 obtained using the PLS method trained on Subject 5.* Simulated magnetic field data (ΔB_{Head}) due to the whole range of head movements have been used to train the linear regression method (PLS) for Subject 5. Probes were simulated as in the cloth probe holder. The prediction results are very poor. This is expected as the relationship between extra-cranial field changes and head movements is highly subject-dependent (Figure 4.10).

In previous chapters, it has been shown using simulated and experimental data that head motion (ΔM) can be monitored by using an NMR field camera to measure the extra-cranial field changes (ΔB) produced by changes in head position ($f(\Delta B) = \Delta M$). The function used to describe the mathematical relationship depends only on ΔB. Although this provides a marker-less approach to head motion monitoring, the extra-cranial field changes are highly subject-specific (Figure 4.8), and it is therefore necessary to learn the relationship between field measurements and head movements for each subject to use the motion tracking to predict head motion. Figure 7.15 shows that very poor performance in motion prediction results when using the model learnt from one subject to analogue data from a different subject. The reason is that when considering data from more than

one subject, the field-motion relationship cannot be described as a bijective function as the same change in head position (output variable) may not correspond to the same change in magnetic field (input variables) because of the change in relative head-probe distances due to different head morphology. So, to generalise the prediction method over different heads, further input parameters are needed ($f(\Delta B, I_1, I_2, ...I_n) = \Delta M$).
In this section, various set of additional parameters have been tested. Initially, they were only dependent on features (such as head volume and dimension), then also scanner parameters (off-centre[2] and angulation[3]) were taken in account.

7.2.1 Preliminary tests

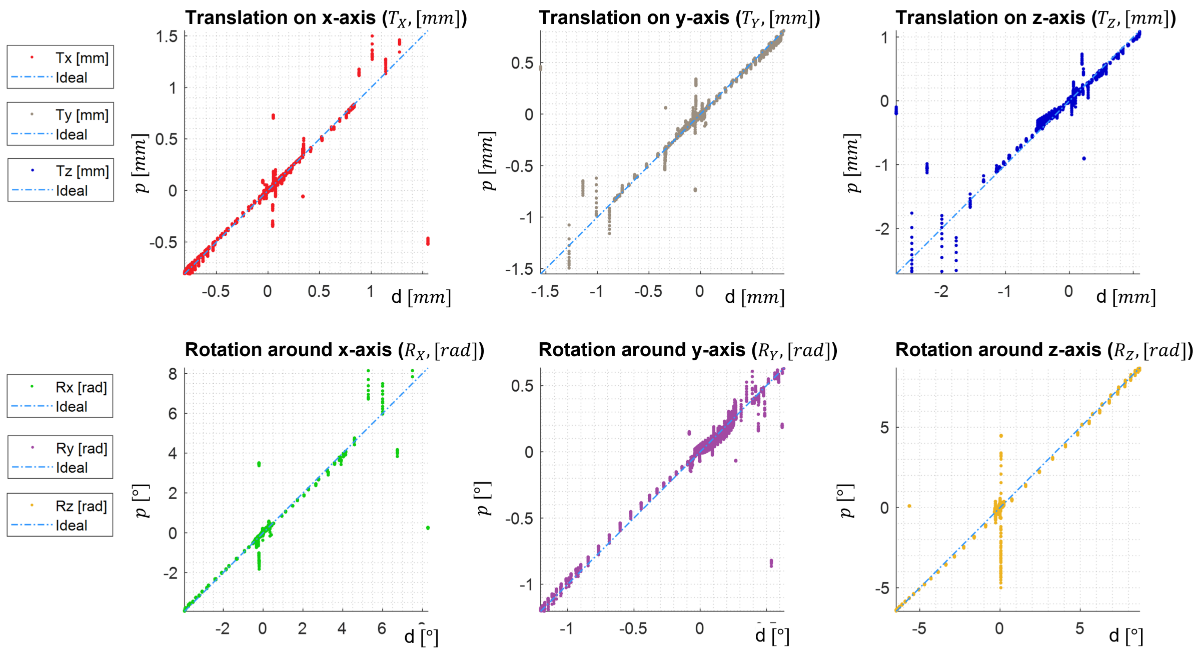

Figure 7.16: *Prediction on head phantoms.* Plots show the prediction (dots), the ideal fit (dashed blue line) and the linear fit (black line) for the 6 motion parameters, obtained by training a $NARX$ network on *simulated* data obtained by moving 11 scaled versions of the *same head* using the *same motion* parameters sets (total: $\approx$ 19300 time steps, corresponding to $\approx$ 50 minutes of acquisition).

An early attempt to generalise the prediction has been made with *ad hoc* simulated and experimental data (Subjects 1, 2, 3 and 6) obtained using the PVC support. In

[2] *off-centre*. Position of the image volume with respect the scanner system of reference.
[3] *Angulation*. Angulation of the image volume with respect the scanner system of reference.

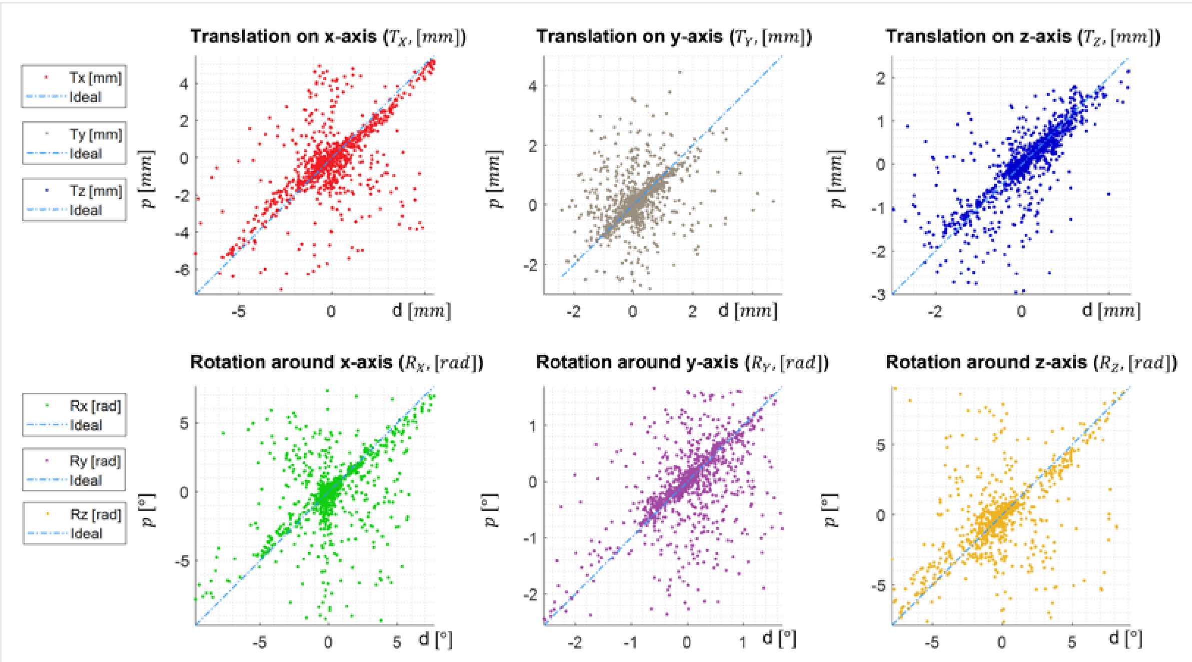

Figure 7.17: *Prediction on subjects.* Plots show the prediction (dots), the ideal fit (dashed blue line) obtained by training a $NARX$ network on real data over 4 different subjects (total: $\approx$ 12800 time steps, corresponding to $\approx$ 31 minutes of acquisition). The variability problem of head dimensions is not overcome due to the small numbers of subjects and time steps. However, a good portion of data lay on the ideal fit line, in particular for larger extents of head motion.

the former case, head models were made by scaling the HUGO head by factors ranging from 50% to 110%. Also, motion parameters were the same for all of the simulations as the smoothed/detrended data series was considered. Probes were simulated to be in the PVC support. These data were in fact the ones used to make Figure 4.8. Predictions were performed using the non-linear auto regressive exogenous model (NARX) as it easily allows to add extra parameters to differentiate the subjects.

The additional neural network inputs were the head dimensions and volume (Figure 4.7), which were used in conjunction with a subset of magnetic field measurements from 8 probes selected by performing PCA on the measurements from all 16 probes. The number of hidden neurons in the model was fixed to 30.

Figures 7.16 and 7.17 show the predicted head motion parameters as a function of the actual movement parameters used in the simulations to predict the head motion of the scaled heads (ideal condition) and for the real subjects, respectively. In Figure 7.16, formed using data from the scaled HUGO model, data points largely fall on lines of unit slope and zero intercept indicating good prediction performance, while in Figure 7.17, formed using experimental data from multiple subjects, only a small portion of data points coincide with the ideal prediction.

For the real subject data shown in Figure 7.17 many variables have changed compared to the ideal situation tested with the phantom head (Figure 7.16) and this may explain the fact that results were much worse. In the former case the same scaled head was used for 11 measurements (large range of head movements), and so the morphology was constant and only the head-probe distances were varying. In the latter case, the number of heads was reduced to 4 and all had different morphologies, and the range of head volumes was smaller. In the former case, all the simulations were made by using the same motion data series, while in the latter the motion data series were different for each subject. The results consequently show the influence of head volume and morphology and extent of movement on the measured fields. Predictions of movement from a simulated data set including data from heads of different sizes, but the same morphology, indicate that incorporating additional information about head size and geometry into the prediction process may improve results.

The reasonably good performance of the NARX method in predicting head movements from simulated and measured extra-cranial field changes when provided information about head size as well as field data from a range of scaled models of the head, provides some motivation for exploring this approach with experimental data. Additional or alternative information such as head position and angulation in the scanner, or 3D anatomical MRI data could also be provided to further improve the accuracy of estimation. These possibilities have been explored using simulated magnetic field changes due to synthetic head motion data from 19 subjects. These data have been used to test the feasibility of predicting head motion parameters over different subjects using the non-linear regression method in close-to-real experimental conditions.

7.2.2 Synthetic head motion data to generate simulated magnetic field data

Time series of head motion parameters have been randomly simulated for each subject, using a superposition of harmonic movements:

$$R(t)_n = Acos(\omega t + \phi) \tag{7.1}$$

$$T(t)_n = \frac{-atan(sind(R(t)_n)}{cos(R(t)_n))}\, 10^{-1} \tag{7.2}$$

where $R(t)_n$ is the basic harmonic function for rotational movements, with amplitude A (in $^\circ$), angular frequency ω ($\omega = 1\pi f$, with f frequency in rad/s), t time and ϕ the phase. $T(t)_n$ represents the projection of the rotation on the z-x plane. The translational motion was scaled down by a factor of 10 in order to make the synthetic movements similar to those in experimental data.

	ω $[rad/s]$	A ($[^\circ]$)	ϕ	**Predominant Movement**
Respiration	[0.2, 0.4]	[0, 5]	[0, 1]	R_x
Heart beat	[0.8, 1.0]	[0, 1]	[0, 1]	*(None)*
Shake	[0.1, 0.9]	[0, 15]	[0, 1]	R_z
Nod	[0.1, 0.9]	[0, 15]	[0, 1]	R_x

Table 7.15: *Synthetic movements parameters.* The values shown in the square brackets are the range of each variable of the Equation 7.1. Values were randomly chosen in these range.

Involuntary and voluntary movements can be represented by changing A, ω, ϕ. These values were randomly selected for each different subject from the range of values experimentally observed (Table 7.15). For the resting condition, the dominant movements are due to the cardiac cycle and chest expansion. In each cardiac cycle, the heart contraction (average $\omega = 0.9$ $[Hz]$) causes a cycling movement of the head [127]. In each breathing cycle (average $\omega = 0.3$ $[Hz]$), the chest expansion causes a cyclic movement of the head (that corresponds to R_x in the scanner frame) [134]. The voluntary movements (e.g. shake, R_z, or nod (R_x) could be simulated by adding a further harmonic centred on the frequency of the movement.

Highly symmetric and periodic data simulated using Equation 7.1 do not represent a real situation and may not help training the neural network on general cases. So, an additional degree of randomness has been added to break the symmetry of the cosine function used to simulate the harmonics. A random series of numbers (r_i) with 0 average and 0.1 STD (as in true optical measurements) has been created using the built-in MATLAB function `normrnd`. This, has been used as input to evaluate an asymmetric function ($a(r_i)$) that depends on a non-linear combination of the inputs:

$$r_i = normrnd(0, 0.1, [1 : i]) \tag{7.3}$$

$$a(r_i) = r_i sin(r_i^2) + r_i^3 \tag{7.4}$$

In real MRI scans, the *off-centre* (in $[mm]$) and *Angulation* (in $[^\circ]$) parameters reflect the offset of the centre of the head from the isocentre of the scanner and its orientation relative to the scanner geometry. These are generally evaluated manually during the survey performed before the MR sequence. They are taken into account during the pre-processing of motion data (section 5.1.2). So, they have been simulated too using random extraction (`normrnd`):

$$Off\ centre = normrnd(0, 15, [1,\ 3]) \tag{7.5}$$
$$Angulation = normrnd(0, 1, [1,\ 3]) \tag{7.6}$$

The resulting head motion time series was similar enough to the real measurement to justify the use of it to generate synthetic head motion data series to be used in the simulation of the extra-cranial magnetic field changes (Chapter 4).

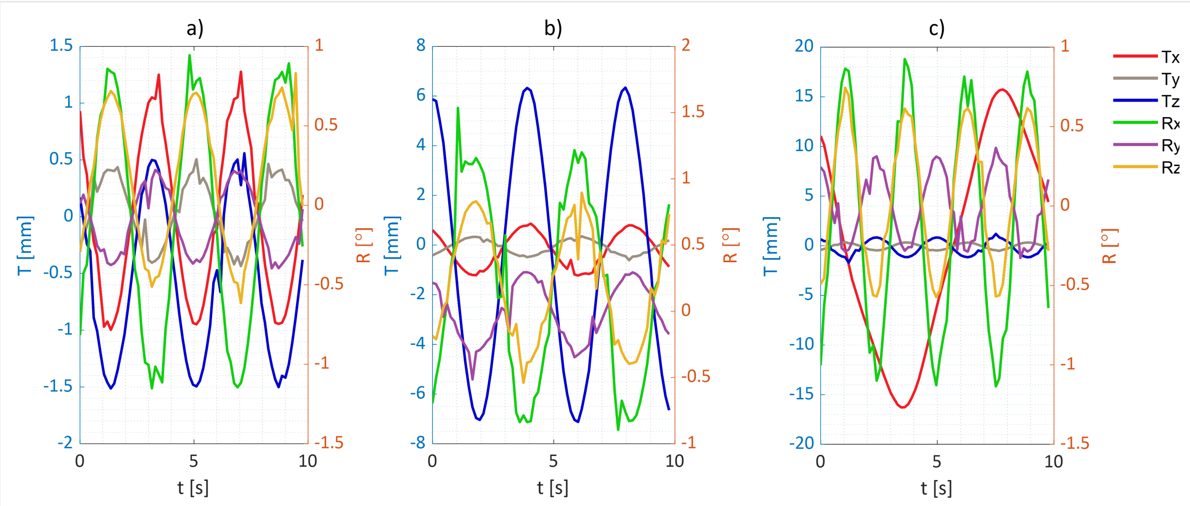

Figure 7.18: *Example of artificial head movements.* The plots show examples of different artificial head movements: (a) at rest, (b) head shaking and (c) head nodding. Data were simulated based on statistics reported in Table 7.15.

7.2.3 Customised head models and simulated magnetic field data

In order to extend the span of data from which the NARX learns the relationship between the magnetic field and the head movements, 19 custom head models were considered, using the simulation approach described in Chapter 4. Two dimensional representations of the models implemented in the simulation are shown in Figure 7.19.

Head motion parameter time series have been randomly generated as explained in the previous section (7.2.2). Harmonic movements were generated using (equation 7.1) (in the rest condition only chest expansion was considered and the symmetry was broken using equation 7.3) and used in a step-by step simulation of the magnetic field perturbation (see the code in the Appendix D.4). Simulated extra-cranial magnetic fields have

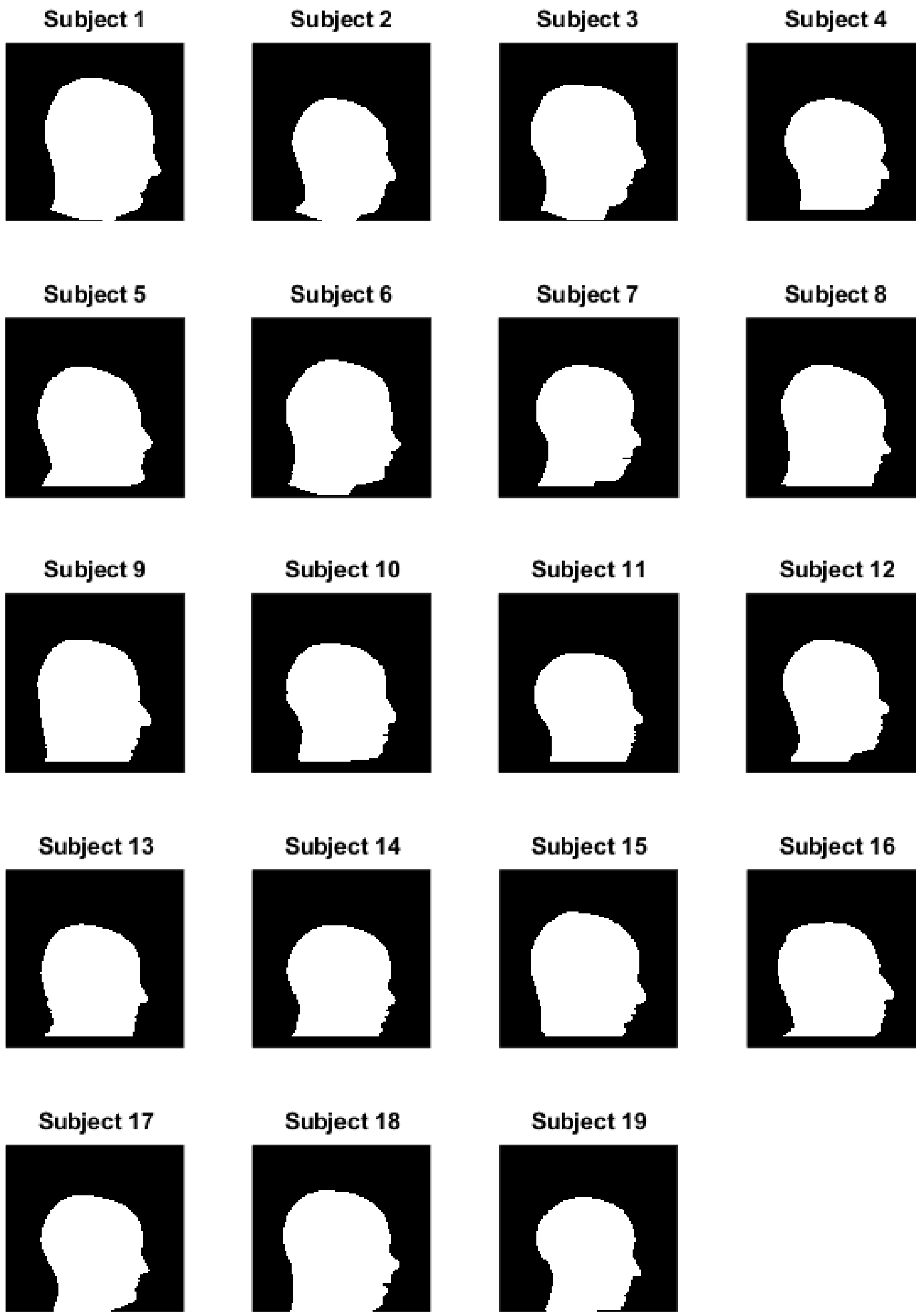

Figure 7.19: *3D head models.* The picture shows a central sagittal slice from each of the 3D head models used for simulations in this chapter Subjects 1 to 19) and in other parts of this dissertation (Subjects 1 to 6). Models have been obtained as described in Figure 4.2. Black regions represent air, white parts correspond to water ($\chi = -9$ *ppm*). [MRI pictures made through years of research in the MEG (Magnetoencephalography) lab at Sir Peter Mansfield Imaging Centre (University of Nottingham). Thanks to the MEG group for providing them for this simulation].

been processed in the same way as was done for data recorded during simultaneous EPI (Figure 7.1). Signals from the probes on the back of the head (probes 10, 11, 15 and 16) were not used to perform head motion tracking done with real data. Neither physiological noise (Section 4.3) nor electronic noise (white Gaussian noise with STD $\approx 10^{-8}$.) were added this time as previous results (Section 5.2.2) showed that this doesn't significantly influence the outcome of the prediction in case of qualitative analysis.

7.2.4 Span of magnetic field data

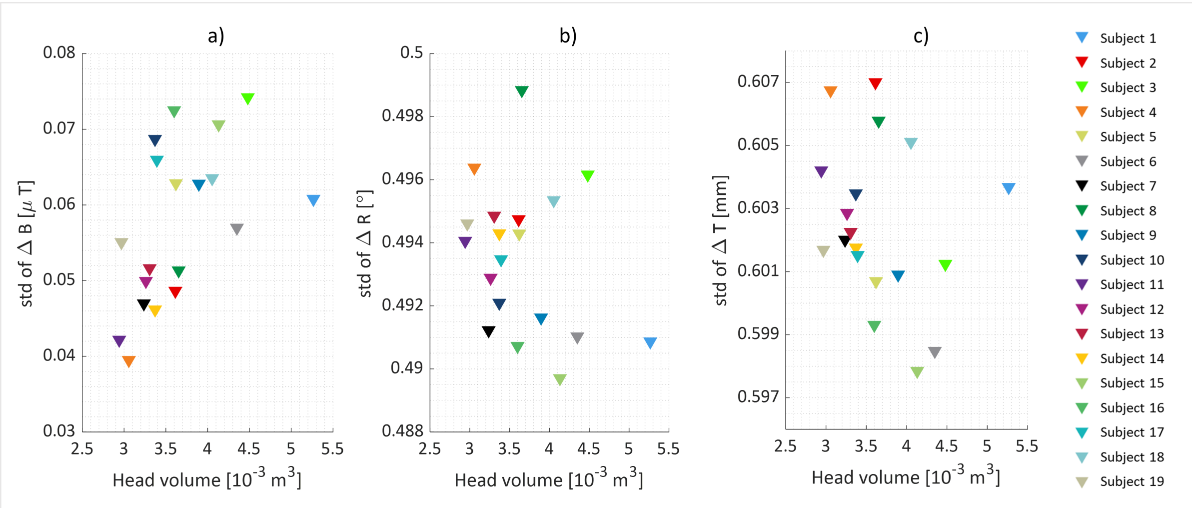

Figure 7.20: *STD of simulated magnetic field data obtained using synthetic head motion data.* (a) Variation of the average over of probes of the standard deviation of the field measurements with simulated head volumes for subject simulations, for resting head motion conditions (similarly to Figure 4.8). The magnetic field was sampled in the cloth probe folder set-up that was used to perform prediction on experimental data acquired with simultaneous EPI scanning (Figure 7.1). Effects of the head-probe distances due to head morphology is still visible as a large head volume corresponds to a larger STD. (b) and (c) show the STD of the rotations and translations, respectively, of the synthetic head motion parameters. These are results comparable with real data reported in section B.2.

Figure 7.20 shows the range of head volumes, ΔB, ΔR and ΔT simulated. These and the random simulated off-centre and angulation values represent the additional input data used to train the NARX. A wider range of combinations has been covered compared to previous data (Figure 4.8). This will help the training of the NARX over n-subjects as the span of head volumes and the consequent variation of the field changes (due to head motion) is better sampled.

In order to avoid to over-fitting the regression model, 1000 simulated time-steps for each subject were used to train the network (19000 time steps in total). As described in Subsection 5.1.3, the non-linear regression models (NARX) were trained using time series comprised of 85% (16150 time steps) of each data-set, in order to save 15% (2850 time steps) of the data for testing. The time correlation of the data was not considered as the training time series was further randomly divided into $90\% - 5\% - 5\%$ to create training, validation, and test data-sets ($1435 - 808 - 808$ time steps respectively).

The model that best performed over 10 training runs (where each time the random selection of subgroups is done) was selected in order to minimize the influence due to the random initialization of neuron weights and so the error on the prediction.

7.2.5 Predicting head motion over several subjects using the non-linear regression method

The best of the 10 trained NARX was used to predict head motion parameters from the new data (2700 time steps). Figure 7.21 shows that the network trained over several subjects (using magnetic field data, head volume, head off-centre and angulation parameters) is able to predict reasonably well (Table 7.16) new data from the same group of subjects.

Subject 1 (Cloth, NARX, Pre-processed, Small)						
	Slope	**Intercept**	$\mathbf{R^2}$	**PC**	**MSE**	**STD**
$\mathbf{T_x}$ [mm]	0.956	−0.006	0.968	0.984	0.016	0.699
$\mathbf{T_y}$ [mm]	0.998	−0.006	0.971	0.986	0.002	0.279
$\mathbf{T_z}$ [mm]	0.978	−0.013	0.981	0.990	0.010	0.700
$\mathbf{R_x}$ [$\circ$]	0.957	0.024	0.973	0.986	0.014	0.699
$\mathbf{R_y}$ [$\circ$]	1.011	0.011	0.936	0.968	0.003	0.210
$\mathbf{R_z}$ [$\circ$]	0.970	−0.010	0.980	0.990	0.004	0.419

Table 7.16: Values of the slope and intercept of the linear fit are reported along with the values of R^2, the standard deviation (STD) and the mean squared error (MSE) and Pearson correlation coefficient (PC), for each of the motion parameters and prediction reported in Figure 7.21. Values have been rounded to three decimal places.

Testing the robustness of the trained non-linear method. The final goal would be to train a network on a subgroup of volunteers (using magnetic field changes, head volumes and the off-centre and angulation information as input variables to predict head motion) and then apply to new groups of volunteers. The trained neural network was therefore tested on new data. In order to avoid to over-fitting the regression model, 1000 simulated time-steps for 18 subjects were used to train the network (18000 time steps in total). Data from Subject 9 were used for the final testing (1000 time steps) of the data for testing. As described in Subsection 5.1.3, the time correlation of the data was not

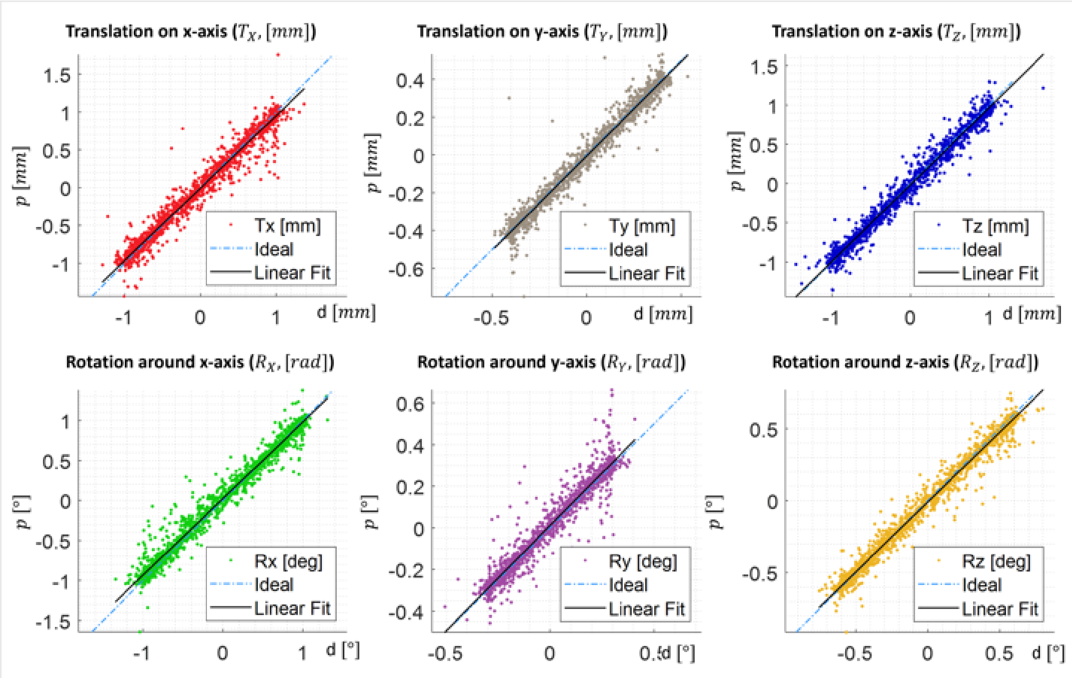

Figure 7.21: The figure shows results obtained for *synthetic* head movements, sampled using the *cloth* probe-holder set-up for *simultaneous* EPI scanning for *subjects* number $1-19$, using 14250 data for training the non-linear regression method on the whole range of subjects. Prediction results are *good* (equation 5.5). Statistical evaluation of the results is reported in Table 7.16.

considered as the training time series was further randomly divided into $90\%-5\%-5\%$ to create training, validation, and test data-sets ($16200-900-900$ time steps respectively).

Data simulated for Subject 9 were used to test the robustness of the network on predicting motion parameters for a new subject as data of Subject 9 fell in the middle of the $STD_{\Delta B}(Volume)$ (Figure 7.20) space sampled. Data were normalised by the scaling factor used for normalising training data. Results are reported in Figure 7.22.

The effects of the head probe distance on magnetic field data is clear: the NARX can somewhat apply the mathematical relationship learned as most of the predicted data lie on a straight line, but the slope of the line is scaled or the intercept is far from zero or both.

7.3 Conclusion

Experimental magnetic field data acquired using the set-up that allows simultaneous imaging has been characterised (Subsection 7.1.1). Data acquired with and without si-

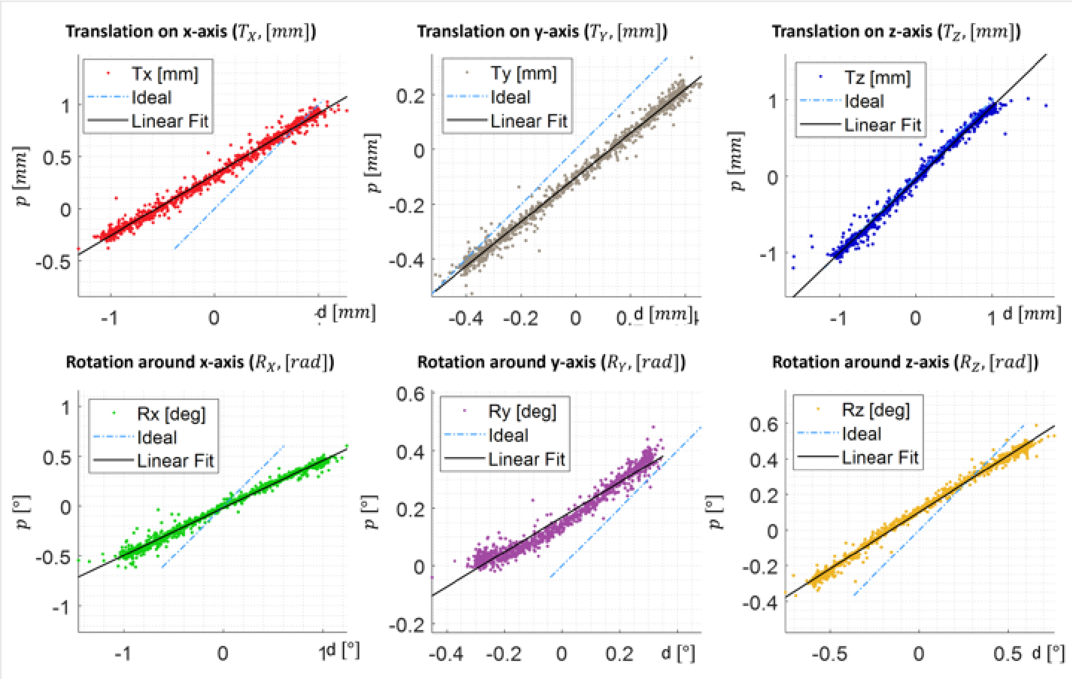

Figure 7.22: The figure shows results obtained for *synthetic* head movements, sampled using the *cloth* probe-holder set-up for *simultaneous* EPI scanning for *Subject* 9, using the best *network* obtained using data from Subjects number 1-18. Prediction results are *poor*, but the data follows a linear behaviour.

multaneous scanning are similar when the field is measured 30 ms after the RF pulse of the EPI acquisition. Magnetic field data acquired with simultaneous scanning (Subsection 7) have been further characterised and this successfully confirmed previous results relating to the efficacy of prediction. Predictions of head motion parameters obtained using both regression methods have been carried out (Section 7.1.5). The non-linear regression method has been confirmed to outperform the linear approach (Figure 7.13).

These data have also been used to flag significant head movements (Subsection 7.1.3) and to measure a respiration-like signal (Subsection 7.1.4) retrospectively. The measured extra-cranial magnetic field has been demonstrated to be a valid contact-less signal for discriminating between tolerated and exaggerated head movements and to evaluate the respiration of the subject also during scanning. Both uses could facilitate a motion prevention technique, as the former could be used as a warning to interrupt the scanning sequence and the latter could be used as respiratory gating trigger for scan acquisition. Furthermore, by training a regression method, the signal could be predicted n-steps ahead and provide information for real-time scanner control.

In the future, the use of purely simulated data to train the regression method might provide a further development of the technique. Improvements on the simulation program would involve further optimisation (e.g. parallel programming) to reduce the time necessary to produce a ≈ 1000 data point time series (equal to ≈ 2 hours with the system used) and a better approximation of the magnitude of the data (e.g. by acquiring the MR image to obtain the head model and the probe positions in the same scanning session and frame of reference).

A tentative way to generalise the results reported in this Chapter over several subjects has been described in Section 7.2. The results show that by adding parameters that take into account the head size and position in the scanner, a trained non-linear method may be able to predict head motion over several subjects without the need for a subject-dependant supervised learning phase. The generalised neural network over 19 Subjects produced reasonable results on new data from a subject that belonged to the former group (Figure 7.21), while not performing as well on predicting head movements from a subject that was not in the group (Figure 7.22). However, the predictions follow a linear behaviour that differs from the ideal one with a slope, that is not equal to unity, a non-zero intercept or both. This suggests that it might be possible to find a proportional factor to re-calibrate the results of the network for new subjects and to avoid the need to train different networks for group of subjects that fit given features (e.g. head volume, Figure 7.20).

7.3.1 Comparison with other tracking systems

The motion tracking and motion detection techniques developed in this thesis compete with existing techniques (Section 2.2, Figure 2.10) in terms of set-up, accuracy and MR compatibility. The fully in-bore probe-holder set-up used (Figure 3.3) has been developed to be compatible with a 32-Channel Nova Head coil, but due to its fully flexible nature, it could be easily adapted to other head coil solutions. Accuracy is limited by the accuracy of the secondary tools used to record the training dataset (± 0.01 *mm or* °), so in its future development this could be improved by choosing a different tracking system (e.g. Figure 3.3.f). The development of a new tracking tool, with higher accuracy than the MPT camera and based on the NMR field probe system, is presented in the next Chapter (Subsection 6.3.1). As the length of the training data set acquisition is on the order of magnitude of 10 minutes (considering the case where training is only done over a small range of head movements), we expect that the choice of the secondary tool would suit most of the subjects. The use of a dedicated navigator scanning sequence would certainly fit most of the cases including pediatric and non-collaborative subjects. Further improvements in the training phase could be realised by the use of an external screen to suggest movements to perform.

To conclude, the technique developed, once the regression method is trained, does not require the use of a mouthpiece, markers nor line-of-sight access neither the need to modify the image sequence to localize the head (e.g. Figure 3.3.a,f), nor the acquisition of extra MR data (e.g. Figure 3.3.a,e). Accuracy limits are ± 0.01 *mm or* $^{\circ}$, which are worse compared to other NMR probe based technique[4] (order of magnitude of the *nm*) and better than self navigator approaches [82] (order of magnitude of 0.1 *mm*). The range of movements has been limited to small head movements to improve the accuracy, but there is a potential to generalise it to a larger range of movements. Also, it required to be trained for each acquisition on the specific subject, but the idea for a future generalisation over several subjects has been presented in this thesis (Section 7.2). Table 7.17 reports the comparison of the method developed in this Thesis to other methods.

A further approach, not explored in this thesis, would be to investigate changes in the trained neural network neurons over a subject to look for mathematical relationships that would allow the trained network easily to adapt to different subjects. Once generalised, the technique would be a fully plug-and-play head motion tracking solution, suitable for PMC and RMC MoCo techniques. It has been evaluated that eight probes would be sufficient to have a valid magnetic field signal for the technique; use of a reduced number of probes would reduce the cost of the implementation.

A further development of the tracking technique might lead to its application to body imaging. The NMR field probes would track the body motion to correct the MR image. Feasible solutions would require a solid structure to be placed around the body that records magnetic field changes due to the body motion. The regression method would be calibrated using MR body images (as is done with the FatNav technique). Another feasible solution would involve coupling the NMR field probes to the body (similar to other NMR-probe-based techniques [4]) and to track probe positions during the scanning sequence.

	Thesis	MPT	NMR markers	Navigator
Method	NMR field probes	MPT camera	NMR field probes	Sequence-based
Need for line of sight access	No	Yes	No	No
Skull-coupling	Contact-less	Marker-based (skin, mouthpiece)	Marker-based (Plastic glasses)	Contact-less
Range of movements	Small range only for better accuracy ($\leq 5\ mm, \leq 5°$), skip-redo strategy for large range	Any range of movements that are in the sight of access area	Any range of movements (up to $\leq 50\ mm, \leq 10°$)[60]	Any range of movements where the head remains in the FOV of the MR image
Accuracy	Limited by the training method (MPT)	$0.1\ mm,\ 0.1°$	$0.05\ mm,\ 0.03°$	$0.2\ mm,\ 0.3°$
Pre-scanning operations	Training the regression method (up to 20 minutes)	Cross-calibration (up to 45 minutes)	No	No
Delay on updating scanner geometry (PMC)	Not tested	$\approx 15ms$	Less than 1 s [60]	Depends where the Nav.sequence happens in the scanning sequence
Generalising over image sequences	As NMR marker method	It doesn't interfere with imaging sequence	Optimal	Optimal
Comfort	Optimal	Poor even over subjects able to tolerate the marker support	Acceptable	Optimal
Generalising over subjects	Good, but it needs to be trained for each subject	Good over subjects able to tolerate the marker support	Good over subjects able to tolerate the marker support	Good

Table 7.17: *Comparisons of various in-bore motion tracking techniques.* The table reports comparisons of the tracking method developed in this Thesis with well-known optical (MPT), NMR markers and Navigator sequence methods [5, 121, 122] (Figure 2.10.d,e,f). The method developed in this thesis will overcome some issues by combining the best features of the compared methods shown in the table. It will be contact-less, fully MR and MR sequence compatible and suitable over subjects.

Chapter 8

Conclusion

In this dissertation, a novel approach to ameliorating motion artefacts in UHF MRI has been explored. It does not require image sequence modification or use of markers that are directly coupled to the head for this implementation. The results on predictions reported here confirm that measurements of extra-cranial field changes made with a field camera (with probes placed between the receiver array and volume transmit head coil) can be used to monitor head position in a 7T MRI scanner. The best predictions of the head motion parameters during EPI scanning were obtained using a non-linear regression method.

8.0.1 Set-ups to hold field camera in the MRI scanner

The use of two set-ups has been explored. The first, was rigid and made of PVC (Figure 3.7). It was sited inside the RF transmit head coil, requiring removal of the standard RF receiver coil array. The second, was flexible and made of cloth and recycled material (Figure 3.3). It allowed the NMR field probes to be positioned in between the RF transmit coil and the receiver coil array (in various positions). This allowed the 32-channel receiver array to be used for signal reception with all the advantages it offers in terms of sensitivity and parallel imaging capability. This second holder allowed extra-cranial magnetic field measurements to be made during scanning with standard MRI sequences (such as EPI).

NMR probe FIDs. The FID signal decays from the NMR probes have been characterized in the different set-ups. The results (Figures 3.7, 3.8) show that the FIDs are well characterised by exponential decays in the case of cloth holder. The decay times were similar to those measured using a foam holder which is the optimal arrangement for signal longevity. This is in contrast to the measurements made with the PVC holder where the decays are more sinc-like and apparent relaxation times are shorter. However,

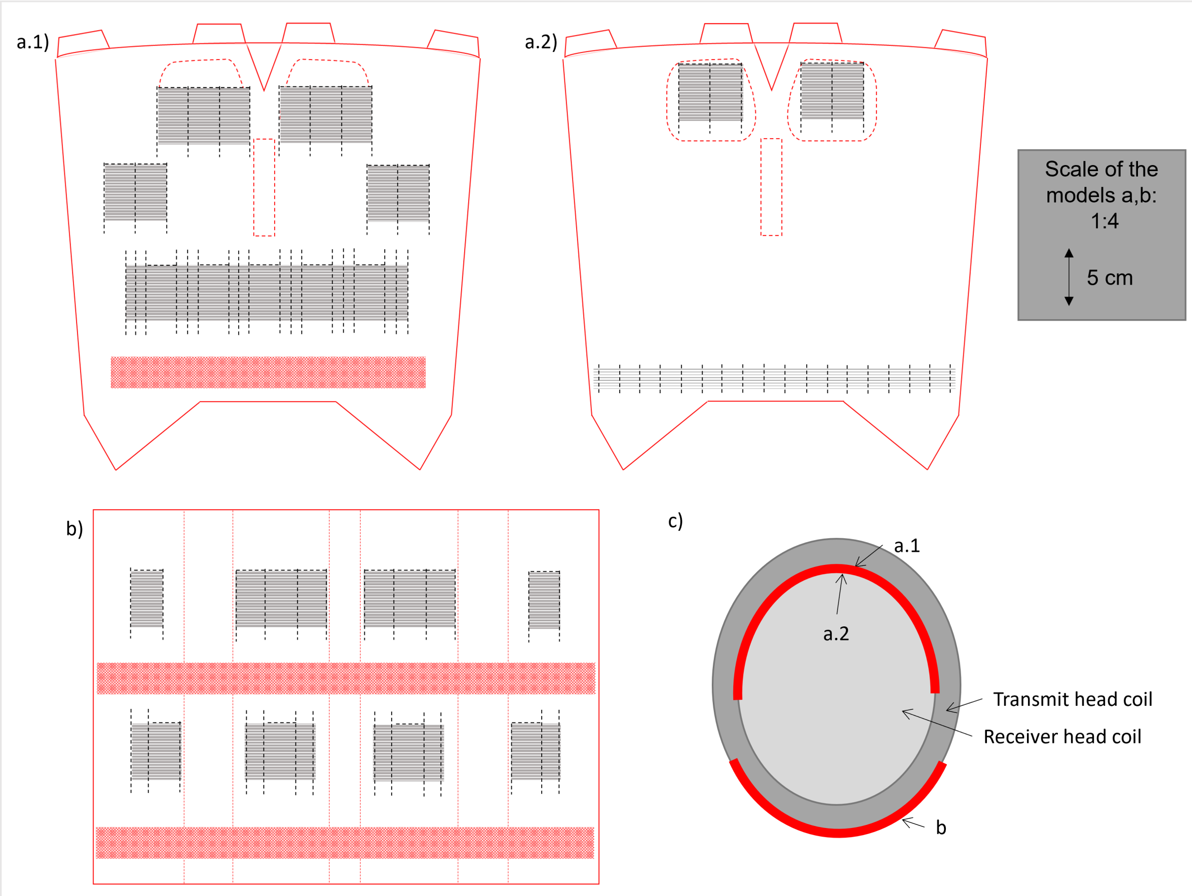

Figure 8.1: *Final design of the probe holder.* Gray: elastic band to hold the probes (31 pockets in total). White: elastic band to hold the cables. Red Velcro used to trap the cables. Dashed red lines: reference lines used to align the support to the head coil. (a) Upper part (a.1 top view, a.2 bottom view). (b) Bottom part. (c) Scheme of the system mounted.

due to the fact that only the first 5 ms of the measurements are generally used to calculate the magnetic field, the measurements made using the PVC probe holder were not significantly influenced by these effects (arising from field inhomogeneities produced by air/PVC boundaries oriented perpendicular to the field).

Probe positions. Comparisons of the effect of different probe positions have been reported in Figure 3.4 and the main difference was due to the more even sampling of the extra-cranial space provided by the PVC holder. The probe positioning influences the standard deviation of the measured data as shown in Figure 4.9 and in data reported in the Appendix B.2. Based on the results of predicting head movements using the different set-ups (Appendix C), the cloth support was adjusted to provide a more symmetrical distribution of probe positions and this set-up was used to acquire data during simultaneous EPI. This has helped to improve the accuracy of the movement parameter predictions (Figure 7.11). The final version of the cloth probe holder is shown in Figure 8.1.

8.0.2 Magnetic field data

SNR of magnetic field data. The background noise in magnetic field measurements inside the 7T scanner has been evaluated as the RMS of one set of empty scanner measurements (Figure 3.9, Section 3.2.1). The results show that the background noise has the order of magnitude of $10^{-8}\,T$. In order to evaluate the SNR over all the measurements (Figure 4.11), it has been assumed that the RMS of the background noise was constant over different days of measurements and experimental set-ups.

Head-probe relative displacements. The relative position and distance between the head and the NMR probes of the field camera determines the standard deviation of the magnetic field changes measured during head movements. Figure 4.9 shows that to produce large field changes the probes need to be placed close to the head such that head movement produces large changes in the head-probe separation. The standard deviation of the magnetic field changes produced by head movement has been further explored by using simulated data and customized head models. Figures 4.8 and 4.10 also indicate that the standard deviation of the magnetic field changes are most influenced by the head-probe distances, showing coherent results over a range of movements and head shapes.

Measurement of extra-cranial field changes during concurrent EPI. In the case where extra-cranial magnetic field measurements were made during simultaneous image acquisition using a multi-slice EPI sequence, it was necessary to evaluate the time delay needed between the end of the EPI acquisition and the field measurement to produce field values that were not affected by the applied gradients and associated eddy currents (section 7.1.1). A delay from the slice selective RF pulse of 30 ms has been chosen based on analysis of Figures 7.3 and 7.4. Measurements with and without simultaneous EPI data acquisition (Table 7.4 and Figures 7.5 and 7.6) confirm that this choice is good as the standard deviation of the field measurements is similar with and without concurrent EPI.

Spatial filter. As shown in Figure 5.6, different sources contributes to the measured extra-cranial magnetic fields. These include: movements of the head, chest expansion and noise (Figures 6.5, 6.5). To perform predictions of head motion parameters, we need to separate out the magnetic field changes due to head motion. A spatial filter has therefore been developed (as described in Section 5.1.1. Code is reported in the Appendix D) and tested on simulated (Figure 5.15) and real data. The filter's core steps involve fitting the magnetic field data using the solid harmonics up to the second order (Figure 5.4), selecting the highest harmonics fits to reduce the influence of physiological noise and then performing feature selection using the hierarchical cluster analysis representation of the signal in principal component space. This filtering successfully reduces the influence of physiological noise on data. However the biggest impact on the prediction is on significantly reduced the time needed for training when finding the model relating the extra-cranial magnetic field measurements to head motion parameters.

Alternative method to evaluate respiration signal. Application of a spatial filter also allows evaluation of the zero order field component, that mainly carries information about the effect of chest movement due to respiration (Figure 6.5). Filtering this signal by applying a temporal band-pass filter allows the respiration to monitored (Figure 6.4). In most MR scanners respiration is monitored using a small set of bellows placed under the sternum and held in place with a respiratory belt that is squeezed in each cycle of respiration. Measuring respiration using NMR field probes has the advantage of not requiring attachment of additional measurement apparatus to the patient during scanning.

8.0.3 Detection of large head movements

The magnitude of the extra-cranial magnetic field changes varies with the extent of motion (Figure 4.8). It is therefore possible to discriminate the size of head motion by evaluating the size of the field changes produced. This allows a threshold for field change/movement to be set (Section 6.1). Once a tolerable level of motion is defined, it can be used to define the thresholds for each channel. Thresholds over the probes were first considered constant (Figure 6.1) and then different (Figures 6.2 and 7.7). In both cases there were a certain number of probes that detected when large head motion occurs. In the former case, the number of probes varies the most, while in the latter it was constant over time. Finding the correct criteria to use in deciding when to stop a scan automatically or to re-scan some k-space data so as to avoid significant motion artefacts will require further work.

8.1 Head motion tracking

A novel head motion tracking technique for MoCo has been developed through the use of both simulated and real data. Prediction results of head motion parameters were coherent over several approaches and the best one identified was then used to perform prediction on data acquired during EPI scan.

8.1.1 Simulated magnetic field data

Simulations provided ideal noiseless data that was useful for evaluating the performance of different approaches. Customized head models of 6 subjects (Figure 4.1) and a well-known segmented head model [26] were used. The extra-cranial magnetic field distribution was evaluated using a FFT method [126] and sampled at probe-like positions. Step-by step simulations of extra-cranial magnetic field changes were made by using true head motion parameters measured using an MPT camera. The process took ≈ 6 s per time step on my personal laptop[1] which is a reasonable time for producing long series of synthetic data. Additional noise sources were also simulated. Magnetic field changes due to chest expansion (Section 4.3) and Gaussian noise were considered (in agreement with the measured noise values reported in Section 3.2.1).

Examples of simulating data with the cloth probe holder are reported in Figures 4.4 and 4.5. Simulated data are shown to be comparable to experimental measurements in terms of order of magnitude and behaviour. Simulated data was then successfully used to identify the best regression method to perform prediction of head motion parameters from extra-cranial magnetic field changes for different ranges of movement and probe set-ups (Figure 5.15).

8.1.2 Set-ups

Both the probe holders were successfully used to acquire valid measurements for predicting head motion parameters from extra-cranial magnetic field changes. As the distance between the head and the probes strongly influences the magnitude of the field changes, the results differ for different set-ups. Thanks to the even sampling of the space due to the even distribution of probe positions, the PVC set up (Figure 3.7) is more sensitive to large head motion (Figure 4.9). The cloth probe holder (Figure 3.3) is more flexible over acquisitions in terms of choosing the position of the probes. To perform measurements, the probes were mainly clustered at the front of the head, at eye-level. This choice lead to a reduction in sensitivity to large head motion. Furthermore, the signals from the three probes placed on the back of the head were mostly influenced by chest movement in respiration and so were not useful for prediction of head movement. To perform measurements with simultaneous EPI data acquisition (Figure 7.1), probes were more evenly spread over the front and sides of the head and the quality of the predictions improved.

[1] Processor: Intel(R) Core(TM), i7-8550U, CPU 1.80G Hz, RAM 16 Gb

8.1.3 Regression methods

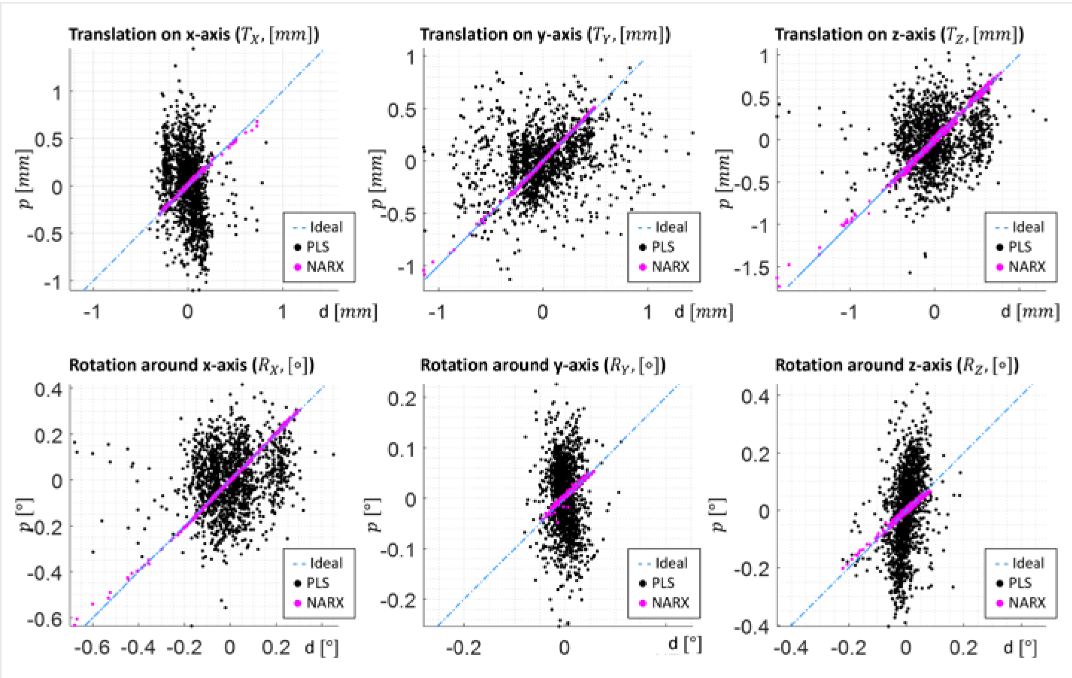

Figure 8.2: *Prediction of head motion parameters during a EPI scan.* Plots overlap worst and best prediction of head motion parameters shown in Section 7.1.7, using PLS and NARX methods (Figures 7.9 and 7.13 respectively) compared with the ideal prediction. It is clear that the NARX method outperforms PLS in the case were training data (both magnetic field and head motion parameters) were acquired without simultaneous EPI and the trained regression method is then used on new data acquired with simultaneous EPI.

The main goal of this project has been achieved by predicting head motion parameters from extra-cranial magnetic field changes (Section 5.1.3). Two different ways to perform predictions have been tested (Sections 5.1.3, code in the Appendix D.2), both producing good results on simulated and real data (Section 5.2.2, Tables 5.3, 5.5 and 7.6). The predictions were evaluated based on linear fit of predicted data plotted as a function of the real data (Appendix 5.1.4). Decisions on how many motion parameters were predicted well out of six was based on the criteria reported in Equation 5.5. Different choice of criteria may lead to different outcomes. The Partial Least Squares method predicts poorly compared to the Non-linear AutoRegressive with eXogenous Inputs (NARX) neural network. The non-linear method should therefore be used for future work.

8.1.4 Range of head movements

During the experiment, the subjects performed various different head movements (rest, feet-wiggling, head shaking or head nodding) in order to sample a variety of head movements potentially to allow to the regression methods to learn the head motion-magnetic field changes mathematical relationship. However, the relationship may differ significantly for different ranges of motion as the magnitude of the magnetic field changes does not vary linearly with the extent of motion for large movements (Figure 4.8).

This was evident from the results obtained. Data were divided into two subgroups for training the regression methods on two ranges of movement; small (rest, feet-wiggling) and large (rest, feet-wiggling, head shaking, head nodding). Both the linear and non-linear methods can be trained to predict a large range of head movements (Figures 5.8, 5.11, 5.12, and Figures in the Appendix C.2, C.4, C.6 and C.8), but the accuracy of prediction for small head movements, the most common condition that occurs during a MRI scan, is then poor (Figure 5.9). To improve prediction of large head movements, different probe positions in the cloth support may be explored in the future. Predictions on small range of head motion obtained by the non-linear regression method when trained on data acquired with a small range of head motion gave excellent results (Figure C.7, C.10). This approach has therefore been further tested on data measured with simultaneous EPI (Figure 8.2) and analysis of this data confirmed the results obtained from data acquired without concurrent image acquisition.

8.1.5 Timing of the prediction process

A combination of the marker-less motion tracking method with image acquisition involves having a training phase (without simultaneous EPI), where simultaneous measurements of head motion parameters and extra-cranial magnetic field changes are acquired, pre-processed and used to train the linear regression method. The method can be used for new data acquired with simultaneous EPI data acquisition.

The training phase to predict small head motion will last approximately 20 minutes as approximately 17 minutes (Table 7.1) are necessary to acquire measurements and approximately 3 minutes are necessary to pre-process data, train 10 Neural Networks and select the best one (Table 7.8).

This represents an improvement compared to using the tracking method for the whole duration of the MRI acquisition.

8.2 Pilot-studies for future works

8.2.1 Active magnetic marker system

A simulation of a new head motion tracking system based on the use of two active magnetic markers (Figure 6.9) was presented. The markers could be fixed onto a pair of glasses worn by the subject. The magnetic field of those could be detected by the NMR field probes and a machine learning technique is used to predict the position of those in the space from that. Results (Figures 6.13, 6.14) show that the prediction of head motion parameters was good for a 1nT noise level. In its future implementation, a higher SNR would help the performance. Since the level of noise in the MRI scanner cannot be changed, it would be necessary to increase the signal. Options are to increase the current that is driven the coils, but this was lead to other issues (e.g. the torque of the small dipoles in the magnet will increase, making the system more unstable) or to increase the number of magnetic markers on the glasses.

This solution represents an improvement compared to other marker-based motion correction techniques as it doesn't require to solve the correspondence problem [69] to find the marker system position, does not require line of sight access from detector to marker [8] does not interfere with the imaging sequence and the markers-NMR probe paired system is fully MRI compatible [35]. Furthermore, the precision of the tracking could be controlled by the stopping criteria of the algorithm rather then the physical property.

The position of the markers has been determined using a least square regression function based method in this simulation, but other options could be explored. For example, it could be worth to try to train a neural network on synthetic data and then applied it on real data as the mathematical model that generate the synthetic data is well defined (Equation 6.4).

8.2.2 Generalized prediction

A pilot study was conducted on simulated data as a proof of concept that training a neural network on a large subgroup of collaborative subjects[2] may lead in the future to a fully marker-lees technique ready to be used on a large groups of subjects (either collaborative or not) without further need for training the network with concurrent optical measurements.

[2] Collaborative subjects are subjects able to wear the bite bar necessary to use the optical method to perform simultaneous measure of magnetic field changes and head position to train the network

The use of additional geometric parameters helps to restore the bijective mathematical relationship between magnetic field changes and head motion parameters. For its future development, additional parameters may be used as inputs. The NMR probe positions could be used as input, but in general these positions very similar in different scanning sessions. It might however be useful to input the distances from features on the head to the probes rather than using the off-centre and angulation information.

A further degree of complexity may be added to the architecture of the network in order to model more complex mathematical relationships. Changes to the architecture might involve increasing the number of hidden neurons (equal to 30 in this work) or adding a further hidden layer (a single hidden layer has been used here). A new balance between the number of neurons over the layers would then need to be found.

Use of more data for training would help the network to learn the relationship between extra-cranial field changes and head pose. This could be achieved with the same number of subjects as used here (19) but using more data-points per subject for training. Alternatively more subjects could be considered keeping the number of data-points fixed.

Changing the architecture and/or the nature of the data might lead to over-fitting. To prevent to over-fitting, it may be also useful to train different networks for different groups of head volumes (e.g. $\in [2.5,\ 3.5]$, $\in [3.0,\ 4.0]$, $\in [3.5,\ 4.5], \ldots\ [10^{-3}m^3]$). Overlapping the head volumes on those groups will lead to there being at least two possible models for each head that can help in motion correction.

Bibliography

[1] Mclaren J et al. "Prospective motion correction in brain imaging: a review." In: *Magneti Resonance in Medicine* 69.3 (2013), pp. 621–636. DOI: doi:10.1002/mrm.24314.

[2] Verma G and Balchandani P. "Ultrahigh field MR Neuroimaging". In: *Top Magn Reson Imaging* 28.3 (2019), pp. 137–144. DOI: doi:10.1097/RMR.0000000000000210. URL: https://www.ncbi.nlm.nih.gov/pmc/articles/PMC6784841/.

[3] Godenschweger F. et al. "Motion correction in MRI of the brain". In: *Phys Med Biol* 61.5 (2016), R32–R56. DOI: https://doi.org/10.1088/0031-9155/61/5/R32. URL: https://www.ncbi.nlm.nih.gov/pmc/articles/PMC4930872/.

[4] Alexander Aranovitch et al. "Prospective motion correction with NMR markers unsing only native sequence elements". In: *Magnetic Resonance in Medicine* (Aug. 2017).

[5] Martin Eschelbach et al. "Comparison of prospective head motion correction with NMR field probes and an optical tracking system". In: *Magnetic Resonance in Medicine (MRM)* (July 2018). DOI: mrm.27343. URL: https://onlinelibrary.wiley.com/doi/full/10.1002/mrm.27343.

[6] Julian Maclaren et al. "Navigator accuracy requirements for prospective motion correction". In: *Magnetic Resonance in Medicine* 63.1 (Jan. 2010), pp. 162–170. DOI: https://doi.org/10.1002/mrm.22191.

[7] Welch EB et al. "Spherical navigator echoes for full 3D rigid body motion measurement in MRI". In: *Magnetic Resonance in Medicine* 47.1 (2002), pp. 32–41. DOI: doi:10.1002/mrm.10012. URL: https://pubmed.ncbi.nlm.nih.gov/11754440/.

[8] Zaitsev M et al. "Magnetic resonance imaging of freely moving objects: prospective real-time motion correction using an external optical motion tracking system". In: *Neuroimage* 31.3 (2006). DOI: doi:10.1016/j.neuroimage.2006.01.039. URL: https://pubmed.ncbi.nlm.nih.gov/16600642/.

[9] Julian Maclaren et al. “Prospective motion correction using coil-mounted cameras: Cross-calibration considerations”. In: *Magn Reson Med.* 79.4 (2017), pp. 1911–1921. DOI: https://doi.org/10.1002/mrm.26838. URL: https://onlinelibrary.wiley.com/doi/abs/10.1002/mrm.26838.

[10] Robert Odenbach et al. “Remotely controllable phantom rotation system for ultra-high field MRI to improve Cross Calibration”. In: *Current Directions in Biomedical Engineering* 5.1 (2019), pp. 429–431. DOI: doi:10.1515/cdbme-2019-1570538325. URL: https://doi.org/10.1515/cdbme-2019-1570538325.

[11] Bortolotti L. et al. “Test of multiple sensor set-up for head motion characterization during MRI acquisition”. In: *University of Bologna* (Oct. 2017). DOI: 14564. URL: https://amslaurea.unibo.it/14564/1/Tesi_LB_2017.pdf.

[12] Laura Bortolotti and Richard Bowtell, eds. *Measuring extracranial magnetic field changes due to head motion during multi-slice EPI acquisition.* 1379. ISMRM, May 2021.

[13] Laura Bortolotti and Richard Bowtell, eds. *Prediction of head motion parameters by measuring extracranial magnetic field changes during multi-slice EPI acquisition.* Vol. MAGMA. S6.P17. ESMRMB, Oct. 2021. URL: https://doi.org/10.1007/s10334-021-00947-8.

[14] Laura Bortolotti et al., eds. *Simulation of external magnetic field changes due to head motion during 7 Tesla MRI scan.* 4432. ISMRM, 2019.

[15] Laura Bortolotti et al., eds. *Measurement of head motion using a field camera in a 7 T scanner.* 0464. ISMRM, 2020.

[16] Laura Bortolotti et al., eds. *Non-contact measurement of head movements inside a 7 T Scanner using a 16-channel field camera.* 4431. ISMRM, May 2019.

[17] Bortolotti Laura and Richard Bowtell, eds. *Non-linear model to predict head motion using a magnetic fieldcamera in a 7 T MRI scanner.* Vol. MAGMA. L01.104. ESMRMB, Oct. 2020. URL: https://link.springer.com/content/pdf/10.1007.

[18] Laura Bortolotti and Richard Bowtell, eds. *Using NMR field probes to flag significant head movement at 7T.* 3363. ISMRM, Aug. 2020.

[19] Laura Bortolotti and Richard Bowtell, eds. *Simulating the use of active magnetic markers for motion correction using NMR field probes on a 7T scanner.* 1365. ISMRM, May 2021.

[20] James A. Smith, Penny Gowland, and Paul Glover. “Motion Correction for MRI using External Tracking Devices”. In: *University of Nottingham* (2018). DOI: 4236650.

[21] Hanson and Lars G. "Is quantum mechanics necessary for understanding magnetic resonance?" In: *Concepts in Magnetic Resonance Part A* 32A.5 (2008), pp. 329–340. DOI: https://doi.org/10.1002/cmr.a.20123. eprint: https://onlinelibrary.wiley.com/doi/pdf/10.1002/cmr.a.20123. URL: https://onlinelibrary.wiley.com/doi/abs/10.1002/cmr.a.20123.

[22] Brian A. Hargreaves. "Bloch equation simulations". In: (2002). URL: http://mrsrl.stanford.edu/~brian/bloch/.

[23] Bloembergen N., Purcell E. M., and R. V. Pound. "Relaxation Effects in Nuclear Magnetic Resonance Absorption". In: *Phys. Rev.* 73 (7 1948), pp. 679–712. DOI: 10.1103/PhysRev.73.679. URL: https://link.aps.org/doi/10.1103/PhysRev.73.679.

[24] McRobbie Donald W. et al. *MRI from Picture to Proton*. 3rd ed. Cambridge University Press, 2017. DOI: 10.1017/9781107706958.

[25] Joel Mispelter, Mihaela Lupu, and Andre Briguet. "NMR PROBEHEADS for biophysical and biomedical experiments - Theorical Principles and Practical Guidelines". In: *Imperial College Press* 1 (2006), p. 21.

[26] Collins CM et al. "Numerical calculations of the static magnetic field in three-dimensional multi-tissue models of the human head." In: *Magnetic Resonance Imaging* 5.20(5) (June 2002), pp. 413–24.

[27] Karin Markenroth Bloch, ed. *7T High Field Physics*. E7841. ISMRM, Aug. 2020. URL: https://cds.ismrm.org/protected/20MPresentations/videos/dcvz/E7841.htm.

[28] Michael N. Hoff et al. "Safety Considerations of 7-T MRI in Clinical Practice". In: *Radiology* 292.3 (2019). DOI: https://doi.org/10.1148/radiol.2019182742. URL: https://pubs.rsna.org/doi/10.1148/radiol.2019182742.

[29] Pohmann R, Speck O, and Scheffler K. "Signal-to-noise ratio and MR tissue parameters in human brain imaging at 3, 7, and 9.4 tesla using current receive coil arrays." In: *Magn Reson Med.* 75.2 (2016), pp. 801–9. DOI: doi:10.1002/mrm.25677.. URL: https://pubmed.ncbi.nlm.nih.gov/25820458/.

[30] Matthias J. P. van Osch and Andrew G. Webb. "Safety of Ultra -High Field MRI: What are the Specific Risks?" In: *Curr Radiol Rep* 2.61 (2014). DOI: https://doi.org/10.1007/s40134-014-0061-0. URL: https://link.springer.com/article/10.1007/s40134-014-0061-0.

[31] Poser BA and Setsompop K. "Pulse sequences and parallel imaging for high spatiotemporal resolution MRI at ultra-high field." In: *Neuroimage* 168 (2017), pp. 101–118. DOI: doi:10.1016/j.neuroimage.2017.04.006.. URL: https://pubmed.ncbi.nlm.nih.gov/28392492/.

[32] Christoph Barmet et al. "A transmit/receive system for magnetic field monitoring of in vivo MRI". In: *Magn Reson Med* (2009). DOI: https://doi.org/10.1002/mrm.21996.

[33] Nicola De Zanche et al. "NMR probes for measuring magnetic fields and field dynamics in MR systems". In: *Magnetic Resonance in Medicine (MRM)* (June 2008). DOI: MagnResonMed60:176186,2008.. URL: https://onlinelibrary.wiley.com/doi/full/10.1002/mrm.21624.

[34] Christoph Barmet, Nicola De Zanche, and Klaas P. Pruessmann. "Spatiotemporal magnetic field monitoring for MR". In: *Magnetic Resonance in Medicine (MRM)* 60 (June 2008), pp. 187–197. URL: https://onlinelibrary.wiley.com/doi/full/10.1002/mrm.21603.

[35] Benjamin E. Dietrich et al. "A field camera for MR sequence monitoring and system analysis". In: *Magnetic Resonance in Medicine (MRM)* (2015). DOI: mrm.25770. URL: https://onlinelibrary.wiley.com/doi/10.1002/mrm.25770.

[36] Niklas Wehkamp et al. "Frequency-adjustable magnetic field probes". In: *Magn Reson Med.* 85.2 (2020), pp. 1123–1133. DOI: https://doi.org/10.1002/mrm.28444. URL: https://onlinelibrary.wiley.com/doi/10.1002/mrm.28444.

[37] Michael Kazhdan, Thomas Funkhouser, and Szymon Rusinkiewicz. "Rotation Invariant Spherical Harmonic Representation of 3D Shape Descriptors". In: *Eurographics Symposium on Geometry Processing* (2003).

[38] *Relating external magnetic field changes to head movement using motion and field cameras.* May 2017. DOI: 0303. URL: cds.ismrm.org/protected/17MPresentations/abstracts/0303.html.

[39] Skope. "Acquisition System (16 Channels, G2), Manual". In: (2016). DOI: https://skope.swiss/.

[40] Oliver Speck, ed. *Motion Compensation and Correction.* E1156. ISMRM, Aug. 2020. URL: https://cds.ismrm.org/protected/20MPresentations/videos/dcvz/E1156.htm.

[41] Jalal B. Andre et al. "Toward Quantifying the Prevalence, Severity, and Cost Associated With Patient Motion During Clinical MR Examinations". In: *Journal of the American College of Radiology* 12.7 (2015), pp. 689–695. ISSN: 1546-1440. DOI: https://doi.org/10.1016/j.jacr.2015.03.007. URL: https://www.sciencedirect.com/science/article/pii/S1546144015001441.

[42] Jakob M. Slipsager et al. "Quantifying the Financial Savings of Motion Correction in Brain MRI: A Model-Based Estimate of the Costs Arising From Patient Head Motion and Potential Savings From Implementation of Motion Correction". In: *Magnetic Resonance in Medicine* 52.3 (2020). DOI: https://doi.org/10.1002/jmri.27112.

[43] Ali Syed H. et al. “Reducing Clinical MRI Motion Degradation Using a Prescan Patient Information Pamphlet”. In: *American Journal of Roentgenology* 200.3 (2013), pp. 630–634. DOI: https://doi.org/10.2214/AJR.12.9015.

[44] E Törnqvist et al. “Impact of extended written information on patient anxiety and image motion artifacts during magnetic resonance imaging”. In: *Acta Radiologica* 47.5 (2006), pp. 474–480. DOI: https://doi.org/10.1080/02841850600690355.

[45] Bruce I. Reiner. “Hidden Costs of Poor Image Quality: A Radiologist’s Perspective”. In: *Journal of the American College of Radiology* 11.10 (2014), pp. 974–978. ISSN: 1546-1440. DOI: https://doi.org/10.1016/j.jacr.2014.04.008. URL: https://www.sciencedirect.com/science/article/pii/S1546144014002117.

[46] Castella R. et al. “Controlling motion artefact levels in MR images by suspending data acquisition during periods of head motion”. In: *Magn Reson Med* (2018). DOI: https://doi.org/10.1002/mrm.27214.

[47] Daniel Stucht et al. “Highest Resolution In Vivo Human Brain MRI Using Prospective Motion Correction”. In: *Magnetic Resonance in Medicine* (2015). DOI: https://doi.org/10.1371/journal.pone.0133921. URL: https://doi.org/10.1371/journal.pone.0133921.

[48] Brian L. Edlow et al. “7 Tesla MRI of the ex vivo human brain at 100 micron resolution”. In: *Scientific Data* 6.244 (2019). DOI: https://doi.org/10.1038/s41597-019-0254-8.

[49] Federau Christian and Gallichan Daniel. “Motion-Correction Enabled Ultra-High Resolution In-Vivo 7T-MRI of the Brain”. In: *PLOS ONE* 11.5 (2016), pp. 1–12. DOI: https://doi.org/10.1371/journal.pone.0154974.

[50] Julian Maclaren et al. “Prospective motion correction in brain imaging: A review”. In: *Magnetic Resonance in Medicine (MRM)* (May 2012). DOI: jmri.24850. URL: https://onlinelibrary.wiley.com/doi/10.1002/jmri.24850.

[51] E.Mark Haacke and John L. Patrick. “Reducing motion artifacts in two-dimensional Fourier transform imaging”. In: *Magnetic Resonance Imaging* 4.4 (1986), pp. 359–376. ISSN: 0730-725X. DOI: https://doi.org/10.1016/0730-725X(86)91046-5. URL: https://www.sciencedirect.com/science/article/pii/0730725X86910465.

[52] Christine C. Lee et al. “Real-time adaptive motion correction in functional MRI”. In: *Magnetic Resonance Imaging* 36.3 (1996), pp. 436–444. DOI: https://doi.org/10.1002/mrm.1910360316. URL: https://onlinelibrary.wiley.com/doi/abs/10.1002/mrm.1910360316.

[53] P G Danias et al. “Prospective navigator correction of image position for coronary MR angiography”. In: *Radiology* 203.3 (1997). DOI: https://doi.org/10.1148/radiology.203.3.9169696. URL: https://pubs.rsna.org/doi/10.1148/radiology.203.3.9169696.

[54] Eviatar H, Saunders JK, and Hoult DI, eds. *Motion compensation by gradient adjustment*. 1898. ISMRM, May 1997.

[55] Eviatar H et al., eds. *Real time head motion correction for functional MRI*. p.269. ISMRM, May 1999.

[56] P G Danias et al. “Dynamic scan-plane tracking using MR position monitoring”. In: *Magnetic Resonance Imaging* 8.4 (2005). DOI: https://doi.org/10.1002/jmri.1880080423. URL: https://onlinelibrary.wiley.com/doi/10.1002/jmri.1880080423.

[57] Stefan Thesen et al. “Prospective acquisition correction for head motion with image-based tracking for real-time fMRI”. In: *Magnetic Resonance Imaging* 44.3 (2000). DOI: https://doi.org/10.1002/1522-2594(200009)44. URL: https://onlinelibrary.wiley.com/doi/full/10.1002/mrm.24314.

[58] *Prediction of Motion Induced Image Degradation Using a Markerless Motion Tracker*. 0297. Siemens mMR Biograph hybrid PET/MRI scanner. ISMRM, May 2016. DOI: 0297.

[59] Juliane Budde et al. “Ultra-high resolution imaging of the human brain using acquisition-weighted imaging at 9.4T”. In: *NeuroImage* 86 (2014), pp. 592–598. DOI: https://doi.org/10.1016/j.neuroimage.2013.08.013.

[60] Alexander Aranovitch et al. “Motion detection with NMR markers using real-time field tracking in the laboratory frame”. In: *Magnetic Resonance in Medicine* 84.1 (Dec. 2019), pp. 89–102. DOI: https://doi.org/10.1002/mrm.28094.

[61] Kamlesh Pawar et al. “Suppressing motion artefacts in MRI using an Inception-ResNet network with motion simulation augmentation”. In: *NMR in Biomedicine* (2019), e4225.

[62] Alessandro Sciarra, Hendrik Mattern, and Oliver Speck. “Machine learning algorithms for detection of motion artifacts: a general approach”. In:

[63] Anderson Adam W. and Gore John C. “Analysis and correction of motion artifacts in diffusion weighted imaging”. In: *Magnetic Resonance in Medicine* 32.3 (1994), pp. 379–387. DOI: https://doi.org/10.1002/mrm.1910320313.

[64] Korin HW et al. “Spatial-frequency-tuned markers and adaptive correction for rotational motion.” In: *Magnetic Resonance in Medicine* 33.5 (1995), pp. 663–669. DOI: doi:10.1002/mrm.1910330511. URL: https://onlinelibrary.wiley.com/doi/abs/10.1002/mrm.1910330511.

[65] Michaela Soellinger et al. “3D cine displacement-encoded MRI of pulsatile brain motion”. In: *Magn Reson Imaging* 61.1 (2009), pp. 153–162. DOI: https://doi.org/10.1002/mrm.21802.

[66] Blaise Simplice Talla Nwotchouang et al. “Accuracy of cardiac-induced brain motion measurement using displacement-encoding with stimulated echoes (DENSE) magnetic resonance imaging (MRI): A phantom study”. In: *Magn Reson Imaging* 85.3 (2021), pp. 1237–1247. DOI: https://doi.org/10.1002/mrm.28490.

[67] Ooi MB et al. “Prospective motion correction using inductively coupled wireless RF coils.” In: *Magnetic Resonance in Medicine* 70.3 (2013), pp. 639–647. DOI: doi:10.1002/mrm.24845. URL: https://www.ncbi.nlm.nih.gov/pmc/articles/PMC4006309/.

[68] Saikat Sengupta, John C. Gore, and E. Brian Welch, eds. *Prospective motion correction using NMR probes.* 2468. ISMRM, May 2020. URL: https://cds.ismrm.org/protected/12MProceedings/PDFfiles/2468.pdf.

[69] Saikat Sengupta and Sasidhar Tadankiand John C. Goreand E. Brian Welch. “Prospective real-time head motion correction using inductively coupled wireless NMR probes”. In: *Magnetic Resonance in Medicine* 72.4 (2013), pp. 971–985. DOI: https://doi.org/10.1002/mrm.25001. URL: https://onlinelibrary.wiley.com/doi/full/10.1002/mrm.25001.

[70] Ooi MB et al. “Prospective real-time correction for arbitrary head motion using active markers.” In: *Magnetic Resonance in Medicine* 62.4 (2009), pp. 943–954. DOI: doi:10.1002/mrm.22082. URL: https://www.ncbi.nlm.nih.gov/pmc/articles/PMC3033410/.

[71] Christoph Forman et al., eds. *Self-encoded marker for optical prospective head motion correction in MRI.* 13(Pt 1):259-66. MICCAI - International Conference of medical Image Computing and Computer assisted intervention, 2010. URL: https://doi.org/10.1007/978-3-642-15705-9_32.

[72] Murat Aksoy et al. “Real-time optical motion correction for diffusion tensor imaging”. In: *Magnetic Resonance in Medicine* 66.2 (2011), pp. 366–378. DOI: https://doi.org/10.1002/mrm.22787. URL: https://onlinelibrary.wiley.com/doi/full/10.1002/mrm.22787.

[73] van Niekerk A, van der Kouwe A, and Meintjes E. “A Method for Measuring Orientation Within a Magnetic Resonance Imaging Scanner Using Gravity and the Static Magnetic Field (VectOrient)”. In: *IEEE Transactions on Medical Imaging* 36.5 (2017), pp. 1129–1139. DOI: doi:10.1109/TMI.2017.2652502. URL: https://pubmed.ncbi.nlm.nih.gov/28129151/.

[74] van Niekerk A, Meintjes E, and van der Kouwe A. "A Wireless Radio Frequency Triggered Acquisition Device (WRAD) for Self-Synchronised Measurements of the Rate of Change of the MRI Gradient Vector Field for Motion Tracking". In: *IEEE Trans Med Imaging* 38.7 (2019), pp. 1610–1621. DOI: doi:10.1109/TMI.2019.2891774. URL: https://pubmed.ncbi.nlm.nih.gov/30629498/.

[75] James G. Pipe. "Motion correction with PROPELLER MRI: Application to head motion and free-breathing cardiac imaging". In: *Magnetic Resonance in Medicine* 42 (1999). DOI: https://onlinelibrary.wiley.com/doi/10.1002/(SICI)1522-2594(199911)42:5$\%$3C963::AID-MRM17$\%$3E3.0.CO;2-L.

[76] M. Babayeva et al. "Accuracy and Precision of Head Motion Information in Multi-Channel Free Induction Decay Navigators for Magnetic Resonance Imaging". In: *IEEE Transactions on Medical Imaging* 34.9 (2015), pp. 1879–1889. ISSN: 1558-254X. DOI: 10.1109/TMI.2015.2413211.

[77] WJohnson PM et al. "Retrospective 3D motion correction using spherical navigator echoes." In: *Magnetic Resonance in Medicine* 34.9 (2016), pp. 1274–1282. DOI: doi:10.1016/j.mri.2016.06.006.. URL: https://pubmed.ncbi.nlm.nih.gov/27451402/.

[78] Cordero-Grande L et al. "Motion-corrected MRI with DISORDER: Distributed and incoherent sample orders for reconstruction deblurring using encoding redundancy". In: *Magnetic Resonance in Medicine* 84.2 (2020), pp. 713–726. DOI: doi:10.1002/mrm.28157. URL: https://pubmed.ncbi.nlm.nih.gov/31898832/.

[79] Emil Ljungberg et al., eds. *MERLIN: Motion Insensitive Silent Neuroimaging.* 0120. ISMRM, May 2021. URL: https://submissions2.mirasmart.com/ISMRM2021/ViewSubmission.aspx?sbmID=544&validate=false.

[80] Martin John MacKinnon et al., eds. *iZTE-fMRI.* 1221. ISMRM, Aug. 2020. URL: https://cds.ismrm.org/protected/20MPresentations/abstracts/1221.html.

[81] White N et al. "PROMO: Real-time prospective motion correction in MRI using image-based tracking". In: *Magnetic Resonance in Medicine* 63.1 (2010), pp. 91–105. DOI: doi:10.1002/mrm.22176.. URL: https://pubmed.ncbi.nlm.nih.gov/20027635/.

[82] Daniel Gallichan, José P. Marques, and Rolf Gruetter. "Retrospective correction of involuntary microscopic head movement using highly accelerated fat image navigators (3D FatNavs) at 7T". In: *Magnetic Resonance in Medicine* 75.3 (2016), pp. 1030–1039. DOI: https://doi.org/10.1002/mrm.25670. URL: https://onlinelibrary.wiley.com/doi/full/10.1002/mrm.25670.

[83] Retsch F, Marques JP, and Gallichan D. “Investigating the accuracy of FatNav-derived estimates of temporal B0 changes and their application to retrospective correction of high-resolution 3D GRE of the human brain at 7T”. In: *Magnetic Resonance in Medicine* 80.2 (2018), pp. 585–597. DOI: doi:10.1002/mrm.27063. URL: https://pubmed.ncbi.nlm.nih.gov/29359352/.

[84] Tom Wilkinson et al., eds. *Motion Estimation for Brain Imaging at Ultra-High Field Using Pilot-Tone: Comparison with DISORDER Motion Compensation.* 0122. ISMRM, May 2021. URL: http://submissions.mirasmart.com/ISMRM2021/ViewSubmission.aspx?sbmID=1660&validate=false.

[85] Johnson PM and Drangova M. “Conditional generative adversarial network for 3D rigid-body motion correction in MRI”. In: *Magnetic Resonance in Medicine* 82.3 (2019), pp. 901–910. DOI: doi:10.1002/mrm.27772.. URL: https://pubmed.ncbi.nlm.nih.gov/31006909/.

[86] Thomas Kustner et al. “Conditional generative adversarial network for 3D rigid-body motion correction in MRI”. In: *Magnetic Resonance in Medicine* 82.4 (2019), pp. 901–910. DOI: https://doi.org/10.1002/mrm.27783. URL: https://onlinelibrary.wiley.com/doi/abs/10.1002/mrm.27783.

[87] Haskell Melissa W., Cauley Stephen F., and Wald Lawrence L. “TArgeted Motion Estimation and Reduction (TAMER): Data Consistency Based Motion Mitigation for MRI Using a Reduced Model Joint Optimization”. In: *IEEE Transactions on Medical Imaging* 37.5 (2018), pp. 1253–1265. DOI: 10.1109/TMI.2018.2791482.

[88] Jakob M. Slipsager et al. “Markerless motion tracking and correction for PET, MRI, and simultaneous PET/MRI”. In: *PLOS one* (2019). DOI: https://doi.org/10.1371/journal.pone.0215524.

[89] Havsteen Inger et al. “Are Movement Artifacts in Magnetic Resonance Imaging a Real Problem? A Narrative Review”. In: *Frontiers in Neurology* 8 (2017). ISSN: 1664-2295. DOI: 10.3389/fneur.2017.00232. URL: https://www.frontiersin.org/article/10.3389/fneur.2017.00232.

[90] Reichenbach JR et al. “Quantitative Susceptibility Mapping: Concepts and Applications”. In: *Clin Neuroradiol* 2 (Oct. 2015), pp. 225–30. DOI: doi:10.1007/s00062-015-0432-9. URL: https://pubmed.ncbi.nlm.nih.gov/26198880/.

[91] Ruetten PPR, Gillard JH, and Graves MJ. “Introduction to Quantitative Susceptibility Mapping and susceptibility Weighted Imaging”. In: *S. Br J Radiol* 92 (2019). DOI: doi:10.1259/bjr.20181016. URL: https://www.ncbi.nlm.nih.gov/pmc/articles/PMC6732929/.

[92] Wang Y and Liu T. “Quantitative susceptibility mapping (QSM): Decoding MRI data for a tissue magnetic biomarker”. In: *Magn Reson Med* 73 (2014), pp. 82–101. DOI: doi:10.1002/mrm.25358. URL: https://www.ncbi.nlm.nih.gov/pmc/articles/PMC4297605/.

[93] Sara Lorio et al. “Quantitative MRI susceptibility mapping reveals cortical signatures of changes in iron, calcium and zinc in malformations of cortical development in children with drug-resistant epilepsy”. In: *NeuroImage* 238 (2021), p. 118102. DOI: https://doi.org/10.1016/j.neuroimage.2021.118102.

[94] Liu Tian et al. “Calculation of susceptibility through multiple orientation sampling (COSMOS): A method for conditioning the inverse problem from measured magnetic field map to susceptibility source image in MRI”. In: *Magnetic Resonance in Medicine* 61.1 (2009), pp. 196–204. DOI: https://doi.org/10.1002/mrm.21828.

[95] de Rochefort Ludovic et al. “Quantitative susceptibility map reconstruction from MR phase data using bayesian regularization: Validation and application to brain imaging”. In: *Magnetic Resonance in Medicine* 63.1 (2010), pp. 194–206. DOI: https://doi.org/10.1002/mrm.22187.

[96] Shmueli Karin et al. “Magnetic susceptibility mapping of brain tissue in vivo using MRI phase data”. In: *Magnetic Resonance in Medicine* 62.6 (2009), pp. 1510–1522. DOI: https://doi.org/10.1002/mrm.22135.

[97] Mattern Hendrik et al. “Prospective motion correction improves high-resolution quantitative susceptibility mapping at 7T”. In: *Magnetic Resonance in Medicine* 81.3 (2019), pp. 1605–1619. DOI: https://doi.org/10.1002/mrm.27509.

[98] Murat Aksoy, Julian Maclaren, and Roland Bammer. “Prospective motion correction for 3D pseudo-continuous arterial spin labeling using an external optical tracking system”. In: *Magnetic Resonance Imaging* 39 (2017), pp. 44–52. DOI: https://doi.org/10.1016/j.mri.2017.01.018.

[99] Robson Philip M. et al. “Strategies for reducing respiratory motion artifacts in renal perfusion imaging with arterial spin labeling”. In: *Magnetic Resonance in Medicine* 61.6 (2009), pp. 1374–1387. DOI: https://doi.org/10.1002/mrm.21960.

[100] Aaron B Tanenbaum et al. “A method for reducing the effects of motion contamination in arterial spin labeling magnetic resonance imaging”. In: *J Cereb Blood Flow Metab* 35 (2015), pp. 1697–1702. DOI: https://doi.org/10.1038/jcbfm.2015.124.

[101] Rita G. Nunes, Peter Jezzard, and Stuart Clare. "Investigations on the efficiency of cardiac-gated methods for the acquisition of diffusion-weighted images". In: *Journal of Magnetic Resonance* 177.1 (2005), pp. 102–110. ISSN: 1090-7807. DOI: https://doi.org/10.1016/j.jmr.2005.07.005.

[102] R.J. Ordidge et al. "Correction of motional artifacts in diffusion-weighted MR images using navigator echoes". In: *Magnetic Resonance Imaging* 12.3 (1994), pp. 455–460. DOI: https://doi.org/10.1016/0730-725X(94)92539-9.

[103] Power JD et al. "Methods to detect, characterize, and remove motion artifact in resting state fMRI". In: *Neuroimage* 84 (2014), pp. 320–41. DOI: https://doi.org/j.neuroimage.2013.08.048.

[104] Maxim Zaitsev et al. "Prospective motion correction in functional MRI". In: *NeuroImage* 154 (2017), pp. 33–42. DOI: https://doi.org/10.1016/j.neuroimage.2016.11.014.

[105] Mitchell DG. "Abdominal magnetic resonance imaging: optimization and artifact suppression". In: *Topics in magnetic resonance imaging : TMRI* 4.3 (1992), pp. 18–34. URL: http://europepmc.org/abstract/MED/1605953.

[106] Barish MA and Jara H. "Motion artifact control in body MR imaging". In: *Magn Reson Imaging Clin N Am.* 7 (1999). DOI: https://pubmed.ncbi.nlm.nih.gov/10382162/.

[107] Earls James P. et al. "Cardiac MRI: Recent progress and continued challenges". In: *Journal of Magnetic Resonance Imaging* 16.2 (2002), pp. 111–127. DOI: https://doi.org/10.1002/jmri.10154.

[108] Busse A et al. "Cardiac MRI—Update 2020". In: *Der Radiologe* 60 (2020), pp. 33–40. DOI: https://doi.org/10.1007/s00117-020-00687-1.

[109] Shivaprasad Ashok Chikop et al. "Automatic motion correction of Musculoskeletal MRI using DSLR camera". In: *Magnetic Resonance Imaging* 48 (2018), pp. 74–79. DOI: https://doi.org/10.1016/j.mri.2017.12.031.

[110] Joseph R. Corea et al. "Screen-printed flexible MRI receive coils". In: *Nature Communications* 7.10839 (2016). DOI: https://doi.org/10.1038/ncomms10839.

[111] Elizaveta Motovilova et al. "Stretchable self-tuning MRI receive coils based on liquid metal technology (LiquiTune)". In: *Scientific Reports* 11.16228 (2021). DOI: https://doi.org/10.1038/s41598-021-95335-6.

[112] Andreas Port et al. "Detector clothes for MRI: A wearable array receiver based on liquid metal in elastic tubes". In: *Scientific Reports* 10.8844 (2020). DOI: https://doi.org/10.1038/s41598-020-65634-5.

[113] Andronesi Ovidiu C. et al. "Motion correction methods for MRS: experts' consensus recommendations". In: *NMR in Biomedicine* 34.5 (2021), e4364. DOI: https://doi.org/10.1002/nbm.4364.

[114] Metria Inc. "Moiré Phase Tracking System User Manual,Model MT 384ib, Metria Innovation, Inc." In: (2014). DOI: https://www.metriainnovation.com/.

[115] Rasmus M. Birn, Robert W. Cox, and Peter A. Bandettini. "Experimental designs and processing strategies for fMRI studies involving overt verbal responses". In: *NeuroImage* 23.3 (2004), pp. 1046–1058. DOI: https://doi.org/10.1016/j.neuroimage.2004.07.039.

[116] Iglesias Juan Eugenio et al. "Retrospective Head Motion Estimation in Structural Brain MRI with 3D CNNs". In: (2017), pp. 314–322. DOI: 10.1007/978-3-319-66185-8_36.

[117] Friston Karl J. et al. "Movement-Related effects in fMRI time-series". In: *Magnetic Resonance in Medicine* 35.3 (1996), pp. 346–355. DOI: https://doi.org/10.1002/mrm.1910350312.

[118] Woods RP, Cherry SR, and Mazziotta JC. "Rapid automated algorithm for aligning and reslicing PET images". In: *J Comput Assist Tomogr.* 16.4 (1992), pp. 620–33. DOI: https://doi.org/10.1097/00004728-199207000-00024.

[119] B. Gwen Windham et al. "Small Brain Lesions and Incident Stroke and Mortality". In: *Annals of Internal Medicine* 163.1 (2015), pp. 22–31. DOI: https://dx.doi.org/10.7326/M14-2057.

[120] Christian Dold et al. "Advantages and limitations of prospective head motion compensation for MRI using an optical motion tracking device". In: *Academic Radiology* 13.9 (2006), pp. 1093–1103. DOI: https://doi.org/10.1016/j.acra.2006.05.010.

[121] Kazim Gumus et al. "Comparison of optical and MR-based tracking". In: *Magn Reson Med* 74.3 (2015), pp. 894–902. DOI: https://doi.org/10.1002/mrm.25472.

[122] Frederic Gretsch et al. "Fat navigators and Moire phase tracking comparison for motion estimation and retrospective correction". In: *Magn Reson Med* 83.1 (2019), pp. 83–93. DOI: https://doi.org/10.1002/mrm.27908.

[123] Donald W. Marquardt. "An Algorithm for Least-Squares Estimation of Nonlinear Parameters". In: *Journal of the Society for Industrial and Applied Mathematics* 11.2 (1963), pp. 431–441. DOI: https://doi.org/10.1137/0111030. URL: https://epubs.siam.org/doi/abs/10.1137/0111030.

[124] Ma J. "Dixon techniques for water and fat imaging." In: *Magnetic Resonance Imaging* 3.28(3) (June 2008), pp. 543–558. DOI: doi:10.1002/jmri.21492.

[125] Mugler JP and Brookeman JR. “Brookeman JR. Three-dimensional magnetization-prepared rapid gradient-echo imaging (3D MP RAGE)”. In: *Magnetic Resonance Imaging* 1.15(1) (June 1990), pp. 152–157. DOI: doi:10.1002/mrm.1910150117.

[126] J.P. Marques and R. Bowtell. “Application of a Fourier-based method for rapid calculation of field inhomogeneity due to spatial variation of magnetic susceptibility”. In: *Concepts in Magnetic Resonance* B.25B (Apr. 2005), pp. 65–78. URL: https://doi.org/10.1002/cmr.b.20034.

[127] Guha Balakrishnan, Fredo Durand, and John Guttag. “Detecting Pulse from Head Motions in Video”. In: (2013).

[128] Devesh Raj et al. “A model for susceptibility artefacts from respiration in functional echo-planar magnetic resonance imaging”. In: *Physics in Medicine & Biology* 45.12 (Sept. 2000). URL: https://iopscience.iop.org/article/10.1088/0031-9155/45/12/321.

[129] Cheney and Kincaid. *umerical Mathematics and Computing*. 2008. ISBN: 978-0-495-11475-8.

[130] Simon Gross et al. “Physiology recording with magnetic field probes for fMRI denoising”. In: *Neuro Image* 154 (July 2017), pp. 106–114. DOI: https://doi.org/10.1016/j.neuroimage.2017.01.022.

[131] Tess E. Wallace et al. “Head motion measurement and correction using FID navigators”. In: *Magnetic Resonance in Medicine* 81.1 (Jan. 2019), pp. 258–274.

[132] Dennison E. “Magnet Formulas”. In: (2018). URL: https://nbviewer.jupyter.org/github/tiggerntatie/emagnet-py/blob/master/index.ipynb.

[133] MATLAB. “fminsearch”. In: (). URL: https://uk.mathworks.com/help/matlab/ref/fminsearch.html.

[134] Gila Benchetrit. “Breathing pattern in humans: diversity and individuality”. In: *Respiration Physiology* 122 (2000), pp. 123–129.

[135] Lin Tsungnan et al. “Learning long-term dependencies in NARX recurrent neural networks”. In: *IEEE Transactions on Neural Networks* 7.6 (Nov. 1996), pp. 1329–1338. DOI: 10.1109/72.548162.

[136] Eugen Diaconescu. “The use of NARX Neural Networks to predict Chaotic Time Series”. In: *WSEAS TRANSACTIONS on COMPUTER RESEARCH* 3.3 (Mar. 2008), pp. 182–191. ISSN: 1991-8755.

[137] Y. Bengio, P. Frasconi, and P. Simard. “The problem of learning long-term dependencies in recurrent networks”. In: *IEEE International Conference on Neural Networks* (1993). Date of Conference: 28 March-1 April 1993. DOI: 10.1109/ICNN.1993.298725. URL: https://ieeexplore.ieee.org/abstract/document/298725.

Appendices

Appendix A

Further consideration of the NARX method

This appendix provides background information about the data analysis techniques used in the thesis work. In particular, the background to the NARX method is explored.

A.1 Time series

A time series can be described as a vector($y(t)$) whose elements depend on time (t) [135]:

$$y(t), t = 0, 1, 2, \dots \tag{A.1}$$

Such a vector can be used to describe a dynamical system sampled at discrete-times.

Prediction (or regression) of a time series involves approximating the continuous function f that [135]:

$$\begin{aligned} y(t), t = 0, 1, 2, \dots \\ \hat{y}(t+D) = f\left(y(t), \dots, y(t-d_y, u(t), \dots, u(t-d_u)\right) \end{aligned} \tag{A.2}$$

where: u, y, d, f represent inputs (exogenous features), outputs, lags and non-linear map function respectively. $\hat{y}(t+D)$ represents the estimation of vector y at time $t+D$, where D represents the number of steps ahead ($D = 1, 2, \dots$).

Some key points are listed below.

1. Based on the *interdependence between time series values* [136], it is possible to discriminate non-deterministic and deterministic time series. A deterministic system whose behaviour is fully predictable from the initial conditions is represented by

a *deterministic* time series whose components auto-correlate [1]. Otherwise, in the case where there is no auto correlation between time series components (or their interdependence is minimal), the time series represents a deterministic system whose behaviour is unpredictable. Time series are then classified as *chaotic* (or random). A further classification can be made based on the interdependence of time series values dividing them into *short* or *long* term interdependences. In the case of *long term dependence*, past events have effects on future events over the long term, so the output of a system at time t_o depends on that state at time $t_b <<< t_o$ and the process has memory of past events. This behaviour is measurable through the autocorrelation which decreases over time following a low power function. The behaviour is *persistent* in the case of a high positive autocorrelation value, e.g. if the series increases for a certain period of time, it will carry on increasing. It is *anti-persistent* positive autocorrelation, e.g. if the series increase for a certain period of time, but then becomes stationary (this behaviour usually corresponds to noisy or self-affine time series).

2. A time series is *stationary* if its average, variance [2] (and covariance) [3] do not change in time.

3. Based on the *number of variables*, a time series can be *univariate*, *bivariate* or *multivariate* (in case of multidimensional input and output). In particular, multivariate analysis is used to analyse observations that have more than one statistical outcome variable.

The time series analysed in this dissertation are *deterministic*, with no *long term dependence*, *stationary* and *multivariate*.

[1] If there is significant auto-correlation, the output value $y(t_i)$ is correlated with the term $y(t_i + d)$ incremented in time by the quantity d

[2] **Variance**. The variance of a data-set is a measurement of the spread of the data point respect their average value. For a continuous variable, it is defined as the square of the standard deviation of the data.

[3] **nt-moments about the mean**. The nt central moment of a random variable is:

$$\mu_n = E\left[(X - E[X])^n\right] = \int_{-\inf}^{+\inf} (x-\mu)^n f(x) dx$$

where: $\mu = E[X]$ is the mean, $f(x)$ is the probability density function of the distribution, E is the expectation operator. $\mu_0 = 1$ is the central momentum; $\mu_1 = 0$ is the first central momentum, under certain condition is equal to the mean; $\mu_2 = \sigma^2$ represents the variance (σ is the standard deviation); μ_3 is the standardize moment used to define skewness; μ_4 is the standardize moment used to define kurtosis;

A.1.1 Pre-processing

Input selection should be performed in order to select the input variables that should be as predictive as possible. Reducing the redundancy of information in the data in general improves the quality of prediction. There are only a few situations where time series are used without any pre-processing. The most commonly used pre-processing methods include those that remove trends and systematic errors. In our case, the data could be easily pre-processed as the regression was performed retrospectively. In the case of prospective application, it would be necessary to evaluate pre-processing parameters on the training data and then apply the same parameters on data used for the prediction.

In the work described in this thesis (Chapter 3), the pre-processing was mainly applied to the magnetic field data, while the only pre-processing applied to the data from the MPT camera was to transform the measurements into the frame of reference of the scanner and then to down-sample the time series to match the sampling frequency of the field camera.

A.2 Data analysis

Methods. Methods to perform data analysis are in general divided into:

- **Unsupervised**. These are used to find patterns or hidden structures in unlabelled data (e.g. finding clusters or correlations between features of the data);
- **Supervised**. The method is trained on fully labelled data and learns to label new inputs. The model is modified during the training phase based on the best fit measure (e.g. minimize the error on the regression)(e.g. Deep neural Network);
- **Reinforcement Learning** (RL). Reinforcement learning methods work in a dynamic environment and can identify the sequence of actions that will generate the optimal outcome.

Techniques applied in this work are *supervised* and non *parametric*, as there is no a priori knowledge about the process that has generated the signal. The trained methods are customised for each different subject.

A.2.1 Partial Least Squares (PLS) Regression

The *Partial Least Squares* (PLS)[4] algorithm is a regression method based on Principal Component Analysis (PCA) [5] and Least Squares regression .
PLS projects the observable variables and the predicted variables into a new space (the latent space) and exploits the covariance between the spaces to perform the regression. In the case explored in this dissertation, the multivariate variables $\vec{M}$ and $\vec{B}$ are projected into their respective latent spaces in a PCA-like manner:

$$\vec{M'} = \vec{U}\vec{Q^T} + E \tag{A.3}$$

$$\vec{B'} = \vec{T}\vec{P^T} + H \tag{A.4}$$

Where E and H represent independent and identically distributed errors[6]. Once the score matrices ($\vec{T}_{t\times l}$, $\vec{U}_{t\times l}$) and the loadings ($\vec{P}_{k\times l}$, $\vec{Q}_{6\times l}$) are estimated during the training phase, they are used to estimate new responses ($\vec{M}_{t\times 6}$) from the predictors ($\vec{B}_{t\times k}$)) at time t.

Loadings (or weights) characterise the contributions of the different variables to the PLS model. Score matrices represent the coordinates of $\vec{M}$ and $\vec{B}$ in their respective latent spaces. As $\vec{T}_{t\times l}$ and $\vec{U}_{t\times l}$ are linearly related, once $\vec{U}_{t\times l}$ is estimated in the training phase $\vec{T}_{t\times l}$ is also known and used for prediction.

k-fold cross validation. The built-in MATLAB function used to perform the PLS method is `plsregress` [7]. The function allows a choice of different methods for validating the prediction. The method chosen was the *k-fold* cross validation with k equal to 6. The k-fold method randomly partitioned the training set into k folds (or subgroups of data). Then, one partition is chosen as a test set and the other $k-1$ subgroups form the training set. This operation is repeated $k - times$ and the final result is formed from the average of the individual results. The method is then robust against the random choice of folds[8].

[4] https://uk.mathworks.com/help/stats/partial-least-squares.html

[5] *Principal component analysis* (PCA) is a multivariate analysis method. It aims to represent the data in a new space described by less dimensions, but in which the variance of the data is preserved. https://uk.mathworks.com/help/stats/principal-component-analysis-pca.html

[6] https://uk.mathworks.com/help/stats/pca.html

[7] https://uk.mathworks.com/help/stats/plsregress.html

[8] https://www.youtube.com/watch?v=TIgfjmp-4BA

A.2.2 Auto Regressive (AR) models

Auto Regressive (AR) models represent random, time-varying processes specifying that the output variables depend linearly on their own previous values and on a stochastic term. Examples of autoregressive models are ARMA (AutoRegressive-Moving-Average) [9] and Vector autoregression (VAR) [10] and include the *Non-linear AutoRegressive with eXogenous Inputs* (NARX) method used for analysis in this dissertation.

A.2.3 Artificial Neural Network (ANN)

An ANN is used to perform time series predictions on non-linear systems. It is a non parametric method that has been shown to be a universal approximator [136]. ANNs are black-box modelling tools used to correlate inputs and outputs that are linked by an unknown mathematical relationship without any limits on space dimension mapping (m-dimension input and n-dimension output). A priori knowledge about the system is crucial for choosing the architecture. Limitations include the need to deal with long duration dependence in time series, number of samples necessary for the training (as increasing the number of samples over a certain limit doesn't improve the performance of the network), and the requirement for a stationary time series.

A.2.4 Recurrent Neural Network (RNN)

The capability to retain information for different amounts of time divides the ANN into *static* and *dynamic* types. Recurrent Neural Networks (RNNs) are dynamic networks that are able to store information from the past input and use them in combination with the current input for future prediction. RNNs trained with a gradient descent algorithm improve performance on time series with short term dependence [137]. RNNs are in general used to represent non-linear dynamic systems [135].

[9] The moving-average model specifies that an output variable depends linearly on the current value and past values of a stochastic term. It is a common approach for modelling univariate time series

[10] Vector autoregression (VAR) is a stochastic process model used to capture the linear interdependencies among multiple time series. VAR models generalize the univariate autoregressive model (AR model) by allowing for more than one evolving variable.

References

[135] Lin Tsungnan et al. “Learning long-term dependencies in NARX recurrent neural networks”. In: *IEEE Transactions on Neural Networks* 7.6 (Nov. 1996), pp. 1329–1338. DOI: 10.1109/72.548162.

[136] Eugen Diaconescu. “The use of NARX Neural Networks to predict Chaotic Time Series”. In: *WSEAS TRANSACTIONS on COMPUTER RESEARCH* 3.3 (Mar. 2008), pp. 182–191. ISSN: 1991-8755.

[137] Y. Bengio, P. Frasconi, and P. Simard. “The problem of learning long-term dependencies in recurrent networks”. In: *IEEE International Conference on Neural Networks* (1993). Date of Conference: 28 March-1 April 1993. DOI: 10.1109/ICNN.1993.298725. URL: https://ieeexplore.ieee.org/abstract/document/298725.

Appendix B

Data

Position of the probes, the standard deviation of real data, simulated data (only due to head motion) and simulated noisy data of both magnetic field changes and head motion parameters are described in this appendix.

B.1 Probe positions

The positions of probes fixed in various experimental set-up are reported. The probe signals are sensitive to their position in the scanner bore. The positions of the probes are measured by the NMR field camera during the calibration process with respect to the isocentre of the scanner. This has been repeated for each measurements as the system (scanner bed, head coil and probe holder are coupled and moved together) is reseated each time a new subject is scanned. The deviation of the probes during the different scans during the same laboratory session has been reported as and example. The average shift resulted $\leq 2\ mm$.

	Subject 1					
	PVC			Cloth		
	x [mm]	y [mm]	z [mm]	x [mm]	y [mm]	z [mm]
$\mathbf{P_1}$	86.7568	90.0045	−34.4014	66.8213	122.4330	23.4649
$\mathbf{P_2}$	−0.1857	136.7108	15.1747	40.1884	124.1966	−27.1726
$\mathbf{P_3}$	103.8605	3.3384	21.2683	95.8099	80.0824	114.4159
$\mathbf{P_4}$	−103.4851	3.9177	22.7314	−40.2865	135.8074	−3.3182
$\mathbf{P_5}$	0.5437	−121.8742	−96.8454	−51.1313	130.4997	−15.1453
$\mathbf{P_6}$	1.0286	129.2809	−100.5363	−66.7111	117.5437	−23.7065
$\mathbf{P_7}$	98.8610	3.5485	−91.5109	−95.2406	89.6777	107.2047
$\mathbf{P_8}$	−99.2621	3.1014	−78.2304	−113.2708	86.9476	4.9440
$\mathbf{P_9}$	0.8499	−128.7906	24.8871	−14.7028	−151.7036	−13.7889
$\mathbf{P_{10}}$	−56.3137	−52.7595	76.2798	47.8963	−141.7751	−16.7057
$\mathbf{P_{11}}$	56.8942	−52.9283	77.8694	61.5525	115.2452	−28.0566
$\mathbf{P_{12}}$	57.4974	61.6319	77.6811	50.0300	120.4717	40.6457
$\mathbf{P_{13}}$	−56.9052	60.8597	79.9303	32.8702	129.8081	20.8307
$\mathbf{P_{14}}$	−	−	−	−0.4053	108.6891	111.1136
$\mathbf{P_{15}}$	86.8275	−82.5530	−36.3411	−56.8995	121.9288	−6.4915
$\mathbf{P_{16}}$	−85.8250	−82.9852	−33.0658	−65.4269	−136.1570	−26.3721

Table B.1: *Data subject 1.* Values of the the probe positions (± 0.0001 mm) for the PVC and Cloth (no EPI) set-ups, for subject 1. Values have been measured to four decimal places.

	Subject 2					
	PVC			Cloth		
	x [mm]	y [mm]	z [mm]	x [mm]	y [mm]	z [mm]
$\mathbf{P_1}$	85.7798	89.9231	−36.9686	69.0316	117.7142	22.2839
$\mathbf{P_2}$	−1.1861	136.7111	12.3813	39.1880	123.9506	−25.3831
$\mathbf{P_3}$	103.0430	3.4504	18.8453	94.8268	80.7814	115.1341
$\mathbf{P_4}$	−104.5718	3.7041	19.9081	−40.7161	135.6523	−3.5936
$\mathbf{P_5}$	−0.0681	−121.6416	−99.4115	−51.3906	130.2805	−15.2444
$\mathbf{P_6}$	0.2165	128.5275	−103.3240	−66.9382	117.3351	−23.5860
$\mathbf{P_7}$	97.6496	3.4850	−94.0568	−95.8049	89.2665	107.4441
$\mathbf{P_8}$	−95.8641	2.7935	−104.1282	−113.7428	86.1246	5.3042
$\mathbf{P_9}$	0.0285	−128.8502	22.3955	−14.7307	−151.7210	−13.8264
$\mathbf{P_{10}}$	−57.2744	−52.8948	73.8164	47.8274	−141.7998	−16.9936
$\mathbf{P_{11}}$	56.2064	−52.9819	75.4302	60.8554	115.5224	−26.1347
$\mathbf{P_{12}}$	56.6017	61.8002	75.0710	49.9230	119.6731	38.7385
$\mathbf{P_{13}}$	−58.0220	61.1028	77.3339	32.6190	130.0569	19.5164
$\mathbf{P_{14}}$	−	−	−	−0.9426	109.1421	111.0470
$\mathbf{P_{15}}$	86.0154	−82.4617	−38.7462	−57.1474	121.7660	−6.8840
$\mathbf{P_{16}}$	−86.5308	−83.1802	−35.8164	−65.3981	−136.1868	−26.4225

Table B.2: *Data subject 2.* Values of the the probe positions (± 0.0001 mm) for the PVC and Cloth (no EPI) set-ups, for subject 2. Values have been measured to four decimal places.

	Subject 3					
	PVC			Cloth		
	x [mm]	y [mm]	z [mm]	x [mm]	y [mm]	z [mm]
$\mathbf{P_1}$	85.4393	89.7941	−48.6707	64.4520	125.3529	26.0042
$\mathbf{P_2}$	−1.0087	136.8883	2.1484	41.6035	125.5726	−27.5297
$\mathbf{P_3}$	103.7136	3.7388	8.2122	96.1636	79.7851	115.0835
$\mathbf{P_4}$	−104.2198	3.5919	9.9471	−39.7374	136.1593	−1.3764
$\mathbf{P_5}$	0.3693	−119.3963	−109.5257	−50.7739	130.8124	−13.6681
$\mathbf{P_6}$	0.0581	126.7170	−113.4125	−66.3606	117.6930	−22.7797
$\mathbf{P_7}$	96.1432	3.8925	−103.9974	−94.4784	90.1963	108.0096
$\mathbf{P_8}$	−98.0966	2.8610	−90.6388	−112.6012	87.9099	5.6409
$\mathbf{P_9}$	0.8967	−128.9827	11.7925	−14.7346	−151.6169	−13.3081
$\mathbf{P_{10}}$	−57.1848	−53.5632	63.9625	47.9073	−141.7031	−16.1656
$\mathbf{P_{11}}$	57.6477	−53.4542	65.2743	62.7212	116.3383	−28.3273
$\mathbf{P_{12}}$	57.7484	62.5828	64.9464	49.4713	121.2712	43.6779
$\mathbf{P_{13}}$	−58.1961	61.6203	67.6431	32.8545	130.0992	23.1222
$\mathbf{P_{14}}$	−	−	−	−0.0640	108.2190	112.5791
$\mathbf{P_{15}}$	86.0569	−81.7143	−49.4886	−56.5268	122.1117	−4.6032
$\mathbf{P_{16}}$	−85.5728	−82.7939	−45.9942	−65.4881	−136.0423	−25.8775

Table B.3: *Data subject 3.* Values of the the probe positions (±0.0001 mm) for the PVC and Cloth (no EPI) set-ups, for subject 3. Values have been measured to four decimal places.

	Subject 4					
	Cloth (simultaneous to EPI)			Cloth		
	x [mm]	y [mm]	z [mm]	x [mm]	y [mm]	z [mm]
$\mathbf{P_1}$	117.7364	71.0659	6.0495	60.3410	127.0775	27.0070
$\mathbf{P_2}$	105.3161	69.7774	115.0006	41.4696	125.6332	−28.5434
$\mathbf{P_3}$	−1.0888	106.5392	108.8131	96.6421	79.6352	114.6062
$\mathbf{P_4}$	50.6361	100.7396	111.3973	−39.6568	136.2114	0.2323
$\mathbf{P_5}$	−26.9214	139.1045	0.8454	−50.7901	130.7093	−12.6932
$\mathbf{P_6}$	−42.1283	132.2753	−18.8072	−66.4634	117.4549	−22.9582
$\mathbf{P_7}$	−100.1147	85.4046	108.2787	−94.0879	90.5175	107.7562
$\mathbf{P_8}$	−129.1525	64.5467	4.9046	−112.1837	88.5014	5.2463
$\mathbf{P_9}$	70.8317	118.6198	19.5755	−14.8402	−151.6908	−12.8170
$\mathbf{P_{10}}$	57.3433	−136.1287	−7.9158	47.9396	−141.7408	−15.5235
$\mathbf{P_{11}}$	115.2406	−81.3538	81.5349	62.4042	116.1893	−29.3340
$\mathbf{P_{12}}$	20.7968	135.4054	14.5597	47.5747	121.0010	45.4449
$\mathbf{P_{13}}$	40.3355	129.4590	−15.7328	30.8555	130.2749	23.3763
$\mathbf{P_{14}}$	−72.3229	119.8504	−7.3401	0.1252	107.1588	112.9469
$\mathbf{P_{15}}$	−41.0143	−145.2305	−7.3843	−56.5766	121.8855	−3.3422
$\mathbf{P_{16}}$	−83.6882	−119.9683	88.5600	−65.6270	−136.1143	−25.3311

Table B.4: *Data subject 4.* Values of the the probe positions (±0.0001 mm) for the Cloth (EPI) and Cloth (no EPI) set-ups, for subject 4. Values have been measured to four decimal places.

	Subject 5		
	Cloth		
	x $[mm]$	y $[mm]$	z $[mm]$
$\mathbf{P_1}$	62.7410	125.9857	27.5188
$\mathbf{P_2}$	41.2882	125.4423	−26.7884
$\mathbf{P_3}$	96.2312	79.5818	116.0222
$\mathbf{P_4}$	−39.8713	135.9589	0.6924
$\mathbf{P_5}$	−50.9262	130.4233	−11.8443
$\mathbf{P_6}$	−66.5620	117.1982	−21.4736
$\mathbf{P_7}$	−94.0133	90.1537	109.4331
$\mathbf{P_8}$	−112.5981	88.1700	7.0779
$\mathbf{P_9}$	−14.5922	−151.7421	−14.0133
$\mathbf{P_{10}}$	48.0501	−141.7926	−16.8368
$\mathbf{P_{11}}$	62.3390	116.1160	−27.6068
$\mathbf{P_{12}}$	48.6579	121.1903	45.4480
$\mathbf{P_{13}}$	31.9937	130.0377	24.4604
$\mathbf{P_{14}}$	0.0784	107.3458	113.9515
$\mathbf{P_{15}}$	−56.6977	121.7070	−2.6713
$\mathbf{P_{16}}$	−65.3650	−136.1539	−26.5422

Table B.5: *Data subject 5.* Values of the the probe positions (± 0.0001 mm) for the Cloth (no EPI) set-ups, for subject 5. Values have been measured to four decimal places.

	Subject 6		
	PVC		
	x $[mm]$	y $[mm]$	z $[mm]$
$\mathbf{P_1}$	85.7044	89.7975	−40.2373
$\mathbf{P_2}$	−1.0793	136.6883	9.2296
$\mathbf{P_3}$	103.2432	3.3752	16.1853
$\mathbf{P_4}$	−104.4468	3.6391	18.1903
$\mathbf{P_5}$	−0.1454	−121.1125	−102.5015
$\mathbf{P_6}$	0.1695	127.9279	−106.5934
$\mathbf{P_7}$	97.1689	3.5022	−97.3606
$\mathbf{P_8}$	−95.3710	2.8259	−106.9928
$\mathbf{P_9}$	0.1690	−128.9603	19.1725
$\mathbf{P_{10}}$	−57.2983	−53.1723	70.8254
$\mathbf{P_{11}}$	56.6436	−53.2567	72.2483
$\mathbf{P_{12}}$	57.0086	61.9392	71.9549
$\mathbf{P_{13}}$	−58.0110	61.2207	74.5956
$\mathbf{P_{14}}$	−	−	−
$\mathbf{P_{15}}$	85.9383	−82.3602	−42.0283
$\mathbf{P_{16}}$	−86.3434	−83.1056	−38.8455

Table B.6: *Data subject 5.* Values of the the probe positions (± 0.0001 mm) for the Cloth (no EPI) set-ups, for subject 5. Values have been measured to four decimal places.

Average shift in probe positions						
	PVC			Cloth		
	x $[mm]$	y $[mm]$	z $[mm]$	x $[mm]$	y $[mm]$	z $[mm]$
$\mathbf{P_1}$	1.1157	0.1663	7.5574	2.6799	−1.5996	−2.2385
$\mathbf{P_2}$	0.9056	−0.0518	7.2549	−0.6989	−0.9531	−0.1114
$\mathbf{P_3}$	0.5272	−0.1830	6.8540	−0.1560	0.1365	−0.7956
$\mathbf{P_4}$	0.9277	0.2726	6.7162	−0.2910	−0.1881	−2.3069
$\mathbf{P_5}$	0.4918	−1.1574	6.9675	−0.1611	−0.0567	−1.7828
$\mathbf{P_6}$	0.8806	1.5568	7.2403	−0.1301	0.1234	−1.0071
$\mathbf{P_7}$	1.8737	−0.0780	6.9607	−0.6444	−0.3558	−0.9561
$\mathbf{P_8}$	−2.8182	0.2746	22.3562	−0.4893	−0.7288	−0.8734
$\mathbf{P_9}$	0.4852	0.1405	7.1002	0.0216	−0.0109	−0.2977
$\mathbf{P_{10}}$	0.9388	0.4507	6.7451	−0.0348	−0.0161	−0.3258
$\mathbf{P_{11}}$	0.0616	0.3026	6.8851	−0.5275	−0.7963	−0.2059
$\mathbf{P_{12}}$	0.3779	−0.4755	7.0237	1.1233	−0.3122	−2.6816
$\mathbf{P_{13}}$	1.1712	−0.4549	6.7395	0.7895	−0.3091	−1.7881
$\mathbf{P_{14}}$	−	−	−	−0.2045	0.7227	−1.5175
$\mathbf{P_{15}}$	0.8239	−0.3743	7.0799	−0.1624	0.0613	−2.1163
$\mathbf{P_{16}}$	0.3240	0.0414	7.1529	0.0426	−0.0327	−0.3288

Table B.7: *Shift in probe positions.* Table reports average shift of the probe positions (± 0.0001 mm) for the PVC and Cloth (no EPI) set-ups. Probe positions of Subject 1 have been considered the initial ones. Values have been rounded to four decimal places.

B.2 Real Data

Probes 14 was faulty during the acquisition using the PVC support and so it has not been considered.

Subject 1

	PVC				Cloth			
	Rest	**Shaking**	**Nodding**	**Feet-wiggling**	**Rest**	**Shaking**	**Nodding**	**Feet-wiggling**
$\mathbf{B_{1[\mu T]}}$	0.015	0.329	0.055	0.026	0.024	0.043	0.029	0.012
$\mathbf{B_{2[\mu T]}}$	0.017	0.030	0.107	0.027	0.041	0.065	0.137	0.018
$\mathbf{B_{3[\mu T]}}$	0.023	0.246	0.052	0.044	0.014	0.029	0.012	0.011
$\mathbf{B_{4[\mu T]}}$	0.025	0.352	0.163	0.071	0.031	0.026	0.062	0.012
$\mathbf{B_{5[\mu T]}}$	0.036	0.033	0.091	0.046	0.034	0.031	0.067	0.013
$\mathbf{B_{6[\mu T]}}$	0.035	0.160	0.121	0.046	0.036	0.062	0.079	0.016
$\mathbf{B_{7[\mu T]}}$	0.036	0.240	0.097	0.065	0.010	0.035	0.009	0.007
$\mathbf{B_{8[\mu T]}}$	0.044	0.444	0.164	0.080	0.018	0.058	0.016	0.012
$\mathbf{B_{9[\mu T]}}$	0.018	0.052	0.232	0.053	0.017	0.023	0.020	0.020
$\mathbf{B_{10[\mu T]}}$	0.030	0.501	0.157	0.040	0.018	0.030	0.021	0.022
$\mathbf{B_{11[\mu T]}}$	0.015	0.147	0.237	0.037	0.037	0.061	0.071	0.019
$\mathbf{B_{12[\mu T]}}$	0.016	0.630	0.119	0.051	0.021	0.030	0.018	0.012
$\mathbf{B_{13[\mu T]}}$	0.025	0.533	0.173	0.050	0.029	0.051	0.064	0.012
$\mathbf{B_{14[\mu T]}}$	–	–	–	–	0.012	0.019	0.017	0.009
$\mathbf{B_{15[\mu T]}}$	0.028	0.087	0.031	0.055	0.028	0.049	0.051	0.013
$\mathbf{B_{16[\mu T]}}$	0.039	0.212	0.088	0.038	0.019	0.026	0.018	0.021
$\mathbf{T_x}$ **[mm]**	0.047	1.631	0.830	0.108	0.355	2.845	4.329	0.310
$\mathbf{T_y}$ **[mm]**	0.038	0.397	0.720	0.071	0.729	5.347	4.638	0.465
$\mathbf{T_z}$ **[mm]**	0.067	0.217	0.119	0.285	0.290	1.751	0.638	0.182
$\mathbf{R_x}$ $[\circ]$	0.082	0.493	2.429	0.140	0.253	1.785	1.382	0.155
$\mathbf{R_y}$ $[\circ]$	0.081	0.291	0.326	0.144	0.089	0.786	0.057	0.046
$\mathbf{R_z}$ $[\circ]$	0.073	2.955	0.433	0.161	0.072	1.951	0.122	0.083

Table B.8: *Data Subject 1.* Values of the the standard deviation (STD) of magnetic field changes and head motion parameters for the two set-ups, four head range of movements (Subject 1). Values have been rounded to three decimal places.

Subject 2

	PVC				Cloth			
	Rest	**Shaking**	**Nodding**	**Feet-wiggling**	**Rest**	**Shaking**	**Nodding**	**Feet-wiggling**
$\mathbf{B_{1}}_{[\mu\mathbf{T}]}$	0.010	0.089	0.100	0.018	0.051	0.070	0.048	0.025
$\mathbf{B_{2}}_{[\mu\mathbf{T}]}$	0.009	0.028	0.082	0.024	0.019	0.021	0.069	0.037
$\mathbf{B_{3}}_{[\mu\mathbf{T}]}$	0.013	0.344	0.113	0.058	0.029	0.047	0.028	0.021
$\mathbf{B_{4}}_{[\mu\mathbf{T}]}$	0.013	0.293	0.213	0.039	0.018	0.047	0.082	0.020
$\mathbf{B_{5}}_{[\mu\mathbf{T}]}$	0.083	0.080	0.344	0.066	0.012	0.048	0.061	0.022
$\mathbf{B_{6}}_{[\mu\mathbf{T}]}$	0.014	0.023	0.301	0.019	0.010	0.065	0.048	0.024
$\mathbf{B_{7}}_{[\mu\mathbf{T}]}$	0.025	0.117	0.170	0.030	0.010	0.043	0.037	0.011
$\mathbf{B_{8}}_{[\mu\mathbf{T}]}$	0.035	0.142	0.341	0.030	0.023	0.107	0.044	0.009
$\mathbf{B_{9}}_{[\mu\mathbf{T}]}$	0.019	0.114	0.138	0.035	0.043	0.034	0.086	0.026
$\mathbf{B_{10}}_{[\mu\mathbf{T}]}$	0.029	0.396	0.159	0.060	0.045	0.030	0.073	0.030
$\mathbf{B_{11}}_{[\mu\mathbf{T}]}$	0.021	0.452	0.155	0.024	0.014	0.050	0.052	0.038
$\mathbf{B_{12}}_{[\mu\mathbf{T}]}$	0.012	0.270	0.088	0.018	0.057	0.072	0.046	0.023
$\mathbf{B_{13}}_{[\mu\mathbf{T}]}$	0.014	0.262	0.155	0.018	0.044	0.055	0.070	0.022
$\mathbf{B_{14}}_{[\mu\mathbf{T}]}$	–	–	–	–	0.013	0.009	0.051	0.016
$\mathbf{B_{15}}_{[\mu\mathbf{T}]}$	0.033	0.115	0.116	0.053	0.016	0.079	0.097	0.020
$\mathbf{B_{16}}_{[\mu\mathbf{T}]}$	0.032	0.230	0.085	0.071	0.033	0.049	0.081	0.026
$\mathbf{T_x}$ [mm]	0.059	2.082	0.912	0.076	2.446	8.793	12.629	0.600
$\mathbf{T_y}$ [mm]	0.097	0.169	0.897	0.092	2.972	22.573	19.348	1.174
$\mathbf{T_z}$ [mm]	0.073	0.656	1.000	0.280	0.621	2.878	3.768	0.492
$\mathbf{R_x}$ [$\circ$]	0.114	0.472	5.785	0.100	1.146	10.646	6.846	0.523
$\mathbf{R_y}$ [$\circ$]	0.080	1.386	0.466	0.096	0.054	1.191	0.800	0.102
$\mathbf{R_z}$ [$\circ$]	0.049	4.515	0.777	0.051	0.513	11.497	3.424	0.481

Table B.9: *Data Subject 2.* Values of the the standard deviation (STD) of magnetic field changes and head motion parameters for the two set-ups, four head range of movements (Subject 2). Values have been rounded to three decimal places.

Subject 3

	PVC				Cloth			
	Rest	**Shaking**	**Nodding**	**Feet-wiggling**	**Rest**	**Shaking**	**Nodding**	**Feet-wiggling**
$\mathbf{B_{1}}_{[\mu \mathbf{T}]}$	0.022	0.093	0.165	0.024	0.030	0.060	0.064	0.022
$\mathbf{B_{2}}_{[\mu \mathbf{T}]}$	0.026	0.024	0.268	0.043	0.027	0.047	0.031	0.023
$\mathbf{B_{3}}_{[\mu \mathbf{T}]}$	0.085	0.577	0.081	0.050	0.013	0.024	0.013	0.015
$\mathbf{B_{4}}_{[\mu \mathbf{T}]}$	0.039	0.739	0.136	0.022	0.023	0.035	0.194	0.016
$\mathbf{B_{5}}_{[\mu \mathbf{T}]}$	0.073	0.038	0.098	0.035	0.025	0.030	0.151	0.014
$\mathbf{B_{6}}_{[\mu \mathbf{T}]}$	0.057	0.066	0.281	0.039	0.032	0.032	0.125	0.014
$\mathbf{B_{7}}_{[\mu \mathbf{T}]}$	0.033	0.138	0.090	0.028	0.014	0.028	0.019	0.011
$\mathbf{B_{8}}_{[\mu \mathbf{T}]}$	0.058	0.165	0.065	0.035	0.021	0.062	0.088	0.012
$\mathbf{B_{9}}_{[\mu \mathbf{T}]}$	0.048	0.049	0.150	0.021	0.043	0.069	0.033	0.017
$\mathbf{B_{10}}_{[\mu \mathbf{T}]}$	0.048	0.546	0.199	0.026	0.044	0.060	0.033	0.025
$\mathbf{B_{11}}_{[\mu \mathbf{T}]}$	0.049	0.468	0.112	0.039	0.025	0.047	0.029	0.018
$\mathbf{B_{12}}_{[\mu \mathbf{T}]}$	0.047	0.688	0.124	0.037	0.039	0.040	0.039	0.028
$\mathbf{B_{13}}_{[\mu \mathbf{T}]}$	0.090	0.685	0.122	0.024	0.037	0.063	0.128	0.019
$\mathbf{B_{14}}_{[\mu \mathbf{T}]}$	–	–	–	–	0.013	0.020	0.023	0.010
$\mathbf{B_{15}}_{[\mu \mathbf{T}]}$	0.043	0.136	0.140	0.025	0.030	0.045	0.234	0.023
$\mathbf{B_{16}}_{[\mu \mathbf{T}]}$	0.087	0.233	0.099	0.042	0.052	0.076	0.043	0.012
$\mathbf{T_x}$ **[mm]**	0.395	3.637	1.074	0.409	0.530	3.072	6.635	0.626
$\mathbf{T_y}$ **[mm]**	0.107	0.685	1.529	0.188	0.665	5.409	9.348	0.579
$\mathbf{T_z}$ **[mm]**	0.333	0.399	0.697	0.098	0.308	1.838	2.089	0.171
$\mathbf{R_x}$ [$\circ$]	0.191	0.400	3.414	0.461	0.309	1.962	3.061	0.192
$\mathbf{R_y}$ [$\circ$]	0.061	1.382	0.320	0.051	0.088	0.837	0.101	0.042
$\mathbf{R_z}$ [$\circ$]	0.341	4.225	0.409	0.078	0.595	2.288	0.821	0.090

Table B.10: *Data Subject 3.* Values of the the standard deviation (STD) of magnetic field changes and head motion parameters for the two set-ups, four head range of movements (Subject 3). Values have been rounded to three decimal places.

Subject 4

	PVC				Cloth			
	Rest	**Shaking**	**Nodding**	**Feet-wiggling**	**Rest**	**Shaking**	**Nodding**	**Feet-wiggling**
$\mathbf{B_{1[\mu T]}}$	–	–	–	–	0.051	0.084	0.082	0.026
$\mathbf{B_{2[\mu T]}}$	–	–	–	–	0.048	0.133	0.066	0.031
$\mathbf{B_{3[\mu T]}}$	–	–	–	–	0.023	0.076	0.018	0.009
$\mathbf{B_{4[\mu T]}}$	–	–	–	–	0.046	0.115	0.024	0.011
$\mathbf{B_{5[\mu T]}}$	–	–	–	–	0.045	0.139	0.019	0.008
$\mathbf{B_{6[\mu T]}}$	–	–	–	–	0.050	0.175	0.033	0.015
$\mathbf{B_{7[\mu T]}}$	–	–	–	–	0.023	0.082	0.010	0.010
$\mathbf{B_{8[\mu T]}}$	–	–	–	–	0.047	0.180	0.048	0.015
$\mathbf{B_{9[\mu T]}}$	–	–	–	–	0.090	0.030	0.061	0.033
$\mathbf{B_{10[\mu T]}}$	–	–	–	–	0.086	0.051	0.054	0.035
$\mathbf{B_{11[\mu T]}}$	–	–	–	–	0.052	0.188	0.050	0.030
$\mathbf{B_{12[\mu T]}}$	–	–	–	–	0.056	0.028	0.129	0.042
$\mathbf{B_{13[\mu T]}}$	–	–	–	–	0.060	0.072	0.112	0.035
$\mathbf{B_{14[\mu T]}}$	–	–	–	–	0.028	0.017	0.044	0.007
$\mathbf{B_{15[\mu T]}}$	–	–	–	–	0.049	0.209	0.025	0.011
$\mathbf{B_{16[\mu T]}}$	–	–	–	–	0.100	0.039	0.044	0.035
$\mathbf{T_x}$ **[mm]**	–	–	–	–	1.334	10.023	7.237	0.687
$\mathbf{T_y}$ **[mm]**	–	–	–	–	2.057	8.894	9.777	0.354
$\mathbf{T_z}$ **[mm]**	–	–	–	–	1.550	2.607	4.669	0.282
$\mathbf{R_x}$ [$\circ$]	–	–	–	–	0.799	4.014	2.604	0.183
$\mathbf{R_y}$ [$\circ$]	–	–	–	–	0.250	2.688	0.453	0.036
$\mathbf{R_z}$ [$\circ$]	–	–	–	–	0.336	4.782	0.752	0.171

Table B.11: *Data Subject 4.* Values of the the standard deviation (STD) of magnetic field changes and head motion parameters for the two set-ups, four head range of movements (Subject 4). Values have been rounded to three decimal places.

Subject 5

	PVC				Cloth			
	Rest	Shaking	Nodding	Feet-wiggling	Rest	Shaking	Nodding	Feet-wiggling
$\mathbf{B_{1}}[\mu\mathbf{T}]$	–	–	–	–	0.016	0.025	0.040	0.027
$\mathbf{B_{2}}[\mu\mathbf{T}]$	–	–	–	–	0.043	0.046	0.217	0.047
$\mathbf{B_{3}}[\mu\mathbf{T}]$	–	–	–	–	0.010	0.043	0.008	0.013
$\mathbf{B_{4}}[\mu\mathbf{T}]$	–	–	–	–	0.041	0.038	0.149	0.040
$\mathbf{B_{5}}[\mu\mathbf{T}]$	–	–	–	–	0.047	0.037	0.166	0.043
$\mathbf{B_{6}}[\mu\mathbf{T}]$	–	–	–	–	0.053	0.037	0.180	0.047
$\mathbf{B_{7}}[\mu\mathbf{T}]$	–	–	–	–	0.009	0.031	0.009	0.011
$\mathbf{B_{8}}[\mu\mathbf{T}]$	–	–	–	–	0.024	0.025	0.034	0.028
$\mathbf{B_{9}}[\mu\mathbf{T}]$	–	–	–	–	0.022	0.039	0.083	0.020
$\mathbf{B_{10}}[\mu\mathbf{T}]$	–	–	–	–	0.022	0.040	0.083	0.018
$\mathbf{B_{11}}[\mu\mathbf{T}]$	–	–	–	–	0.036	0.036	0.172	0.040
$\mathbf{B_{12}}[\mu\mathbf{T}]$	–	–	–	–	0.017	0.029	0.023	0.026
$\mathbf{B_{13}}[\mu\mathbf{T}]$	–	–	–	–	0.025	0.033	0.077	0.034
$\mathbf{B_{14}}[\mu\mathbf{T}]$	–	–	–	–	0.010	0.011	0.017	0.011
$\mathbf{B_{15}}[\mu\mathbf{T}]$	–	–	–	–	0.045	0.039	0.153	0.042
$\mathbf{B_{16}}[\mu\mathbf{T}]$	–	–	–	–	0.024	0.047	0.080	0.017
$\mathbf{T_x}$ [mm]	–	–	–	–	1.356	3.606	9.131	1.418
$\mathbf{T_y}$ [mm]	–	–	–	–	2.375	7.752	9.518	2.110
$\mathbf{T_z}$ [mm]	–	–	–	–	0.519	2.684	0.937	0.320
$\mathbf{R_x}$ [$\circ$]	–	–	–	–	0.817	2.291	3.015	0.661
$\mathbf{R_y}$ [$\circ$]	–	–	–	–	0.180	1.133	0.187	0.041
$\mathbf{R_z}$ [$\circ$]	–	–	–	–	0.236	2.623	0.338	0.187

Table B.12: *Data Subject 5.* Values of the the standard deviation (STD) of magnetic field changes and head motion parameters for the two set-ups, four head range of movements (Subject 5). Values have been rounded to three decimal places.

Subject 6

	PVC				Cloth			
	Rest	Shaking	Nodding	Feet-wiggling	Rest	Shaking	Nodding	Feet-wiggling
$\mathbf{B_{1[\mu T]}}$	0.014	0.229	0.088	0.029	–	–	–	–
$\mathbf{B_{2[\mu T]}}$	0.018	0.134	0.168	0.024	–	–	–	–
$\mathbf{B_{3[\mu T]}}$	0.024	0.808	0.120	0.045	–	–	–	–
$\mathbf{B_{4[\mu T]}}$	0.023	0.813	0.119	0.041	–	–	–	–
$\mathbf{B_{5[\mu T]}}$	0.063	0.109	0.186	0.089	–	–	–	–
$\mathbf{B_{6[\mu T]}}$	0.040	0.126	0.256	0.045	–	–	–	–
$\mathbf{B_{7[\mu T]}}$	0.042	0.282	0.101	0.085	–	–	–	–
$\mathbf{B_{8[\mu T]}}$	0.035	0.237	0.115	0.080	–	–	–	–
$\mathbf{B_{9[\mu T]}}$	0.026	0.058	0.152	0.036	–	–	–	–
$\mathbf{B_{10[\mu T]}}$	0.132	0.373	0.330	0.265	–	–	–	–
$\mathbf{B_{11[\mu T]}}$	0.135	0.373	0.654	0.240	–	–	–	–
$\mathbf{B_{12[\mu T]}}$	0.050	1.105	0.236	0.073	–	–	–	–
$\mathbf{B_{13[\mu T]}}$	0.046	1.735	0.088	0.087	–	–	–	–
$\mathbf{B_{14[\mu T]}}$	–	–	–	–	–	–	–	–
$\mathbf{B_{15[\mu T]}}$	0.039	0.199	0.085	0.077	–	–	–	–
$\mathbf{B_{16[\mu T]}}$	0.034	0.243	0.048	0.082	–	–	–	–
$\mathbf{T_x}$ [mm]	0.108	3.768	0.621	0.129	–	–	–	–
$\mathbf{T_y}$ [mm]	0.096	0.770	0.665	0.158	–	–	–	–
$\mathbf{T_z}$ [mm]	0.168	0.453	0.954	0.447	–	–	–	–
$\mathbf{R_x}$ [$\circ$]	0.266	1.217	3.306	0.204	–	–	–	–
$\mathbf{R_y}$ [$\circ$]	0.096	0.761	0.372	0.167	–	–	–	–
$\mathbf{R_z}$ [$\circ$]	0.116	7.871	0.427	0.163	–	–	–	–

Table B.13: *Data Subject 6.* Values of the the standard deviation (STD) of magnetic field changes and head motion parameters for the two set-ups, four head range of movements (Subject 6). Values have been rounded to three decimal places.

Slow and Fast movements

	Subject 3				Subject 6			
	Shaking	**S.Fast**	**Nodding**	**N.Fast**	**Shaking**	**S.Fast**	**Nodding**	**N.Fast**
$\mathbf{B_{1[\mu T]}}$	0.093	0.077	0.165	0.107	0.229	0.168	0.088	0.085
$\mathbf{B_{2[\mu T]}}$	0.024	0.044	0.268	0.189	0.134	0.036	0.168	0.229
$\mathbf{B_{3[\mu T]}}$	0.577	0.282	0.081	0.088	0.808	0.556	0.120	0.157
$\mathbf{B_{4[\mu T]}}$	0.739	0.391	0.136	0.157	0.813	0.556	0.119	0.163
$\mathbf{B_{5[\mu T]}}$	0.038	0.059	0.098	0.098	0.109	0.068	0.186	0.270
$\mathbf{B_{6[\mu T]}}$	0.066	0.082	0.281	0.188	0.126	0.058	0.256	0.368
$\mathbf{B_{7[\mu T]}}$	0.138	0.105	0.090	0.091	0.282	0.210	0.101	0.151
$\mathbf{B_{8[\mu T]}}$	0.165	0.125	0.065	0.085	0.237	0.152	0.115	0.121
$\mathbf{B_{9[\mu T]}}$	0.049	0.115	0.150	0.123	0.058	0.054	0.152	0.167
$\mathbf{B_{10[\mu T]}}$	0.546	0.356	0.199	0.217	0.373	0.423	0.330	0.260
$\mathbf{B_{11[\mu T]}}$	0.468	0.334	0.112	0.067	0.373	0.745	0.654	0.591
$\mathbf{B_{12[\mu T]}}$	0.688	0.354	0.124	0.120	1.105	0.714	0.236	0.265
$\mathbf{B_{13[\mu T]}}$	0.685	0.339	0.122	0.135	1.735	1.341	0.088	0.110
$\mathbf{B_{14[\mu T]}}$	–	–	–	–	–	–	–	–
$\mathbf{B_{15[\mu T]}}$	0.136	0.193	0.140	0.095	0.199	0.116	0.085	0.115
$\mathbf{B_{16[\mu T]}}$	0.233	0.200	0.099	0.099	0.243	0.172	0.048	0.137
$\mathbf{T_x}$ [mm]	3.637	2.018	1.074	0.794	3.768	2.592	0.621	1.380
$\mathbf{T_y}$ [mm]	0.685	0.266	1.529	1.344	0.770	0.400	0.665	1.066
$\mathbf{T_z}$ [mm]	0.399	0.610	0.697	0.608	0.453	0.487	0.954	1.189
$\mathbf{R_x}$ [$\circ$]	0.400	0.602	3.414	2.576	1.217	0.417	3.306	4.538
$\mathbf{R_y}$ [$\circ$]	1.382	0.610	0.320	0.498	0.761	0.629	0.372	0.610
$\mathbf{R_z}$ [$\circ$]	4.225	1.773	0.409	0.605	7.871	5.023	0.427	0.496

Table B.14: *Large head movements, slow and fast.* Values of the the standard deviation (STD) of magnetic field changes and head motion parameters for the PVC set-ups, two head range of movements (Subject 3 and 6). Values have been rounded to three decimal places.

B.3 Simulated data from real head movements

Data represent only the magnetic field changes due to the head movements. Standard deviation of head motion parameters were reported in the previous section. Head movements and probe positions are coherent with the measurements.

Subject 1

	PVC				Cloth			
	Rest	**Shaking**	**Nodding**	**Feet-wiggling**	**Rest**	**Shaking**	**Nodding**	**Feet-wiggling**
$\mathbf{B_{1[\mu T]}}$	0.015	0.222	0.166	0.034	0.038	0.180	0.085	0.030
$\mathbf{B_{2[\mu T]}}$	0.040	0.037	0.078	0.050	0.050	0.336	0.136	0.030
$\mathbf{B_{3[\mu T]}}$	0.081	0.080	0.073	0.081	0.032	0.144	0.080	0.016
$\mathbf{B_{4[\mu T]}}$	0.029	0.109	0.053	0.067	0.034	0.331	0.233	0.027
$\mathbf{B_{5[\mu T]}}$	0.044	0.071	0.064	0.044	0.036	0.389	0.246	0.027
$\mathbf{B_{6[\mu T]}}$	0.091	0.168	0.283	0.050	0.041	0.456	0.274	0.029
$\mathbf{B_{7[\mu T]}}$	0.065	0.258	0.137	0.105	0.021	0.400	0.157	0.021
$\mathbf{B_{8[\mu T]}}$	0.045	0.217	0.114	0.061	0.047	0.380	0.318	0.036
$\mathbf{B_{9[\mu T]}}$	0.022	0.048	0.265	0.032	0.065	0.111	0.127	0.044
$\mathbf{B_{10[\mu T]}}$	0.038	0.039	0.045	0.036	0.073	0.152	0.314	0.041
$\mathbf{B_{11[\mu T]}}$	0.082	0.158	0.526	0.097	0.042	0.288	0.096	0.027
$\mathbf{B_{12[\mu T]}}$	0.044	0.272	0.195	0.041	0.070	0.242	0.223	0.046
$\mathbf{B_{13[\mu T]}}$	0.051	0.352	0.394	0.067	0.048	0.328	0.191	0.040
$\mathbf{B_{14[\mu T]}}$	0.022	0.243	0.068	0.037	0.073	0.887	0.439	0.064
$\mathbf{B_{15[\mu T]}}$	0.118	0.120	0.281	0.110	0.047	0.451	0.329	0.036
$\mathbf{B_{16[\mu T]}}$	0.026	0.046	0.190	0.015	0.052	0.122	0.078	0.030

Table B.15: *Simulated data Subject 1.* Values of the the standard deviation (STD) of magnetic field changes and head motion parameters for the two set-ups, four head range of movements (Subject 1). Values have been rounded to three decimal places. Head motion parameters are reported in Table B.8.

Subject 2

	PVC				Cloth			
	Rest	Shaking	Nodding	Feet-wiggling	Rest	Shaking	Nodding	Feet-wiggling
$\mathbf{B_1}_{[\mu \mathbf{T}]}$	0.029	0.038	0.206	0.039	0.055	1.028	0.716	0.043
$\mathbf{B_2}_{[\mu \mathbf{T}]}$	0.011	0.044	0.102	0.020	0.092	1.977	1.593	0.047
$\mathbf{B_3}_{[\mu \mathbf{T}]}$	0.124	0.297	0.276	0.123	0.027	0.674	0.226	0.018
$\mathbf{B_4}_{[\mu \mathbf{T}]}$	0.020	0.088	0.048	0.064	0.087	2.837	2.087	0.028
$\mathbf{B_5}_{[\mu \mathbf{T}]}$	0.069	0.077	0.789	0.029	0.115	2.454	4.845	0.038
$\mathbf{B_6}_{[\mu \mathbf{T}]}$	0.014	0.062	0.539	0.019	0.149	1.996	2.867	0.050
$\mathbf{B_7}_{[\mu \mathbf{T}]}$	0.088	0.295	0.245	0.061	0.074	0.748	1.139	0.021
$\mathbf{B_8}_{[\mu \mathbf{T}]}$	0.031	0.149	0.074	0.031	0.172	1.146	1.640	0.060
$\mathbf{B_9}_{[\mu \mathbf{T}]}$	0.085	0.130	0.217	0.092	0.255	2.271	1.133	0.119
$\mathbf{B_{10}}_{[\mu \mathbf{T}]}$	0.036	0.390	0.131	0.066	0.298	6.240	1.367	0.135
$\mathbf{B_{11}}_{[\mu \mathbf{T}]}$	0.053	1.274	2.268	0.194	0.080	1.519	1.071	0.044
$\mathbf{B_{12}}_{[\mu \mathbf{T}]}$	0.045	0.112	0.836	0.028	0.072	1.019	0.868	0.050
$\mathbf{B_{13}}_{[\mu \mathbf{T}]}$	0.025	0.054	0.596	0.023	0.050	0.898	0.920	0.034
$\mathbf{B_{14}}_{[\mu \mathbf{T}]}$	0.013	0.029	0.120	0.024	0.132	1.932	2.000	0.047
$\mathbf{B_{15}}_{[\mu \mathbf{T}]}$	0.053	0.489	0.541	0.204	0.151	4.509	4.478	0.052
$\mathbf{B_{16}}_{[\mu \mathbf{T}]}$	0.031	0.114	0.061	0.042	0.148	0.953	0.659	0.104

Table B.16: *Simulated data Subject 2.* Values of the the standard deviation (STD) of magnetic field changes and head motion parameters for the two set-ups, four head range of movements (Subject 2). Values have been rounded to three decimal places. Head motion parameters are reported in Table B.9.

Subject 3

	PVC				Cloth			
	Rest	Shaking	Nodding	Feet-wiggling	Rest	Shaking	Nodding	Feet-wiggling
$\mathbf{B_1}_{[\mu \mathbf{T}]}$	0.012	0.014	0.054	0.019	0.014	0.088	0.134	0.014
$\mathbf{B_2}_{[\mu \mathbf{T}]}$	0.036	0.067	0.174	0.026	0.017	0.182	0.297	0.019
$\mathbf{B_3}_{[\mu \mathbf{T}]}$	0.067	0.161	0.284	0.066	0.016	0.114	0.079	0.017
$\mathbf{B_4}_{[\mu \mathbf{T}]}$	0.082	0.064	0.121	0.055	0.022	0.204	0.995	0.022
$\mathbf{B_5}_{[\mu \mathbf{T}]}$	0.039	0.055	0.354	0.052	0.033	0.300	1.426	0.031
$\mathbf{B_6}_{[\mu \mathbf{T}]}$	0.065	0.191	0.105	0.051	0.046	0.388	1.287	0.043
$\mathbf{B_7}_{[\mu \mathbf{T}]}$	0.118	0.380	0.231	0.038	0.026	0.289	0.592	0.028
$\mathbf{B_8}_{[\mu \mathbf{T}]}$	0.058	0.103	0.380	0.026	0.040	0.289	0.839	0.040
$\mathbf{B_9}_{[\mu \mathbf{T}]}$	0.099	0.069	0.160	0.051	0.088	0.398	0.656	0.081
$\mathbf{B_{10}}_{[\mu \mathbf{T}]}$	0.082	0.819	0.140	0.092	0.066	0.382	0.707	0.071
$\mathbf{B_{11}}_{[\mu \mathbf{T}]}$	0.047	1.159	1.007	0.167	0.017	0.151	0.208	0.018
$\mathbf{B_{12}}_{[\mu \mathbf{T}]}$	0.033	0.154	0.162	0.050	0.021	0.130	0.271	0.019
$\mathbf{B_{13}}_{[\mu \mathbf{T}]}$	0.054	0.120	0.689	0.063	0.013	0.084	0.251	0.011
$\mathbf{B_{14}}_{[\mu \mathbf{T}]}$	0.037	0.074	0.145	0.035	0.034	0.402	0.736	0.035
$\mathbf{B_{15}}_{[\mu \mathbf{T}]}$	0.063	0.717	0.212	0.041	0.039	0.326	1.385	0.038
$\mathbf{B_{16}}_{[\mu \mathbf{T}]}$	0.083	0.399	0.552	0.068	0.050	0.243	0.299	0.047

Table B.17: *Simulated data Subject 3.* Values of the the standard deviation (STD) of magnetic field changes and head motion parameters for the two set-ups, four head range of movements (Subject 3). Values have been rounded to three decimal places. Head motion parameters are reported in Table B.10.

Subject 4

	PVC				Cloth			
	Rest	Shaking	Nodding	Feet-wiggling	Rest	Shaking	Nodding	Feet-wiggling
$\mathbf{B_1}[\mu\mathbf{T}]$	–	–	–	–	0.093	0.139	0.292	0.023
$\mathbf{B_2}[\mu\mathbf{T}]$	–	–	–	–	0.082	0.277	0.290	0.020
$\mathbf{B_3}[\mu\mathbf{T}]$	–	–	–	–	0.046	0.168	0.129	0.026
$\mathbf{B_4}[\mu\mathbf{T}]$	–	–	–	–	0.107	0.889	0.502	0.031
$\mathbf{B_5}[\mu\mathbf{T}]$	–	–	–	–	0.098	1.137	0.499	0.031
$\mathbf{B_6}[\mu\mathbf{T}]$	–	–	–	–	0.100	1.648	0.542	0.035
$\mathbf{B_7}[\mu\mathbf{T}]$	–	–	–	–	0.019	0.785	0.102	0.018
$\mathbf{B_8}[\mu\mathbf{T}]$	–	–	–	–	0.138	1.421	0.674	0.044
$\mathbf{B_9}[\mu\mathbf{T}]$	–	–	–	–	0.205	0.442	0.865	0.048
$\mathbf{B_{10}}[\mu\mathbf{T}]$	–	–	–	–	0.225	0.729	1.095	0.051
$\mathbf{B_{11}}[\mu\mathbf{T}]$	–	–	–	–	0.072	0.142	0.237	0.020
$\mathbf{B_{12}}[\mu\mathbf{T}]$	–	–	–	–	0.153	0.245	0.500	0.033
$\mathbf{B_{13}}[\mu\mathbf{T}]$	–	–	–	–	0.129	0.360	0.471	0.026
$\mathbf{B_{14}}[\mu\mathbf{T}]$	–	–	–	–	0.115	0.864	0.585	0.031
$\mathbf{B_{15}}[\mu\mathbf{T}]$	–	–	–	–	0.146	1.224	0.709	0.043
$\mathbf{B_{16}}[\mu\mathbf{T}]$	–	–	–	–	0.133	0.214	0.463	0.035

Table B.18: *Simulated data Subject 4.* Values of the the standard deviation (STD) of magnetic field changes and head motion parameters for the two set-ups, four head range of movements (Subject 4). Values have been rounded to three decimal places. Head motion parameters are reported in Table B.11.

Subject 5

	PVC				Cloth			
	Rest	Shaking	Nodding	Feet-wiggling	Rest	Shaking	Nodding	Feet-wiggling
$\mathbf{B_1}[\mu\mathbf{T}]$	–	–	–	–	0.071	0.124	0.068	0.047
$\mathbf{B_2}[\mu\mathbf{T}]$	–	–	–	–	0.209	0.522	0.489	0.148
$\mathbf{B_3}[\mu\mathbf{T}]$	–	–	–	–	0.010	0.205	0.022	0.011
$\mathbf{B_4}[\mu\mathbf{T}]$	–	–	–	–	0.226	0.537	0.655	0.170
$\mathbf{B_5}[\mu\mathbf{T}]$	–	–	–	–	0.273	0.735	0.836	0.208
$\mathbf{B_6}[\mu\mathbf{T}]$	–	–	–	–	0.297	0.861	0.969	0.233
$\mathbf{B_7}[\mu\mathbf{T}]$	–	–	–	–	0.055	0.392	0.266	0.053
$\mathbf{B_8}[\mu\mathbf{T}]$	–	–	–	–	0.191	0.547	0.750	0.166
$\mathbf{B_9}[\mu\mathbf{T}]$	–	–	–	–	0.161	0.257	0.749	0.138
$\mathbf{B_{10}}[\mu\mathbf{T}]$	–	–	–	–	0.203	0.603	1.191	0.195
$\mathbf{B_{11}}[\mu\mathbf{T}]$	–	–	–	–	0.164	0.401	0.354	0.113
$\mathbf{B_{12}}[\mu\mathbf{T}]$	–	–	–	–	0.084	0.136	0.134	0.065
$\mathbf{B_{13}}[\mu\mathbf{T}]$	–	–	–	–	0.103	0.211	0.180	0.076
$\mathbf{B_{14}}[\mu\mathbf{T}]$	–	–	–	–	0.178	0.722	0.591	0.151
$\mathbf{B_{15}}[\mu\mathbf{T}]$	–	–	–	–	0.294	0.770	0.939	0.230
$\mathbf{B_{16}}[\mu\mathbf{T}]$	–	–	–	–	0.107	0.120	0.316	0.081

Table B.19: *Simulated data Subject 5.* Values of the the standard deviation (STD) of magnetic field changes and head motion parameters for the two set-ups, four head range of movements (Subject 5). Values have been rounded to three decimal places. Head motion parameters are reported in Table B.12.

Subject 6

	PVC				Cloth			
	Rest	**Shaking**	**Nodding**	**Feet-wiggling**	**Rest**	**Shaking**	**Nodding**	**Feet-wiggling**
$\mathbf{B_{1[\mu T]}}$	0.027	0.200	0.061	0.034	–	–	–	–
$\mathbf{B_{2[\mu T]}}$	0.045	0.088	0.124	0.048	–	–	–	–
$\mathbf{B_{3[\mu T]}}$	0.106	0.213	0.296	0.071	–	–	–	–
$\mathbf{B_{4[\mu T]}}$	0.079	0.130	0.086	0.074	–	–	–	–
$\mathbf{B_{5[\mu T]}}$	0.063	0.325	0.822	0.054	–	–	–	–
$\mathbf{B_{6[\mu T]}}$	0.036	0.090	0.340	0.057	–	–	–	–
$\mathbf{B_{7[\mu T]}}$	0.081	0.449	0.176	0.088	–	–	–	–
$\mathbf{B_{8[\mu T]}}$	0.072	0.229	0.157	0.063	–	–	–	–
$\mathbf{B_{9[\mu T]}}$	0.120	0.178	0.364	0.070	–	–	–	–
$\mathbf{B_{10[\mu T]}}$	0.184	1.420	0.221	0.260	–	–	–	–
$\mathbf{B_{11[\mu T]}}$	0.232	1.170	0.229	0.330	–	–	–	–
$\mathbf{B_{12[\mu T]}}$	0.062	0.958	0.303	0.109	–	–	–	–
$\mathbf{B_{13[\mu T]}}$	0.096	0.708	0.537	0.062	–	–	–	–
$\mathbf{B_{14[\mu T]}}$	0.074	0.151	0.420	0.020	–	–	–	–
$\mathbf{B_{15[\mu T]}}$	0.078	0.120	0.173	0.106	–	–	–	–
$\mathbf{B_{16[\mu T]}}$	0.064	0.241	0.457	0.086	–	–	–	–

Table B.20: *Simulated data Subject 6.* Values of the the standard deviation (STD) of magnetic field changes and head motion parameters for the two set-ups, four head range of movements (Subject 6). Values have been rounded to three decimal places. Head motion parameters are reported in Table B.13.

B.4 Simulated Data due to head motion and noise sources

Subject 1

	PVC				Cloth			
	Rest	**Shaking**	**Nodding**	**Feet-wiggling**	**Rest**	**Shaking**	**Nodding**	**Feet-wiggling**
$\mathbf{B_{1[\mu T]}}$	0.038	0.224	0.164	0.046	0.043	0.181	0.088	0.032
$\mathbf{B_{2[\mu T]}}$	0.054	0.045	0.085	0.055	0.056	0.337	0.138	0.033
$\mathbf{B_{3[\mu T]}}$	0.100	0.091	0.091	0.090	0.039	0.144	0.084	0.022
$\mathbf{B_{4[\mu T]}}$	0.063	0.120	0.077	0.078	0.041	0.331	0.236	0.030
$\mathbf{B_{5[\mu T]}}$	0.177	0.187	0.209	0.163	0.044	0.389	0.248	0.030
$\mathbf{B_{6[\mu T]}}$	0.100	0.170	0.288	0.057	0.049	0.456	0.276	0.033
$\mathbf{B_{7[\mu T]}}$	0.092	0.269	0.152	0.122	0.027	0.400	0.156	0.024
$\mathbf{B_{8[\mu T]}}$	0.076	0.224	0.139	0.083	0.055	0.381	0.320	0.040
$\mathbf{B_{9[\mu T]}}$	0.093	0.098	0.292	0.084	0.101	0.117	0.128	0.067
$\mathbf{B_{10[\mu T]}}$	0.065	0.062	0.076	0.060	0.102	0.155	0.309	0.063
$\mathbf{B_{11[\mu T]}}$	0.102	0.167	0.536	0.104	0.050	0.289	0.099	0.030
$\mathbf{B_{12[\mu T]}}$	0.047	0.274	0.194	0.051	0.073	0.243	0.225	0.048
$\mathbf{B_{13[\mu T]}}$	0.057	0.354	0.391	0.074	0.052	0.329	0.193	0.042
$\mathbf{B_{14[\mu T]}}$	0.048	0.245	0.087	0.051	0.074	0.886	0.437	0.064
$\mathbf{B_{15[\mu T]}}$	0.151	0.147	0.281	0.137	0.054	0.451	0.332	0.039
$\mathbf{B_{16[\mu T]}}$	0.099	0.101	0.228	0.082	0.093	0.128	0.085	0.057

Table B.21: *Simulated data Subject 1.* Values of the the standard deviation (STD) of magnetic field changes and head motion parameters for the two set-ups, four head range of movements (Subject 1). Values have been rounded to three decimal places. Head motion parameters are reported in Table B.8.

Subject 2

	PVC				Cloth			
	Rest	**Shaking**	**Nodding**	**Feet-wiggling**	**Rest**	**Shaking**	**Nodding**	**Feet-wiggling**
$\mathbf{B_{1}}[\mu\mathbf{T}]$	0.046	0.050	0.215	0.049	0.059	1.027	0.716	0.050
$\mathbf{B_{2}}[\mu\mathbf{T}]$	0.026	0.049	0.100	0.033	0.094	1.975	1.592	0.053
$\mathbf{B_{3}}[\mu\mathbf{T}]$	0.128	0.297	0.272	0.136	0.033	0.675	0.229	0.031
$\mathbf{B_{4}}[\mu\mathbf{T}]$	0.050	0.097	0.072	0.080	0.090	2.834	2.086	0.037
$\mathbf{B_{5}}[\mu\mathbf{T}]$	0.192	0.216	0.764	0.199	0.116	2.453	4.844	0.045
$\mathbf{B_{6}}[\mu\mathbf{T}]$	0.029	0.066	0.545	0.034	0.151	1.994	2.866	0.057
$\mathbf{B_{7}}[\mu\mathbf{T}]$	0.110	0.304	0.241	0.101	0.077	0.751	1.141	0.033
$\mathbf{B_{8}}[\mu\mathbf{T}]$	0.076	0.173	0.086	0.084	0.173	1.145	1.639	0.066
$\mathbf{B_{9}}[\mu\mathbf{T}]$	0.120	0.152	0.214	0.125	0.266	2.276	1.138	0.157
$\mathbf{B_{10}}[\mu\mathbf{T}]$	0.064	0.390	0.147	0.091	0.307	6.237	1.373	0.167
$\mathbf{B_{11}}[\mu\mathbf{T}]$	0.071	1.277	2.281	0.201	0.083	1.517	1.071	0.052
$\mathbf{B_{12}}[\mu\mathbf{T}]$	0.055	0.119	0.829	0.049	0.075	1.017	0.867	0.056
$\mathbf{B_{13}}[\mu\mathbf{T}]$	0.043	0.067	0.589	0.044	0.053	0.896	0.919	0.042
$\mathbf{B_{14}}[\mu\mathbf{T}]$	0.030	0.038	0.130	0.038	0.133	1.934	2.001	0.053
$\mathbf{B_{15}}[\mu\mathbf{T}]$	0.112	0.496	0.524	0.251	0.152	4.506	4.477	0.057
$\mathbf{B_{16}}[\mu\mathbf{T}]$	0.095	0.152	0.115	0.113	0.166	0.968	0.669	0.144

Table B.22: *Simulated data Subject 2.* Values of the the standard deviation (STD) of magnetic field changes and head motion parameters for the two set-ups, four head range of movements (Subject 2). Values have been rounded to three decimal places. Head motion parameters are reported in Table B.9.

Subject 3

	PVC				Cloth			
	Rest	**Shaking**	**Nodding**	**Feet-wiggling**	**Rest**	**Shaking**	**Nodding**	**Feet-wiggling**
$\mathbf{B_{1}}[\mu\mathbf{T}]$	0.037	0.035	0.046	0.030	0.095	0.140	0.294	0.029
$\mathbf{B_{2}}[\mu\mathbf{T}]$	0.046	0.072	0.163	0.032	0.083	0.279	0.292	0.027
$\mathbf{B_{3}}[\mu\mathbf{T}]$	0.084	0.167	0.263	0.070	0.049	0.171	0.131	0.033
$\mathbf{B_{4}}[\mu\mathbf{T}]$	0.097	0.077	0.124	0.061	0.108	0.891	0.502	0.037
$\mathbf{B_{5}}[\mu\mathbf{T}]$	0.203	0.197	0.288	0.140	0.100	1.139	0.500	0.037
$\mathbf{B_{6}}[\mu\mathbf{T}]$	0.070	0.191	0.103	0.054	0.102	1.651	0.543	0.041
$\mathbf{B_{7}}[\mu\mathbf{T}]$	0.140	0.393	0.209	0.065	0.024	0.784	0.104	0.025
$\mathbf{B_{8}}[\mu\mathbf{T}]$	0.089	0.124	0.413	0.052	0.140	1.423	0.675	0.050
$\mathbf{B_{9}}[\mu\mathbf{T}]$	0.137	0.102	0.134	0.077	0.211	0.441	0.864	0.089
$\mathbf{B_{10}}[\mu\mathbf{T}]$	0.097	0.815	0.131	0.097	0.230	0.723	1.093	0.087
$\mathbf{B_{11}}[\mu\mathbf{T}]$	0.074	1.165	1.033	0.171	0.074	0.145	0.239	0.028
$\mathbf{B_{12}}[\mu\mathbf{T}]$	0.049	0.154	0.148	0.054	0.154	0.246	0.502	0.038
$\mathbf{B_{13}}[\mu\mathbf{T}]$	0.063	0.125	0.675	0.070	0.130	0.362	0.472	0.032
$\mathbf{B_{14}}[\mu\mathbf{T}]$	0.053	0.078	0.163	0.042	0.116	0.862	0.585	0.036
$\mathbf{B_{15}}[\mu\mathbf{T}]$	0.116	0.717	0.182	0.076	0.147	1.226	0.710	0.048
$\mathbf{B_{16}}[\mu\mathbf{T}]$	0.128	0.419	0.601	0.096	0.142	0.223	0.465	0.080

Table B.23: *Simulated data Subject 3.* Values of the the standard deviation (STD) of magnetic field changes and head motion parameters for the two set-ups, four head range of movements (Subject 3). Values have been rounded to three decimal places. Head motion parameters are reported in Table B.10.

Subject 4

	PVC				Cloth			
	Rest	Shaking	Nodding	Feet-wiggling	Rest	Shaking	Nodding	Feet-wiggling
$\mathbf{B_{1}}[\mu\mathbf{T}]$	–	–	–	–	0.024	0.090	0.130	0.021
$\mathbf{B_{2}}[\mu\mathbf{T}]$	–	–	–	–	0.027	0.184	0.293	0.025
$\mathbf{B_{3}}[\mu\mathbf{T}]$	–	–	–	–	0.024	0.116	0.076	0.023
$\mathbf{B_{4}}[\mu\mathbf{T}]$	–	–	–	–	0.029	0.205	0.991	0.028
$\mathbf{B_{5}}[\mu\mathbf{T}]$	–	–	–	–	0.038	0.302	1.422	0.036
$\mathbf{B_{6}}[\mu\mathbf{T}]$	–	–	–	–	0.050	0.389	1.282	0.046
$\mathbf{B_{7}}[\mu\mathbf{T}]$	–	–	–	–	0.032	0.289	0.597	0.032
$\mathbf{B_{8}}[\mu\mathbf{T}]$	–	–	–	–	0.046	0.290	0.834	0.045
$\mathbf{B_{9}}[\mu\mathbf{T}]$	–	–	–	–	0.110	0.409	0.681	0.100
$\mathbf{B_{10}}[\mu\mathbf{T}]$	–	–	–	–	0.094	0.392	0.732	0.091
$\mathbf{B_{11}}[\mu\mathbf{T}]$	–	–	–	–	0.027	0.153	0.203	0.025
$\mathbf{B_{12}}[\mu\mathbf{T}]$	–	–	–	–	0.030	0.132	0.267	0.025
$\mathbf{B_{13}}[\mu\mathbf{T}]$	–	–	–	–	0.024	0.087	0.246	0.020
$\mathbf{B_{14}}[\mu\mathbf{T}]$	–	–	–	–	0.037	0.403	0.740	0.037
$\mathbf{B_{15}}[\mu\mathbf{T}]$	–	–	–	–	0.044	0.327	1.380	0.042
$\mathbf{B_{16}}[\mu\mathbf{T}]$	–	–	–	–	0.081	0.258	0.326	0.073

Table B.24: *Simulated data Subject 4.* Values of the the standard deviation (STD) of magnetic field changes and head motion parameters for the two set-ups, four head range of movements (Subject 4). Values have been rounded to three decimal places. Head motion parameters are reported in Table B.11.

Subject 5

	PVC				Cloth			
	Rest	Shaking	Nodding	Feet-wiggling	Rest	Shaking	Nodding	Feet-wiggling
$\mathbf{B_{1}}[\mu\mathbf{T}]$	–	–	–	–	0.072	0.125	0.069	0.049
$\mathbf{B_{2}}[\mu\mathbf{T}]$	–	–	–	–	0.209	0.523	0.489	0.149
$\mathbf{B_{3}}[\mu\mathbf{T}]$	–	–	–	–	0.020	0.205	0.026	0.016
$\mathbf{B_{4}}[\mu\mathbf{T}]$	–	–	–	–	0.227	0.538	0.655	0.170
$\mathbf{B_{5}}[\mu\mathbf{T}]$	–	–	–	–	0.273	0.735	0.836	0.209
$\mathbf{B_{6}}[\mu\mathbf{T}]$	–	–	–	–	0.298	0.860	0.969	0.233
$\mathbf{B_{7}}[\mu\mathbf{T}]$	–	–	–	–	0.058	0.392	0.266	0.054
$\mathbf{B_{8}}[\mu\mathbf{T}]$	–	–	–	–	0.192	0.547	0.750	0.167
$\mathbf{B_{9}}[\mu\mathbf{T}]$	–	–	–	–	0.172	0.262	0.751	0.142
$\mathbf{B_{10}}[\mu\mathbf{T}]$	–	–	–	–	0.211	0.606	1.193	0.198
$\mathbf{B_{11}}[\mu\mathbf{T}]$	–	–	–	–	0.165	0.401	0.354	0.114
$\mathbf{B_{12}}[\mu\mathbf{T}]$	–	–	–	–	0.085	0.137	0.134	0.067
$\mathbf{B_{13}}[\mu\mathbf{T}]$	–	–	–	–	0.104	0.212	0.180	0.077
$\mathbf{B_{14}}[\mu\mathbf{T}]$	–	–	–	–	0.179	0.722	0.591	0.151
$\mathbf{B_{15}}[\mu\mathbf{T}]$	–	–	–	–	0.294	0.770	0.938	0.231
$\mathbf{B_{16}}[\mu\mathbf{T}]$	–	–	–	–	0.122	0.132	0.320	0.088

Table B.25: *Simulated data Subject 5.* Values of the the standard deviation (STD) of magnetic field changes and head motion parameters for the two set-ups, four head range of movements (Subject 5). Values have been rounded to three decimal places. Head motion parameters are reported in Table B.12.

Subject 6

	PVC				Cloth			
	Rest	Shaking	Nodding	Feet-wiggling	Rest	Shaking	Nodding	Feet-wiggling
$\mathbf{B_{1}}_{[\mu \mathbf{T}]}$	0.039	0.204	0.070	0.048	–	–	–	–
$\mathbf{B_{2}}_{[\mu \mathbf{T}]}$	0.051	0.091	0.128	0.052	–	–	–	–
$\mathbf{B_{3}}_{[\mu \mathbf{T}]}$	0.111	0.231	0.301	0.085	–	–	–	–
$\mathbf{B_{4}}_{[\mu \mathbf{T}]}$	0.091	0.131	0.097	0.084	–	–	–	–
$\mathbf{B_{5}}_{[\mu \mathbf{T}]}$	0.166	0.396	0.844	0.184	–	–	–	–
$\mathbf{B_{6}}_{[\mu \mathbf{T}]}$	0.042	0.097	0.340	0.063	–	–	–	–
$\mathbf{B_{7}}_{[\mu \mathbf{T}]}$	0.101	0.453	0.188	0.114	–	–	–	–
$\mathbf{B_{8}}_{[\mu \mathbf{T}]}$	0.091	0.257	0.180	0.092	–	–	–	–
$\mathbf{B_{9}}_{[\mu \mathbf{T}]}$	0.144	0.215	0.374	0.105	–	–	–	–
$\mathbf{B_{10}}_{[\mu \mathbf{T}]}$	0.188	1.422	0.230	0.266	–	–	–	–
$\mathbf{B_{11}}_{[\mu \mathbf{T}]}$	0.234	1.166	0.233	0.331	–	–	–	–
$\mathbf{B_{12}}_{[\mu \mathbf{T}]}$	0.069	0.958	0.306	0.110	–	–	–	–
$\mathbf{B_{13}}_{[\mu \mathbf{T}]}$	0.100	0.711	0.539	0.069	–	–	–	–
$\mathbf{B_{14}}_{[\mu \mathbf{T}]}$	0.079	0.154	0.421	0.036	–	–	–	–
$\mathbf{B_{15}}_{[\mu \mathbf{T}]}$	0.113	0.175	0.200	0.145	–	–	–	–
$\mathbf{B_{16}}_{[\mu \mathbf{T}]}$	0.102	0.265	0.468	0.131	–	–	–	–

Table B.26: *Simulated data Subject 6.* Values of the the standard deviation (STD) of magnetic field changes and head motion parameters for the two set-ups, four head range of movements (Subject 6). Values have been rounded to three decimal places. Head motion parameters are reported in Table B.13.

Appendix C

Predictions

This appendix reports all the prediction described in Chapter 5, section 5.3. Predictions were reported as plots (predicted motion data, p, as a function of the measured motion data, d) and statistical evaluation. Each one has been called by the "Set-up, Regression Method, Data, Range of head motion, Subject number" to help to navigate the chapter. In general, numbers have been rounded to the three decimal places. Plots, that report results over multiple subjects, have not been fitted, while predictions on single subjects were. Results over 3 out of 6 subjects are then displayed with both plots and statistical evaluation, while plots that summarise the results over the subject do not have an associated the statistical evaluation.

C.0.1 PVC, PLS, Raw, Small

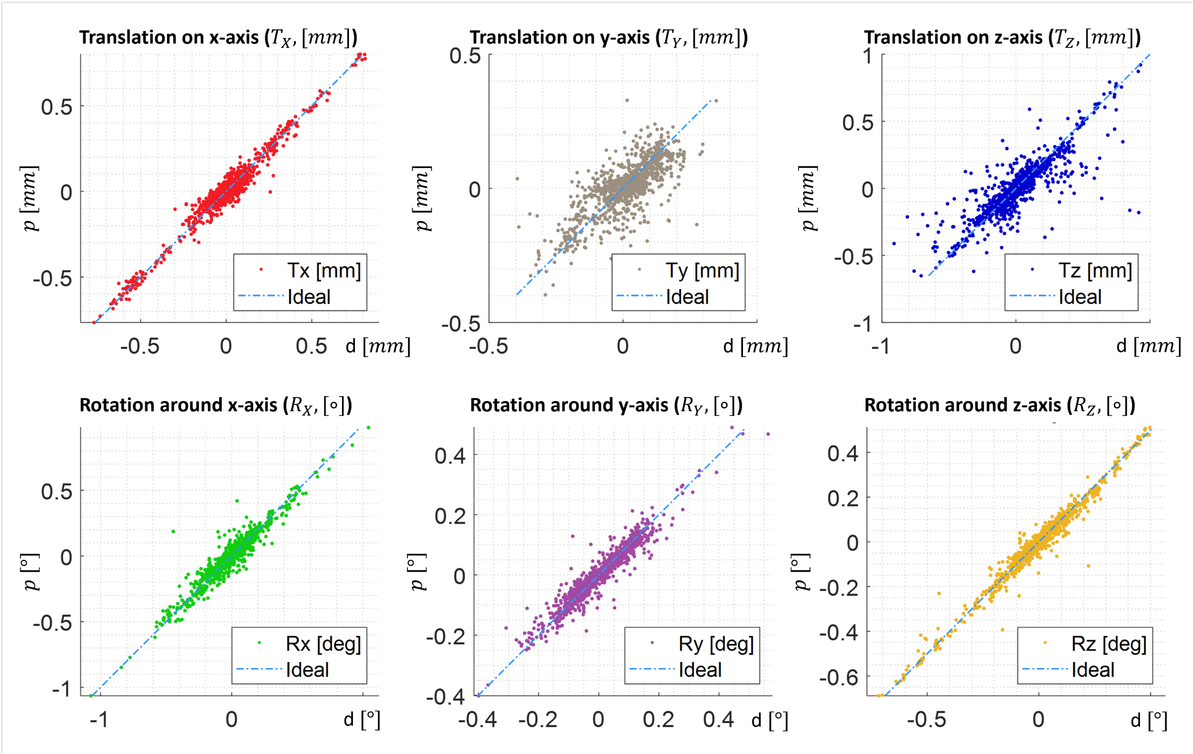

Figure C.1: The figure shows results obtained for *small* head movements, sampled using the *PVC* probe-holder set-up for *all* the subjects, using *raw* data for training the *linear* regression method (Table 5.1.3). Prediction results are *good* for translations/rotations except for translation along y axis.

Subject 1 (PVC, PLS, Raw, Small)						
	Slope	**Intercept**	$\mathbf{R^2}$	**PC**	**MSE**	**STD**
$\mathbf{T_x}$ [mm]	0.567	−0.001	0.551	0.742	0.002	0.072
$\mathbf{T_y}$ [mm]	−0.005	0.004	0.005	0.070	0.212	0.457
$\mathbf{T_z}$ [mm]	0.037	0.014	0.024	0.154	0.275	0.529
$\mathbf{R_x}$ [∘]	0.787	0.001	0.790	0.889	0.002	0.103
$\mathbf{R_y}$ [∘]	0.917	−0.004	0.945	0.972	0.001	0.109
$\mathbf{R_z}$ [∘]	0.958	0.001	0.950	0.975	0.001	0.104

Table C.1: *Subject 1.* Values of the slope and intercept of the linear fit are reported along with the values of R^2, the standard deviation (STD) and the mean squared error (MSE) and Pearson correlation coefficient (PC), for each of the motion parameters and prediction reported in Figure C.1. Values have been rounded to three decimal places.

Subject 2 (PVC, PLS, Raw, Small)						
	Slope	**Intercept**	$\mathbf{R^2}$	**PC**	**MSE**	**STD**
$\mathbf{T_x}$ **[mm]**	0.645	−0.004	0.631	0.794	0.002	0.065
$\mathbf{T_y}$ **[mm]**	0.536	−0.014	0.286	0.535	0.010	0.098
$\mathbf{T_z}$ **[mm]**	0.618	−0.019	0.566	0.752	0.014	0.178
$\mathbf{R_x}$ [$\circ$]	0.738	0.003	0.755	0.869	0.003	0.116
$\mathbf{R_y}$ [$\circ$]	0.814	−0.003	0.845	0.919	0.001	0.085
$\mathbf{R_z}$ [$\circ$]	0.652	0.001	0.668	0.818	0.001	0.048

Table C.2: *Subject 2.* Values of the slope and intercept of the linear fit are reported along with the values of R^2, the standard deviation (STD) and the mean squared error (MSE) and Pearson correlation coefficient (PC), for each of the motion parameters and prediction reported in Figure C.1. Values have been rounded to three decimal places.

Subject 3 (PVC, PLS, Raw, Small)						
	Slope	**Intercept**	$\mathbf{R^2}$	**PC**	**MSE**	**STD**
$\mathbf{T_x}$ **[mm]**	0.991	−0.002	0.993	0.996	0.001	0.391
$\mathbf{T_y}$ **[mm]**	0.860	< 0.001	0.909	0.953	0.002	0.145
$\mathbf{T_z}$ **[mm]**	0.939	0.002	0.956	0.978	0.004	0.283
$\mathbf{R_x}$ [$\circ$]	0.961	< 0.001	0.974	0.987	0.002	0.283
$\mathbf{R_y}$ [$\circ$]	0.904	−0.001	0.902	0.950	< 0.001	0.057
$\mathbf{R_z}$ [$\circ$]	0.990	0.003	0.993	0.996	0.001	0.284

Table C.3: *Subject 3.* Values of the slope and intercept of the linear fit are reported along with the values of R^2, the standard deviation (STD) and the mean squared error (MSE) and Pearson correlation coefficient (PC), for each of the motion parameters and prediction reported in Figure 5.17. Values have been rounded to three decimal places.

Subject 6 (PVC, PLS, Raw, Small)						
	Slope	**Intercept**	$\mathbf{R^2}$	**PC**	**MSE**	**STD**
$\mathbf{T_x}$ **[mm]**	0.871	0.002	0.830	0.911	0.002	0.117
$\mathbf{T_y}$ **[mm]**	0.643	−0.007	0.633	0.796	0.006	0.126
$\mathbf{T_z}$ **[mm]**	0.625	−0.017	0.655	0.809	0.032	0.301
$\mathbf{R_x}$ [$\circ$]	0.903	−0.002	0.886	0.941	0.006	0.236
$\mathbf{R_y}$ [$\circ$]	0.890	−0.004	0.926	0.962	0.001	0.131
$\mathbf{R_z}$ [$\circ$]	0.947	−0.003	0.930	0.965	0.001	0.143

Table C.4: *Subject 6.* Values of the slope and intercept of the linear fit are reported along with the values of R^2, the standard deviation (STD) and the mean squared error (MSE) and Pearson correlation coefficient (PC), for each of the motion parameters and prediction reported in Figure 5.18. Values have been rounded to three decimal places.

C.0.2 PVC, PLS, Raw, Large

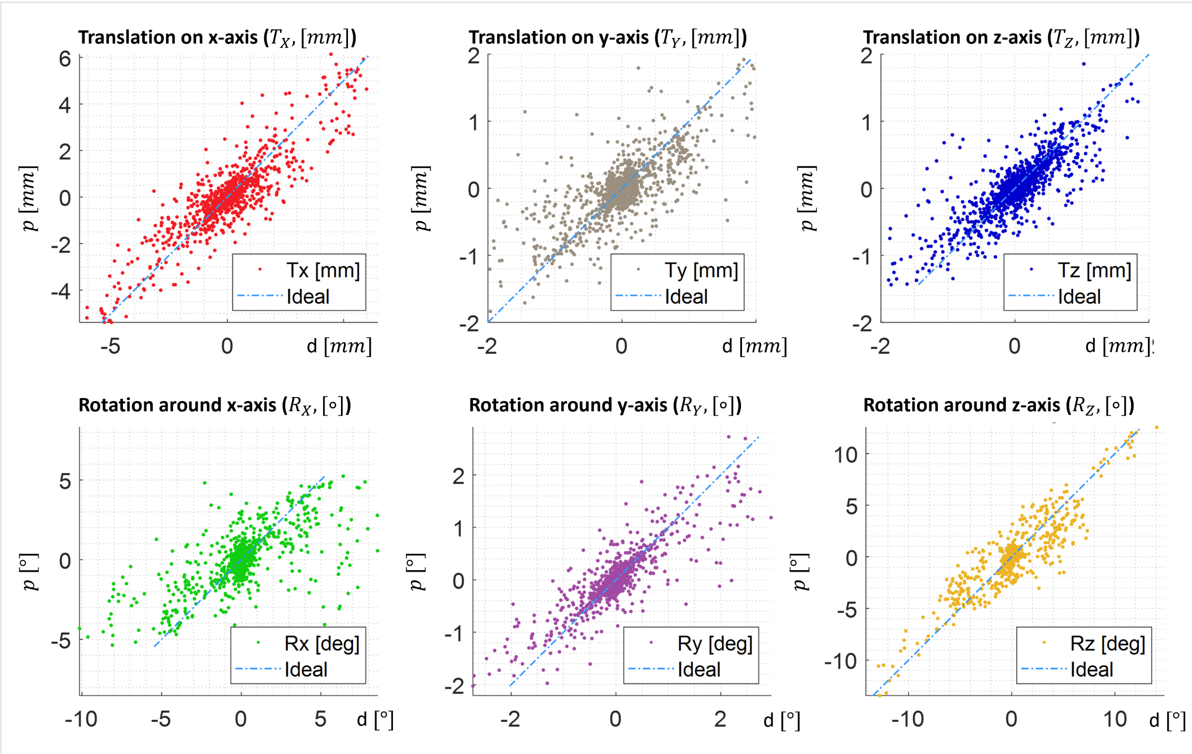

Figure C.2: The figure shows results obtained for *large* head movements, sampled using the *PVC* probe-holder set-up for *all* the subjects, using *raw* data for training the *linear* regression method (Table 5.1.3). Prediction results are *poor* for all the motion parameters.

Subject 1 (PVC, PLS, Raw, Large)						
	Slope	**Intercept**	$\mathbf{R^2}$	**PC**	**MSE**	**STD**
$\mathbf{T_x}$ [mm]	0.545	0.026	0.523	0.723	0.320	0.819
$\mathbf{T_y}$ [mm]	0.227	0.014	0.225	0.474	0.194	0.501
$\mathbf{T_z}$ [mm]	0.107	0.009	0.151	0.389	0.158	0.429
$\mathbf{R_x}$ [$\circ$]	0.519	-0.014	0.521	0.722	0.571	1.093
$\mathbf{R_y}$ [$\circ$]	0.737	0.008	0.767	0.876	0.012	0.227
$\mathbf{R_z}$ [$\circ$]	0.495	0.052	0.451	0.672	0.953	1.314

Table C.5: *Subject 1.* Values of the slope and intercept of the linear fit are reported along with the values of R^2, the standard deviation (STD) and the mean squared error (MSE) and Pearson correlation coefficient (PC), for each of the motion parameters and prediction reported in Figure C.2. Values have been rounded to three decimal places.

Subject 2 (PVC, PLS, Raw, Large)						
	Slope	**Intercept**	$\mathbf{R^2}$	**PC**	**MSE**	**STD**
$\mathbf{T_x}$ **[mm]**	0.464	−0.032	0.466	0.683	0.499	0.967
$\mathbf{T_y}$ **[mm]**	0.083	−0.010	0.093	0.304	0.702	0.880
$\mathbf{T_z}$ **[mm]**	0.394	0.000	0.439	0.663	0.245	0.658
$\mathbf{R_x}$ [$\circ$]	0.309	0.065	0.318	0.564	4.496	2.569
$\mathbf{R_y}$ [$\circ$]	0.516	−0.017	0.502	0.709	0.183	0.607
$\mathbf{R_z}$ [$\circ$]	0.479	−0.044	0.478	0.692	1.902	1.911

Table C.6: *Subject 2.* Values of the slope and intercept of the linear fit are reported along with the values of R^2, the standard deviation (STD) and the mean squared error (MSE) and Pearson correlation coefficient (PC), for each of the motion parameters and prediction reported in Figure C.2. Values have been rounded to three decimal places.

Subject 3 (PVC, PLS, Raw, Large)						
	Slope	**Intercept**	$\mathbf{R^2}$	**PC**	**MSE**	**STD**
$\mathbf{T_x}$ **[mm]**	0.730	−0.039	0.740	0.860	0.712	1.654
$\mathbf{T_y}$ **[mm]**	0.577	0.002	0.538	0.733	0.259	0.747
$\mathbf{T_z}$ **[mm]**	0.820	−0.003	0.747	0.864	0.040	0.394
$\mathbf{R_x}$ [$\circ$]	0.555	0.012	0.511	0.715	1.189	1.554
$\mathbf{R_y}$ [$\circ$]	0.775	−0.015	0.732	0.856	0.090	0.578
$\mathbf{R_z}$ [$\circ$]	0.730	−0.043	0.725	0.852	0.896	1.805

Table C.7: *Subject 3.* Values of the slope and intercept of the linear fit are reported along with the values of R^2, the standard deviation (STD) and the mean squared error (MSE) and Pearson correlation coefficient (PC), for each of the motion parameters and prediction reported in Figure 5.19. Values have been rounded to three decimal places.

Subject 6 (PVC, PLS, Raw, Large)						
	Slope	**Intercept**	$\mathbf{R^2}$	**PC**	**MSE**	**STD**
$\mathbf{T_x}$ **[mm]**	0.966	0.011	0.970	0.985	0.096	1.791
$\mathbf{T_y}$ **[mm]**	0.890	0.003	0.899	0.948	0.025	0.497
$\mathbf{T_z}$ **[mm]**	0.792	−0.020	0.785	0.886	0.062	0.537
$\mathbf{R_x}$ [$\circ$]	0.842	0.007	0.856	0.925	0.378	1.624
$\mathbf{R_y}$ [$\circ$]	0.896	0.002	0.900	0.949	0.014	0.372
$\mathbf{R_z}$ [$\circ$]	0.950	0.025	0.966	0.983	0.454	3.642

Table C.8: *Subject 6.* Values of the slope and intercept of the linear fit are reported along with the values of R^2, the standard deviation (STD) and the mean squared error (MSE) and Pearson correlation coefficient (PC), for each of the motion parameters and prediction reported in Figure 5.20. Values have been rounded to three decimal places.

Subject 3 (Fast) (PVC, PLS, Raw, Large)						
	Slope	**Intercept**	$\mathbf{R^2}$	**PC**	**MSE**	**STD**
$\mathbf{T_x}$ **[mm]**	0.350	−0.008	0.373	0.611	0.534	0.923
$\mathbf{T_y}$ **[mm]**	0.179	0.007	0.114	0.338	0.319	0.589
$\mathbf{T_z}$ **[mm]**	0.680	0.001	0.738	0.859	0.053	0.447
$\mathbf{R_x}$ [$\circ$]	0.205	−0.026	0.111	0.333	1.167	1.099
$\mathbf{R_y}$ [$\circ$]	0.352	−0.008	0.431	0.656	0.079	0.367
$\mathbf{R_z}$ [$\circ$]	0.413	−0.026	0.430	0.656	0.354	0.787

Table C.9: *Subject 3.* Values of the slope and intercept of the linear fit are reported along with the values of R^2, the standard deviation (STD) and the mean squared error (MSE) and Pearson correlation coefficient (PC), for each of the motion parameters and prediction reported in Figure 5.21. Values have been rounded to three decimal places.

Subject 6 (Fast) (PVC, PLS, Raw, Large)						
	Slope	**Intercept**	$\mathbf{R^2}$	**PC**	**MSE**	**STD**
$\mathbf{T_x}$ **[mm]**	0.675	−0.002	0.683	0.827	0.535	1.302
$\mathbf{T_y}$ **[mm]**	0.392	−0.002	0.385	0.620	0.162	0.513
$\mathbf{T_z}$ **[mm]**	0.549	0.008	0.568	0.754	0.163	0.616
$\mathbf{R_x}$ [$\circ$]	0.369	−0.017	0.342	0.585	2.576	1.977
$\mathbf{R_y}$ [$\circ$]	0.545	−0.011	0.541	0.736	0.071	0.392
$\mathbf{R_z}$ [$\circ$]	0.811	−0.024	0.811	0.901	0.943	2.238

Table C.10: *Subject 6.* Values of the slope and intercept of the linear fit are reported along with the values of R^2, the standard deviation (STD) and the mean squared error (MSE) and Pearson correlation coefficient (PC), for each of the motion parameters and prediction reported in Figure 5.22. Values have been rounded to three decimal places.

C.0.3 Cloth, PLS, Raw, Small

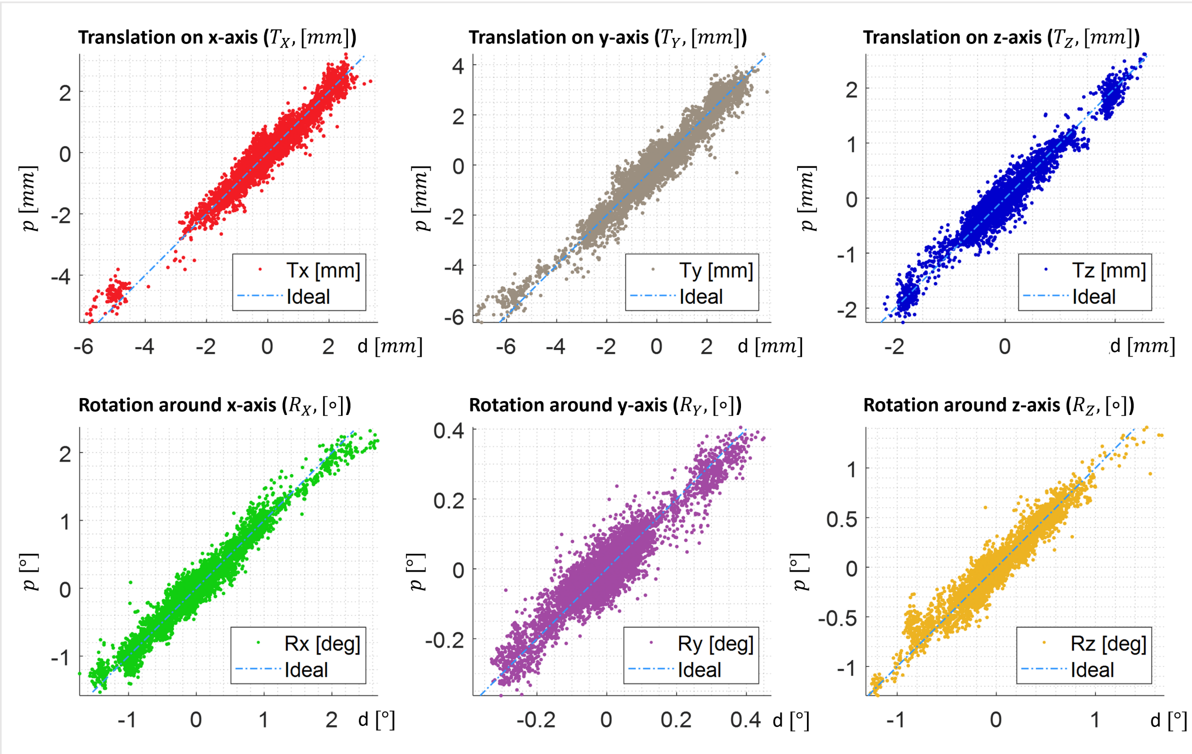

Figure C.3: The figure shows results obtained for *small* head movements, sampled using the *cloth* probe-holder set-up for *all* the subjects, using *raw* data for training the *linear* regression method (Table 5.1.3). Prediction results are poor for all the head motion parameters.

Subject 1 (Cloth, PLS, Raw, Small)						
	Slope	**Intercept**	$\mathbf{R^2}$	**PC**	**MSE**	**STD**
$\mathbf{T_x}$ [mm]	0.969	−0.008	0.971	0.985	0.118	2.016
$\mathbf{T_y}$ [mm]	0.957	−0.007	0.957	0.978	0.274	2.521
$\mathbf{T_z}$ [mm]	0.953	−0.003	0.943	0.971	0.020	0.589
$\mathbf{R_x}$ [$\circ$]	0.964	0.000	0.964	0.982	0.035	0.986
$\mathbf{R_y}$ [$\circ$]	0.716	−0.001	0.714	0.845	0.002	0.077
$\mathbf{R_z}$ [$\circ$]	0.910	−0.004	0.909	0.954	0.024	0.514

Table C.11: *Subject 1.* Values of the slope and intercept of the linear fit are reported along with the values of R^2, the standard deviation (STD) and the mean squared error (MSE) and Pearson correlation coefficient (PC), for each of the motion parameters and prediction reported in Figure C.3. Values have been rounded to three decimal places.

Subject 2 (Cloth, PLS, Raw, Small)						
	Slope	**Intercept**	$\mathbf{R^2}$	**PC**	**MSE**	**STD**
$\mathbf{T_x}$ **[mm]**	0.732	−0.008	0.716	0.846	0.033	0.338
$\mathbf{T_y}$ **[mm]**	0.666	−0.022	0.645	0.803	0.154	0.657
$\mathbf{T_z}$ **[mm]**	0.853	0.006	0.855	0.924	0.009	0.255
$\mathbf{R_x}$ [$\circ$]	0.715	0.008	0.697	0.835	0.015	0.224
$\mathbf{R_y}$ [$\circ$]	0.761	0.002	0.773	0.879	0.001	0.076
$\mathbf{R_z}$ [$\circ$]	0.502	0.001	0.548	0.740	0.003	0.082

Table C.12: *Subject 2.* Values of the slope and intercept of the linear fit are reported along with the values of R^2, the standard deviation (STD) and the mean squared error (MSE) and Pearson correlation coefficient (PC), for each of the motion parameters and prediction reported in Figure C.3. Values have been rounded to three decimal places.

Subject 3 (Cloth, PLS, Raw, Small)						
	Slope	**Intercept**	$\mathbf{R^2}$	**PC**	**MSE**	**STD**
$\mathbf{T_x}$ **[mm]**	0.854	0.006	0.859	0.927	0.046	0.575
$\mathbf{T_y}$ **[mm]**	0.712	0.007	0.722	0.849	0.116	0.646
$\mathbf{T_z}$ **[mm]**	0.618	−0.002	0.609	0.780	0.027	0.262
$\mathbf{R_x}$ [$\circ$]	0.809	−0.002	0.811	0.900	0.014	0.272
$\mathbf{R_y}$ [$\circ$]	0.542	< 0.001	0.518	0.720	0.002	0.072
$\mathbf{R_z}$ [$\circ$]	0.956	−0.001	0.957	0.978	0.010	0.478

Table C.13: *Subject 3.* Values of the slope and intercept of the linear fit are reported along with the values of R^2, the standard deviation (STD) and the mean squared error (MSE) and Pearson correlation coefficient (PC), for each of the motion parameters and prediction reported in Figure 5.23. Values have been rounded to three decimal places.

Subject 4 (Cloth, PLS, Raw, Small)						
	Slope	**Intercept**	$\mathbf{R^2}$	**PC**	**MSE**	**STD**
$\mathbf{T_x}$ **[mm]**	0.940	0.006	0.939	0.969	0.081	1.151
$\mathbf{T_y}$ **[mm]**	0.944	0.006	0.951	0.975	0.138	1.673
$\mathbf{T_z}$ **[mm]**	0.964	0.000	0.966	0.983	0.053	1.258
$\mathbf{R_x}$ [$\circ$]	0.959	−0.003	0.965	0.982	0.015	0.654
$\mathbf{R_y}$ [$\circ$]	0.933	−0.001	0.936	0.967	0.003	0.202
$\mathbf{R_z}$ [$\circ$]	0.941	−0.001	0.949	0.974	0.004	0.293

Table C.14: *Subject 4.* Values of the slope and intercept of the linear fit are reported along with the values of R^2, the standard deviation (STD) and the mean squared error (MSE) and Pearson correlation coefficient (PC), for each of the motion parameters and prediction reported in Figure C.3. Values have been rounded to three decimal places.

Subject 5 (Cloth, PLS, Raw, Small)						
	Slope	**Intercept**	$\mathbf{R^2}$	**PC**	**MSE**	**STD**
$\mathbf{T_x}$ [mm]	0.970	0.009	0.964	0.982	0.065	1.348
$\mathbf{T_y}$ [mm]	0.982	0.011	0.974	0.987	0.127	2.216
$\mathbf{T_z}$ [mm]	0.975	0.001	0.975	0.987	0.005	0.444
$\mathbf{R_x}$ [$\circ$]	0.986	−0.003	0.979	0.989	0.012	0.740
$\mathbf{R_y}$ [$\circ$]	0.933	0.001	0.938	0.968	0.001	0.141
$\mathbf{R_z}$ [$\circ$]	0.910	−0.002	0.897	0.947	0.005	0.212

Table C.15: *Subject 5.* Values of the slope and intercept of the linear fit are reported along with the values of R^2, the standard deviation (STD) and the mean squared error (MSE) and Pearson correlation coefficient (PC), for each of the motion parameters and prediction reported in Figure 5.24. Values have been rounded to three decimal places.

C.0.4 Cloth, PLS, Raw, Large

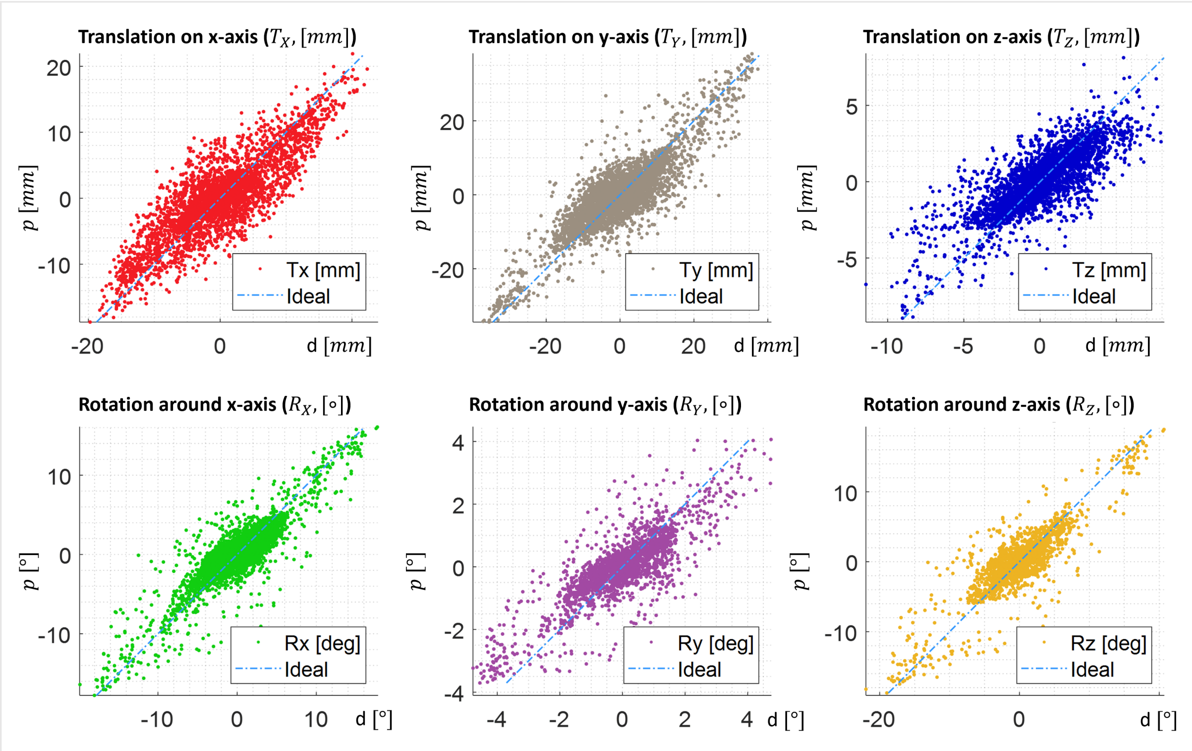

Figure C.4: The figure shows results obtained for *large* head movements, sampled using the *cloth* probe-holder set-up for *all* the subjects, using *raw* data for training the *linear* regression method (Table 5.1.3). Prediction results are *poor* for all the head motion parameters.

Subject 1 (Cloth, PLS, Raw, Large)						
	Slope	**Intercept**	$\mathbf{R^2}$	**PC**	**MSE**	**STD**
$\mathbf{T_x}$ **[mm]**	0.310	−0.044	0.300	0.548	3.336	2.181
$\mathbf{T_y}$ **[mm]**	0.284	−0.051	0.277	0.526	6.266	2.941
$\mathbf{T_z}$ **[mm]**	0.343	0.007	0.322	0.568	0.427	0.793
$\mathbf{R_x}$ [∘]	0.292	0.017	0.288	0.537	0.628	0.939
$\mathbf{R_y}$ [∘]	0.318	0.000	0.293	0.541	0.074	0.323
$\mathbf{R_z}$ [∘]	0.378	0.003	0.371	0.609	0.393	0.790

Table C.16: *Subject 1.* Values of the slope and intercept of the linear fit are reported along with the values of R^2, the standard deviation (STD) and the mean squared error (MSE) and Pearson correlation coefficient (PC), for each of the motion parameters and prediction reported in Figure C.4. Values have been rounded to three decimal places.

Subject 2 (Cloth, PLS, Raw, Large)						
	Slope	**Intercept**	$\mathbf{R^2}$	**PC**	**MSE**	**STD**
$\mathbf{T_x}$ **[mm]**	0.846	−0.044	0.847	0.920	6.436	6.480
$\mathbf{T_y}$ **[mm]**	0.849	−0.018	0.857	0.926	22.262	12.482
$\mathbf{T_z}$ **[mm]**	0.685	0.046	0.665	0.816	1.269	1.941
$\mathbf{R_x}$ [∘]	0.846	0.021	0.857	0.926	4.050	5.323
$\mathbf{R_y}$ [∘]	0.780	0.011	0.779	0.883	0.075	0.580
$\mathbf{R_z}$ [∘]	0.843	0.026	0.861	0.928	3.547	5.050

Table C.17: *Subject 2.* Values of the slope and intercept of the linear fit are reported along with the values of R^2, the standard deviation (STD) and the mean squared error (MSE) and Pearson correlation coefficient (PC), for each of the motion parameters and prediction reported in Figure C.4. Values have been rounded to three decimal places.

Subject 3 (Cloth, PLS, Raw, Large)						
	Slope	**Intercept**	$\mathbf{R^2}$	**PC**	**MSE**	**STD**
$\mathbf{T_x}$ **[mm]**	0.708	0.050	0.711	0.843	2.804	3.113
$\mathbf{T_y}$ **[mm]**	0.695	0.065	0.703	0.839	6.246	4.588
$\mathbf{T_z}$ **[mm]**	0.778	−0.002	0.790	0.889	0.304	1.204
$\mathbf{R_x}$ [∘]	0.699	−0.021	0.711	0.843	0.695	1.550
$\mathbf{R_y}$ [∘]	0.666	0.004	0.681	0.825	0.043	0.365
$\mathbf{R_z}$ [∘]	0.685	−0.010	0.712	0.844	0.342	1.087

Table C.18: *Subject 3.* Values of the slope and intercept of the linear fit are reported along with the values of R^2, the standard deviation (STD) and the mean squared error (MSE) and Pearson correlation coefficient (PC), for each of the motion parameters and prediction reported in Figure 5.25. Values have been rounded to three decimal places.

Subject 4 (Cloth, PLS, Raw, Large)						
	Slope	**Intercept**	$\mathbf{R^2}$	**PC**	**MSE**	**STD**
$\mathbf{T_x}$ **[mm]**	0.593	0.065	0.590	0.768	10.178	4.982
$\mathbf{T_y}$ **[mm]**	0.567	0.104	0.562	0.749	12.905	5.421
$\mathbf{T_z}$ **[mm]**	0.646	−0.064	0.637	0.798	2.011	2.352
$\mathbf{R_x}$ [◦]	0.619	−0.030	0.611	0.782	1.494	1.959
$\mathbf{R_y}$ [◦]	0.681	−0.008	0.696	0.834	0.358	1.084
$\mathbf{R_z}$ [◦]	0.627	0.004	0.629	0.793	1.364	1.918

Table C.19: *Subject 4.* Values of the slope and intercept of the linear fit are reported along with the values of R^2, the standard deviation (STD) and the mean squared error (MSE) and Pearson correlation coefficient (PC), for each of the motion parameters and prediction reported in Figure C.4. Values have been rounded to three decimal places.

Subject 5 (Cloth, PLS, Raw, Large)						
	Slope	**Intercept**	$\mathbf{R^2}$	**PC**	**MSE**	**STD**
$\mathbf{T_x}$ **[mm]**	0.819	0.026	0.831	0.912	3.230	4.368
$\mathbf{T_y}$ **[mm]**	0.712	0.027	0.724	0.851	8.511	5.553
$\mathbf{T_z}$ **[mm]**	0.515	0.010	0.520	0.721	0.753	1.252
$\mathbf{R_x}$ [◦]	0.729	−0.006	0.741	0.861	0.776	1.729
$\mathbf{R_y}$ [◦]	0.474	0.004	0.480	0.693	0.129	0.498
$\mathbf{R_z}$ [◦]	0.413	−0.002	0.420	0.648	0.726	1.119

Table C.20: *Subject 5.* Values of the slope and intercept of the linear fit are reported along with the values of R^2, the standard deviation (STD) and the mean squared error (MSE) and Pearson correlation coefficient (PC), for each of the motion parameters and prediction reported in Figure 5.26. Values have been rounded to three decimal places.

C.0.5 PVC, NARX, Raw, Small

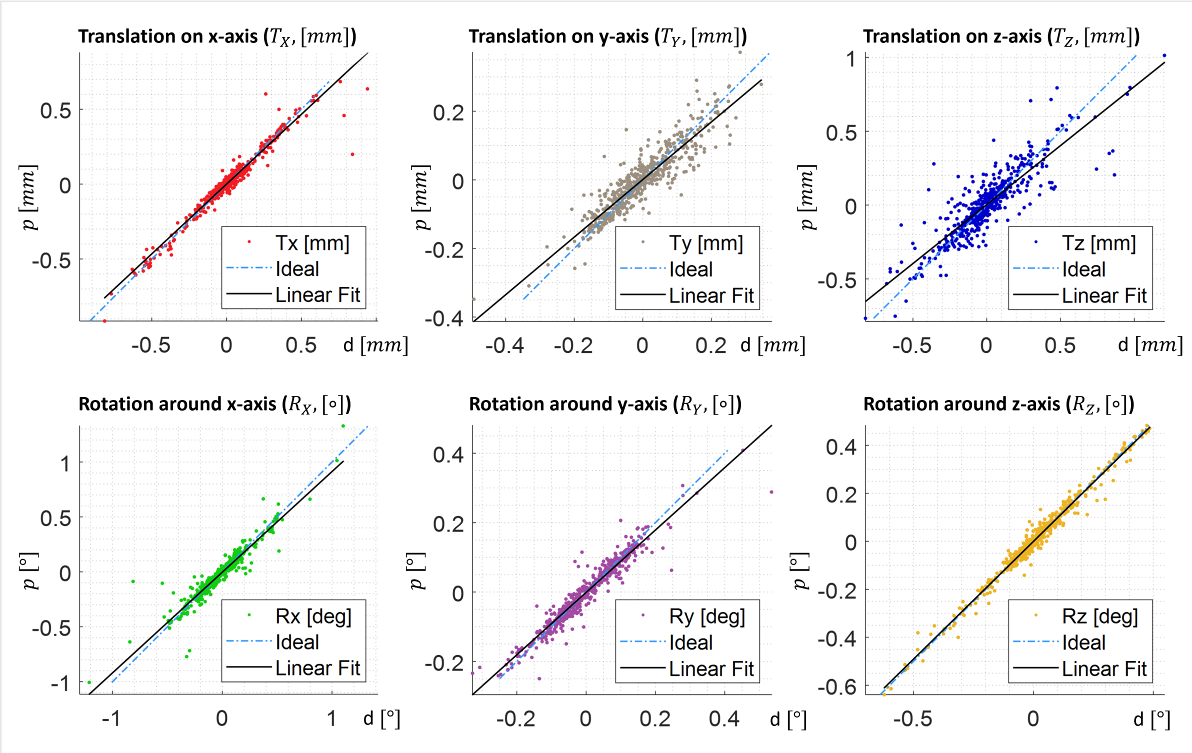

Figure C.5: The figure shows results obtained for *small* head movements, sampled using the *PVC* probe-holder set-up for *all* the subjects, using *raw* data for training the *non − linear* regression method (Table 5.1.3). Prediction results are *good* for translation along x axis and rotation around z axis.

Subject 1 (PVC, NARX, Raw, Small)						
	Slope	**Intercept**	$\mathbf{R^2}$	**PC**	**MSE**	**STD**
$\mathbf{T_x}$ **[mm]**	0.845	0.008	0.909	0.953	0.001	0.078
$\mathbf{T_y}$ **[mm]**	0.545	0.001	0.598	0.773	0.001	0.051
$\mathbf{T_z}$ **[mm]**	0.658	0.000	0.542	0.736	0.012	0.161
$\mathbf{R_x}$ $[\circ]$	0.984	0.000	0.907	0.953	0.001	0.089
$\mathbf{R_y}$ $[\circ]$	0.969	−0.004	0.975	0.988	0.000	0.106
$\mathbf{R_z}$ $[\circ]$	0.980	0.004	0.959	0.979	0.000	0.107

Table C.21: *Subject 1.* Values of the slope and intercept of the linear fit are reported along with the values of R^2, the standard deviation (STD) and the mean squared error (MSE) and Pearson correlation coefficient (PC), for each of the motion parameters and prediction reported in Figure C.5. Values have been rounded to three decimal places.

Subject 2 (PVC, NARX, Raw, Small)						
	Slope	**Intercept**	$\mathbf{R^2}$	**PC**	**MSE**	**STD**
$\mathbf{T_x}$ **[mm]**	0.814	0.000	0.871	0.933	0.001	0.069
$\mathbf{T_y}$ **[mm]**	0.713	−0.002	0.723	0.850	0.003	0.099
$\mathbf{T_z}$ **[mm]**	0.785	0.002	0.683	0.827	0.009	0.165
$\mathbf{R_x}$ [$\circ$]	0.921	−0.009	0.907	0.952	0.001	0.104
$\mathbf{R_y}$ [$\circ$]	0.901	0.001	0.885	0.941	0.001	0.084
$\mathbf{R_z}$ [$\circ$]	0.911	−0.002	0.857	0.926	0.000	0.045

Table C.22: *Subject 2.* Values of the slope and intercept of the linear fit are reported along with the values of R^2, the standard deviation (STD) and the mean squared error (MSE) and Pearson correlation coefficient (PC), for each of the motion parameters and prediction reported in Figure C.5. Values have been rounded to three decimal places.

Subject 3 (PVC, NARX, Raw, Small)						
	Slope	**Intercept**	$\mathbf{R^2}$	**PC**	**MSE**	**STD**
$\mathbf{T_x}$ **[mm]**	0.945	−0.008	0.956	0.978	0.007	0.387
$\mathbf{T_y}$ **[mm]**	0.953	0.001	0.947	0.973	0.001	0.132
$\mathbf{T_z}$ **[mm]**	0.901	−0.006	0.888	0.942	0.009	0.278
$\mathbf{R_x}$ [$\circ$]	0.908	0.003	0.865	0.930	0.013	0.307
$\mathbf{R_y}$ [$\circ$]	0.814	−0.001	0.838	0.915	0.001	0.061
$\mathbf{R_z}$ [$\circ$]	0.994	−0.002	0.989	0.994	0.001	0.275

Table C.23: *Subject 3.* Values of the slope and intercept of the linear fit are reported along with the values of R^2, the standard deviation (STD) and the mean squared error (MSE) and Pearson correlation coefficient (PC), for each of the motion parameters and prediction reported in Figure 5.27. Values have been rounded to three decimal places.

Subject 6 (PVC, NARX, Raw, Small)						
	Slope	**Intercept**	$\mathbf{R^2}$	**PC**	**MSE**	**STD**
$\mathbf{T_x}$ **[mm]**	0.894	0.001	0.891	0.944	0.001	0.113
$\mathbf{T_y}$ **[mm]**	0.831	0.008	0.808	0.899	0.003	0.116
$\mathbf{T_z}$ **[mm]**	0.746	0.021	0.715	0.845	0.025	0.292
$\mathbf{R_x}$ [$\circ$]	0.921	−0.009	0.936	0.967	0.004	0.247
$\mathbf{R_y}$ [$\circ$]	0.873	−0.002	0.922	0.960	0.001	0.133
$\mathbf{R_z}$ [$\circ$]	0.940	−0.003	0.963	0.981	0.001	0.148

Table C.24: *Subject 6.* Values of the slope and intercept of the linear fit are reported along with the values of R^2, the standard deviation (STD) and the mean squared error (MSE) and Pearson correlation coefficient (PC), for each of the motion parameters and prediction reported in Figure 5.28. Values have been rounded to three decimal places.

C.0.6 PVC, NARX, Raw, Large

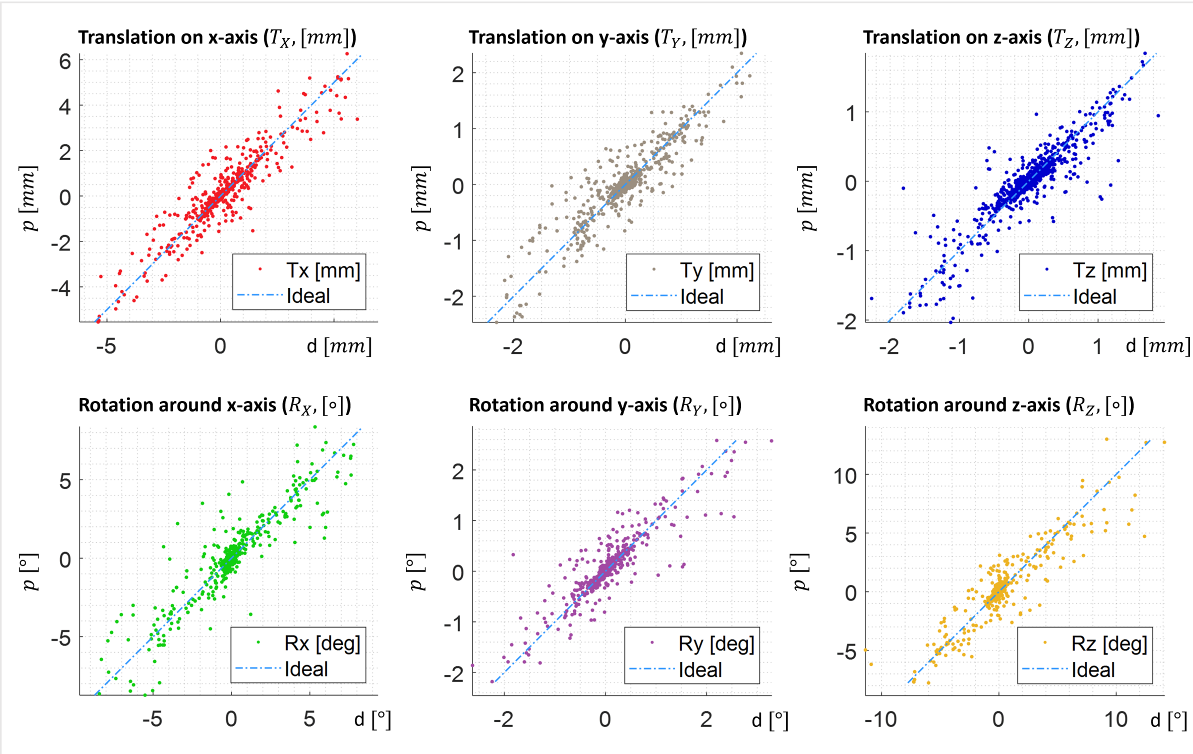

Figure C.6: The figure shows results obtained for *large* head movements, sampled using the *PVC* probe-holder set-up for *all* the subjects, using *raw* data for training the *non − linear* regression method (Table 5.1.3). Prediction results are *poor* for all the motion parameters.

Subject 1 (PVC, NARX, Raw, Large)						
	Slope	**Intercept**	$\mathbf{R^2}$	**PC**	**MSE**	**STD**
$\mathbf{T_x}$ [mm]	0.886	−0.023	0.826	0.909	0.133	0.866
$\mathbf{T_y}$ [mm]	0.929	0.005	0.862	0.928	0.016	0.338
$\mathbf{T_z}$ [mm]	0.598	0.009	0.711	0.843	0.012	0.195
$\mathbf{R_x}$ [○]	1.019	−0.017	0.897	0.947	0.101	0.920
$\mathbf{R_y}$ [○]	0.948	0.003	0.940	0.970	0.003	0.213
$\mathbf{R_z}$ [○]	0.857	−0.040	0.829	0.910	0.352	1.431

Table C.25: *Subject 1.* Values of the slope and intercept of the linear fit are reported along with the values of R^2, the standard deviation (STD) and the mean squared error (MSE) and Pearson correlation coefficient (PC), for each of the motion parameters and prediction reported in Figure C.6. Values have been rounded to three decimal places.

Subject 2 (PVC, NARX, Raw, Large)						
	Slope	**Intercept**	$\mathbf{R^2}$	**PC**	**MSE**	**STD**
$\mathbf{T_x}$ **[mm]**	0.806	−0.013	0.723	0.850	0.268	0.969
$\mathbf{T_y}$ **[mm]**	0.750	−0.009	0.680	0.825	0.058	0.424
$\mathbf{T_z}$ **[mm]**	0.824	−0.034	0.769	0.877	0.081	0.586
$\mathbf{R_x}$ [$\circ$]	0.843	0.015	0.780	0.883	1.730	2.780
$\mathbf{R_y}$ [$\circ$]	0.810	−0.017	0.782	0.884	0.096	0.661
$\mathbf{R_z}$ [$\circ$]	0.808	−0.125	0.725	0.852	0.996	1.852

Table C.26: *Subject 2.* Values of the slope and intercept of the linear fit are reported along with the values of R^2, the standard deviation (STD) and the mean squared error (MSE) and Pearson correlation coefficient (PC), for each of the motion parameters and prediction reported in Figure C.6. Values have been rounded to three decimal places.

Subject 3 (PVC, NARX, Raw, Large)						
	Slope	**Intercept**	$\mathbf{R^2}$	**PC**	**MSE**	**STD**
$\mathbf{T_x}$ **[mm]**	0.885	0.139	0.812	0.901	0.467	1.523
$\mathbf{T_y}$ **[mm]**	0.905	0.020	0.850	0.922	0.095	0.785
$\mathbf{T_z}$ **[mm]**	0.976	0.012	0.926	0.962	0.016	0.458
$\mathbf{R_x}$ [$\circ$]	0.943	−0.013	0.865	0.930	0.387	1.652
$\mathbf{R_y}$ [$\circ$]	0.863	0.049	0.850	0.922	0.060	0.626
$\mathbf{R_z}$ [$\circ$]	0.892	0.145	0.803	0.896	0.560	1.622

Table C.27: *Subject 3.* Values of the slope and intercept of the linear fit are reported along with the values of R^2, the standard deviation (STD) and the mean squared error (MSE) and Pearson correlation coefficient (PC), for each of the motion parameters and prediction reported in Figure 5.29. Values have been rounded to three decimal places.

Subject 6 (PVC, NARX, Raw, Large)						
	Slope	**Intercept**	$\mathbf{R^2}$	**PC**	**MSE**	**STD**
$\mathbf{T_x}$ **[mm]**	0.916	−0.010	0.937	0.968	0.178	1.677
$\mathbf{T_y}$ **[mm]**	0.814	0.012	0.840	0.917	0.047	0.543
$\mathbf{T_z}$ **[mm]**	0.840	−0.038	0.792	0.890	0.076	0.598
$\mathbf{R_x}$ [$\circ$]	0.931	0.128	0.863	0.929	0.469	1.792
$\mathbf{R_y}$ [$\circ$]	0.764	0.012	0.683	0.826	0.045	0.371
$\mathbf{R_z}$ [$\circ$]	0.822	−0.005	0.884	0.940	1.329	3.316

Table C.28: *Subject 6.* Values of the slope and intercept of the linear fit are reported along with the values of R^2, the standard deviation (STD) and the mean squared error (MSE) and Pearson correlation coefficient (PC), for each of the motion parameters and prediction reported in Figure 5.30. Values have been rounded to three decimal places.

C.0.7 Cloth, NARX, Raw, Small

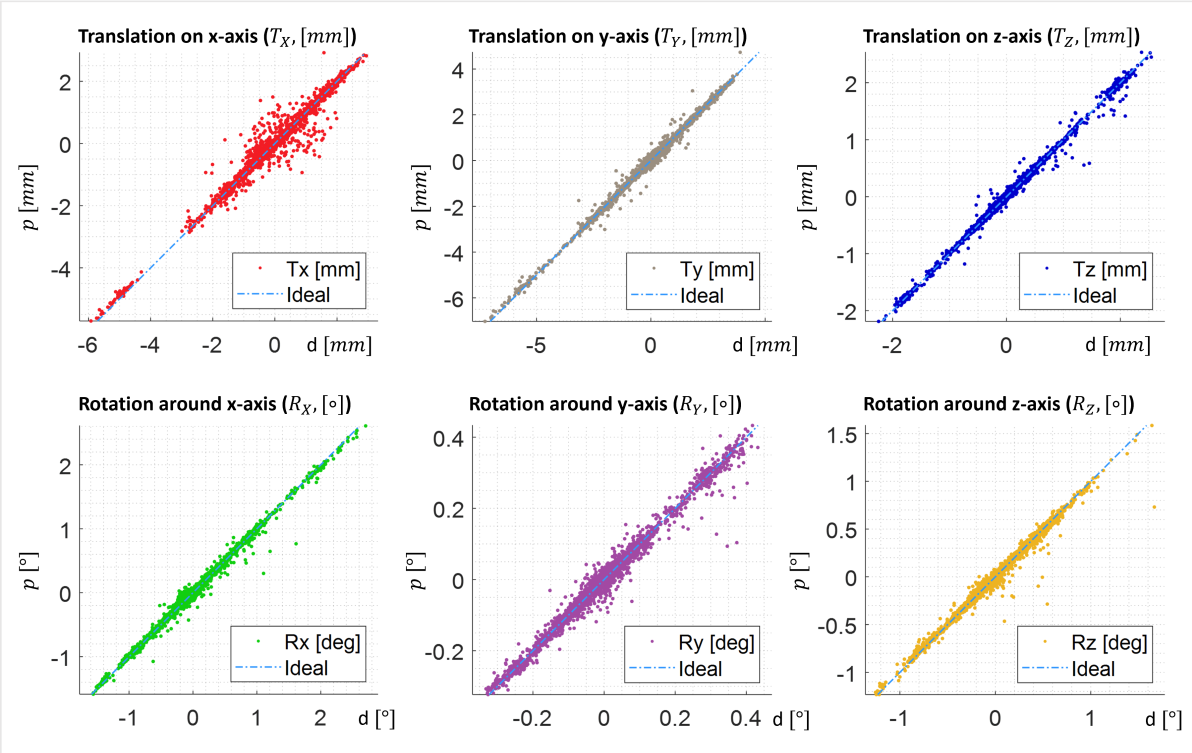

Figure C.7: The figure shows results obtained for *small* head movements, sampled using the *cloth* probe-holder set-up for *all* the subjects, using *raw* data for training the *non − linear* regression method (Table 5.1.3). Prediction results are *good* for all the motion parameters.

Subject 1 (Cloth, NARX, Raw, Small)

	Slope	Intercept	R^2	PC	MSE	STD
T_x [mm]	0.981	−0.002	0.984	0.992	0.002	0.322
T_y [mm]	0.969	−0.009	0.989	0.994	0.004	0.609
T_z [mm]	0.997	0.000	0.992	0.996	0.001	0.253
R_x [∘]	0.971	0.003	0.986	0.993	0.001	0.212
R_y [∘]	0.980	−0.001	0.977	0.988	0.000	0.075
R_z [∘]	0.957	−0.002	0.945	0.972	0.000	0.075

Table C.29: *Subject 1.* Values of the slope and intercept of the linear fit are reported along with the values of R^2, the standard deviation (STD) and the mean squared error (MSE) and Pearson correlation coefficient (PC), for each of the motion parameters and prediction reported in Figure C.7. Values have been rounded to three decimal places.

Subject 2 (Cloth, NARX, Raw, Small)						
	Slope	**Intercept**	$\mathbf{R^2}$	**PC**	**MSE**	**STD**
$\mathbf{T_x}$ **[mm]**	0.981	0.003	0.998	0.999	0.008	1.868
$\mathbf{T_y}$ **[mm]**	0.988	−0.003	0.998	0.999	0.010	2.346
$\mathbf{T_z}$ **[mm]**	0.994	0.002	0.999	0.999	0.000	0.564
$\mathbf{R_x}$ [$\circ$]	0.985	0.000	0.998	0.999	0.002	0.924
$\mathbf{R_y}$ [$\circ$]	0.967	0.001	0.978	0.989	0.000	0.078
$\mathbf{R_z}$ [$\circ$]	0.976	−0.003	0.993	0.997	0.002	0.495

Table C.30: *Subject 2.* Values of the slope and intercept of the linear fit are reported along with the values of R^2, the standard deviation (STD) and the mean squared error (MSE) and Pearson correlation coefficient (PC), for each of the motion parameters and prediction reported in Figure C.7. Values have been rounded to three decimal places.

Subject 3 (Cloth, NARX, Raw, Small)						
	Slope	**Intercept**	$\mathbf{R^2}$	**PC**	**MSE**	**STD**
$\mathbf{T_x}$ **[mm]**	0.950	−0.001	0.939	0.969	0.016	0.516
$\mathbf{T_y}$ **[mm]**	0.981	−0.004	0.960	0.980	0.014	0.590
$\mathbf{T_z}$ **[mm]**	0.951	0.009	0.965	0.982	0.002	0.257
$\mathbf{R_x}$ [$\circ$]	0.969	0.004	0.976	0.988	0.002	0.253
$\mathbf{R_y}$ [$\circ$]	0.959	0.003	0.940	0.970	< 0.001	0.070
$\mathbf{R_z}$ [$\circ$]	0.972	0.001	0.993	0.996	0.002	0.459

Table C.31: *Subject 3.* Values of the slope and intercept of the linear fit are reported along with the values of R^2, the standard deviation (STD) and the mean squared error (MSE) and Pearson correlation coefficient (PC), for each of the motion parameters and prediction reported in Figure 5.31. Values have been rounded to three decimal places.

Subject 4 (Cloth, NARX, Raw, Small)						
	Slope	**Intercept**	$\mathbf{R^2}$	**PC**	**MSE**	**STD**
$\mathbf{T_x}$ **[mm]**	0.912	0.001	0.867	0.931	0.176	1.140
$\mathbf{T_y}$ **[mm]**	0.998	0.002	0.991	0.996	0.024	1.664
$\mathbf{T_z}$ **[mm]**	0.992	−0.005	0.995	0.997	0.008	1.276
$\mathbf{R_x}$ [$\circ$]	0.985	−0.005	0.987	0.994	0.006	0.658
$\mathbf{R_y}$ [$\circ$]	0.977	−0.003	0.979	0.990	0.001	0.207
$\mathbf{R_z}$ [$\circ$]	0.955	−0.003	0.954	0.977	0.004	0.296

Table C.32: *Subject 4.* Values of the slope and intercept of the linear fit are reported along with the values of R^2, the standard deviation (STD) and the mean squared error (MSE) and Pearson correlation coefficient (PC), for each of the motion parameters and prediction reported in Figure C.7. Values have been rounded to three decimal places.

Subject 5 (Cloth, NARX, Raw, Small)						
	Slope	**Intercept**	$\mathbf{R^2}$	**PC**	**MSE**	**STD**
$\mathbf{T_x}$ [mm]	0.994	−0.003	0.996	0.998	0.007	1.319
$\mathbf{T_y}$ [mm]	0.998	0.002	0.999	0.999	0.007	2.199
$\mathbf{T_z}$ [mm]	0.990	−0.002	0.995	0.998	0.001	0.444
$\mathbf{R_x}$ [$\circ$]	0.996	−0.001	0.998	0.999	0.001	0.734
$\mathbf{R_y}$ [$\circ$]	0.993	−0.002	0.995	0.997	< 0.001	0.141
$\mathbf{R_z}$ [$\circ$]	0.982	< 0.001	0.989	0.994	0.001	0.215

Table C.33: *Subject 5.* Values of the slope and intercept of the linear fit are reported along with the values of R^2, the standard deviation (STD) and the mean squared error (MSE) and Pearson correlation coefficient (PC), for each of the motion parameters and prediction reported in Figure 5.32. Values have been rounded to three decimal places.

C.0.8 Cloth, NARX, Raw, Large

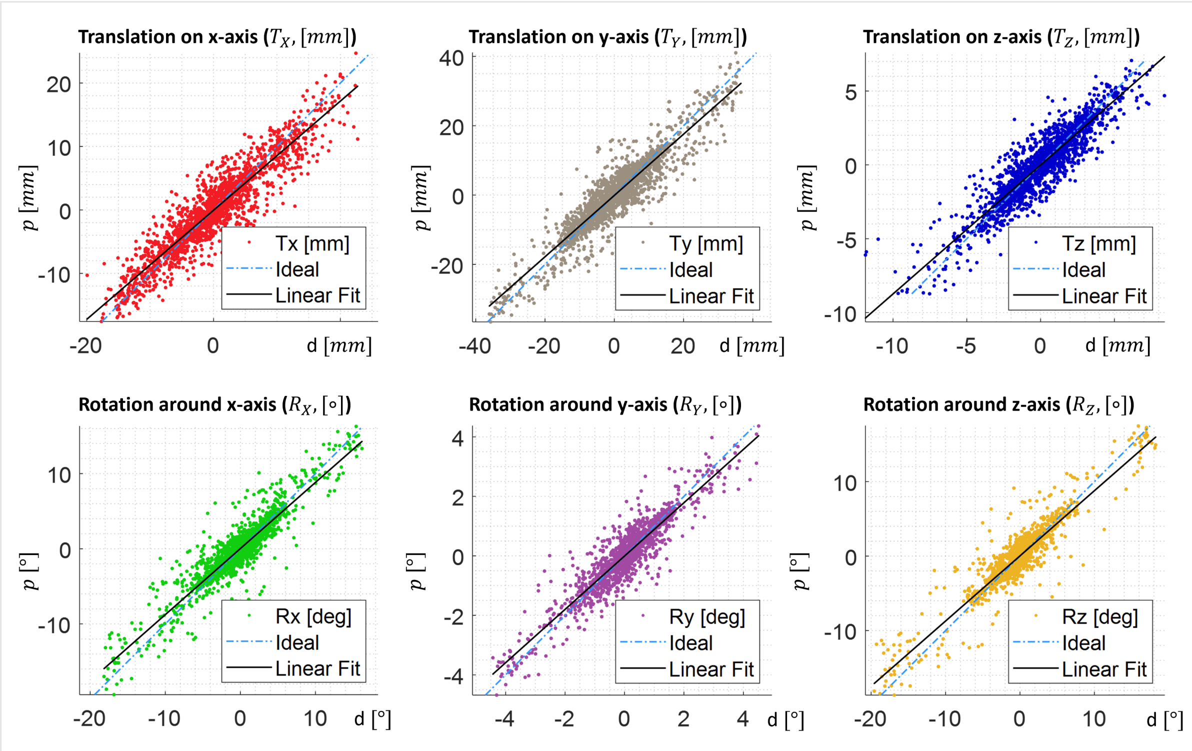

Figure C.8: The figure shows results obtained for *large* head movements, sampled using the *cloth* probe-holder set-up for *all* the subjects, using *raw* data for training the *non − linear* regression method (Table 5.1.3). Prediction results are *poor* for all the head motion parameters.

Subject 1 (Cloth, NARX, Raw, Large)						
	Slope	**Intercept**	$\mathbf{R^2}$	**PC**	**MSE**	**STD**
$\mathbf{T_x}$ **[mm]**	0.897	−0.001	0.801	0.895	1.024	2.207
$\mathbf{T_y}$ **[mm]**	0.883	0.057	0.780	0.883	2.191	3.066
$\mathbf{T_z}$ **[mm]**	0.888	0.016	0.757	0.870	0.177	0.817
$\mathbf{R_x}$ [∘]	0.884	−0.021	0.782	0.885	0.222	0.981
$\mathbf{R_y}$ [∘]	0.891	0.007	0.752	0.867	0.033	0.346
$\mathbf{R_z}$ [∘]	0.884	−0.031	0.778	0.882	0.174	0.856

Table C.34: *Subject 1.* Values of the slope and intercept of the linear fit are reported along with the values of R^2, the standard deviation (STD) and the mean squared error (MSE) and Pearson correlation coefficient (PC), for each of the motion parameters and prediction reported in Figure C.8. Values have been rounded to three decimal places.

Subject 2 (Cloth, NARX, Raw, Large)						
	Slope	**Intercept**	$\mathbf{R^2}$	**PC**	**MSE**	**STD**
$\mathbf{T_x}$ **[mm]**	0.896	−0.187	0.879	0.937	5.408	6.642
$\mathbf{T_y}$ **[mm]**	0.910	−0.405	0.878	0.937	18.928	12.326
$\mathbf{T_z}$ **[mm]**	0.873	0.038	0.821	0.906	0.703	1.965
$\mathbf{R_x}$ [∘]	0.896	0.175	0.872	0.934	3.532	5.215
$\mathbf{R_y}$ [∘]	0.872	0.006	0.862	0.928	0.044	0.565
$\mathbf{R_z}$ [∘]	0.872	0.143	0.862	0.928	3.270	4.844

Table C.35: *Subject 2.* Values of the slope and intercept of the linear fit are reported along with the values of R^2, the standard deviation (STD) and the mean squared error (MSE) and Pearson correlation coefficient (PC), for each of the motion parameters and prediction reported in Figure C.8. Values have been rounded to three decimal places.

Subject 3 (Cloth, NARX, Raw, Large)						
	Slope	**Intercept**	$\mathbf{R^2}$	**PC**	**MSE**	**STD**
$\mathbf{T_x}$ **[mm]**	0.735	−0.067	0.808	0.899	1.844	3.040
$\mathbf{T_y}$ **[mm]**	0.788	−0.115	0.831	0.912	3.323	4.399
$\mathbf{T_z}$ **[mm]**	0.813	0.008	0.883	0.940	0.172	1.186
$\mathbf{R_x}$ [∘]	0.795	0.033	0.831	0.912	0.376	1.485
$\mathbf{R_y}$ [∘]	0.821	−0.004	0.818	0.904	0.026	0.377
$\mathbf{R_z}$ [∘]	0.874	0.004	0.801	0.895	0.225	1.046

Table C.36: *Subject 1.* Values of the slope and intercept of the linear fit are reported along with the values of R^2, the standard deviation (STD) and the mean squared error (MSE) and Pearson correlation coefficient (PC), for each of the motion parameters and prediction reported in Figure 5.33. Values have been rounded to three decimal places.

Subject 4 (Cloth, NARX, Raw, Large)						
	Slope	**Intercept**	$\mathbf{R^2}$	**PC**	**MSE**	**STD**
$\mathbf{T_x}$ **[mm]**	0.860	0.006	0.847	0.921	3.948	5.086
$\mathbf{T_y}$ **[mm]**	0.876	−0.031	0.855	0.925	4.316	5.452
$\mathbf{T_z}$ **[mm]**	0.874	−0.029	0.884	0.940	0.638	2.344
$\mathbf{R_x}$ $[\circ]$	0.867	−0.005	0.854	0.924	0.590	2.011
$\mathbf{R_y}$ $[\circ]$	0.907	−0.020	0.868	0.932	0.168	1.119
$\mathbf{R_z}$ $[\circ]$	0.903	0.032	0.861	0.928	0.547	1.971

Table C.37: *Subject 4.* Values of the slope and intercept of the linear fit are reported along with the values of R^2, the standard deviation (STD) and the mean squared error (MSE) and Pearson correlation coefficient (PC), for each of the motion parameters and prediction reported in Figure C.8. Values have been rounded to three decimal places.

Subject 5 (Cloth, NARX, Raw, Large)						
	Slope	**Intercept**	$\mathbf{R^2}$	**PC**	**MSE**	**STD**
$\mathbf{T_x}$ **[mm]**	0.827	0.004	0.873	0.935	2.267	4.191
$\mathbf{T_y}$ **[mm]**	0.831	−0.029	0.833	0.912	4.911	5.418
$\mathbf{T_z}$ **[mm]**	0.923	−0.051	0.790	0.889	0.367	1.253
$\mathbf{R_x}$ $[\circ]$	0.821	−0.002	0.835	0.914	0.469	1.685
$\mathbf{R_y}$ $[\circ]$	0.919	−0.018	0.772	0.879	0.064	0.500
$\mathbf{R_z}$ $[\circ]$	0.855	0.009	0.746	0.864	0.333	1.112

Table C.38: *Subject 5.* Values of the slope and intercept of the linear fit are reported along with the values of R^2, the standard deviation (STD) and the mean squared error (MSE) and Pearson correlation coefficient (PC), for each of the motion parameters and prediction reported in Figure 5.34. Values have been rounded to three decimal places.

C.0.9 Cloth, NARX, Pre-processed, Large (Less dynamics)

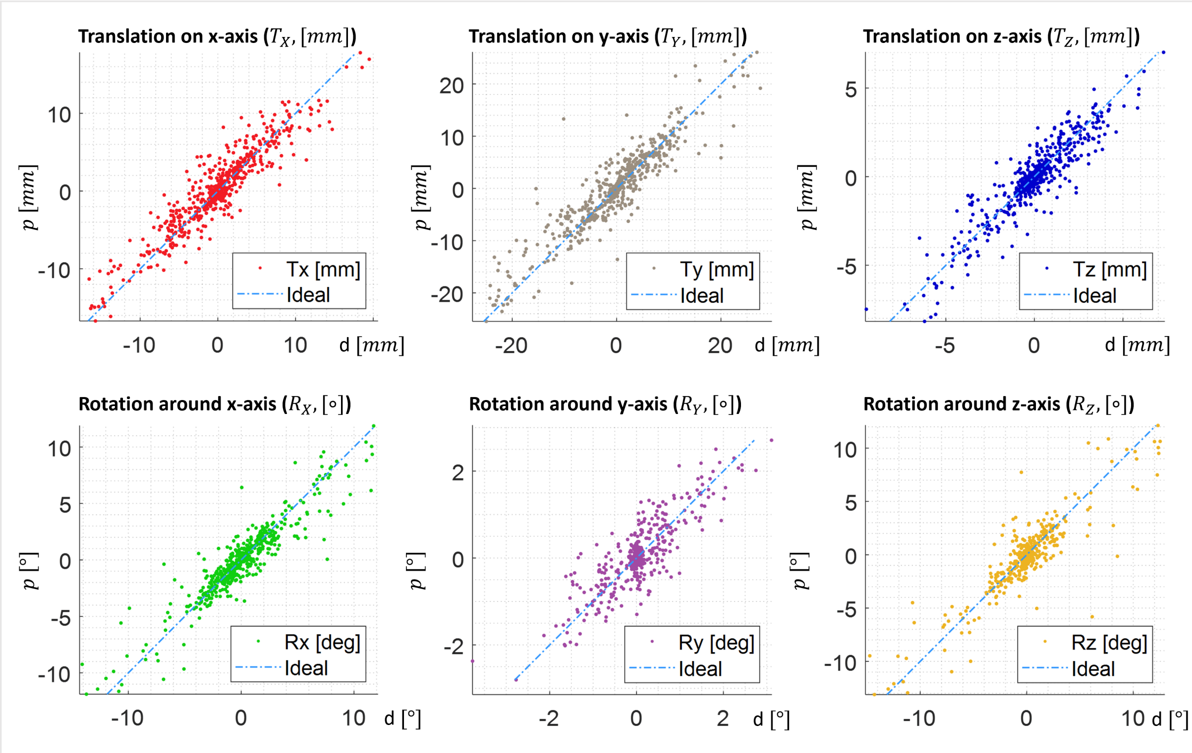

Figure C.9: The figure shows results obtained for *large* head movements, sampled using the *cloth* probe-holder set-up for *all* the subjects, using *raw* data for training the $non - linear$ regression method (Table 5.1.3). Prediction results are *poor* for all the head motion parameters.

C.0.10 Cloth, NARX, Pre-processed, Small

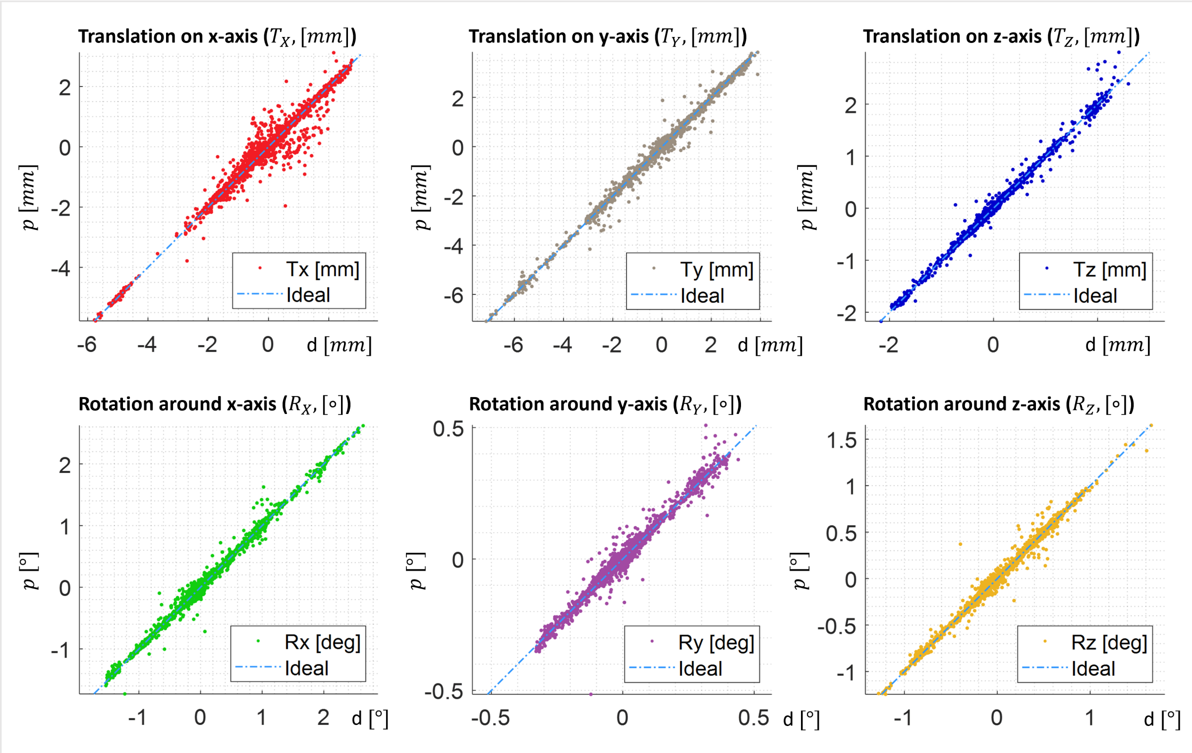

Figure C.10: The figure shows results obtained for *small* head movements, sampled using the *cloth* probe-holder set-up for *all* the subjects, using *pre − processed* data for training the *non − linear* regression method (Table 5.1.3). Prediction results are *good* for the most of the head motion parameters.

Subject 1 (Cloth, NARX, Pre-processed, Small)

	Slope	Intercept	R^2	PC	MSE	STD
T_x [mm]	0.996	−0.005	0.981	0.991	0.002	0.328
T_y [mm]	1.000	−0.008	0.992	0.996	0.003	0.630
T_z [mm]	0.997	0.000	0.997	0.998	0.000	0.259
R_x [∘]	0.998	0.002	0.991	0.995	0.000	0.219
R_y [∘]	0.993	−0.001	0.996	0.998	0.000	0.076
R_z [∘]	0.941	0.000	0.969	0.984	0.000	0.075

Table C.39: *Subject 1.* Values of the slope and intercept of the linear fit are reported along with the values of R^2, the standard deviation (STD) and the mean squared error (MSE) and Pearson correlation coefficient (PC), for each of the motion parameters and prediction reported in Figure C.10. Values have been rounded to three decimal places.

Subject 2 (Cloth, NARX, Pre-processed, Small)						
	Slope	**Intercept**	$\mathbf{R^2}$	**PC**	**MSE**	**STD**
$\mathbf{T_x}$ **[mm]**	0.997	-0.008	0.998	0.999	0.011	2.080
$\mathbf{T_y}$ **[mm]**	0.994	-0.007	0.998	0.999	0.016	2.577
$\mathbf{T_z}$ **[mm]**	0.993	0.003	0.996	0.998	0.001	0.586
$\mathbf{R_x}$ [$\circ$]	0.993	0.003	0.997	0.998	0.003	1.003
$\mathbf{R_y}$ [$\circ$]	0.992	0.001	0.982	0.991	0.000	0.072
$\mathbf{R_z}$ [$\circ$]	0.987	0.000	0.994	0.997	0.001	0.505

Table C.40: *Subject 2.* Values of the slope and intercept of the linear fit are reported along with the values of R^2, the standard deviation (STD) and the mean squared error (MSE) and Pearson correlation coefficient (PC), for each of the motion parameters and prediction reported in Figure C.10. Values have been rounded to three decimal places.

Subject 3 (Cloth, NARX, Pre-processed, Small)						
	Slope	**Intercept**	$\mathbf{R^2}$	**PC**	**MSE**	**STD**
$\mathbf{T_x}$ **[mm]**	0.949	0.001	0.901	0.949	0.030	0.542
$\mathbf{T_y}$ **[mm]**	0.967	-0.011	0.941	0.970	0.023	0.615
$\mathbf{T_z}$ **[mm]**	0.981	0.009	0.983	0.991	0.001	0.270
$\mathbf{R_x}$ [$\circ$]	0.990	< 0.001	0.967	0.983	0.002	0.265
$\mathbf{R_y}$ [$\circ$]	0.980	0.004	0.942	0.970	< 0.001	0.078
$\mathbf{R_z}$ [$\circ$]	0.993	-0.003	0.995	0.997	0.001	0.468

Table C.41: *Subject 3.* Values of the slope and intercept of the linear fit are reported along with the values of R^2, the standard deviation (STD) and the mean squared error (MSE) and Pearson correlation coefficient (PC), for each of the motion parameters and prediction reported in Figure 5.35. Values have been rounded to three decimal places.

Subject 4 (Cloth, NARX, Pre-processed, Small)						
	Slope	**Intercept**	$\mathbf{R^2}$	**PC**	**MSE**	**STD**
$\mathbf{T_x}$ **[mm]**	0.896	-0.012	0.857	0.926	0.188	1.137
$\mathbf{T_y}$ **[mm]**	0.997	-0.018	0.988	0.994	0.034	1.646
$\mathbf{T_z}$ **[mm]**	1.003	0.004	0.994	0.997	0.009	1.247
$\mathbf{R_x}$ [$\circ$]	0.998	0.006	0.987	0.994	0.005	0.645
$\mathbf{R_y}$ [$\circ$]	1.024	0.002	0.982	0.991	0.001	0.201
$\mathbf{R_z}$ [$\circ$]	1.005	0.003	0.974	0.987	0.002	0.287

Table C.42: *Subject 4.* Values of the slope and intercept of the linear fit are reported along with the values of R^2, the standard deviation (STD) and the mean squared error (MSE) and Pearson correlation coefficient (PC), for each of the motion parameters and prediction reported in Figure C.10. Values have been rounded to three decimal places.

Subject 5 (Cloth, NARX, Pre-processed, Small)						
	Slope	**Intercept**	$\mathbf{R^2}$	**PC**	**MSE**	**STD**
$\mathbf{T_x}$ [mm]	1.000	−0.007	0.997	0.998	0.006	1.359
$\mathbf{T_y}$ [mm]	0.998	−0.005	0.999	0.999	0.006	2.278
$\mathbf{T_z}$ [mm]	0.995	0.001	0.993	0.997	0.001	0.458
$\mathbf{R_x}$ [∘]	1.000	−0.001	0.998	0.999	0.001	0.762
$\mathbf{R_y}$ [∘]	0.982	−0.002	0.984	0.992	< 0.001	0.146
$\mathbf{R_z}$ [∘]	0.976	0.001	0.976	0.988	0.001	0.222

Table C.43: *Subject 5.* Values of the slope and intercept of the linear fit are reported along with the values of R^2, the standard deviation (STD) and the mean squared error (MSE) and Pearson correlation coefficient (PC), for each of the motion parameters and prediction reported in Figure 5.36. Values have been rounded to three decimal places.

C.0.11 Cloth, NARX, Pre-processed, Small (Less dynamics)

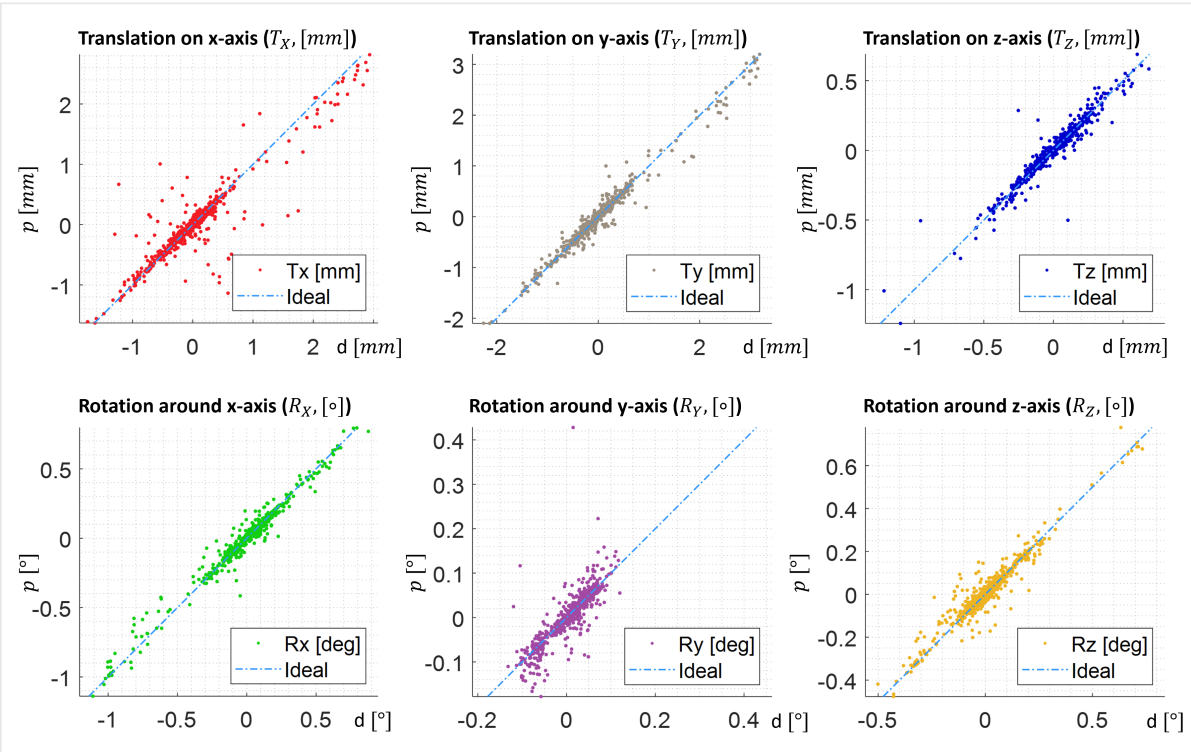

Figure C.11: The figure shows results obtained for *small* head movements, sampled using the *cloth* probe-holder set-up for *all* the subjects, using $pre-processed$ data for training the $non-linear$ regression method (Table 5.1.3). Prediction results are close to $ideal/good$ for translations/rotations around x/y/z axes.

Subject 1 (Less dynamics) (Cloth, NARX, Pre-processed, Small)						
	Slope	**Intercept**	$\mathbf{R^2}$	**PC**	**MSE**	**STD**
$\mathbf{T_x}$ **[mm]**	0.955	0.005	0.923	0.961	0.001	0.122
$\mathbf{T_y}$ **[mm]**	0.984	−0.002	0.980	0.990	0.001	0.216
$\mathbf{T_z}$ **[mm]**	0.961	0.005	0.985	0.992	0.000	0.109
$\mathbf{R_x}$ [∘]	0.962	0.005	0.967	0.983	0.000	0.070
$\mathbf{R_y}$ [∘]	1.051	−0.003	0.982	0.991	0.000	0.050
$\mathbf{R_z}$ [∘]	0.941	0.002	0.807	0.899	0.000	0.032

Table C.44: *Subject 1.* Values of the slope and intercept of the linear fit are reported along with the values of R^2, the standard deviation (STD) and the mean squared error (MSE) and Pearson correlation coefficient (PC), for each of the motion parameters and prediction reported in Figure C.11. Values have been rounded to three decimal places.

Subject 2 (Less dynamics) (Cloth, NARX, Pre-processed, Small)						
	Slope	**Intercept**	$\mathbf{R^2}$	**PC**	**MSE**	**STD**
$\mathbf{T_x}$ **[mm]**	0.921	−0.044	0.990	0.995	0.027	1.296
$\mathbf{T_y}$ **[mm]**	0.955	−0.030	0.991	0.996	0.023	1.489
$\mathbf{T_z}$ **[mm]**	1.021	0.006	0.973	0.986	0.002	0.258
$\mathbf{R_x}$ [∘]	0.949	0.004	0.988	0.994	0.004	0.528
$\mathbf{R_y}$ [∘]	1.229	−0.009	0.641	0.800	0.003	0.056
$\mathbf{R_z}$ [∘]	0.929	0.028	0.949	0.974	0.004	0.256

Table C.45: *Subject 2.* Values of the slope and intercept of the linear fit are reported along with the values of R^2, the standard deviation (STD) and the mean squared error (MSE) and Pearson correlation coefficient (PC), for each of the motion parameters and prediction reported in Figure C.11. Values have been rounded to three decimal places.

Subject 3 (Less dynamics) (Cloth, NARX, Pre-processed, Small)						
	Slope	**Intercept**	$\mathbf{R^2}$	**PC**	**MSE**	**STD**
$\mathbf{T_x}$ **[mm]**	0.910	0.018	0.626	0.791	0.027	0.232
$\mathbf{T_y}$ **[mm]**	0.966	0.014	0.865	0.930	0.018	0.353
$\mathbf{T_z}$ **[mm]**	0.842	0.003	0.686	0.828	0.006	0.136
$\mathbf{R_x}$ [∘]	0.964	−0.005	0.903	0.950	0.002	0.150
$\mathbf{R_y}$ [∘]	0.883	0.000	0.804	0.897	0.000	0.036
$\mathbf{R_z}$ [∘]	0.989	−0.001	0.976	0.988	0.001	0.166

Table C.46: *Subject 3.* Values of the slope and intercept of the linear fit are reported along with the values of R^2, the standard deviation (STD) and the mean squared error (MSE) and Pearson correlation coefficient (PC), for each of the motion parameters and prediction reported in Figure C.11. Values have been rounded to three decimal places.

Subject 4 (Less dynamics) (Cloth, NARX, Pre-processed, Small)						
	Slope	**Intercept**	$\mathbf{R^2}$	**PC**	**MSE**	**STD**
$\mathbf{T_x}$ **[mm]**	0.910	0.018	0.626	0.791	0.027	0.232
$\mathbf{T_y}$ **[mm]**	0.966	0.014	0.865	0.930	0.018	0.353
$\mathbf{T_z}$ **[mm]**	0.842	0.003	0.686	0.828	0.006	0.136
$\mathbf{R_x}$ [$\circ$]	0.964	−0.005	0.903	0.950	0.002	0.150
$\mathbf{R_y}$ [$\circ$]	0.883	0.000	0.804	0.897	0.000	0.036
$\mathbf{R_z}$ [$\circ$]	0.989	−0.001	0.976	0.988	0.001	0.166

Table C.47: *Subject 1.* Values of the slope and intercept of the linear fit are reported along with the values of R^2, the standard deviation (STD) and the mean squared error (MSE) and Pearson correlation coefficient (PC), for each of the motion parameters and prediction reported in Figure C.11. Values have been rounded to three decimal places.

Subject 5 (Less dynamics) (Cloth, NARX, Pre-processed, Small)						
	Slope	**Intercept**	$\mathbf{R^2}$	**PC**	**MSE**	**STD**
$\mathbf{T_x}$ **[mm]**	0.964	0.004	0.929	0.964	0.006	0.287
$\mathbf{T_y}$ **[mm]**	0.947	0.005	0.954	0.977	0.004	0.300
$\mathbf{T_z}$ **[mm]**	0.966	0.001	0.970	0.985	0.001	0.144
$\mathbf{R_x}$ [$\circ$]	0.925	−0.001	0.914	0.956	0.001	0.093
$\mathbf{R_y}$ [$\circ$]	0.973	0.002	0.924	0.961	0.000	0.040
$\mathbf{R_z}$ [$\circ$]	0.922	0.000	0.845	0.919	0.001	0.056

Table C.48: *Subject 5.* Values of the slope and intercept of the linear fit are reported along with the values of R^2, the standard deviation (STD) and the mean squared error (MSE) and Pearson correlation coefficient (PC), for each of the motion parameters and prediction reported in Figure C.11. Values have been rounded to three decimal places.

Appendix D

MATLAB code

D.1 Pre-processing of magnetic field data:

Magnetic field data from the magnetic field camera are extracted using a given MATLAB function made by the Skope company `AcqSys`.

Function I made are reported below.

D.1.1 Unfiltered data

```
B(channels,:); % Raw magnetic field data of Channels that were not ...
    faulty.
% size of B : 16 rows, N-columns (time steps or dynamics)
DB = bsxfun(@minus, B, mean (B,2)); % Magnetic field changes as ...
    zero-mean data series
```

D.1.2 Filtered data

```
B(channels,:); % Raw magnetic field data of Channels that were not ...
    faulty.
% size of B : 16 rows, N-columns (time steps or dynamics)
P; % Probe positions
DB = bsxfun(@minus, B, mean (B,2)); % Magnetic field changes as ...
    zero-mean data series
B_fit = sphfit(DB, P); % Function I made to compute the fit
DB = B_fit.Second; % Second harmonics order fit of DB
[DB,¬] = mapstd(DB); % Map DB by rows to have zero mean and unit ...
    standard deviation time series
```

```
[¬,indexes,¬] = ClustersPCA(DB, [1:size(DB,2)]); % Function that I ...
    made during my Master Thesis. It computes the feature selection ...
    using PCA and the HCA.
DB = DB(indexes,:); % Select the channels
STD = std(DB,[],'all'); % Normalisation factor
DB = DB./STD; % Same normalisation factor for all the rows
```

D.1.3 Custom functions

Solid Harmonics fit

```
function B_fit = sphfit(DB,P)
% Perform the solid harmonic fit
%%
    hh = sphfun(position); % Calculate spherical harmonics using the ...
        positions of the probes
    for i = 1:size(DB,2)
    % 1) Evaluate the Coeff over the whole positions
        Coeff(:,i) = linsolve(hh,DB(:,i));  % fit at each time point ...
            (note order)
    % 2) Evaluate the fit on the hormonics only
        B_fit.Zero(:,i) = hh(:,1)*Coeff(1,i);
        B_fit.First(:,i) = hh(:,2:4)*Coeff(2:4,i);
        B_fit.Second(:,i) = hh(:,5:9)*Coeff(5:9,i);
end
% Nested function
function SPH = sphfun(P)
% Definitions of solid harmonics
%%
for n = 1:size(P,1) %n = probe's number
    x = P(n,1)./0.1;
    y = P(n,2)./0.1;
    z = P(n,3)./0.1;
    % First order
    SPH(n,1) = 1;
    SPH(n,2) = x;
    SPH(n,3) = y;
    SPH(n,4) = z;
    % Second Order
    SPH(n,5) = x*y;
    SPH(n,6) = z*y;
    SPH(n,7) = 3*z^2-(x^2 + y^2 + z^2);
    SPH(n,8) = x*z;
    SPH(n,9) = x^2 - y^2;
% Third order - not used
```

```
%      SPH(n,10) = 3*y*x^2 - y^3;
%      SPH(n,11) = x*y*z;
%      SPH(n,12) = (5*z^2-(x^2+y^2+z^2))*y;
%      SPH(n,13) = 5*z^3 -3*z*(x^2+y^2+z^2);
%      SPH(n,14) = (5*z^2-(x^2+y^2+z^2))*x;
%      SPH(n,15) = x^2 *z - y^2 * z;
%      SPH(n,16) = x^3 - 3*x*y^2;
end
```

PCA and HCA

```
function [C,indexes,In]= ClustersPCA(DB, Channels)
% Function to perform the feature selection
%%
    DB = DB(Channels,:);
    % 1) Clusters (C) of the channels selected by PCA and HCA
    [¬,¬,¬,C] = Dendro(DB, Channels); % First column of C represents ...
        the channel number; second column of C represents the ...
        cluster number whose the channel belong to
    % 2) Select the final subgroup of probes identify the cluster ...
        that correspond to the probes that carries the most of the ...
        variance. It is necessary to have a subgroup with more than ...
        6 channels as motion data have 6 degrees of freedom.
    [¬,Index] = sort(var(bfield,0,2),'descend'); % Sort the channels ...
        based on the variance of DB. First row will report the ...
        channels with the bigger variance.
    indexes = []; % Initialisation of the variable
    w = 0; % While loop test variable
    while size(indexes,1)<6
        w = w+1;
        Clusters = C(Index(w,1),2); % Cluster's number (C's column) ...
            of the probes (Index's row) that reports the bigger variance
        c = ismember(C(:,2),Clusters); % Select the other channels ...
            that belong to the same cluster. ismember(a,b) gives ...
            "true" if the element in "a" is a member of "b".So, it ...
            stores this information in a Boolean vector
        indexes = [indexes ; C(c,1)]; % To store the indexes of the ...
            channel's numbers (C's first column)
        indexes = unique(indexes); % Eliminate repetitions
    end
    indexes = sort(indexes,'ascend'); % Sort the channels
end
% Nested function
function [¬,¬,¬,C] = Dendro(DB, Channels)
%%
```

```
    DB = transpose(DB); % Bring DB in the correct format for pca() ...
        (time steps-row times variables-columns)
    coeff = pca(DB); % Perform principal component analysis to ...
        obtain the principal component coefficients (eigenvalue of ...
        the principal components)
    % Hierarchical Cluster Analysis (HCA)
    tree = linkage(coeff(:,1:3),'ward'); % Create a hierarchical ...
        binary cluster tree using linkage.
    cutoff = 0.7*max(tree(:,3)); % Cut-off the linkage at the 70% of ...
        the maximum distance
    C(:,2) = cluster(tree,'Cutoff',cutoff,'Criterion','distance'); % ...
        Construct agglomerative clusters from linkages
    C(:,1) = Channels; % Name of the channel
```

D.1.4 Pre-processing of Motion data

Motion data are given from the camera as quaternion $(x, y, z, qx, qy, qz, qr)$. A function [20] is used to convert those in the scanner reference frame by using the information obtained from the calibration. Then, data are refer to the isocentre (F-vector) using the MRI image acquired during the survey. Lately, as explained in my master thesis [11], data are down sampled to match the acquisition frequency of the camera. In the code below, I assume that these steps were already made and the time series represents the translation and rotation around the x,y,z axes of the head, referred to the scanner system of reference.

```
M; % Motion data .
% size of M : 6 rows(Tx, Ty, Tz, Rx, Ry, Rz in mm or degrees), ...
    N-columns (time steps or dynamics)
DM = bsxfun(@minus, M, mean (M,2)); % Magnetic field changes as ...
    zero-mean data series
```

Motion data do no require to be normalised as they are already in the range $\approx 10^1$ that is optimal for perform regression. By subtracting the average to both `DB` and `DM` we assuming that at ”zero” head movement correspond ”zero” magnetic field changes and so if the head doesn't move, the magnetic field doesn't' change. This is not entirely true as there are other factors that influences the changing in in magnetic field, those are mostly removed by the spatial filter.

D.2 Regression methods

Once the pre-processing (with or without the filter) is done, we have one input data series (called `DB`) and one output data series (called `DM`) ready to be used for the training of the regression method.

D.2.1 Linear method: PLS

```
rng('seed'); % Randomisation of the starting point for the ...
    subsequent random extraction and inisialization of regression ...
    method weights
Input = DB; Output = DM; % Variables to train the regression method
[trainInd,¬,testInd] = dividerand(size(Output,2),0.75,0,0.15); % ...
    Random extraction of indexes to select the training (trainInd) ...
    and new data (testInd) to test the trained method.
[¬,¬,¬,¬,BETAfit,¬,MSE,¬] = ...
    plsregress(Input(:,trainInd).',Output(:,trainInd).',size(Input,1),'CV',6); ...
    % Partial Least Regression Method using the k-fold ...
    cross-validation (k = 6) to validate it.
     % MSE is the mean squared error of the fit (it could be used to ...
        evaluate over fitting)
     % BETAfit is the matrix of coefficients uses to perform new ...
        predictions
OutputFit = [ones(size(Input(:,testInd).',1),1) ...
    Input(:,testInd).']*BETAfit; % Prediction on new data. The ...
    matrix in the square brackets is in the format request by the ...
    function
```

D.2.2 Non-Linear Method: NARX

The code has been developed by the information founded on MATLAB website (https://uk.mathworks.com/help/deeplearning/gs/neural-network-time-series-prediction-a html, https://uk.mathworks.com/help/deeplearning/ug/design-time-series-narx-feedback-n html, https://uk.mathworks.com/help/deeplearning/modeling-and-prediction-with-narx-and html)

```
rng('seed'); % Randomisation of the starting point for the ...
    subsequent random extraction and inisialization of regression ...
    method weights
Input = DB; Output = DM; % Variables to train the regression method
% 10 NARX have been trained. The one that best performs on new data ...
    has been seved.
for n = 1:10
    [trainInd,¬,testInd] = dividerand(size(Output,2),0.75,0,0.15); % ...
        Random extraction of indexes to select the training ...
        (trainInd) and new data (testInd) to test the trained method.
    tic
```

```
    [nets] = NARX(Input(:,trainInd),Output(:,trainInd),30); % ...
        Function that I made to train the NARX Neural Network
    toc
    [¬,¬,performance,¬] = ...
        ApplyNARX(nets,Input(:,testInd),Output(testInd)); % Function ...
        that I made to apply the network
    NNPerf(n,:) = [n performance]; % Store the performance of the ...
        networks
end
[BEST,¬] = find(NNPerf(:,2) == min(NNPerf(:,2))); % Find the network ...
    that perform the best:
```

Custom function

See Chapter A to further explanation on the main parameters to set to built a NARX. For the sake of clarity, options to visualize the network (`viev(net)`) or to visualize built-in analysis (`nntraintool`) have been removed in the code above.

This function trains a NARX with 1 hidden layer. `DB_train` represents the Input (magnetic field changes measured witht the magnetic field camera), `DM_train` represents the output (head position measured with the optical camera), `hn` represents the number of hidden neuron. The version of the function reported uses a fixed number of hidden neuron. An older version was made to automatically found the best number of the neuron in the single hidden layer method, but results over hundreds of run reports that there were not a privileged number of neurons (Figure ??).

```
function nets = NARX(DB_train,DM_train,hn)
    % This function trains a
    % DB_train = Input, magnetic field changes
    % DM_train = Output, head positions
    % hn = number of hidden neuron
    %%
    rng('shuffle');
    % Convert Input and Output data to standard neural network cell ...
        array form
    X = tonndata(DB_train,true,false);
    T = tonndata(DM_train,true,false);
    % Set the parameters of the Network:
    trainFcn = 'trainlm'; % Choose a Training Function - 'trainlm' ...
        corresponds to Levenberg-Marquardt backpropagation algorithm
    inputDelays = 1:2; % Delayed Input
    feedbackDelays = 1:2; % Feedback input
    hiddenLayerSize = hn;
    % Create the open-loop network used for the training
```

```
    net = ...
        narxnet(inputDelays,feedbackDelays,hiddenLayerSize,'open',trainFcn);
    % Further preprocessing/postprocessing
    net.inputs{1}.processFcns = {'removeconstantrows'};
    net.inputs{2}.processFcns = {'removeconstantrows'};
    [x,xi,ai,t] = preparets(net,X,{},T); % Prepare the Data for Training
    % Setup Division of Data for Training, Validation, Testing
    net.divideFcn = 'dividerand';  % Divide data randomly
    net.divideMode = 'time';  % Divide up every sample
    net.divideParam.trainRatio = 90/100;
    net.divideParam.valRatio = 5/100;
    net.divideParam.testRatio = 5/100;
    net.performFcn = 'mse'; % Choose a Performance Function
    [net,tr] = train(net,x,t,xi,ai); % Train the Network
    % Test the Network
    y = net(x,xi,ai);
    e = gsubtract(t,y);
    performance = perform(net,t,y);
    % Convert the network into a Step-Ahead Prediction Network ...
        (outputs are shifted one timestep)
    nets = removedelay(net);
    nets.name = [net.name ' - Predict One Step Ahead'];
    [xs,xis,ais,ts] = preparets(nets,X,{},T);
    ys = nets(xs,xis,ais);
    stepAheadPerformance = perform(nets,ts,ys);
end
```

The function applies the trained network using new input data (`Input`) and new output data (`Target`).

```
function  [Pred,Target,performance,Rmse] = ApplyNARX(nets,Input,Target)
    % Convert Input and Output data to standard neural network cell ...
        array form
    IN = tonndata(Input,true,false);
    TA = tonndata(Target,true,false);
    % Prepare the data for the NARX network
    [x,xi,ai,t] = preparets(nets,IN,{},TA);
    y = nets(x,xi,ai); % Predicted data
    e = gsubtract(t,y); % residuals
    % Evaluates the performance of the network
    performance = perform(nets,t,y);
    % Shift the predicted and target data
    Pred = cell2mat(y); Pred = Pred(:,3:end-1);
    Target = cell2mat(t); Target = Target(:,3:end-1);
    % Evaluate the error in the prediction (non built-in function)
    Rmse = ErrEval(Target.', Pred.', 'rmse');
end
```

D.3 Analysis of the results

Errors

This function calculate various statistical measurements for errors: Residual Sum of Squares (RSS) otherwise called Sum of Square due to Error (SSE); Total Sum of square (TSS); Coefficient of determination (R^2); Mean squared error (MSE); Root Mean Square Deviation (RMSD) otherwise Root Mean Square Error (RMSE); Normalized root-mean-square deviation (NRMSD, Normalizing the RMSD facilitates the comparison between data-sets or models with different scales.);

```matlab
function Err = ErrEval(Data,Prediction,Type)
    residuals = Data - Prediction;
    if strcmpi(Type,'rss') % Residual Sum of Squares
        rss = sum(residuals.^2,1);
        RSS = transpose(rss);
        Err = RSS;
    elseif strcmpi(Type,'tss') % Total Sum of square
        rss = sum(residuals.^2,1);
        tss = sum((Data - mean(Data,1)).^2,1);
        rsquare = rss./tss;
        RSquared = transpose(rsquare);
        Err = RSquared;
    elseif ...
        strcmpi(Type,'mse')||strcmpi(Type,'rmse')||strcmpi(Type,'nrmsd')
        mse = mean(residuals.^2,1);
            if strcmpi(Type,'mse') % Mean squared error (MSE)
                MSE = transpose(mse);
                Err = MSE;
                return
            end
                rmse = sqrt(mse);
            if strcmpi(Type,'rmse') % RMSE or RMSD(Root Mean Square ...
                Deviation)
                RMSE = transpose(rmse);
                Err = RMSE;
                return
            end
            if strcmpi(Type,'nrmsd') % Normalized root-mean-square ...
                deviation (NRMSD)
                NRMSD = rmse./(max(Data)-min(Data)); % ...
                    [Smallest,Largest] = bounds(M,2);
                NRMSD = transpose(NRMSD);
                Err = NRMSD*100;
                return
            end
    end
end
```

Linear Fit

Code to fit the predicted data as function of the measured data. Both the time series were motion data (6 rows, n-time-steps of columns). One head motion parameter (1 row, n-time-steps of columns) per time was analysed.

```
function [Results]= FitPredictions(Pred, Target)
% Pred = predicted data
% Targ = measured data (not used to train the regression method)
% Results = Table to summarise the results
%%
    % Initialisation of variables
    New = []; Predict = []; FitLine = []; Coeff = []; R2 = []; RMSE ...
        = []; PC = [];
    for m = 1:6
        % Select the motion parameters to analyse
        New = Target(m,:);
        Predict = Pred(m,:);
        % Perform the linear fit
        [fitresult, gof] = LinearFit(New, Predict); % See nested ...
            function
        Coeff(m,:) = coeffvalues(fitresult); % Extract the ...
            coefficients of the linear fit
        FitLine = Coeff(m,1).*New + Coeff(m,2); % Fitted line
        R2(m,1) = gof.rsquare; % R-squared (coefficient of ...
            determination) of the fit
        RMSE(m,1) = gof.rmse; % Root mean squared error (standard error)
        PearsCorr = corrcoef(FitLine,Predict); % Pearson coefficient
        PC(m,1) = PearsCorr(1,2);
        MSE(m,1) = ErrEval(New.',Predict.','MSE'); % Mean squared ...
            error of the prediction
        STD(m,1) = std(New,[],2); % Standard deviation
    end
% Summarise the results in a table
    Results = table(Coeff,R2,STD,MSE,PC,'RowNames', {'Tx [mm]','Ty ...
        [mm]','Tz [mm]','Rx [deg]','Ry [deg]','Rz [deg]'});
Results.Properties.VariableDescriptions ={...
    'Slope and Intercept coefficients of the linear regression: y = ...
        ax + b (ideal condition: a->1, b->0)',...
    'R^2 of the fit (how well the data are fitted by a line)',...
    'Standard deviation of the movements',...
    'Mean Squared Error of the prediction compared to the fit ()',...
    'Pearson Coefficient. 1 = correlate; 0 = non correlate; -1 = ...
        anti-correlate;'};
end
```

```
% Nested function that compute the linear fit
function [fitresult, gof] = LinearFit(NewData, Prediction)
    [xData, yData] = prepareCurveData( NewData, Prediction );
    ft = fittype( {'x', '1'}, 'independent', 'x', 'dependent', 'y', ...
        'coefficients', {'a', 'b'} ); % Set up fittype and options.
    [fitresult, gof] = fit( xData, yData, ft ); % Fit model to data.
end
```

D.4 Simulation of the extra-cranial magnetic field

Assuming that a head model is available, head motion parameters (`Tx, Ty, Tz, Rx, Ry, Rz`) and respiration signal (`RESP`) and distance between the probes and the stern (`ProbesStern`) have been measured.

```
% Code to simulate the magnetic field changes due to motion
    Head; % Head model
    Head = Victor(Head); % Non built-in function, see next ...
        subsection. Return a binary representation of the volume
    Head = Head.*-9; % Assign Magnetic susceptibility of water to ...
        the pixels classify as head tissue and cavity (1)

    % Rotate the Head model:
    Head = HeadMov(Head, Tx, Ty, Tz, Rx, Ry, Rz, varargin)

    % Evaluate the magnetic field [T]
    Field_0 = FieldFFT(Head); % Non built-in function, see next session.

    % Once the field has been evaluated, it is sampled at the ...
        coordinates that correspond to the probe positions. This ...
        part has not been reported as it depends on the ...
        configuration chosen.

    DB_p = Field_0(X_coordinates, Y_coordinates, Z_coordinates); % ...
        Magnetic field sampled at probe position

    % Mangetic field changing due to respiration [T]
    DB_r = NoiseRESP(RESP, ProbesStern);

    % White noise [T] due to the electronics and other sources ...
        evaluated experimentally
    rng('shuffle');
    White = random('Normal',0,1,size(B,1),size(B,2)).*1e-8;

    % The components can be then superimposed:
    % DB = DB_p; % Magnetic field due to only the head movements
```

```
    % DB = DB_p + DB_r + White; % Approximation of real measurements
```

D.4.1 Non built-in function

Create a binary 3D model of the head. From the head model obtained from the segmentation of the MR images, a head model where pixels representing air are classified as 0 and pixels that represents head (wothout no cavity) are classified as 1 is created.

```
function Victor = Victor(ntest)
% ntest = head model obtained from the segmentation of the MR images
% Victor = head model where pixels representing air are classified ...
    as 0 and pixels that represents head (wothout no cavity) are ...
    classified as 1
%%
    Victor = zeros(size(ntest)); % Pre-allocate memory
    % 2) Find the external faces
    for z = 1: size(ntest,3)
        for x = 1: size(ntest,1)
            Anterior = find(ntest(x,:,z),1,'first'); % 'first', ...
                which finds the first n indices corresponding to nonzero
            Posterior = find(ntest(x,:,z),1,'last'); % 'last', finds ...
                the last n indices corresponding to nonzero
            Victor(x,Anterior:Posterior,z) = 1;
        end
    end
end
```

Homogeneous transformation for 3D head rotation

```
function Head = HeadMov(Volume, Tx, Ty, Tz, Rx, Ry, Rz, varargin)
% Function to rotate the head model.
    alpha = Rx; beta = Ry; gamma = Rz;% Assign head motion ...
        parameters to angles
    % Rotation matrix:
        R_x = [1 0 0 ;0 cosd(alpha) -sind(alpha); 0 sind(alpha) ...
            cosd(alpha)];
        R_y = [cosd(beta) 0 sind(beta); 0 1 0; -sind(beta) 0 ...
            cosd(beta)];
        R_z = [cosd(gamma) -sind(gamma) 0; sind(gamma) cosd(gamma) ...
            0; 0 0 1];
        R_head = R_z*R_y*R_x; %Simulation Frame
        % Trasformation matrix (Matlab format)
        t(1:3,1:3) = transpose(R_head);
        t(4,1:3) = transpose([Tx Ty Tz]);
```

```
        t(1:4,4)=[0 0 0 1];
        tform = affine3d(t); % Compute the affine 3D rotation
    Rin = imref3d(size(Volume)); % Reference the volume to World ...
        coordinate
    if nargin > 7
        if strcmpi(varargin{1,1},'Centre') % performing rotation by ...
            the centre of the volume
            Rin.XWorldLimits = Rin.XWorldLimits-mean(Rin.XWorldLimits);
            Rin.YWorldLimits = Rin.YWorldLimits-mean(Rin.YWorldLimits);
            Rin.ZWorldLimits = Rin.ZWorldLimits-mean(Rin.ZWorldLimits);
        end
        Head = imwarp(Volume,Rin,tform,'OutputView',Rin); % Apply ...
            the geometric transformation
    else
        Head = imwarp(Volume,tform);
    end
end
```

Physiological Noise

```
function  DB = NoiseRESP(RESP, ProbesStern)
% Code to simulate the Physiological Noise from paper (Raj D et all, ...
    September 2000)
% RESP = respiration signal recorded using the belt
% ProbesStern = 3D coordinates [m] of the distance between the ...
    probes and the stern
%%
    Dchi = 9.4*10^-6; % Magnetic susceptibility of the air (20% ...
        Oxigen mixture)
    %
    % Numerator:
    B0 = 7; %[T]
    R = 0.08; % [m], 8 cm radius of the sphere
    x = ProbesStern(:,1); y = ProbesStern(:,2); z = ProbesStern(:,3);
    num = (Dchi*B0*R^3*(2*z.^2-x.^2-y.^2))/3; % minmax() = 0.0005    ...
        0.0012 T
    num = num.*RESP;
    % Denominatore
    den = sqrt(sum(ProbesStern.^2,2)).^5;
    % Results:
    DB = num./den;
end
```

FFT method

It requires square 3D volume that represents the head.

```
% Code to simulate the magnetic field changes
function Field = FieldFFT(Head)
% This function i based on the paper (Marques, Bowtell 2008)
% Head = Head model
%%
%
u0 = 4*pi*1e-7; % Permeability of the vacum. Bo = u0(H+M)
EMkz = fftn(Head)*B0/u0; % 3D FFT of the data set
% Make 3D arrays of k_x, k_y and k_z allowing for the FFTshift ...
    organisation
% of data
dims = size(Head);
kx = fftshift((-dims(1)/2):(dims(1)/2-1));
ky = fftshift((-dims(2)/2):(dims(2)/2-1));
kz = fftshift((-dims(3)/2):(dims(3)/2-1));
kxmat = repmat(reshape(kx,[dims(1) 1 1]),[1 dims(2) dims(3)]);
kymat = repmat(reshape(kx,[1 dims(2) 1]),[dims(1) 1 dims(3)]);
kzmat = repmat(reshape(kx,[1 1 dims(3)]),[dims(1) dims(2) 1]);
% Original formula from the paper:
% DipFieldk = ...
    -u0/3*(3*(kzmat*cos(theta)-kymat*sin(theta)).^2./(kxmat.^2+kymat.^2+kzmat.^2)-1).*
% Has been simplified as head model is imputed already rotated ...
    (theta = 0)
DipFieldk = -u0/3*(3*(kzmat).^2./(kxmat.^2+kymat.^2+kzmat.^2)-1).*EMkz;
DipFieldk(1,1,1)=0;
DipField = real(ifftn(DipFieldk)); % inverse 3D FFT to get dta in ...
    real space
% The field is usually simulated in Tesla:
Field = 10^-6 *DipField; %[T]
% but it could be simulated in Hz by: Field = 42.57  *DipField; %[Hz]
%
end
```

D.5 Coils

D.5.1 Simulate the magnetic field generated by the coil system

This code assume that the movements of the probes are defined (Mov), translations are expressed in meters and rotations are expressed in radiants.

```
% Define the coils origins and orientations:
sa = [0; -1; 0] ;  % first dipole direction, (direction: anterior)
rca = [0.02;-0.08;0.02]; % [m] first dipole position
sb = [0; 0; 1] ; % second dipole direction, (direction: feet head)
rcb = [-0.02;-0.08;-0.02];% [m] second dipole position
```

```
% Define the probe positions
[Probes,¬]= Elly('np',100,'nr',50);
% To select only the upper part of the ellipses, only the probes ... with negative coordinate along the y (AP) axes are selected
Probes = Probes(find(Probes(:,2)≤0),:);
% % Create the grid coordinate:
X = Probes(:,1); X = reshape(X,[50,50]);
Y = Probes(:,2); Y = reshape(Y,[50,50]);
Z = Probes(:,3); Z = reshape(Z,[50,50]);

% - % This part need to be repeated for each time-steps to simulate
for t = 1:size(M,2)
    % Displacement (milli meters):
    dx = Mov(1,t); dy = Mov(2,t);dz = Mov(3,t); % Tx,Ty,Tz [mm]
    % Define rotations (degrees):
    pitch = Mov(4,t); roll = Mov(5,t); yaw = Mov(6,t); % Rx, Ry, Rz ... [rad]
Tr = HomoExtr(dx,dy, dz, pitch, roll, yaw,'Rad'); % Apply the ... homogeneous transformation, see below for the code
% New position and orientations of the coils at t:
    rca_1 = Tr * [rca ; 1];
    rcb_1 = Tr * [rcb ; 1];
    rca_1 = rca_1(1:3);
    rcb_1 = rcb_1(1:3);

    Ts = HomoExtr2(0, 0, 0, pitch, roll, yaw, 'Rad'); % Coil ... orientation after the transformation
    R = Ts(1:3,1:3);
    sa_1 = R*sa;
    sb_1 = R*sb;
    % To check if the norm of the vector is still 1 (otherwise it ... doesn't represents orientation): norm(san) = 1; norm(sbn) = 1;
% Calculate the Bz fields for t:
    % Coil A
    [x,y,z] = ProbesCoilDist(X,Y,Z,rca_1);
    Bzsa = fincoilmultiturn_LB2(sa_1,x,y,z);
    clear x y z;
    % Coil B
    [x,y,z] = ProbesCoilDist(X,Y,Z,rcb_1);
    Bzsb = fincoilmultiturn_LB2(sb_1,x,y,z);
    % White Gaussian noise to model NMR probes noise
    White = random('Normal',0,1).*W.*1e-8;
% Resulted field:
    Bzs(:,t) = Bzsa + Bzsb + White;
end
```

D.5.2 Prediction

Once data have been simulated (`Bzs`), they can be used for the prediction. This code assumes that the magnetic momentum of the dipole (`M`), and probe positions coordinates (`X`,`Y`,`Z`) are defined. Also, the standard deviation of the movements (`STD`) has been evaluated previously ($10^{-}4$ m or deg).

```
 % M = magnetic momentum of the dipole
 % X = probe positions coordinate
 % Y = probe positions coordinate
 % Z = probe positions coordinate
 % STD = standard deviation of the motion parameters

for t = 2:size(Bzs,2)
    % Evaluate the changing in magnetic field
    Bzdifftest = Bze(:,t)-Bzs(:,1);

 % Set the options for fminsearch function
    options = ...
        optimset('MaxFunEvals',1000000,'TolX',1e-14,'TolFun',1e-14); ...
        %'PlotFcns',@optimplotfval,'Display','final',

if t == 2 % First guess of the prediction
    dxg = random('Normal',0,STD(1,1));%.*f;
    dyg = random('Normal',0,STD(2,1));%.*f;
    dzg = random('Normal',0,STD(3,1));%.*f;
    pitchg = random('Normal',0,STD(4,1));%.*f;
    rollg = random('Normal',0,STD(5,1));%.*f;
    yawg = random('Normal',0,STD(6,1));%.*f;
 else
    % P(:,t-1) is the predicted value at the previous time step
    dxg = P(1,1) + random('Normal',0,STD(1,1)).*f;
    dyg = P(2,1) + random('Normal',0,STD(2,1)).*f;
    dzg = P(3,1) + random('Normal',0,STD(3,1)).*f;
    pitchg = P(4,1) + random('Normal',0,STD(4,1)).*f;
    rollg = P(5,1) + random('Normal',0,STD(5,1)).*f;
    yawg = P(6,1) + random('Normal',0,STD(6,1)).*f;
    clear P
 end

     P0 = [dxg dyg dzg pitchg rollg yawg];
     [P,fval,exitflag,output,Time] = ...
        PredictionCoils('P0', P0, 'options', options, 'M', M, 'sa', ...
            sa, 'sb', sb, 'rca', rca,...
             'rcb',rcb, 'X', X, 'Y', Y, 'Z', Z, 'Bzs', Bzs, ...
                 'Bzdifftest', Bzdifftest);
 % Store the prediction: P(:,t)
```

```
end
```

D.5.3 Custom functions

Coils parameters

Coils parameters have been stored in a mock function to be recalled in each code that have been used.

```
function [N, I, A] = Coil_m(varargin)
    nwz = 10; %number of windings along the axis
    nwr = 10; %number of windings along the radius
    wt = 0.23*1e-3; %0.25 mm *1e-3 = [m], wire thickness
    rc = mean([2.69,2.52])*1e-3; % 2.6 *1e-3 = [m], internal radius
    % internal diameter = 5 mm
    R = 12;%[Ohm]
    V = 3.6;%[V]
    % Parameters:
    N = nwz*nwr; % Turns of the copper wire in the coil
    I = Current(R,V); %[A] % Current (¬100 mA) current to pilot the coil
    A = AvAreaDip(rc,wt,nwr); % Average area over different radii
end

%% Nested functions
function A = AvAreaDip(rc,wt,nwr)
% A = pi*r^2 , area of the circumference
% To evaluate the average area over different radius
    A = 0;
    for ir = 1:nwr
        r = rc+(ir-0.5)*wt;
        A = A+pi*r^2;
    end
    A = A/nwr;
end
%
function I = Current(R,V)
    % If V = R*I [Volt]
    I = V/R; %[Ampere]
end
```

Define the coordinates of the grid of probes

This function has been used to define a uniformly distributed points to sample the simulated magnetic field in a transmit-head coil shape

```
function [Probes, NameE] = Elly(varargin)
% Considering the Oval ring
% 'np' number of point
% 'nr' number of rings
% 'Proj' = Project actual position of probes on ellipses surface
% 'Cy' = Cylinder,
    % rM=Rm
% 'Minor' = [mm] value of the minor axes
    % rm = mean([abs(Probes1(3,1)-Probes1(4,1)), ...
        abs(Probes1(7,1)-Probes1(8,1))],2);
% 'Major' = [mm] value of the major axes
    % rM = mean([abs(Probes1(5,2)-Probes1(6,2)), ...
        abs(Probes1(2,2)-Probes1(9,2))],2);
% 'Res' = resolution of the simulation mm/px and proportional constant
    % Res = 0.5 [mm/px]
% 'Iso' = Centre of coordinate, defoult = [0 0 0]
    % Simulation: Iso = [350 350 350]
% 'Shift' = shift the probes position to adjust the projection [m]

% 'Limits' = Coordinate z of the first and last ring to simulate
    % [min(Probes1(:,3)),max(Probes1(:,3)];
%'Prop' = Proportional factor to scale the ellipses given
%%
%% Check varargin
if exist('varargin') %LineWidth, RM, Conf options
    for a = 1:size(varargin,2)
        if strcmpi(varargin{1,a},'nr') % 'nr' number of rings
            nr = varargin{1,a+1};
        end
        if strcmpi(varargin{1,a},'np') % 'np' number of point
            np = varargin{1,a+1};
        end
        if strcmpi(varargin{1,a},'Proj') % Project actual position ...
           of probes on ellipses surface
            Probes = varargin{1,a+1};
            Proj = true;
        end
        if strcmpi(varargin{1,a},'Cy') % 'Cy' = Cylinder,
            rM = varargin{1,a+1};
            Rm = varargin{1,a+1};
        end
        if strcmpi(varargin{1,a},'Minor') % Minor axes of the ellipses
            Rm = varargin{1,a+1};
        end
        if strcmpi(varargin{1,a},'Major') % Major axes of the ellipses
            rM = varargin{1,a+1};
        end

        if strcmpi(varargin{1,a},'Res') % Unit of measure
```

```
            res = varargin{1,a+1};
        end
        if strcmpi(varargin{1,a},'Iso') % Isocentre
            Iso = varargin{1,a+1};
        end
        if strcmpi(varargin{1,a},'Shift') % To do not centre the ...
           system compare to the isocentre
            Shift = varargin{1,a+1};
        end
        if strcmpi(varargin{1,a},'Limits') % Edges on head feet ...
           direction
            Limits = varargin{1,a+1};
        end
        if strcmpi(varargin{1,a},'Prop') % Factor to scale the ellipses
           Prop = varargin{1,a+1};
        end
    end
end
clear a;
% If you give just one axes, the other is evaluated in proportion: ...
   rM:Rm = major:minor
if or(exist('Rm'),exist('rM'))
    if not(exist('Rm')) % minor:
        Rm = 260*rM/281;
    elseif not(exist('rM')) % major:
        rM = 281*Rm/260;
    end
end

% Check wich variables have been created and define the default values
if not(exist('Proj','var'))
     Proj = false;
end
if not(exist('Rm','var')) % minor:
    %[m] Default value minor axes of ellipses
     Rm = (190+(260-190)/2)*10^-3; % [m]
end
if not(exist('rM','var'))% major:
    %[m] Default value major axes of ellipses
    rM = (250+(281-250)/2)*10^-3;
end
if not(exist('res','var'))
    res = 1; %[mm/px] Default resolution
end
if not(exist('Iso','var'))
    Iso = [0 0 0]; %[mm] Default resolution
end
if not(exist('Shift','var'))
    Shift = [0 0 0]; %[mm] Do not shift
```

```
end
if not(exist('Prop','var'))% Change the diameter of the ellipses
    Prop = 1; %Default proportional constant
end
if not(exist('Limits','var'))% Change the diameter of the ellipses
%     Limits = [-(225)/2, +(225)/2]; %Default dimension of the head coil
Limits = [-(225)/2.*10^-3, +(225)/2.*10^-3]; %Default dimension of ...
    the head coil
end
%%
if Proj == false %Proj == false
% Define a series of angles: 360/ number of probes
theta = linspace(0,2*pi,np);
for t = 1:np
%     % Prop changes the diameter of the ellipses
    Y(1,t) = ((Prop*rM)/2)*cos(theta(1,t));
    X(1,t) = ((Prop*Rm)/2)*sin(theta(1,t));
end
%
% Generate the coordinate z (HF direction) of the rings dividing ...
    Limits/number of rings
av = linspace(Limits(1,1), Limits(1,2),nr);
    % create a new probes positions
    p = 1;
    for r =1:nr %number of rings
        for n = 1:np % coordinate
        Probes(p,:) = [X(1,n),Y(1,n),av(1,r)];
        NameE{p,:} = sprintf(['P%d' '_' '%d'],r,n);
        p = p+1;
        end
    end
clear r n p

elseif Proj==true
% Name associated with the Position
NameE = cell(size(Probes,1),1);
    for p = 1:size(Probes,1) % coordinate
    NameE{p,:} = sprintf(['P%d'],p);
    end
clear p

% Projecting given position on the ellipse surface
    a = Rm/2; % [m]
    b = rM/2; % [m]

    for p = 1:size(Probes,1)
        if Probes(p,2)<0
            Probes(p,2) = ...
                -realsqrt(abs((1-((Probes(p,1)^2)/(a^2)))*b^2));
```

```
        else
            % Probes on the back are closer to the head
            Probes(p,2) = ...
                +realsqrt(abs((1-((Probes(p,1)^2)/(a^2)))*b^2));
        end
    end

end
% Shift the ellipses to stay closer to the head [m]
if size(Shift,1)<size(Probes,1)
    Probes = Probes + repmat(Shift,size(Probes,1),1);
elseif size(Shift,1)== size(Probes,1)
    Probes = Probes + Shift;
end
% Change the frame
if res ==1
    Probes = (Probes./res) + repmat(Iso,size(Probes,1),1); % [m]
else
    Probes = round((Probes./res) + repmat(Iso,size(Probes,1),1)); % px
    %round((Probes./0.0005)+350));
end
```

Probe-coils distances

This function has been used to evaluate the difference between the position of each probes and coils:

```
function [x,y,z] = ProbesCoilDist(X,Y,Z,rc)
    % rc = coil position [x y z];
    % X grid on x plane
    % Y grid on y plane
    % Z grid on z plane
    %%
    x = X-rc(1);
    y = Y-rc(2);
    z = Z-rc(3);
end
```

Evaluate the B_z field

```
function [Bz] = fincoilmultiturn(s,x,y,z)
% See ...
    http://nbviewer.jupyter.org/github/tiggerntatie/emagnet-py/blob/...
        master/offaxis/off_axis_loop.ipynb for fully code explanation
```

```
% s = orientation [rad]
% x,y,z = position [m]
%%
% Define coil parameters:
I = 0.3; % Current [Ampere]
NR = 10; % number of turns in radial direction
NZ = 10; % number of turns in z-direction
wt = 0.23e-3; % wire diameter [mm]
Rin = 2.6e-3; % radius of bobbin on which coil is wound [m]
%

Bz = zeros(size(x)); % assume x,y,z measured to coil centre

for ir = 1:NR
    a = Rin+(2*ir-1)/2*wt; % radius of this coil loop
    for iz = 1:NZ
        zoff = (iz-(NZ+1)/2)*wt; % z-offset from coil centre of this ...
           loop
        zt = z+zoff;
        zs = s(1)*x+s(2)*y+s(3)*zt;  % component of field point to ...
           coil distance vector that is parallel to coil axis
        rhosx = x-zs*s(1); % find component that is perpendicular to ...
           coil axis ie radial wrt to coil
        rhosy = y-zs*s(2);
        rhosz = zt-zs*s(3);
        rhos = sqrt(rhosx.^2+rhosy.^2+rhosz.^2);  % length of radial ...
           part
        unirhosz = rhosz./rhos; % tells about angle vector makes in ...
           coil plane
        unirhosz(isnan(unirhosz)) = 0;
        unirhosz(isinf(unirhosz)) = 0;

        alpha = rhos./a;
        beta = zs./a;
        gamma = zs./rhos;
        Q = (1+alpha).^2+beta.*beta;
        M = (4*alpha./Q);
        B_0 = I*2*pi*1.0e-7/a;
        [K,E] = ellipke(M); % elliptical integrals

        Bzp = ...
           B_0/pi./sqrt(Q).*(E.*(1-alpha.*alpha-beta.*beta)./(Q-4.*alpha)+K); ...
                  % axial field
        Brp = ...
           B_0*gamma./pi./sqrt(Q).*(E.*(1+alpha.*alpha+beta.*beta)./(Q-4.*alpha)-K);
           % radial field
    Bz = Bz+Bzp*s(3)+Brp.*unirhosz;
    end
end
```

```

end
```

Homogeneous transformation

```
function Tr = HomoExtr(dx, dy, dz,pitch, roll, yaw)
    Tr = zeros(4); % Transformation matrix
    Tr(1:3,1:3) = RotationRad(pitch, roll, yaw); % Rotation matrix ... for extrinsic rotation % Rotation
    Tr(1:3,4) = [dx; dy; dz]; % displacement along the axes
    Tr(4,4) = 1; % scaling factor
%
% Nested function
function R = RotationRad(pitch, roll, yaw)
    % Extrinsic rotation: https://en.wikipedia.org/wiki/Rotation_matrix
    % Body rotation referred to external system of reference.
    %%
    alpha = yaw; beta = pitch; gamma = roll;
    Rx = [1 0 0;0 cos(alpha) -sin(alpha);0 sin(alpha) cos(alpha)];
    Ry =  [cos(beta) 0 -sin(beta); 0 1 0; sin(beta) 0 cos(beta)];
    Rz = [cos(gamma) -sin(gamma) 0; sin(gamma) cos(gamma) 0; 0 0 1];
    R = Rz*Ry*Rx; %Rotation matrix for extrinsic rotation
end
end
```

Prediction

```
function  varargout = PredictionCoils(varargin)
% ... https://uk.mathworks.com/help/matlab/math/parameterizing-functions.html
% https://uk.mathworks.com/help/optim/ug/passing-extra-parameters.html
% Arg In
tic
for n = 1: nargin-1
    if strcmpi(varargin{1,n},'P0')
        P0 = varargin{1,n+1};
    elseif strcmpi(varargin{1,n},'Options')
        options = varargin{1,n+1};
     elseif strcmpi(varargin{1,n},'sa')
        sa = varargin{1,n+1};
     elseif strcmpi(varargin{1,n},'sb')
        sb = varargin{1,n+1};
```

```
     elseif strcmpi(varargin{1,n},'rca')
        rca = varargin{1,n+1};
     elseif strcmpi(varargin{1,n},'rcb')
        rcb = varargin{1,n+1};
     elseif strcmpi(varargin{1,n},'M')
        M = varargin{1,n+1};
     elseif strcmpi(varargin{1,n},'X')
        X = varargin{1,n+1};
     elseif strcmpi(varargin{1,n},'Y')
        Y = varargin{1,n+1};
     elseif strcmpi(varargin{1,n},'Z')
        Z = varargin{1,n+1};
     elseif strcmpi(varargin{1,n},'Bzs')
        Bzs = varargin{1,n+1};
     elseif strcmpi(varargin{1,n},'Bzdifftest')
        Bzdifftest = varargin{1,n+1};
    end
end

[P,fval,exitflag,output] = ...
    Regression(P0,options,M,sa,sb,rca,rcb,X,Y,Z,Bzs,Bzdifftest);

varargout{1,1} = P;
varargout{1,2} = fval;
varargout{1,3} = exitflag;
varargout{1,4} = output;
varargout{1,5} = toc;

%%
% Nested functions
function [P,fval,exitflag,output] = ...
    Regression(P0,options,M,sa,sb,rca,rcb,X,Y,Z,Bzs,Bzdifftest)
    % To trick the nested function and to give the input as a paired ...
        list of name and variable
    [P,fval,exitflag,output] = fminsearch(@costfn_Ex_Mult,P0,options);
end
%
function [F] = costfn_Ex_Mult(P0)
    % Cost function is equal to the simulation code
    dx = P0(1);
    dy = P0(2);
    dz = P0(3);
    pitch = P0(4);
    roll = P0(5);
    yaw = P0(6);

    Tr = HomoExtr(dx, dy, dz, pitch, roll, yaw, 'Rad');

    % New position vector:
```

```
    rca_1 = Tr * [rca ; 1];
    rcb_1 = Tr * [rcb ; 1];
    rcan = rca_1(1:3);
    rcbn = rcb_1(1:3);
    clear rca_1 rcb_1 Tr;
    % % Do rotation and translation:
    % rcan = R*rca; %rca new
    % rcbn = R*rcb; %rcb new
    % %coil position after a rotation
    % rcan = rcan + T;
    % rcbn = rcbn + T;

    % Coil orientation after a rotation and translation
    Ts = HomoExtr2(0, 0, 0, pitch, roll, yaw, 'Rad');
    R = Ts(1:3,1:3); clear Ts;
    san = R*sa;
    sbn = R*sb;

    % Difference in position of each probe point and coil
    [x,y,z] = ProbesCoilDist(X,Y,Z,rcan);
    Bzea = fincoilmultiturn_LB2(san,x,y,z);
    [x,y,z] = ProbesCoilDist(X,Y,Z,rcbn);
    Bzeb = fincoilmultiturn_LB2(sbn,x,y,z);
    Bze = Bzea+Bzeb;

    % Changing
    Bzdiff = Bze-Bzs;

    difference = Bzdiff-Bzdifftest;
    F = norm(difference);
end

end
```

D.6 Synthetic head movements

```
function [Mov] = ArtHeadMov(varargin)
%'Time',t
% Resp =[0,1] -> f_resp within [0.20 - 0.40]
% PPU =[0,1] -> f_ppu within [0.80 - 1.00]
% Nod =[0,1] -> f_nod within [0.10 - 0.9]
% Shake =[0,1] -> f_shake within [0.01 - 0.05]
% Modulation =[0,1] -> f_mod within [0.01 - 0.05]

% Example to call the function:
```

```
% input arguments equal to 1 indicated components of the movement ...
    that will be simulated
% ...
    ArtHeadMov('Time',linspace(0,0.15*1000,1000),'Resp',1,'Ppu',0,'Nod',0,'Shake',0,'N
%%
for v = 1: nargin
    if strcmpi(varargin{1,v},'Time')
        t = varargin{1,v+1};
% % Time vector. Skope repetition time: 0.150 ms.
% % Example: take 1000 Dynamic, TR = 150 ms -> 1000*150 = 150 s
% t = linspace(0,0.15*1000,1000);
%
    elseif strcmpi(varargin{1,v},'Resp')
    % Respiration
%           Resp = varargin{1,v+1};
        if varargin{1,v+1} %if Resp is not 0
            f_resp = Rand(0.2,0.4);
            a_resp = Rand(0,5);
            Resp = MOV(f_resp, a_resp,t,'Resp');
            Resp = mapminmax(Resp);
            Resp = repmat([1e0; 4*1e-1; 1e0; 1e0; 3*1e-1; ...
                6*1e-1;],[1,size(Resp,2)]).*Resp;
            Mov.Resp.Frequency = f_resp;
            Mov.Resp.Amplitude = a_resp;
            Mov.Resp.Mov = Resp;
        else
            Resp = zeros(6,size(t,2));
            Mov.Resp.Frequency = 0;
            Mov.Resp.Amplitude = 0;
            Mov.Resp.Mov = Resp;
        end

    elseif strcmpi(varargin{1,v},'Ppu')
    % Peripheral pulse
        if varargin{1,v+1} %if Resp is not 0
            f_ppu = Rand(0.8,1.0);
            a_ppu = Rand(0,1);
            Ppu = MOV(f_ppu, a_ppu,t,'Ppu');
            Mov.Ppu.Frequency = f_ppu;
            Mov.Ppu.Amplitude = a_ppu;
            Mov.Ppu.Mov = Ppu;
        else
            Ppu = zeros(6,size(t,2));
            Mov.Ppu.Frequency = 0;
            Mov.Ppu.Amplitude = 0;
            Mov.Ppu.Mov = Ppu;
        end

    elseif strcmpi(varargin{1,v},'Nod')
```

```
    % Head nodding movement
        if varargin{1,v+1} %if Resp is not 0
            f_nod = Rand(0.1,0.9);
            a_nod = Rand(0,15);
            Nod = MOV(f_nod, a_nod,t,'Nod');
            Mov.Nod.Frequency = f_nod;
            Mov.Nod.Amplitude = a_nod;
            Mov.Nod.Mov = Nod;
        else
            Nod = zeros(6,size(t,2));
            Mov.Nod.Frequency = 0;
            Mov.Nod.Amplitude = 0;
            Mov.Nod.Mov = Nod;
        end

    elseif strcmpi(varargin{1,v},'Shake')
    % Head shaking movement
        if varargin{1,v+1} %if Resp is not 0
            f_shake = Rand(0.1,0.9);
            a_shake = Rand(0, 15);
            Shake = MOV(f_shake, a_shake,t,'Shake');
            Mov.Shake.Frequency = f_shake;
            Mov.Shake.Amplitude = a_shake;
            Mov.Shake.Mov = Shake;
        else
            Shake = zeros(6,size(t,2));
            Mov.Shake.Frequency = 0;
            Mov.Shake.Amplitude = 0;
            Mov.Shake.Mov = Shake;
        end

    elseif strcmpi(varargin{1,v},'Modulation')
        if varargin{1,v+1} %if Resp is not 0
            Mod_r = zeros(6,size(t,2));
%             % Random component
            for r = 1:6
                x = normrnd(0,0.1,[1,size(t,2)]);
                Mod(r,:) = x.*sin(x.^2)+x.^3;
                Mod(r,:) = mapminmax(Mod(r,:));
            end
            Mod = repmat([1e0; 4*1e-1; 1e0; 1e0; 3*1e-1; ...
                6*1e-1;],[1,size(Mod,2)]).*Mod;
            Mov.Mod.Mov = Mod;
        else
            Mod = zeros(6,size(t,2));
            Mov.Mod.Frequency = 0;
            Mov.Mod.Amplitude = 0;
            Mov.Mod.Mov = Mod;
        end
```

```
    end
 end

Mov.Mov = Resp + Ppu + Nod + Shake + Mod;
Mov.Time = t;

% Offcentre
Mov.OffCentre = sort(normrnd(0,15,[1 3])).';
% Angulations
Mov.Angulation = sort(normrnd(0,1,[1 3])).';

end

%% %Local functions

function r = Rand(min,max)
%% Frequency in a given range
% ...
    https://uk.mathworks.com/help/matlab/math/floating-point-numbers-within-specific-
         r = (max-min).*rand(1,1) + min;
end
%%

%%
function m = MOV(f,a,t,mov)
% frequency
% Amplitude
% Which movement
%% Amplitutdes of each contribute
%r = normrnd(mu,sigma,sz) generates an array of normal random ...
    numbers, where vector sz specifies size(r).
A = sort(normrnd(0,a,[1 3])); % Amplitude of [Rx, Ry, Rz]

    if strcmpi(mov,'Resp')
        A = [A(1,3); A(1,1); A(1,2)]; % Most of the contribuition on Rx
    elseif strcmpi(mov,'Ppu')
        A = [A(1,3); A(1,1); A(1,3)];  % Most of the contribuition ...
            on Rx, Rz
    elseif strcmpi(mov,'Nod')
        A = [A(1,3); 0; 0]; % Most of the contribuition on Rx
    elseif strcmpi(mov,'Shake')
        A = [0; 0; A(1,3)]; % Most of the contribuition on Rx
    elseif strcmpi(mov,'Modulation')
        A = [A(1,2); A(1,1); A(1,2)]; % Most of the contribuition on ...
            Rx, Rz
    end

% Wave equation: S(t) = A cos( omega t + phy)
```

```
% Rotation simulated as as superimposition of waves
R = A.* cos(2*pi*f.*t + rand());

% Translation as projection of rotation
T = -atan(sind(R)./cosd(R)).*1e-1;

% Movements
m = [T;R];
end
```

D.7 List of built-in Matlab functions used

- bsxfun - https://uk.mathworks.com/help/matlab/ref/bsxfun.html
- mapstd - https://uk.mathworks.com/help/deeplearning/ref/mapstd.html
- std - https://uk.mathworks.com/help/matlab/ref/std.html
- pca - https://uk.mathworks.com/help/stats/pca.html
- linkage - https://uk.mathworks.com/help/stats/linkage.html
- max - https://uk.mathworks.com/help/matlab/ref/max.html
- cluster - https://uk.mathworks.com/help/stats/cluster.html
- sort - https://uk.mathworks.com/help/matlab/ref/sort.html
- var - https://uk.mathworks.com/help/matlab/ref/var.html
- ismember - https://uk.mathworks.com/help/matlab/ref/double.ismember.html
- unique - https://uk.mathworks.com/help/matlab/ref/double.unique.html
- rng - https://uk.mathworks.com/help/matlab/ref/rng.html
- dividerand - https://uk.mathworks.com/help/deeplearning/ref/dividerand.html
- plsregress - https://uk.mathworks.com/help/stats/plsregress.html
- tonndata - https://uk.mathworks.com/help/deeplearning/ref/tonndata.html
- narxnet - https://uk.mathworks.com/help/deeplearning/ref/narxnet.html
- preparets - https://uk.mathworks.com/help/deeplearning/ref/preparets.html
- openloop - https://uk.mathworks.com/help/deeplearning/ref/openloop.html
- closeloop - https://uk.mathworks.com/help/deeplearning/ref/closeloop.html
- trainlm - https://uk.mathworks.com/help/deeplearning/ref/trainlm.html
- sum - https://uk.mathworks.com/help/matlab/ref/sum.html
- transpose - https://uk.mathworks.com/help/matlab/ref/transpose.html
- mean - https://uk.mathworks.com/help/matlab/ref/mean.html
- sqrt - https://uk.mathworks.com/help/matlab/ref/sqrt.html

- preparecurvedata - https://uk.mathworks.com/help/curvefit/preparecurvedata.html
- fit - https://uk.mathworks.com/help/curvefit/fit.html
- coeffvalues - https://uk.mathworks.com/help/curvefit/cfit.coeffvalues.html
- corrcoef - https://uk.mathworks.com/help/matlab/ref/corrcoef.html
- find - https://uk.mathworks.com/support/search.html
- affine3d - https://uk.mathworks.com/help/images/ref/affine3d.html
- imref3d - https://uk.mathworks.com/help/images/ref/imref3d.html
- imwarp - https://uk.mathworks.com/help/images/ref/imwarp.html
- fminsearch - https://uk.mathworks.com/help/matlab/ref/fminsearch.html